EXPERIMENTAL AND ANALYTICAL INVESTIGATIONS OF THE THERMAL BEHAVIOR OF PRESTRESSED CONCRETE BRIDGE GIRDERS INCLUDING IMPERFECTIONS

A Thesis
Presented to
The Academic Faculty

by

Jong-Han Lee

In Partial Fulfillment
of the Requirements for the Degree
Doctor of Philosophy in the
School of Civil and Environmental Engineering

Georgia Institute of Technology
Atlanta, GA

August 2010

EXPERIMENTAL AND ANALYTICAL INVESTIGATIONS OF THE THERMAL BEHAVIOR OF PRESTRESSED CONCRETE BRIDGE GIRDERS INCLUDING IMPERFECTIONS

Approved by:

Dr. Kenneth M. Will, Chairman
School of Civil and Environmental Engineering
Georgia Institute of Technology

Dr. Leroy Z. Emkin
School of Civil and Environmental Engineering
Georgia Institute of Technology

Dr. Lawrence F. Kahn
School of Civil and Environmental Engineering
Georgia Institute of Technology

Dr. Yogendra Joshi
School of Mechanical Engineering
Georgia Institute of Technology

Dr. Abdul-Hamid Zureick
School of Civil and Environmental Engineering
Georgia Institute of Technology

Data Approved: [7/01/2010]

ACKNOWLEDGEMENTS

First and foremost, I would like to gratefully and sincerely thank my advisor, Dr. Kenneth M. Will, for his unwavering support, guidance, and understanding relating to various matters during my research. His profound knowledge and his invaluable insights into structural concepts and physical behaviors helped me enhance my knowledge of structural engineering, a goal that I wished to attain during my Ph.D. studies. I would also like to express my gratitude to Dr. Lawrence F. Kahn for his support and advice on my research and special thanks for his assistance and input about the difficulties and situations that could be ignored in my experiment. I would also like to extend my gratitude to the members of my thesis committee—Dr. Abdul-Hamid Zureick, Dr. Leroy Emkin, and Dr. Yogendra Joshi—for their comments and advice on the completion of my dissertation.

I would also like to express my deepest appreciation to Dr. Yong Myung Park for his unfailing attention to my studies and his profound belief in my abilities. I'd also like to express my gratitude to Dr. Chung Bang Yun for his attention and advice over the years. I would also like to take this opportunity to thank all the members of the Structural Dynamics Laboratory at the Korea Advanced Institute of Science and Technology for their encouragement.

Thanks also to all of my fellow students, laboratory technicians, and friends in the School of Civil and Environmental Engineering at Georgia Tech for their kind words and friendly support when needed. I also have had great the pleasure of working with my office mates, Ben Deaton, Murat Efe Guney, Mustafa Can Kara, Jennifer Modugno, and

Jennifer Dunbeck, and with all the members of the Computer-Aided Structural Engineering Center at Georgia Institute of Technology for the past five years.

Finally, and most importantly, I wish to thank my parents and my sister for their love and support. I am particularly extremely grateful to my mom for her endless support and love. A special thank to my wife, Kyung Hye, for her continuous encouragement and unwavering belief when it was most required through the completion of my degree.

TABLE OF CONTENTS

LIST OF TABLES

LIST OF FIGURES

LIST OF SYMBOLS

A	Area of the bearing pad
C_s	Stefan-Boltzman radiation constant (=5.669×10^{-4} W/m^2·K^4)
D	Diameter of the hole in the bearing
E_c	Modulus elastic of concrete
E_s	Compressive modulus elastic of the bearing pad
E_{ps}	Modulus elastic of prestressing strand
H	Daily total solar radiation
$I(t)$	Total solar radiation on a horizontal surface as a function of time t
I	Total solar radiation on a horizontal surface
I_b	Direct solar radiation, or beam radiation, on a horizontal surface
I_d	Diffused solar radiation on a horizontal surface
I_s	Extraterrestrial solar radiation
I_{sc}	Solar constant (=1367 W/m^2)
I_x	Moment of inertia of the cross-section with respect to the x-axis
I_y	Moment of inertia of the cross-section with respect to the y-axis
I_T	Total solar radiation on an inclined surface
L	Length of the elastomeric bearing pad (Equation 6.1) Length of the prestressed concrete bridge girder (Equation 6.6)
T	Length of day in hours
T_a	Ambient air temperature
T_a^*	Absolute temperature of ambient air
$T_{air}(t)$	Air temperature as a function of time t
T_b	Mean seasonal temperature (Figure 1.4) Temperature in the bottom slab (Figure 1.5)

T_{max}	Daily maximum air temperature
T_{min}	Daily minimum air temperature
T_o	Temperature at casting of concrete (Figure 1.4)
T_s	Concrete surface temperature
T_s^*	Absolute temperature of concrete surface
T_{top}	Temperature on the top surface of the deck slab (Figure 1.3)
T_w	Temperature in the web (Figure 1.5)
ΔT	Temperature difference between the top and bottom of the concrete deck slab (Figure 1.4)
$\Delta T(x)$	Transverse temperature differential at a width x
$\Delta T(y)$	Vertical temperature differential at a depth y
$U1$	Displacement in the lateral direction
$U2$	Displacement in the vertical direction
$U3$	Displacement in the longitudinal direction
W	Width of the elastomeric bearing pad
$b(x)$	Depth of the girder section a with x
$b(y)$	Width of the girder section a depth y
c	Specific heat capacity of concrete
d	Depth of superstructure (Figure 1.7) Shadow length on the web (Figure 3.1)
d_T	Shadow length on the bottom flange (Figure 3.1)
$f_c^{'}$	*C*ompressive strength of concrete
f_{ps}	Stress of prestressing strand
h_c	Convection heat transfer coefficient
h_{rmax}	Thickness of the thickest elastomeric layer in the elastomeric bearing
h_{web}	Height of the web

h_{max}	Occurrence time of the daily maximum air temperature
h_{min}	Occurrence time of the daily minimum air temperature
k	Thermal conductivity of concrete
k_1, k_2	Compressive stiffness of the spring element
k_T	Clearness index
n	Total number of the measured or predicted points
q_c	Heat convection
q_r	Heat radiation to the surrounding atmosphere
q_s	Heat irradiation from the sun
v	Wind speed
w	Solar hour angle
w_c	Density of concrete
w_s	Solar hour angle at sunrise
w_{top}	Width of the top flange overhang
w_{bot}	Width of the bottom flange from the web
α	Solar absorptivity of concrete (Equation 3.9) Coefficient of thermal expansion (Table 4.1 & 4.2)
α_s	Solar altitude angle
$ß$	Surface angle relative to the horizontal plane
$ß_T$	Inclined angle of the bottom flange relative to the horizontal plane
γ	Surface azimuth angle
γ_s	Solar azimuth angle
δ	Declination angle of the sun
δ_x	Lateral thermal deformation
δ_v	Vertical thermal deformation
ε	Surface emissivity of concrete

$\varepsilon_t\,(y)$	Free thermal strain at a depth y from the center of the gravity of the cross-section
ε_o	*S*train at the center of the gravity of the cross-section
ε_{ps}	*S*train of the prestressing strand after its yielding strain
θ	Incident angle between the beam solar radiation and the surface normal
θ_z	Solar zenith angle between the line overhead and the line to the sun
ρ	Reflectance value of the ground
ϕ	Curvature of the prestressed concrete bridge girder Latitude
υ	Poisson's ratio of concrete
ω_c	Density of concrete

LIST OF ABBREVIATIONS

AAE	Average absolute error
BC	Boundary condition
CTE	Coefficient of thermal expansion
EB	Elastomeric bearing
E-W	East-west
FDOT	Florida department of transportation
GDOT	Georgia department of transportation
MAE	Maximum absolute error
NSRDB	National solar radiation data base
NCDC	National climatic data center
S-N	South-north
SE-NW	Southeast-northwest
SS	Simply supported
SW-NE	Southwest-northwest
2D	Two dimensional
3D	Three dimensional

SUMMARY

Bridge engineers have increased the span of prestressed concrete bridge girders by using high-strength concrete and optimized cross-sections. However, the lengthening of the girders has also increased the possibility of a stability failure in the girders especially during construction. In particular, unexpected imperfections in the girder and the supports during fabrication and construction could adversely affect the stability of the girders especially when the girders are exposed to thermal effects from the environment.

An experimental and analytical study was conducted on a BT-63 prestressed concrete girder segment to investigate the thermal effects on the girder. A 2D finite element heat transfer analysis model was then developed which accounted for heat conduction in the concrete, heat convection between the surroundings and the concrete surface, heat irradiation from the sun, and heat radiation to the surroundings. The solar radiation was predicted using the location and geometry of the girder, variations in the solar position, and the shadow from the top flange on other girder surfaces. The girder temperatures obtained from the 2D heat transfer analysis matched well with the measurements. Using the temperatures from the 2D heat transfer analysis, a 3D solid finite element analysis was performed assuming the temperatures constant along the length of the girder. The maximum vertical displacement due to measured environmental conditions was found to be 0.29 inches and the maximum lateral displacement was found to be 0.57 inches.

Using the proposed numerical approach, extremes in thermal effects including seasonal variations and bridge orientations were investigated around the United States to propose vertical and transverse thermal gradients which could then be used in the design of I-shaped prestressed concrete bridge girders. A simple beam model was developed to calculate the vertical and lateral thermal deformations which were shown to be within 6%

of the 3D finite element analyses results. Finally, equations were developed to predict the maximum thermal vertical and lateral movements in terms of the span length of the girders for four AASHTO-PCI standard girders.

To analyze the combined effects of thermal response, initial sweep, and bearing support slope on a 100-foot long BT-63 prestressed concrete girder, a 3D finite element sequential analysis procedure was developed which accounted for the changes in the geometry and stress state of the girder in each construction stage. The final construction stage then exposed the girder to thermal effects and performed a geometric nonlinear analysis which also considered the nonlinear behavior of the elastomeric bearing pads. This solution detected an instability under the following conditions: support slope of 5° and initial sweep of 4.5 inches.

This research also performed a sensitivity study to evaluate the effects of changes in the thermal properties of concrete, as well as the solar absorptivity and emissivity of concrete surface on temperature distributions in the prestressed concrete girder. The solar absorptivity was determined to have the largest effect on the girder temperatures. In general, for the prestressed concrete bridge girder subjected to environmental thermal effects, the influences of the thermal properties of concrete would be minimal when thermal properties are within reasonable ranges. The thermal behavior of the girder was then evaluated using the 3D thermal stress analysis with variations in the coefficient of thermal expansion (CTE) of concrete. With increases in the CTE, the vertical and transverse movements proportionally increased.

CHAPTER 1

INTRODUCTION

1.1 Problem Description

Since precast prestressed concrete girders were introduced in the late 1930s, the use of the girders has rapidly increased for bridge design and construction. In recent years, bridge engineers have increased the span of the precast prestressed concrete girders by using high-strength concrete. However, the lengthening of the girders has also increased the possibility of a stability failure in the girders especially during construction before the addition of the slab and diaphragms.

In the fall of 2005, 150-foot long prestressed concrete girders 90 inches deep and 28 inches wide collapsed during construction in Pennsylvania as shown in Figure 1.1. A possible cause or contribution to this failure was the uneven heating of the girder due to solar radiation which introduced additional lateral deformation. In the summer of 2007, nine 114-foot long prestressed concrete girders collapsed during the construction of the Red Mountain Freeway in Arizona as shown in Figure 1.2. The 63-inch deep girders rested on elastic supports without any cross and diagonal bracing. According to an investigation conducted by the CTLGroup (Oesterle et al., 2007), the collapse of the nine girders was caused by lateral instability in only one girder, and the resulting rollover failure produced the progressive collapse of the adjacent eight girders. The CTLGroup (Oesterle et al., 2007) stated that lateral instability in the girder was probably due to a number of factors including "bearing eccentricity, initial sweep, thermal sweep, creep sweep, and support slopes in both the transverse and longitudinal directions."

The initial sweep of prestressed concrete girders can be attributed to imperfections during fabrication and deformations during shipping and handling. The eccentricity of prestressed strands can be a fabrication error that creates an unexpected

initial sweep in the girder. The shipping and handling can subject the girder to unaccounted loads or boundary conditions which also affect the initial sweep. In addition, the girder could experience additional lateral deformations when placed on supports which are not level. After the prestressed concrete girders were rested on a bearing support, environmental thermal effects can produce additional sweep that may contribute to instability of the girders prior to placement of diaphragm and the bridge deck. However, no specific research pertaining to temperature variations in prestressed concrete girders and the behavior of the girders during construction has been conducted. The lack of understanding of the behavior of prestressed concrete girders when subjected to the combined effects of thermal response, initial sweep, and support slope during construction demonstrates a need for research on this topic.

Figure 1.1: The collapse of prestressed concrete bridge girders, 90 inches deep and 28 inches wide, on I-80 in Pennsylvania (Zureick, Kahn, and Will, 2005).

Figure 1.2: The collapse of prestressed concrete AASHTO Type-V modified girders, 63 inches deep, 40 inches wide in the top flange, and 26 inches wide in the bottom flange, on the Red Mountain Freeway in Arizona (Oesterle et al., 2007).

1.2 Previous Studies

Concrete and prestressed concrete bridge girders subjected to environmental thermal effects experience vertical and transverse temperature variations which produce additional thermal sweep during construction. This research first reviewed previous studies relevant to the environmental thermal effects in concrete bridges. In addition to the thermal effects, initial sweep and support conditions of the bridge girders are combined to adversely affect the behavior of the girders particularly during construction. Therefore, previous research pertaining to the effects of initial sweep and support conditions on the behavior of the girders was also reviewed.

1.2.1 Environmental Thermal Effects in Concrete Bridges

Since Leonhardt et al. (1965) first described the lateral movements and the cracks caused by nonlinear temperature gradients in the prestressed concrete box girder of the Jagst Bridge in Germany, researchers and bridge engineers have been interested in the thermal response of concrete and prestressed concrete bridges subjected to temperature variations under environmental conditions.

Early studies on the temperature effects in the 1950s and 1960s generally focused on one-dimensional heat flow in the vertical direction using experimental data or empirical formulas. Zuk (1961) developed a method for computing thermal deflections and stresses from linear temperature gradients in statically determinate composite steel bridges. Later, Zuk (1965) also attempted to predict the maximum surface temperature of a composite steel bridge in Virginia using an equation originally proposed by Barber (1957) to estimate the maximum surface temperature in pavement. In addition, Zuk (1965) presented an equation for determining the maximum vertical temperature differentials between the top and bottom of the composite steel bridge. The computed maximum temperature differential was 24°F, and the computed maximum deck temperature was 102°F.

Based on a parametric study on the environmental thermal effects in prestressed concrete bridges such as slabs, box girders, and T-section bridges, Priestley (1976) proposed a vertical temperature gradient to be considered in the design of concrete bridge sections. The vertical gradient proposed by Priestley is shown in Figure 1.3, in which a maximum temperature difference on the top surface of the deck slab, T_{top}, nonlinearly decreases to a zero at a depth of 1,200 mm (47.2 in.). The nonlinear variation was represented by fifth-degree parabola. Over the bottom 200 mm (7.9 in.) of the section, the temperature distribution was assumed to be linear as shown in Figure 1.3. The proposed vertical temperature gradient was adopted in bridge design specifications in the United States, Canada, England, and New Zealand.

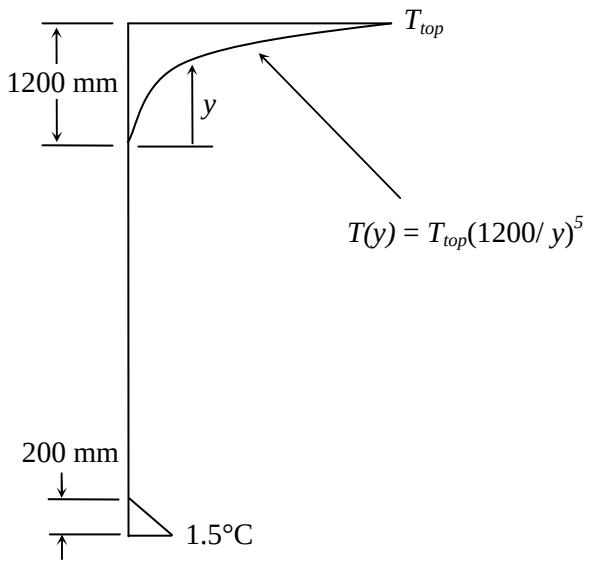

Figure 1.3: Vertical temperature gradient proposed by Priestley (1976).

In order to predict temperature distributions in bridges, Emerson (1973) developed a one-dimensional finite difference method for calculating temperature distributions in concrete, steel, and composite bridges due to solar radiation, ambient air temperature, and wind speed. The calculation of temperature distributions started from uniform temperature distributions at 8 a.m. in the summer and 4 p.m. in the winter. For concrete structures, the maximum temperature differentials occurred at 4±1 p.m. for a thick slab and a box section and at 3±1 p.m. for a thin slab in the summer. The maximum reversed temperature differentials occurred at 6±1 a.m. for the thick slab and the box section and at 5±1 a.m. for the thin slab in the winter.

Will et al. (1975, 1977) developed finite element programs for the transient heat conduction and thermal stress analysis of bridge structures. The transient heat conduction program employed two-dimensional finite elements to predict internal temperature distributions. The thermal stress program, based on bridge temperatures obtained from the two-dimensional analysis, used shell elements to calculate thermal movements and

stresses for the bridges. The thermally-induced movements obtained from the analytical procedures correlated well with field measurements.

Emanuel and Hulsey (1978) used the finite element method to present maximum and minimum deck temperatures and vertical temperature differences in concrete steel composite bridges exposed to mid-Missouri weather conditions. The results showed that maximum and minimum deck temperatures were around 150°F (66°C) and -10°F (-23°C) for a hot summer and for a cold winter day, respectively. The vertical temperature differences between the top and bottom of the deck were a maximum of 39°F (22°C) in the summer and a minimum of 31°F (17°C) in the winter.

Dilger et al. (1981, 1983) accounted for the geometry, the location, and the orientation of the bridge when computing bridge temperatures using a one-dimensional finite difference method. The predicted temperatures showed good agreement with the measured data at the Muskwa River Bridge in British Columbia, Canada. Thermal stresses were computed using the extreme of the predicted temperatures. This study found that the highest temperature differences occurred under the following conditions:

(1) High intensity of solar radiation
(2) Large daily variation in ambient temperature
(3) Non-existence of wind
(4) Dark surface of the steel box
(5) Large size of the steel box
(6) Small or no shade of the box flange overhang

Kenney and Soliman (1986, 1987), whose research was based on past several theoretical and experimental results, proposed a simple vertical temperature distribution and temperature differentials in steel and concrete composite bridges for the summer and winter season. The temperature distribution recommended for the middle Atlantic States

and Southern Ontario, Canada was linear through the depth of the concrete deck and uniform through the depth of the steel girder. This recommended vertical temperature distribution is shown in Figure 1.4, in which ΔT is temperature differential between the top and bottom of the concrete deck slab, T_b is mean seasonal temperature or ambient air temperature found from a map of isotherms for the bridge site, and T_o is temperature at casting of the concrete.

Moorty and Roeder (1992) also used the finite element method to evaluate the thermal response of steel and concrete composite bridges exposed to environmental conditions. The concrete deck was modeled using plate elements, and the steel girder was modeled using three-dimensional beam elements. The temperature distributions and thermal movements obtained from the analytical models were compared with the measurements for the verification of the proposed method. Furthermore, this study discussed the influence of different bridge geometry and support conditions on temperature distributions and thermal responses in the composite bridges.

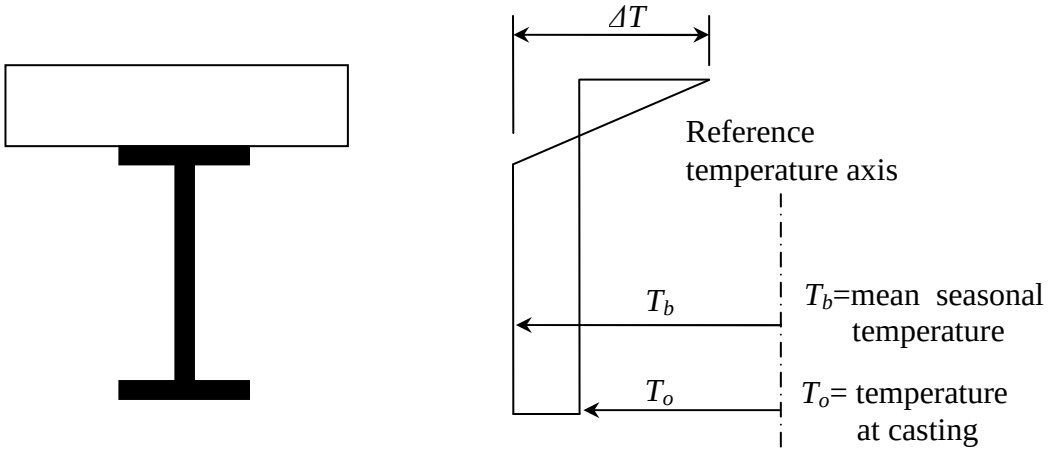

Seasons	Maximum ΔT	Minimum ΔT
Summer	40°F (4.4°C)	-7.5°F (-12.9°C)
Winter	20°F (-6.7°C)	-7.5°F (-12.9°C)

Figure 1.4: The vertical temperature distributions of steel and concrete composite bridges in the summer and the winter (Kennedy and Soliman, 1987).

For the analysis of thermal effects in a concrete box bridge, Elbadry and Ghali (1983) performed a parametric study for the effects of bridge orientation, girder geometry, climatological conditions, and surface conditions on bridge temperatures and thermal stresses using a two-dimensional finite element analysis. According to the study, the combination of environmental and surface conditions necessary to produce the temperature field related to the largest curvature and stresses in the concrete box girder were as follows:

(1) One side of the box girder is protected from solar radiation during the summer
(2) Daily range of ambient temperature is large
(3) Deck is covered by asphalt.

Later, Ghali and Elbadry (1986, 1989) discussed tensile stresses and concrete cracks induced by the nonlinear temperature distributions in a concrete bridge and presented a minimum amount of reinforcements to control the width of thermal cracks. Mirambell et al. (1990) also presented an analytical model based on a two-dimensional finite difference method to determine temperature and stress distributions in concrete box girder bridges. In the study, they emphasized the importance of transverse temperature differences between the external air and the air enclosed in the concrete box which can induce tensile stresses at the outside or inside of the slab and the web of the box girder.

In addition to theoretical and numerical evaluation of the thermal behavior in concrete bridges, experimental studies were carried out by several researchers. Dilger et al. (1981) monitored the behavior of a continuous concrete and steel composite box bridge during the construction of a concrete deck and the first three years of the operation. The field measurements reported cracks in the concrete deck and nonlinear strain distributions across the depth and the width of the steel boxes which were

attributed to temperature increases in concrete deck, the shrinkage of the concrete, and the rapid heating of steel boxes exposed to direct sunlight. For the section of a double box concrete bridge, Churchward and Sokai (1981) measured temperatures during construction and provided empirical expressions for vertical temperature profiles and average temperatures as a function of maximum differential temperature, base temperature, and ambient air temperature.

Roberts-Wollman et al. (2002) collected concrete temperature data over a section of a segmental box girder bridge in San Antonio, Texas. The maximum positive and negative vertical thermal gradients measured in the study were compared to those recommended in the *AASHTO LRFD Bridge Design Specifications* (1994) and *AASHTO Segmental Specifications* (1999). For the positive thermal gradient, the *AASHTO LRFD Bridge Design Specifications* (1994) showed larger vertical differentials for the surface without a topping. The vertical differential recorded when topped with asphalt was close to that of the *AASHTO LRFD Bridge Design Specifications* (1994). The *AASHTO Segmental Specifications* (1999) exhibited larger vertical differentials for both conditions. The negative vertical thermal gradients were also larger for both surface conditions when compared to the AASHTO Specifications (1994, 1999). Furthermore, this study evaluated the relationships between the measured girder temperatures and ambient climatic conditions for predicting positive temperature differentials.

Saetta et al. (1995) presented a numerical procedure based on the finite element method for predicting temperature variations and stress levels in a concrete dam and a concrete box bridge girder. Assuming uncoupled temperature and stress fields, this study first calculated the temperature field of the concrete structures including environmental boundary conditions and internal heat generation. The obtained temperature field was transferred to thermal loads in the stress-strain analysis based on the linear elastic behavior of material. For the effectiveness and validation of the proposed numerical

method, the results obtained in this study were compared with the experimental results reported in the literature.

Suchinda and Will (1999, 2000) developed a method for predicting the thermal behavior of fiber reinforced polymeric (FRP) V-shaped bridge decks and demonstrated the need to consider thermal response caused by environmental conditions in the design. In the study, a two-dimensional heat transfer finite element analysis using measured environmental boundary conditions was performed to determine temperature distributions in the bridge deck. The obtained temperature distributions were transferred to a thermal stress analysis using shell elements, and deck temperatures and movements were predicted. In addition, parametric studies to demonstrate the influence of the solar absorptivity and heat emissivity of the FRP plate on thermal responses were conducted.

Gilland and Dilger (1997) measured temperature variations, solar radiation, ambient air temperature, and wind speed during the construction of the Confederation Bridge, a prestressed concrete box bridge located in Atlantic, Canada. Temperature data showed that before the removal of the formwork, concrete temperatures began to gradually increase due to the heat of hydration. After the formwork was removed, the concrete members experienced sudden thermal gradients due to their exposure to surrounding weather conditions. Li et al. (2004) also analyzed the thermal response of the Confederation Bridge based on experimental data for three cross-sections: approximately 512 inches (13,000 mm), 343 inches (8,700 mm), and 177 inches (4,500 mm) deep. Compared with the Canadian highway bridge design code (CAN/CSA-S60-00) and the Priestley model (1976), the 177-inch deep bridge section showed good agreement with the Priestley model in the summer, but the other two deeper sections exhibited higher temperature in the web and lower temperature in the slabs. Therefore, based on the Priestley model, this study proposed a modified third-order vertical temperature gradient for extremely deep prestressed girder sections. Figure 1.5 shows the proposed model, called the Calgary model, in which T_{top}, T_w, and T_b are the temperatures

at the top surface, in the web, and in the bottom slab. The temperature variation along the depth of the web increases linearly from 0°C at a depth of 1.2m to T_w at L_s and a constant temperature T_w up to the lower part of the web. The distance of L_s is defined as approximately two times the length of the cantilever (overhang) in the box girder.

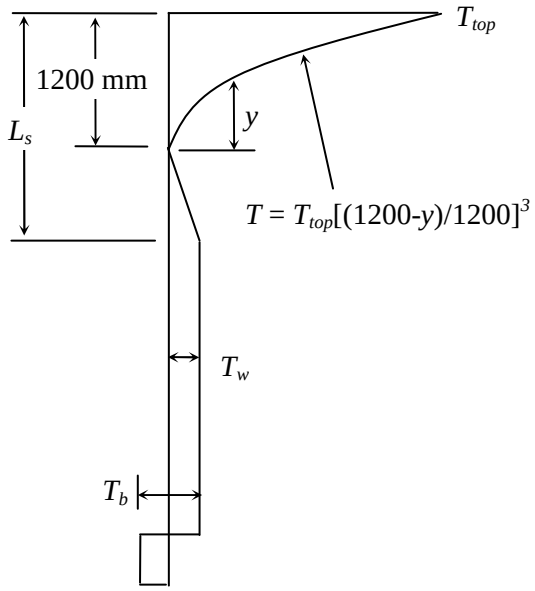

Figure 1.5: The Calgary model proposed by Li et al. (2004) for extremely deep prestressed concrete box girders.

In addition, Pisani (2004) evaluated the effect of nonlinear thermal strains caused by daily and seasonal changes in environmental factors in reinforced and prestressed concrete bridge decks. The investigation showed that the thermal effects did not significantly affect load capacity of the sections but markedly changed the stresses and strains of the concrete under service loads. Moreover, Barr et al. (2005) observed temperature variations in precast prestressed concrete girders during both fabrication and service and evaluated the effects of the temperature variations on stresses, strains, and cambers. Curing temperatures reduced the original prestressing stress by 3 to 7% and the initial camber by 26 to 40%. In addition, the bottom tensile stress in the girder due to the temperature profile provided in the *AASHTO LRFD Bridge Design Specifications* (1998)

was 370 psi which corresponds to 60% of the allowable concrete tensile stress of $6\sqrt{f_c'}$, in which f_c' is compressive strength of concrete in psi.

The AASHTO bridge specifications were also reviewed for recommendations or guidelines relevant to the thermal behavior of bridge systems induced by environmental conditions. Prior to 1989, the America Association of State Highway and Transportation Officials (AASHTO) provided only uniform temperature changes and did not address thermal gradients for the design of bridge structures. According to Roberts-Wollman et al. (2002), bridge engineers who were concerned about the effects of thermal gradients on concrete bridges generally referred to the Priestley model (Priestley, 1976) as previously shown in Figure 1.3 or used vertical and transverse temperature differentials, 10°C (18°F) and 15°C (27°F), respectively, recommended by the Post Tensioning Institute (PTI, 1977). However, the temperatures provided in the PTI manual are not appropriate for selecting proper temperature differentials in bridge structures.

In 1989, the AASHTO, based on the National Cooperative Highway Research Program (NCHRP) Report 276, provided uniform bridge temperatures and differential temperature distributions and published the *AASHTO Guide Specifications, Thermal Effects in Concrete Bridge Superstructures* (1989) for the design of reinforced and prestressed concrete bridge superstructures. The uniform bridge temperatures, which result in the expansion and contraction of bridge superstructures, were termed “effective bridge temperatures” in the AASHTO Guide Specifications (1989). The guidelines provided the values of maximum and minimum effective bridge temperatures based on maximum and minimum normal air temperatures at the bridge site. Table 1.1 presents the temperatures correlated with the normal daily air temperatures for concrete bridges. The profile and values of the vertical temperature differentials from the 1989 AASHTO Guide Specifications are presented in Figure 1.6. The maximum temperature differences were defined in terms of four solar radiation zones for the United States as shown in Figure 1.7.

Table 1.1: Correlation between the effective bridge temperatures and normal daily air temperatures (AASHTO, 1989).

Normal Daily Minimum Temperature, (°F)	Minimum Effective Bridge Temperature (°F)	Normal Daily Maximum Temperature, (°F)	Maximum Effective Bridge Temperature (°F)
-30	- 3		
-25	0	55	66
-20	3	60	69
-15	5	65	73
-10	8	70	77
- 5	11	75	80
0	13	80	84
5	16	85	88
10	19	90	92
15	22	95	95
20	25	100	98
25	29	105	101
30	32	110	105
35	35		
40	38		

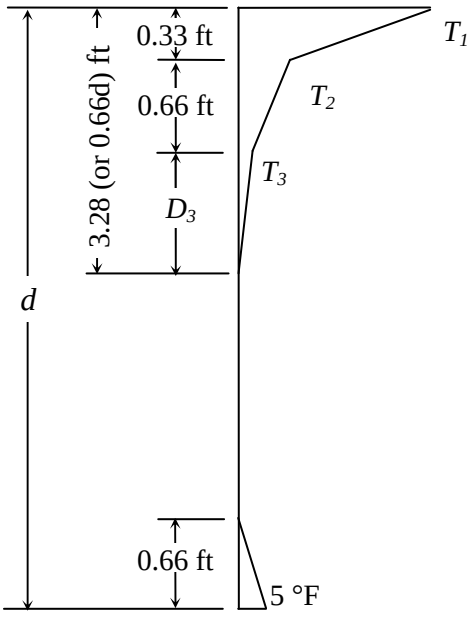

Zone	T_1 (°F)	T_2 (°F)	T_3 (°F)
1	54	14	5
2	46	12	4
3	41	11	4
4	38	9	3

Figure 1.6: Vertical temperature gradient for concrete superstructures (AASHTO, 1989).

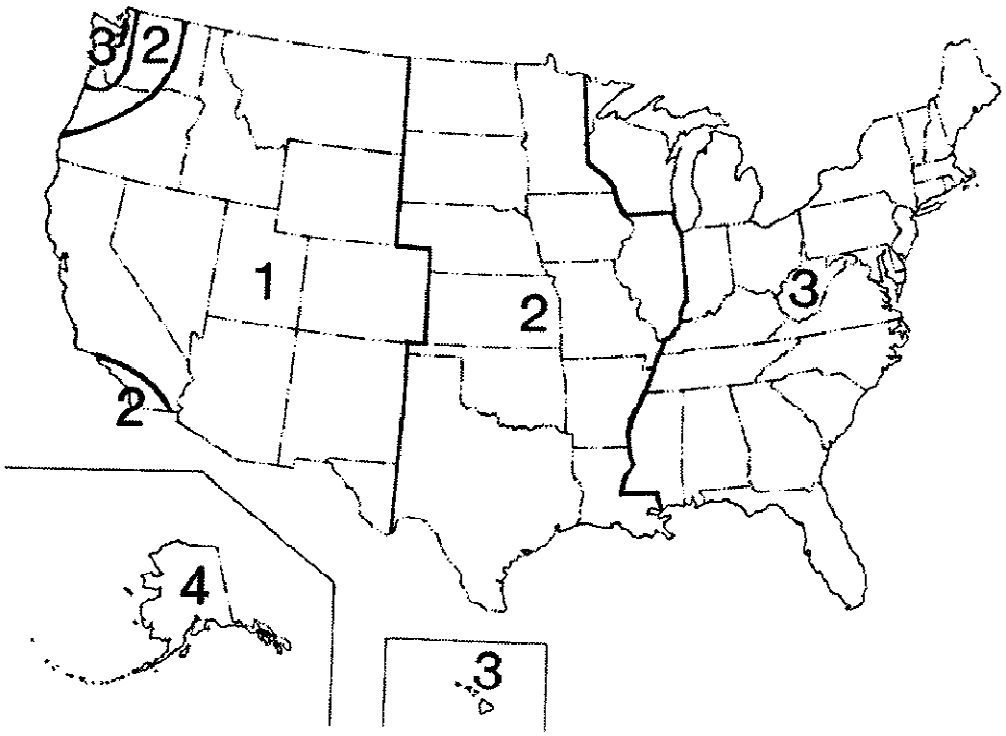

Figure 1.7: Solar radiation zones for the United States (AASHTO, 1989).

Based on the AASHTO Guide Specifications (1989), the *AASHTO LRFD Bridge Design Specifications* (2007) simplified the uniform temperatures and vertical temperature gradients. Section 3.12.2 specifies minimum and maximum temperatures associated with uniform thermal movements. For concrete deck bridges with concrete girders, the minimum and maximum temperatures are specified as 10°F and 80°F in a moderate climate and 0°F and 80°F in a cold climate. From the AASHTO Specifications (2007), the climate is determined by the number of freezing days, defined as daily average temperature of less than 32°F. If the total freezing days a year are less than 14 days, the climate is considered to be moderate. In addition, Section 3.12.3 provides the vertical temperature gradient. Figure 1.8 shows the vertical temperature gradient in concrete superstructures with concrete decks. The magnitude of the temperature gradients, T_1 and T_2, are determined in accordance with solar radiation zones, shown in

Figure 1.7. Dimension *A* in Figure 1.8 is 12.0 inches for concrete superstructures which are 16.0 inches or more in depth. For concrete sections shallower than 16.0 inches, Dimension *A* is the smaller of 4.0 inches and the depth of concrete superstructure. Temperature value T_3 in Figure 1.8 can be taken as 0.0°F unless a site-specific study is made to determine an appropriate value.

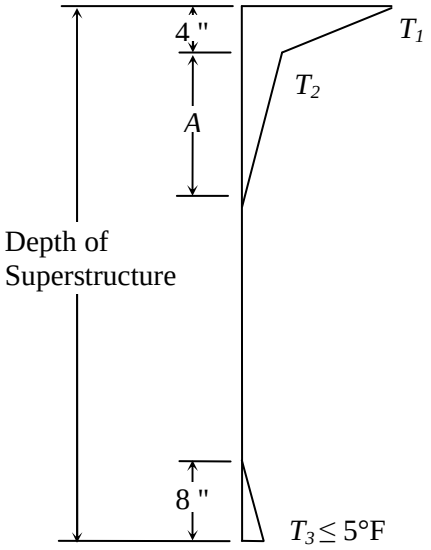

Zone	T_1 (°F)	T_2 (°F)
1	54	14
2	46	12
3	41	11
4	38	9

Figure 1.8: Vertical temperature gradient for concrete superstructures (AASHTO, 2007).

1.2.2 Girder Sweep and Support Conditions in Prestressed Concrete Girders

For stability problems associated with girder imperfections and support conditions in the prestressed concrete bridge girders, few studies have been carried out. Some initial research were conducted by Laszlo and Imper (1987) and Mast (1989, 1993) for a girder suspended from lifting devices and for a girder on elastic supports during transportation. For the girder on elastic supports, they proposed a method to evaluate the girder safety against overturning. The method, which differed from a traditional stability analysis, was based on the ratio of a resisting moment at the support to an overturning moment induced by the girder sweep and support slopes. However, to the author's knowledge, no specific

method or guideline that can analyze the lateral stability of the girders placed on elastic bearing supports during construction has been provided. Consequently, Oesterle et al. (2007) alternatively used the method proposed by Mast (1989, 1993) for a girder on elastic supports during transportation and investigated prestressed concrete girders which collapsed after placing on elastic bearing supports prior to the installation of lateral and cross bracing in Arizona. According to the investigation conducted by Oesterle et al. (2007), a number of factors such as initial sweep, thermal sweep, and support slopes could combine to cause the lateral instability of the girders during construction. The report recommended that the position of the girder ends and the surfaces of all the bearings should be carefully checked during the erection of the girders. In addition, bracing at the both ends of the girders should be added as soon as the girders are erected.

Furthermore, the *PCI Bridge Design Manual* (2003) was reviewed for guidelines and recommendations relevant to the support conditions of precast prestressed concrete bridge girders. Section 3.6 of the PCI Manual describes methods and procedures to install precast concrete bridge components. Section 3.6.2 emphasizes the establishment of uniform bearings at the beam ends for the stability of precast flexural concrete members. For this purpose, this Section indicates that "The support surfaces should be checked for horizontal and vertical control, as well as flatness and level or slope". The flatness of the support is limited to 1/16 inches as a tolerance. Since the beams can also fall off the support due to forces of natures, including wind, earthquake, or thermally-induced sweep, Section 3.7 of the PCI Manual which treats temporary diaphragm for construction indicates that "After the beams have been erected, and before they are permanently connected into the structure … temporary braces consisting of steel or timber are used to stabilize the beams".

In addition, Section 8.3 of the *PCI Bridge Design Manual* (2003), based on the studies conducted by Mast (1989, 1993), addresses the lateral stability of slender members during handling and shipping. For a beam hanging from lifting devices, the

rollover of the beam is primarily governed by the properties of the beam while for a beam supported on flexible supports being transported on a truck, the rollover is significantly influenced by the conditions of the support and the geometry of the roadway. For the evaluation of the safety and stability against rollover (or, overturning) failure during shipping and lifting, Section 8.3 provides explicit calculation procedures and minimum sweep tolerances in which the initial sweep of the prestressed concrete I-beams is limited to be 1/8 inches per 10 feet of member length. The *PCI Bridge Design Manual* (2003), however, does not provide any specific guidelines and recommendations for the beams in an erected condition, especially during construction prior to the installation of diaphragms. Furthermore, according to the PCI Manual, elastomeric bearing pads, used predominantly as beam supports, can become highly nonlinear when the reaction load is outside the kern of the bearing pads. Therefore, the nonlinear response of the bearing pads can result in serious stability problem associated with a beam rollover. In addition, the *PCI Tolerance Manual for Precast and Prestressed Concrete Construction* (2000) was reviewed for the construction tolerance of the bridge girders. Only Section 12.11 of the PCI Tolerance Manual limits bearing eccentricity which is defined as the difference between the centerline of the bottom of the beam and the centerline of the elastomeric bearing pads as shown in Figure 1.9, to ±1 inch.

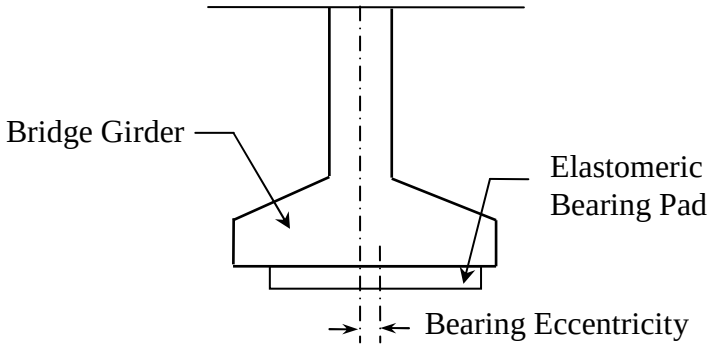

Figure 1.9: The eccentricity of elastomeric bearing pad relative to the centerline of the bottom of the girder.

The AASHTO bridge design and construction specifications were also reviewed for the stability of precast prestressed concrete girders related to girder sweep and support conditions. Section 5.14.1.2.1 of the *AASHTO LRFD Bridge Design Specifications* (2007) requires the responsibility of the contractor for the safe shipping and erection, and Section 5.14.3.3 states the need to consider the potential of the bucking in tall thin web sections. For the uncertainties of bearing contacts, Section 14.4.2.1 of the specifications provides a rotation of 0.005 rad. as a tolerance. Moreover, in the *AASHTO LRFD Bridge Construction Specifications* (2004), Section 8.13.6 indicates that "the contractor shall be responsible for the safety of precast members during all stages of construction" and "after a member has been erected and until it secured to the structure, temporary braces shall be provided as necessary to resist wind or other loads". Neither the *AASHTO LRFD Bridge Design Specifications* (2007) nor the *AASHTO LRFD Bridge Construction Specifications* (2004) provide any specific guidelines related to the stability of precast prestressed concrete girders during construction.

1.3 Research Scope and Objectives

The objectives of this research are to investigate variations in the temperature distributions of precast prestressed concrete bridge girders under various environmental conditions and to evaluate the global behavior of the bridge girders due to the combination of these thermal movements, initial imperfections, and support conditions.

For the environmental thermal effects and temperature variations in the prestressed concrete bridge girders, this research conducted a one-year experiment on a BT-63 prestressed concrete girder segment to investigate the relationships between vertical and transverse temperature distributions and environmental conditions. A two-dimensional transient finite element heat transfer model was developed to predict the temperature variations and distributions in the bridge girder based on environmental conditions. For the validation of the proposed heat transfer model, the girder temperatures obtained from the heat transfer analysis were compared with the measurements. This study also determined extremes in seasonal environmental conditions pertaining to the largest vertical and transverse temperature differentials and proposed vertical and transverse thermal gradients for the design of the prestressed concrete bridge girders. The effects of seasonal variations and different bridge orientations on the vertical and transverse temperature differentials are also examined.

Based on these extreme temperature distributions, the thermal response and global behavior of the prestressed concrete bridge girder at the time of construction (without the deck or diaphragms) were investigated using a three-dimensional finite element analysis. This analysis included the effects of initial geometry imperfections and support slopes combined with thermal movements on the behavior of the bridge girder. To account for the nonlinear behavior of elastomeric bearing pads used as a support system in precast prestressed concrete bridge girders, this study also considered the compressive stiffness of the bearing pads.

This research also performed a sensitivity study to determine the effects of changes in the thermal conductivity, the specific heat, the solar absorptivity, and the coefficient of thermal expansion of concrete on the temperature distributions and thermal movements.

1.4 Overview and Structure of the Thesis

Chapter 2 describes an experimental investigation into environmental thermal effects and temperature variations over the section of a BT-63 girder and investigates variations in vertical and transverse temperature differentials and the corresponding environmental conditions from the measurements taken from April 2009 to March 2010. Using the measured environmental boundary conditions, Chapter 3 presents a two-dimensional finite element heat transfer model which accounts for heat convection, heat conduction, heat irradiation, and heat radiation. In the numerical analysis, the intensity of solar radiation incident on each surface of the girder is estimated considering the location and orientation of the bridge, the geometry and shadow of the girder, the position of the sun, and the solar radiation measured on a horizontal surface. The temperature variations and distributions obtained from the heat transfer analysis are compared with those obtained from the measurements for validation. In Chapter 4, the temperature fields defined from the heat transfer analysis are transferred to a three-dimensional finite element model, and the thermal stress analysis is then performed to determine the thermal response of the BT-63 girder. The prestressing forces are modeled as initial stress conditions and the support conditions as simply-supported boundary conditions.

Chapter 5 determines extremes in seasonal environmental conditions pertaining to the maximum vertical and transverse temperature distributions. Based on the extreme environmental conditions, the two-dimensional heat transfer model is employed to evaluate the effects of seasonal variations and different bridge orientations on the temperature distributions in four AASHTO-PCI standard sections. As a result, this

chapter proposes revised vertical and new transverse thermal gradients applicable to the design of concrete and prestressed concrete bridge girders in the United States. Chapter 6 uses three-dimensional thermal stress analysis to determine thermal response induced by the maximum temperature distributions. In addition to the thermal movements, this chapter evaluates the effects of initial geometry imperfections and bearing slopes on the global behavior of a prestressed concrete bridge girder during construction. The nonlinear behavior of elastomeric bearing pads is idealized by nonlinear springs with the effective compressive stiffness of the bearing pad. Furthermore, this study proposes a simple beam model that can calculate thermal movements induced by nonlinear temperature distributions.

Chapter 7 discusses the influence of thermal properties of concrete on temperature distributions and thermal movements in prestressed concrete bridge girders. The parameters associated with the temperature distributions are thermal conductivity, specific heat, and solar absorptivity. For the thermal movements, the influence of the coefficient of thermal expansion is evaluated using the three-dimensional thermal stress analysis. Finally, Chapter 8 summarizes the results of the current study and recommends future studies for the thermal responses and global behavior of concrete and prestressed concrete bridges.

CHAPTER 2

EXPERIMENTAL INVESTIGATION OF THERMAL EFFECTS

2.1 Introduction

This study carries out an experimental investigation to determine the temperature distributions in a prestressed concrete bridge girder due to solar radiation, ambient air temperature, and wind speed. Since prestressed concrete girders have commonly been designed using AASHTO-PCI sections (PCI, 2003), this study chose an AASHTO BT-63 for the cross-section of a test girder. The length of the test girder was designed to be five feet since temperature distributions were assumed to be constant in the longitudinal direction. The experiment was conducted during the months of April 2009 to March 2010 in the east-west direction so that only the top surface and one side of the girder received direct solar radiation from the sun. This orientation would provide the girder with extremes in transverse temperature distributions.

2.2 Specimen Preparation

The five-foot long test bridge girder was cast at a precasting plant of Standard Concrete Products in Atlanta, Georgia on October 27, 2008. Prestressing forces were produced by a total of twelve low relaxation strands, 0.5 inches in diameter. Four strands were set in the top flange, and the other eight strands were distributed in a layer of the bottom flange as shown in Figure 2.1. These strands were prestressed to 10,700 pounds per strand in the top flange and to 35,000 pounds per strand in the bottom flange. As a result, the total jacking force on the test girder was 322,800 pounds. Three days after the concrete pouring, the tension forces of the strands were released and the steel molds were removed from the five-foot girder on October 29, 2008. At 28 days, the compressive strength tests were performed on three 6-inch and 12-inch cylinder specimens, resulting in an average compressive strength of 9.0 ksi.

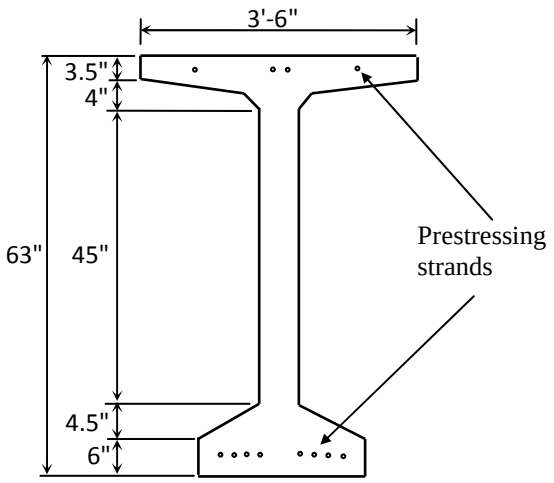

Figure 2.1: The cross-section of the BT-63 specimen and the layout of the prestressing strands.

On November 14, 2008, the five-foot girder was moved to the Structures Laboratory at Georgia Institute of Technology. Both ends of the girder were insulated by extruded polystyrene sheets to minimize heat transfer between the end of the girder and the air. The pickup steel exposed to the air was wrapped with polyethylene pipe insulation to minimize heat transfer between the steel and the air. The specimen was then moved to the parking lot of the Structures Laboratory and placed in an area approximately 75 feet away from the main building since the shadow of the main building was calculated to be a maximum 74 feet long in December. Moreover, to reduce heat radiation from the ground to the bottom of the girder, steel blocks were used to raise the girder approximately 1.5 feet above the ground. A wooden board was also placed between the specimen and the steel block to minimize heat transfer between the steel block and the concrete. In addition, a dark foam sheet was placed on the ground underneath the girder to minimize the heat reflection and radiation from the ground. Data acquisition systems collecting the measurements were installed next to the specimen. Figure 2.2 illustrates the specimen set-up in the parking lot of the Structures Laboratory.

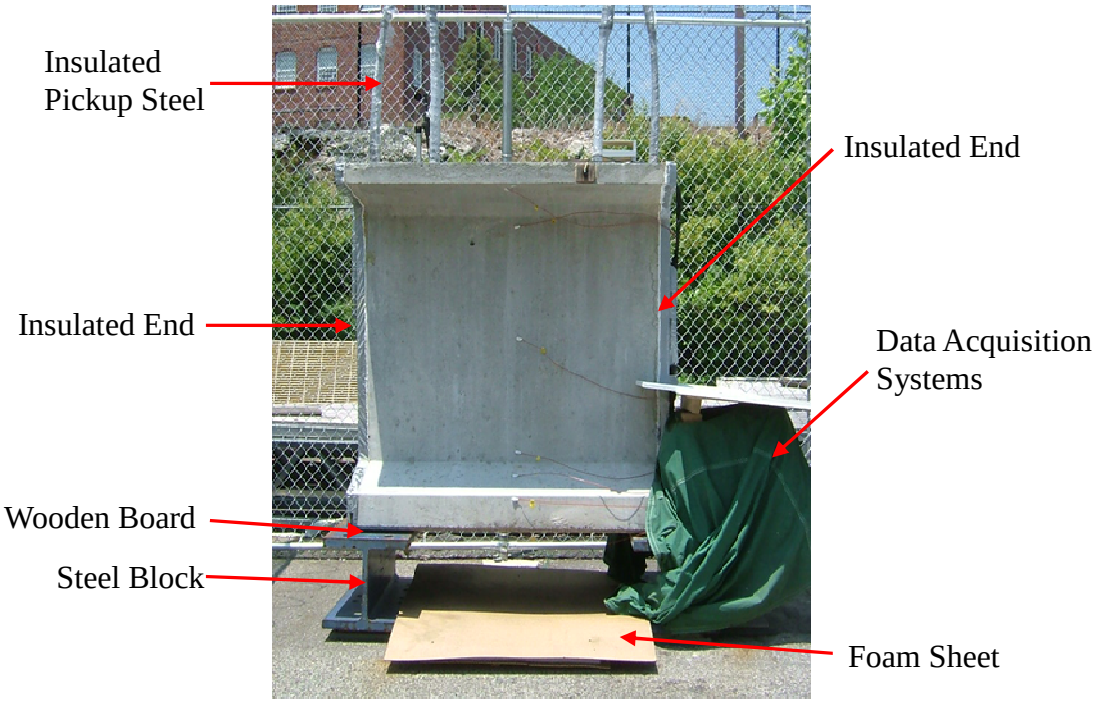

Figure 2.2: The specimen set-up in the parking lot of the Structures Laboratory.

2.3 Instrumentation

The primary environmental factors affecting the temperature variation in bridges are solar radiation, ambient air temperature, and wind speed. The intensity of solar radiation incident on the surfaces of the girder was measured on the horizontal and vertical surfaces of the top flange of the test girder. Ambient air temperature and wind speed were recorded approximately one foot above the top surface of the girder. A total of twenty-eight thermocouples were used to measure the internal and external temperatures of the girder. Eleven thermocouples were placed inside the girder and seventeen thermocouples on the outside surface.

2.3.1 Environmental Variables

Two SP-110 pyranometers manufactured by Apogee Instruments were used to measure the intensity of solar radiation incident on a horizontal and vertical surface of the girder. One pyranometer was installed on the top surface of the top flange to measure solar radiation on a horizontal surface, and another was installed on the side of the top flange to measure vertical solar radiation. Figure 2.3 shows the two pyranometers on the surfaces of the top flange in the girder.

Figure 2.3: Pyranometers installed at the top flange of the test girder.

One Type-K bare lead thermocouple was installed to measure ambient air temperature approximately one foot above the corner of the top surface. The thermocouple was covered by plywood to avoid contact with water on a rainy day and to minimize the influence of direct solar radiation during the day. The wind speed was measured with a three-cup anemometer, 03001 Wind Sentry Set manufactured by Campbell Scientific. The anemometer was also installed approximately one foot above the top surface on the other side of the girder. Figure 2.4 shows the thermocouple used to measure ambient air temperature and the anemometer installed on the top surface of the girder.

(a) Thermocouple for ambient air temperature

(b) Anemometer for wind speed

Figure 2.4: Thermocouple and anemometer installed on the top surface of the test girder.

2.3.2 Girder Temperatures

For the investigation of the temperature variations of the girder in the vertical and lateral directions, a total of 28 Type-K thermocouples were installed at mid-span. Figure 2.5 shows the specific locations of all the internal and external thermocouples. Internal temperatures were measured using eleven Type-K bare lead thermocouples, and surface temperatures were measured using seventeen Type-K washer thermocouples with PFA insulation. As shown in Figure 2.6, the eleven internal thermocouples were placed inside the girder at mid-span prior to the concrete pour. Figure 2.7 shows the seventeen external thermocouples installed on the BT-63 girder at mid-span.

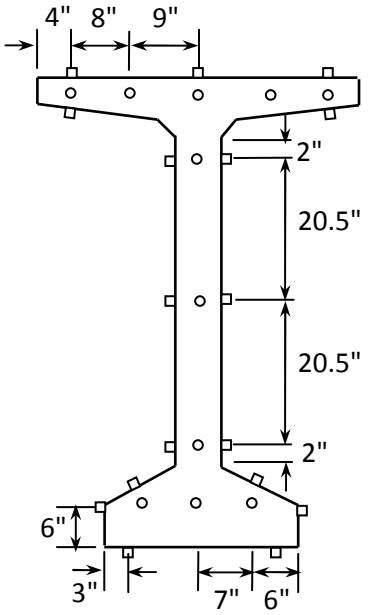

(a) Thermocouple locations

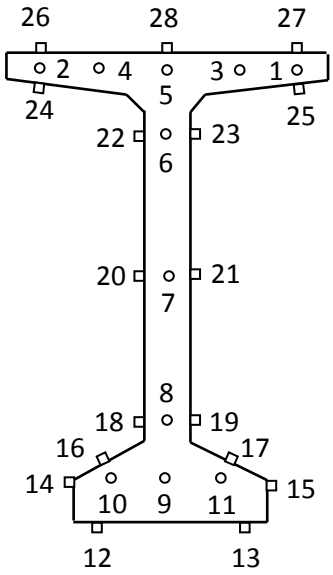

(b) Thermocouple numbers

Figure 2.5: The locations of thermocouples installed at mid-span.

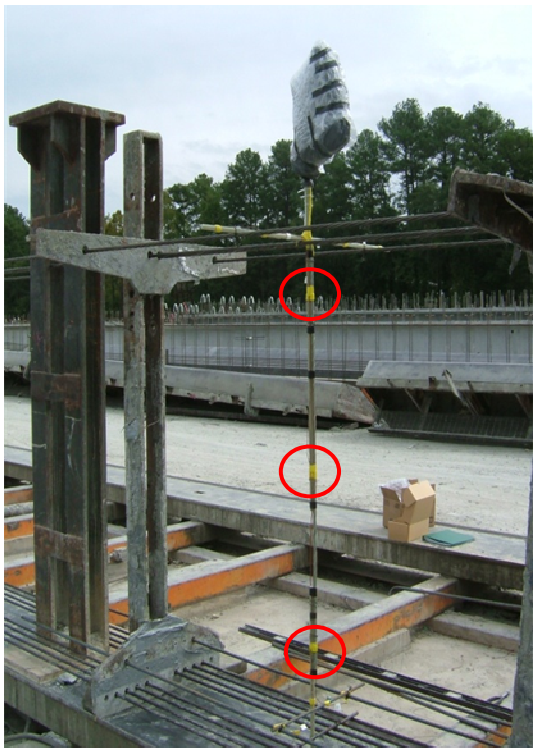

(a) In the web

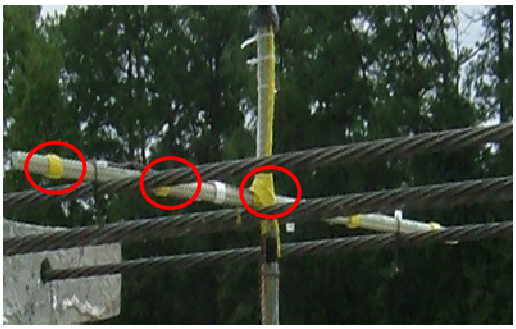

(b) In the top flange

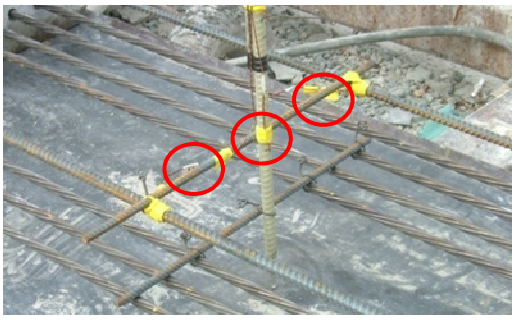

(c) In the bottom flange

Figure 2.6: Internal thermocouples installed at mid-span.

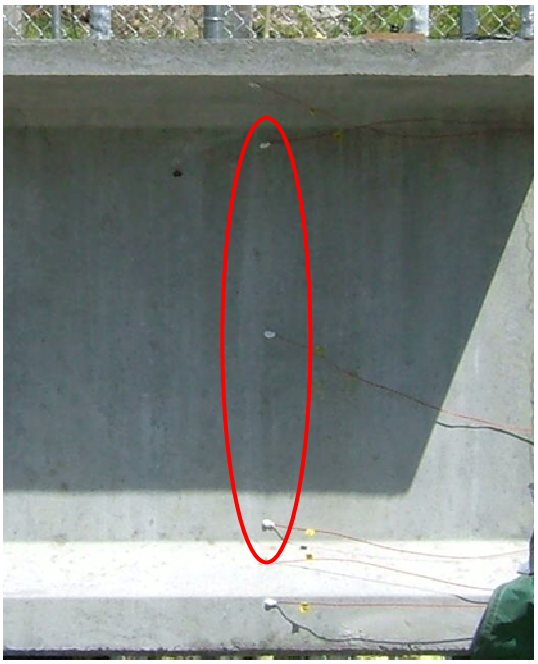

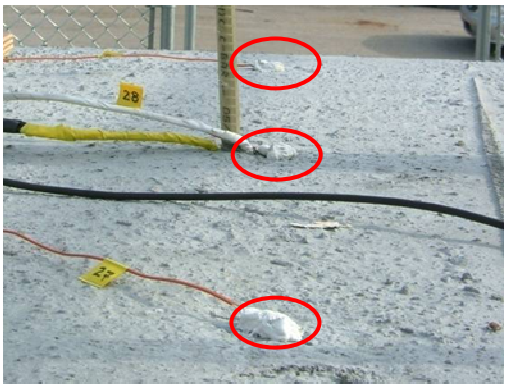

(b) On the top surface of the top flange

(a) On the surfaces of the web and bottom flanges

Figure 2.7: External thermocouples installed at mid-span.

2.3.3 Data Acquisition Systems

To collect data measured in the experiment automatically, this study employed two data acquisition systems: an SCXI-1000 chassis and a USB-6008 device. First, this experiment used the National Instruments SCXI-1000 chassis, which holds an SCXI-1102 module and an SCXI-1303 terminal block, to measure girder temperatures, ambient air temperature, and solar radiation. The measurements were controlled through a National Instruments DAQCard Al-16E-4 with a PSHR68-68M I/O cable using a sampling rate of 100 Hertz every five minutes. This experiment also used the National Instruments USB-6008 device to measure wind speed in AC volts at a sampling rate of 1,000 Hertz at the same interval of five minutes since the rotation of the cup wheel produces an AC sine wave with a frequency proportional to the wind speed. Figure 2.8 illustrates the configuration of the two data acquisition systems in detail.

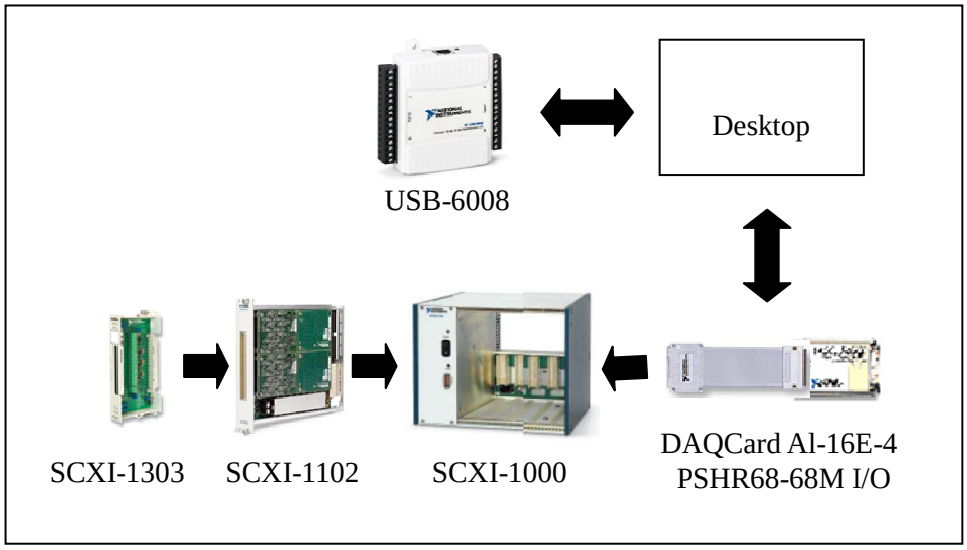

Figure 2.8: The configuration of data acquisition systems for the measurements.

2.4 Measurements of Environmental Conditions and Girder Temperatures

This section presents the results of solar radiation, ambient air temperature, and wind speed taken from April 2009 to March 2010. Internal and external girder temperatures were also measured simultaneously with the environmental factors.

2.4.1 Environmental Conditions

From the measurements taken from April 2009 to March 2010, this study assessed variations in daily environmental conditions, solar radiation, ambient air temperature, and wind speed. Table 2.1 summarizes the daily solar radiation, daily maximum and minimum air temperatures, and daily average wind speed calculated from the measurements for selected sunny days, on which large vertical and/or transverse temperature distributions were measured.

Table 2.1: The daily environmental conditions for selected sunny days during the measurements from April 2009 to March 2010.

Dates	Daily Solar Radiation (MJ/m^2)		Daily Air Temperature (°C)			Daily Wind speed, (m/sec)	
	Horizontal	Vertical	Maximum	Minimum	Variance	Average	Maximum
4/24/2009	27.0	10.9	32.1	13.6	18.5	0.6	3.1
5/20	27.5	8.8	25.8	15.6	10.2	1.3	5.3
5/30	29.5	7.7	30.4	15.6	14.8	0.5	2.5
6/ 1	28.8	7.4	33.3	18.8	14.5	0.4	2.8
6/23	26.4	7.2	34.4	24.1	10.3	0.5	7.0
7/18	28.8	7.5	29.3	18.3	11.0	0.8	5.1
8/25	22.0	10.0	32.3	21.4	10.9	0.6	3.0
9/30	21.0	16.8	24.6	10.0	14.6	0.4	2.8
10/ 1	20.6	16.4	26.1	10.8	15.3	0.4	2.5
10/20	18.0	17.8	20.8	4.2	16.6	0.2	1.9
11/ 8	13.8	14.3	23.9	7.3	16.6	0.2	1.9
11/15	14.7	19.0	23.3	8.6	14.7	0.3	2.4
11/20	13.6	18.0	18.7	4.2	14.5	0.2	2.4
12/22	11.1	17.8	15.1	0.2	14.9	0.4	2.6
1/13/2010	12.8	20.7	7.8	-5.1	12.9	0.2	1.8
2/ 8	13.6	15.6	9.8	-1.2	11.0	0.6	3.5
2/19	15.8	16.5	12.4	2.5	9.9	0.4	2.3
2/28	18.6	18.6	10.3	1.0	9.3	0.9	2.9
3/ 5	20.4	18.6	10.5	1.2	9.3	0.5	3.2
3/23	19.4	13.0	17.9	3.2	14.7	1.0	5.3

Solar Radiation

Figure 2.9 illustrates variations in the daily solar radiation on the horizontal and vertical surfaces during the months of April 2009 to March 2009. The gaps in the data were due to system repair and maintenance. The daily horizontal and vertical solar radiation shown in Figure 2.9 were calculated by using the trapezoid method to integrate the radiation data measured on the horizontal and vertical surfaces. With seasonal changes in the intensity of solar radiation on the horizontal and vertical surfaces, the highest solar radiation on the horizontal surface was recorded in the summer during the months of June, July, and August, and the highest solar radiation on the vertical surface was recorded in the late fall and winter during the months of November, December, and January.

Figure 2.10 shows variations in solar radiation on the horizontal and vertical surfaces for June 1, October 1, and November 15, 2009. June 1 and November 15 exhibited the largest vertical and transverse temperature distributions during the measurements. October 1 was selected to evaluate the transition of the environmental conditions from the summer to the late fall. Table 2.2 summarizes daily solar radiation calculated from the measurements. From June 1 to November 15, 2009, the daily horizontal solar radiation reduced from 28.8 to 14.7 MJ/m^2 while the daily vertical solar radiation increased from 7.4 to 20.9 MJ/m^2. Similarly, the intensity of solar radiation on the horizontal surface was the highest on June 1, and the solar radiation on the vertical surface was the highest on November 15.

Table 2.2: Solar radiation measured on the horizontal and vertical surfaces on June 1, October 1, and November 15, 2009.

Dates	Daily Solar Radiation (MJ/m^2)		Maximum Solar Radiation (W/m^2)	
	Horizontal	Vertical	Horizontal	Vertical
June 1	28.8	7.4	1,052	302
October 1	20.8	16.7	862	672
November 15	14.7	20.9	674	867

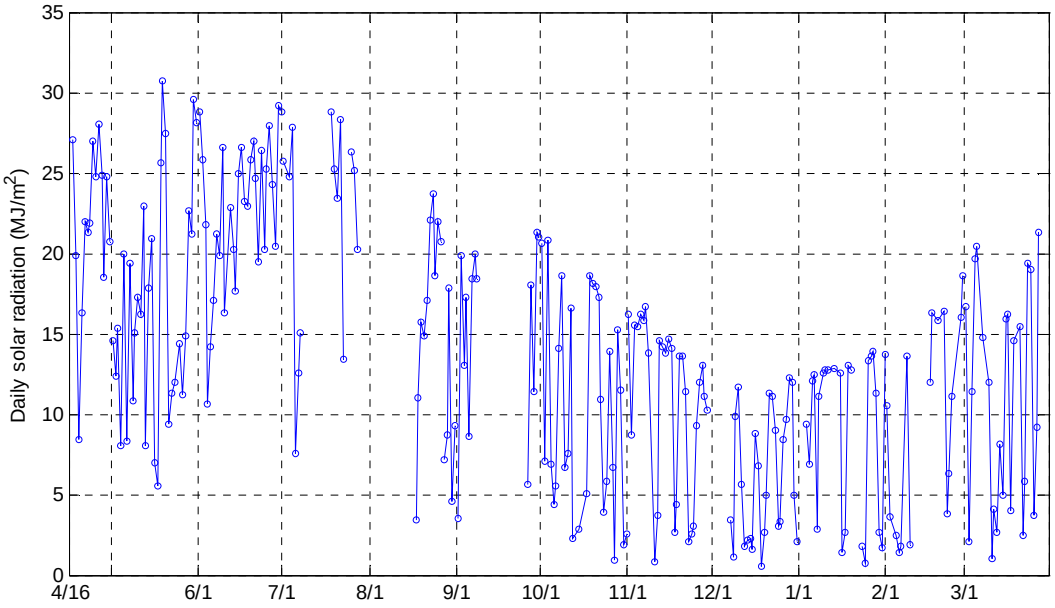

(a) Daily solar radiation on the horizontal surface

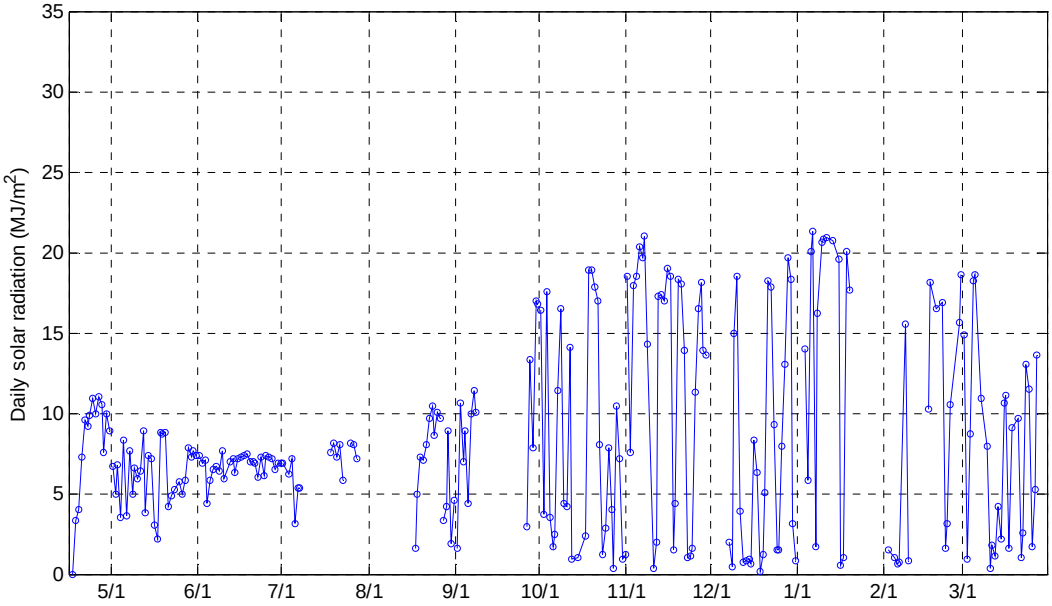

(b) Daily solar radiation on the vertical surface

Figure 2.9: Variation in daily solar radiation on horizontal and vertical surfaces during the months of April 2009 to March 2010.

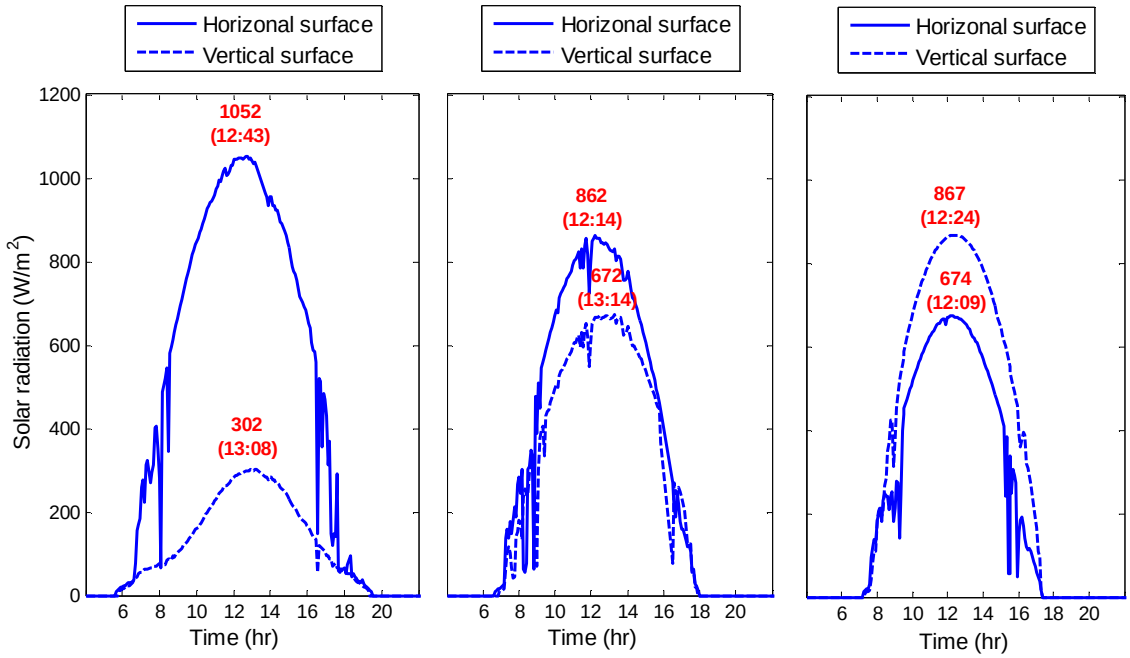

(a) June 1 (b) October 1 (c) November 15

Figure 2.10: Solar radiation measured on the horizontal and vertical surfaces on June 1, October 1, and November 15, 2009.

Air Temperature

The maximum and minimum measured ambient air temperatures from April 2009 to March 2010 are shown in Figure 2.11. As expected, the daily maximum and minimum air temperatures increased in the summer and decreased from the summer to the winter. For the three days, June 1, October 1, and November 15, Figure 2.12 shows variations in the ambient air temperatures as a function of the time of day, in which minimum temperatures were measured around sunrise, and maximum temperatures were measured around 2 or 3 p.m.

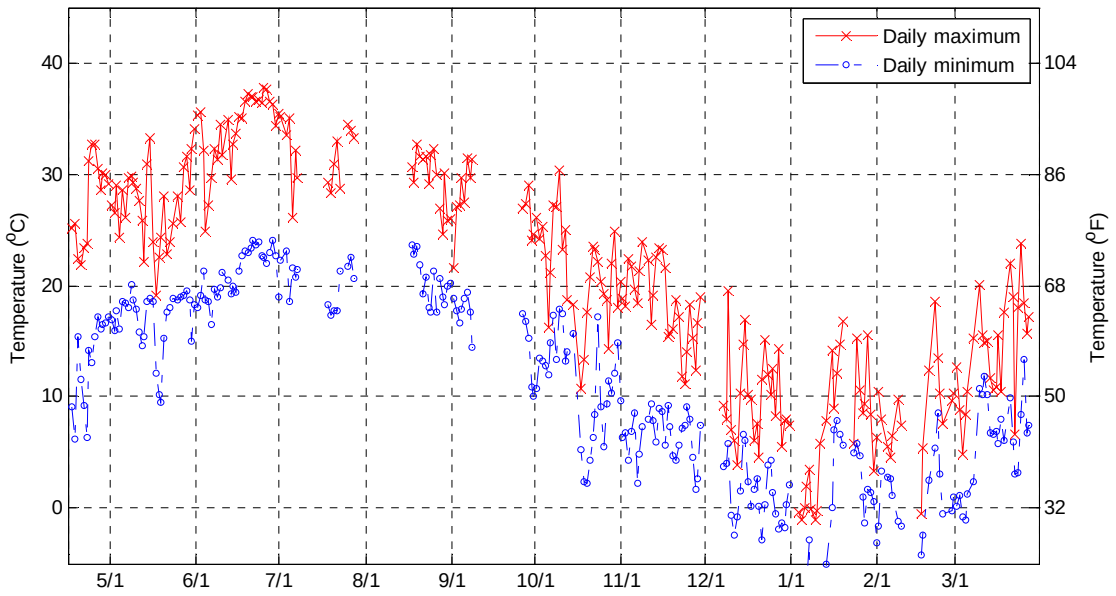

Figure 2.11: Variation in daily maximum and minimum air temperatures during the months of April 2009 to March 2010.

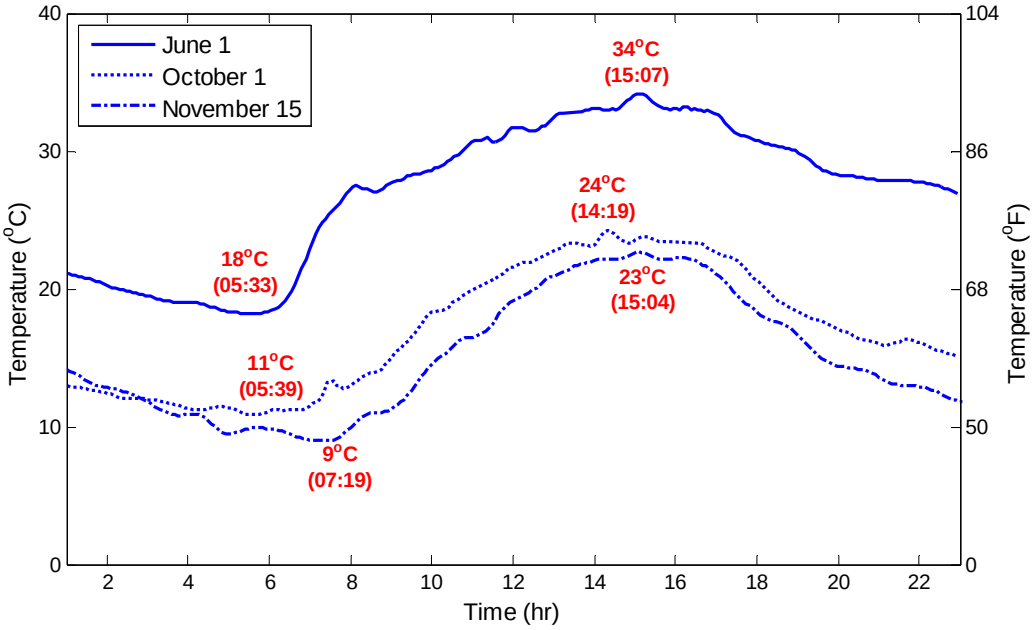

Figure 2.12: Ambient air temperatures measured on June 1, October 1, and November 15, 2009.

Wind Speed

This study also evaluated variations in daily average wind speed which was calculated by integrating the measurements using the trapezoid numerical method and dividing the integration by the total measurement time of the day. The daily average wind speed shown in Figure 2.13 is less than 3 m/sec, or 6.7 mph during the measurements taken from April 2009 to March 2010, even though somewhat higher values occurred in the winter. The record maximum wind speed, or the highest wind speed during the measurements, was 14.9 m/sec, or 33.2 mph, on June 8, 2009. In addition, Figure 2.14 shows the wind speed less than 1 m/sec, or 2.2 mph, for June 1, October 1, and November 15.

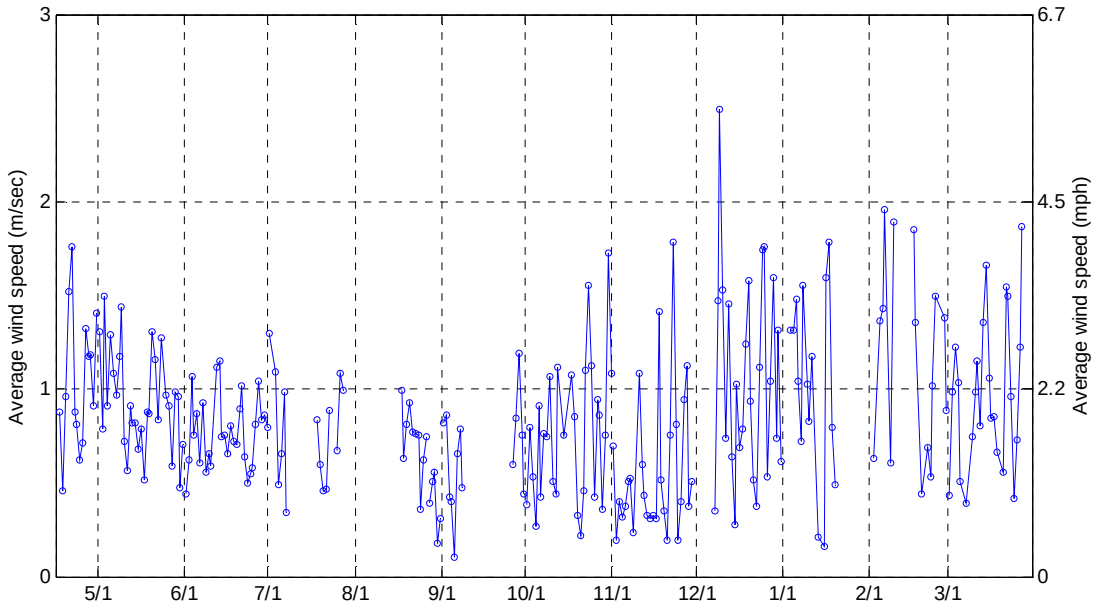

Figure 2.13: Variation in daily average wind speed during the months of April 2009 to March 2010.

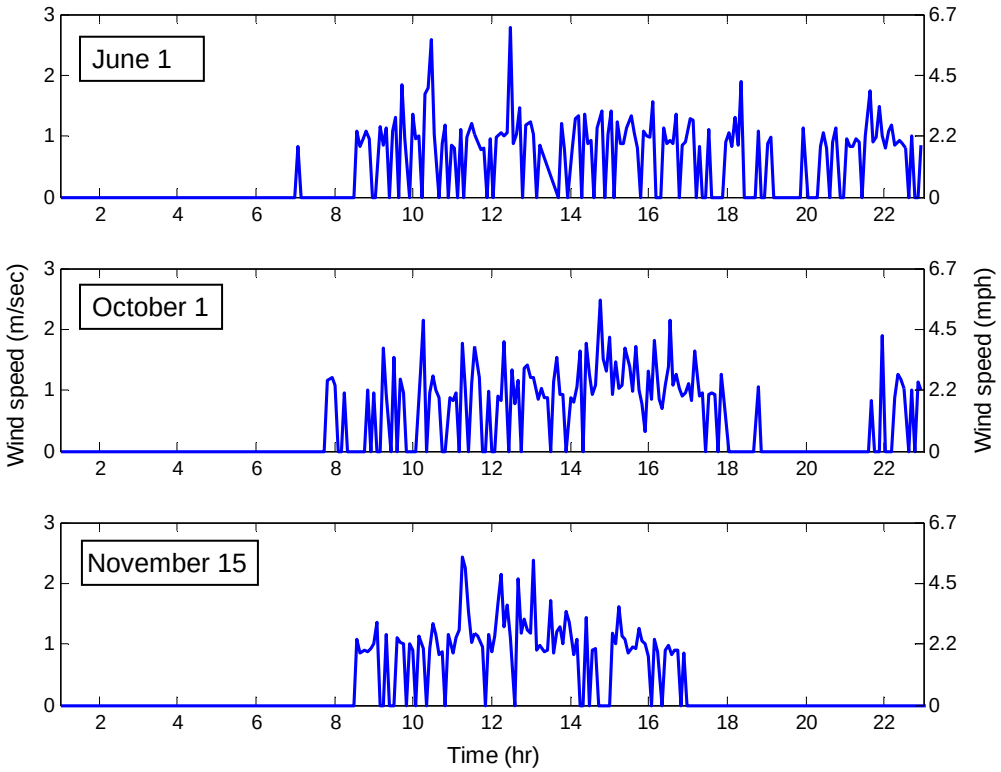

Figure 2.14: Wind speed measured on June 1, October 1, and November 15, 2009.

2.4.2 Girder Temperatures

In addition to variations in daily environmental conditions, Figures 2.15 to 2.19 illustrate variations in daily highest and lowest girder temperatures measured in the top flange, the web, and the bottom flange during the months of April 2009 to March 2010. As mentioned earlier, the readings contain several gaps due to system repair and maintenance.

For the top flange, Figures 2.15 and 2.16 show the daily highest and lowest temperature changes on the south side (thermocouple 2) and on the top surface (thermocouple 28) during the measurements, respectively. With high solar radiation and high air temperature in the summer, the temperatures of the top flange were the maximum in the summer and decreased with seasonal changes from the summer to the winter.

Variations in the daily highest and lowest temperatures in the middle of the girder web (thermocouple 7) are presented in Figure 2.17, which indicates as expected that the maximum temperature was recorded in the summer, and the minimum temperature was recorded in the winter. In addition, Figures 2.18 and 2.19 show variations in the daily highest and lowest temperatures on the south vertical surface (thermocouple 14) and on the bottom surface of the bottom flange (thermocouple 13), respectively.

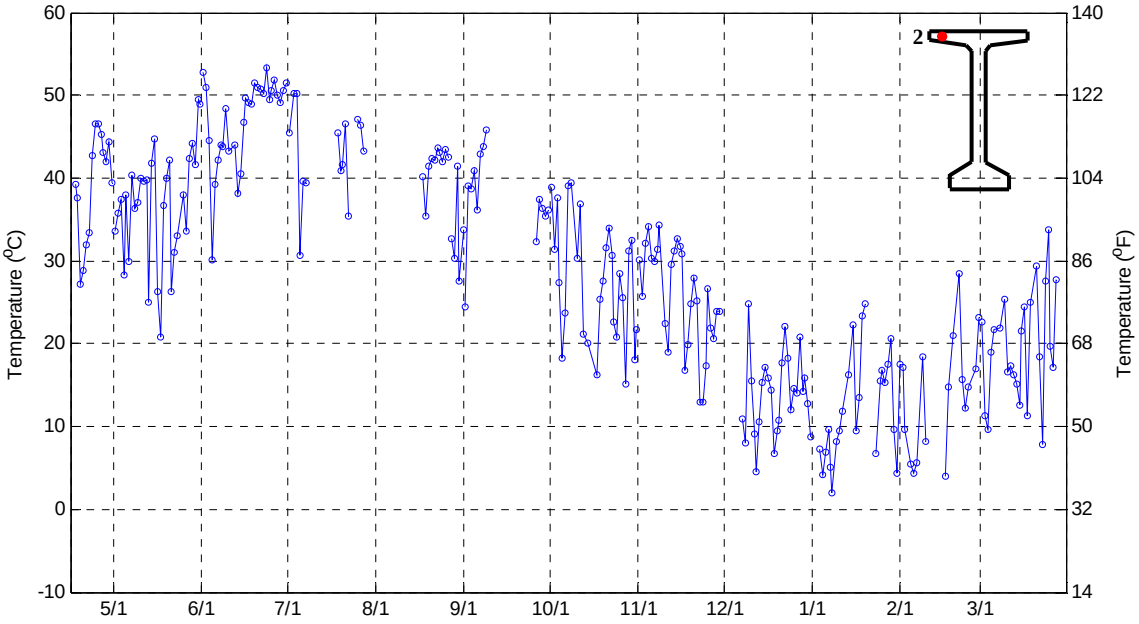

(a) Daily highest temperature

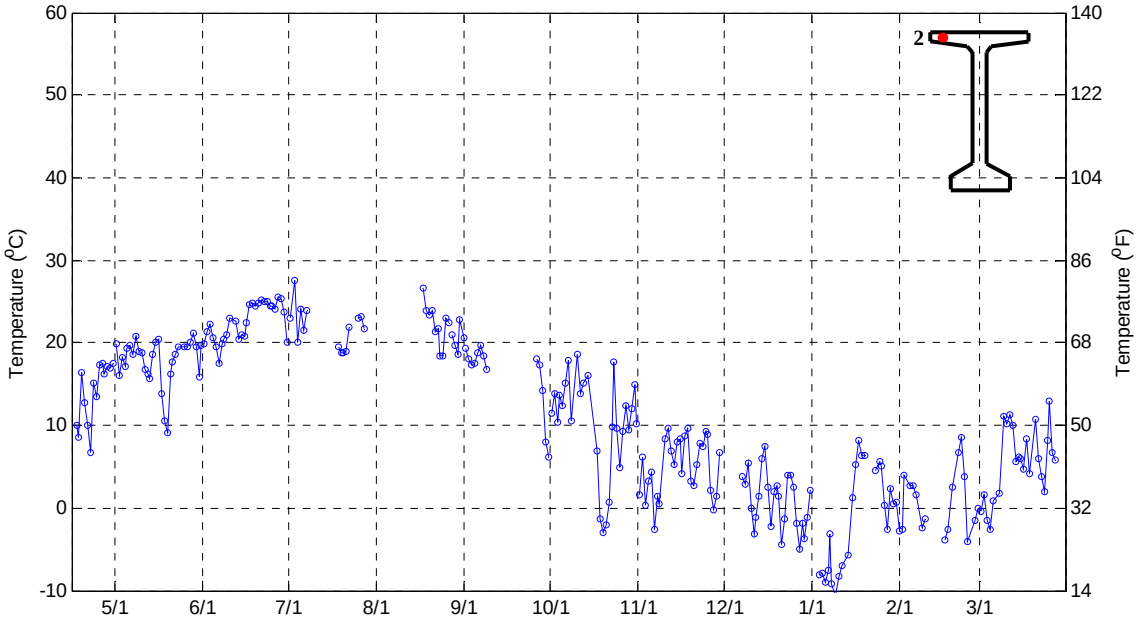

(b) Daily lowest temperature

Figure 2.15: Variation in the daily highest and lowest temperatures in the south side of the top flange (thermocouple 2) during the months of April 2009 to March 2010.

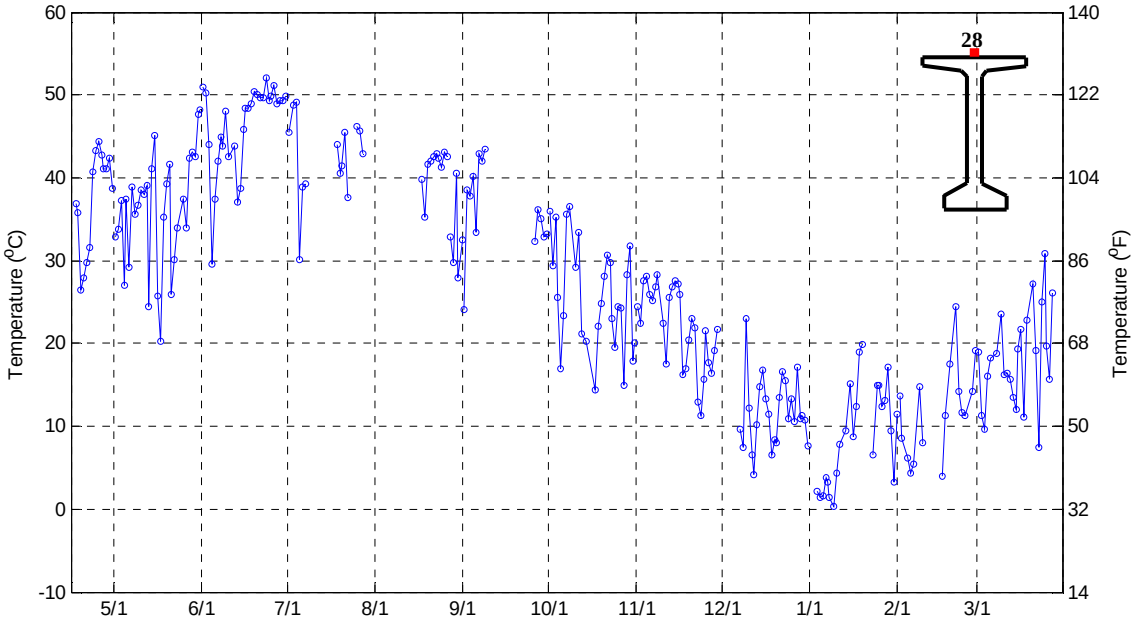

(a) Daily highest temperature

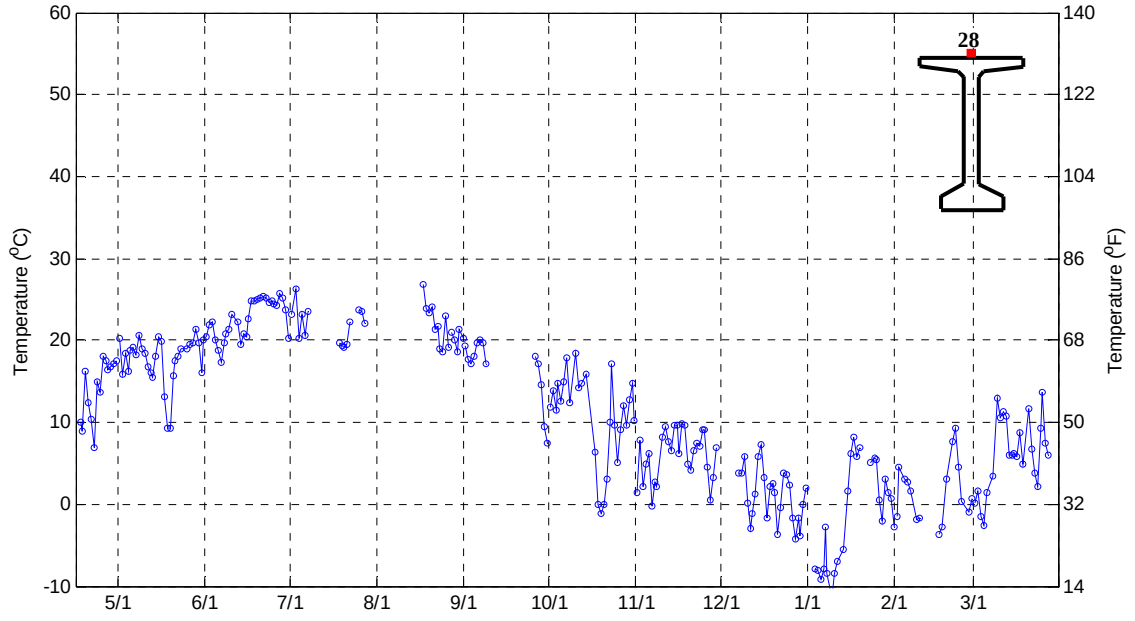

(b) Daily lowest temperature

Figure 2.16: Variation in the daily highest and lowest temperatures on the top surface of the girder (thermocouple 28) during the months of April 2009 to March 2010.

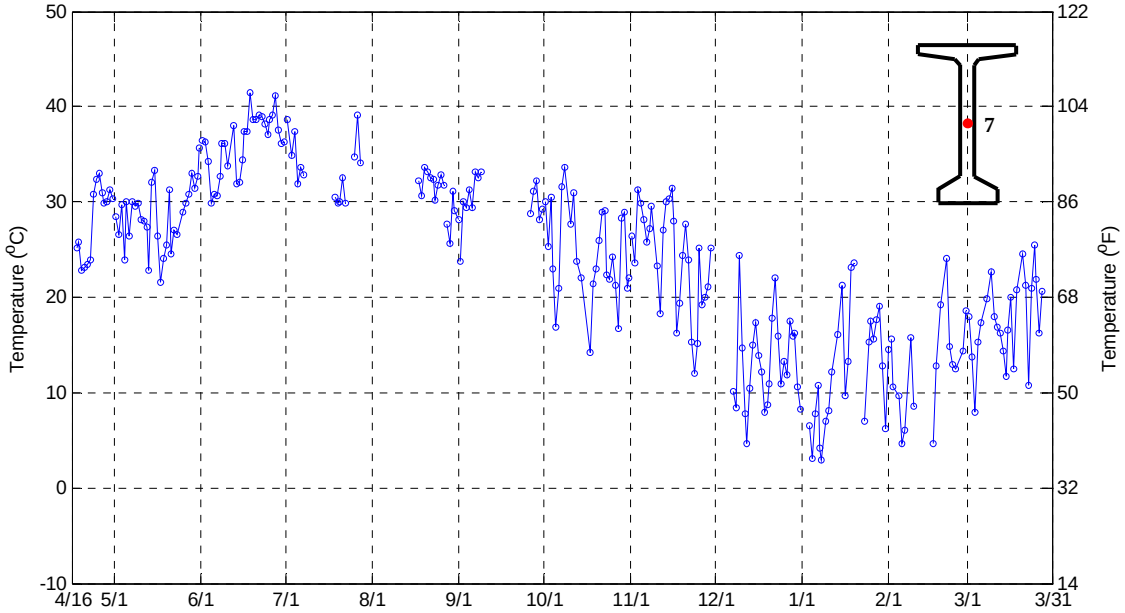

(a) Daily highest temperature

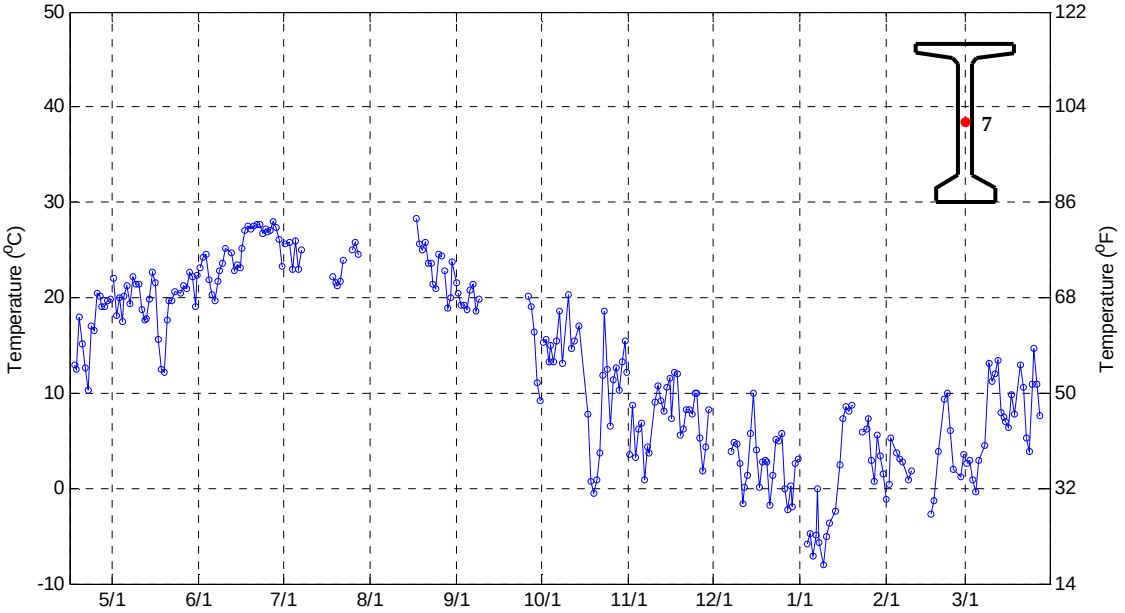

(b) Daily lowest temperature

Figure 2.17: Variation in the daily highest and lowest temperatures in the middle of the girder web (thermocouple 7) during the months of April 2009 to March 2010.

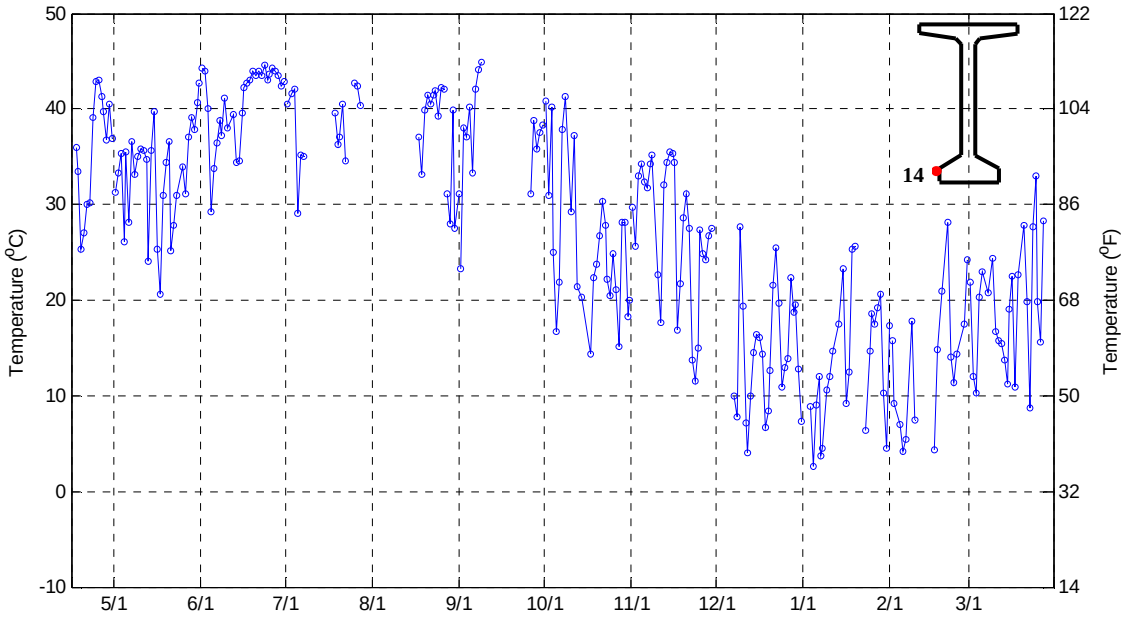

(a) Daily highest temperature

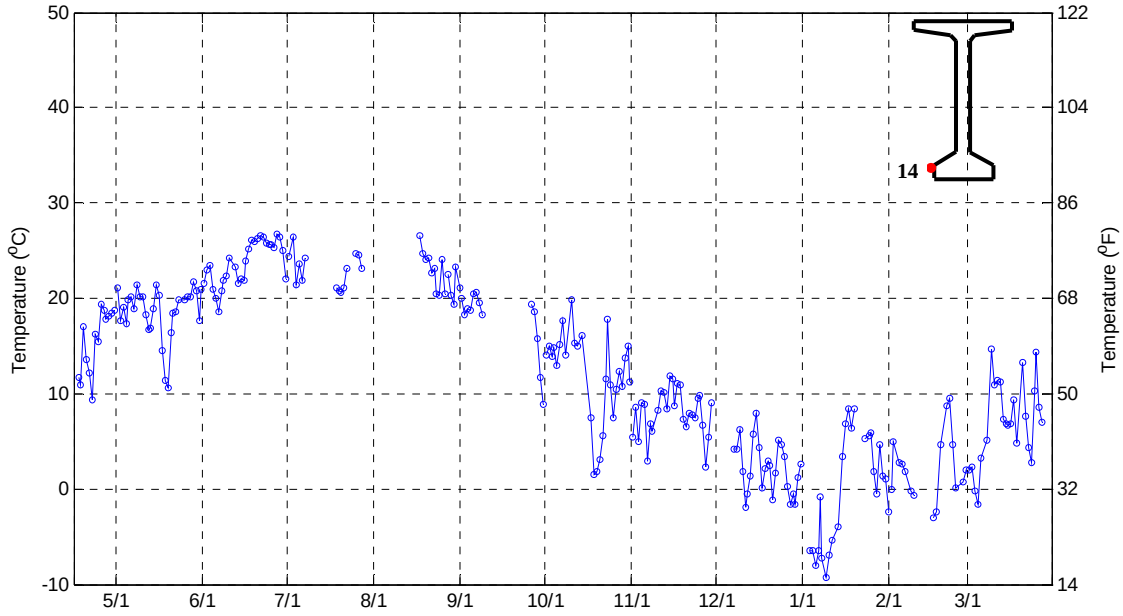

(b) Daily lowest temperature

Figure 2.18: Variation in the daily highest and lowest temperatures on the south vertical surface of the bottom flange (thermocouple 14) during the months of April 2009 to March 2010.

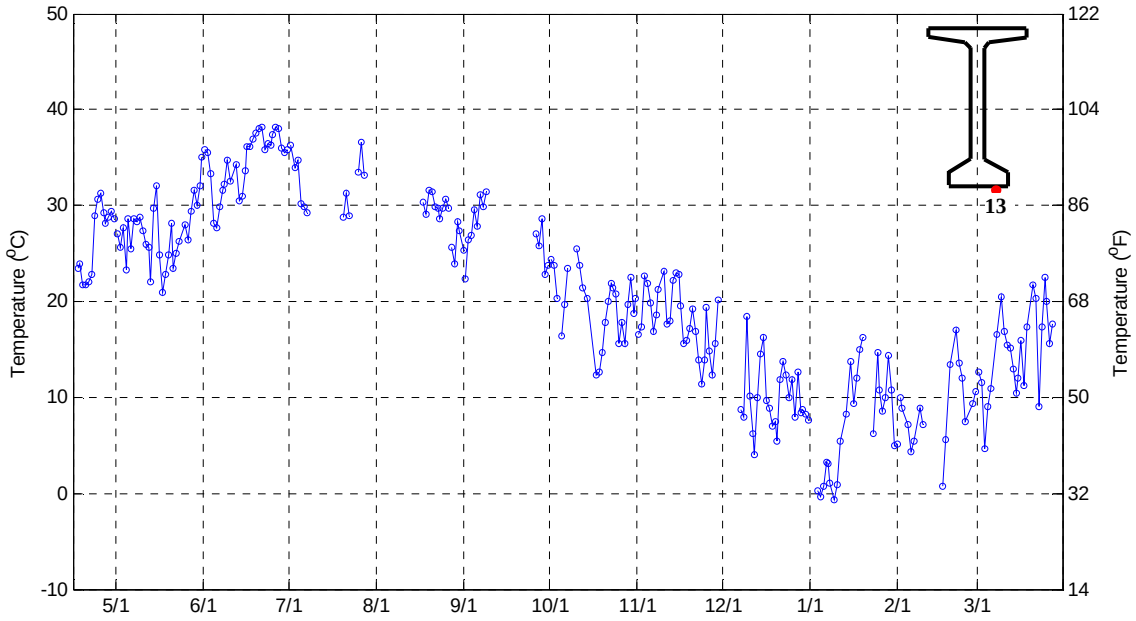

(a) Daily highest temperature

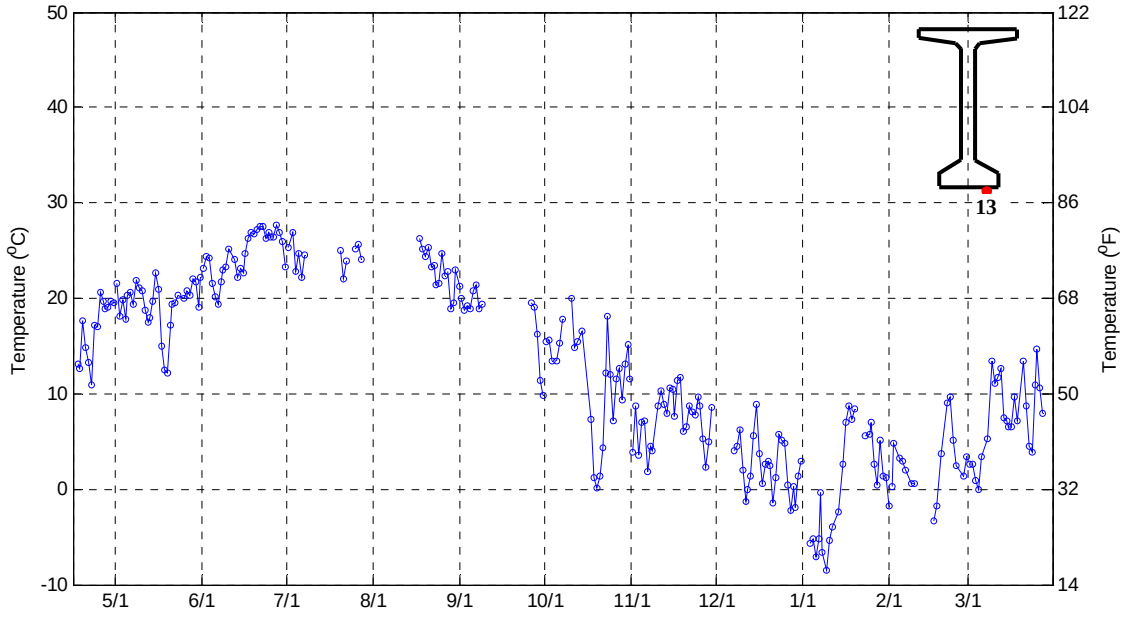

(b) Daily lowest temperature

Figure 2.19: Variation in the daily highest and lowest temperatures on the bottom surface of the girder (thermocouple 13) during the months of April 2009 to March 2010.

2.5 Variations in Vertical and Transverse Temperature Differences

Based on the measurements, the vertical temperature differences were determined from the difference of the highest and lowest temperatures along the depth of the girder (thermocouples 28, 5, 6, 7, 8, 9, 12, 13), and the transverse temperature differences were determined from the temperature differences across the top flange (thermocouples 2, 4, 5, 3, 1), the girder web (thermocouples 20, 7, 21), and the bottom flange (thermocouples 14, 10, 9, 11, 15).

2.5.1 Vertical Temperature Differences

The highest temperature in the BT-63 section was measured on the top surface while the lowest temperature was measured in the bottom flange. Figure 2.20 shows a variation in the daily vertical temperature changes along the depth of the girder (thermocouples 28, 5, 6, 7, 8, 9, 12, 13) during the measurements. The two largest vertical temperature differences, 20.9°C (37.6°F) and 20.4°C (36.7°F), were measured on May 30 and June 1, 2009, respectively. Along with the daily highest temperatures on the top surface shown in Figure 2.16(a), Table 2.3 summarizes the daily vertical temperature differences for selected sunny days during the measurements from April 2009 to March 2010. In the summer during the months of May to July, the highest daily girder temperatures ranged from 46°C (115°F) to 54°C (129°F) and the daily vertical temperature differences from 18°C (32°F) to 21°C (38°F). With seasonal changes from the summer to the winter, the highest girder temperatures decreased approximately to 13°C (55°F), and the vertical temperature differences decreased to 9°C (16°F).

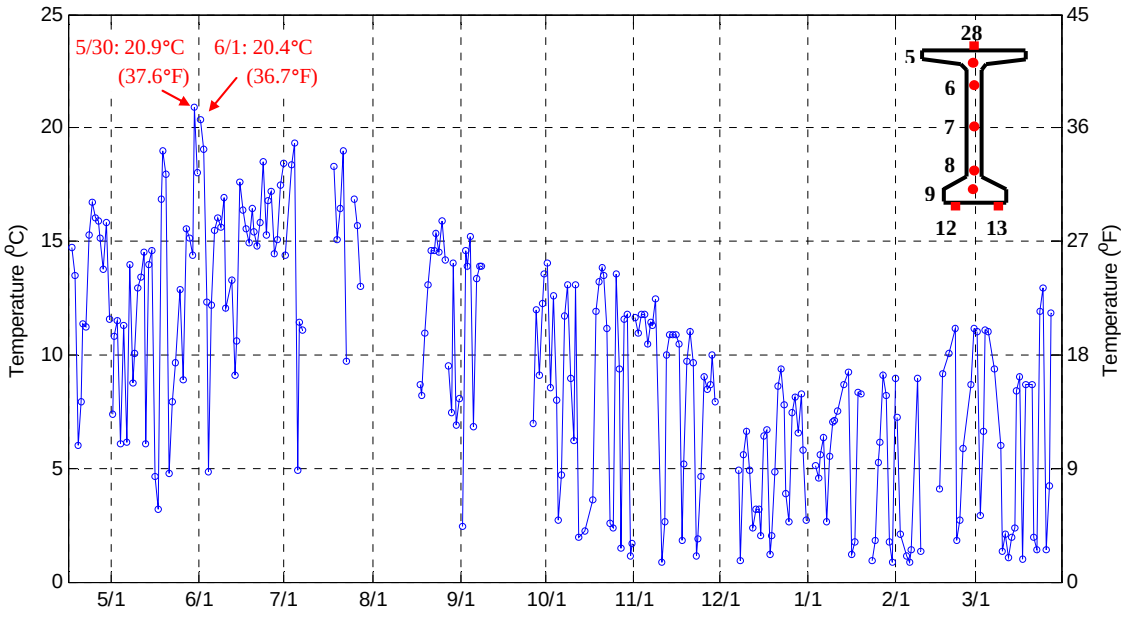

Figure 2.20: Variation in the daily vertical temperature differences along the depth of the girder during the months of April 2009 to March 2010.

Table 2.3: The highest daily girder temperatures and the daily vertical temperature differences for selected sunny days during the months of April 2009 to March 2010.

Dates	Highest Girder Temperatures, °C (°F)	Vertical Temperature Differences, °C (°F)
4/24/2009	45.5 (113.9)	16.7 (30.1)
5/20	41.6 (106.9)	18.0 (32.3)
5/30	49.4 (121.0)	20.9 (37.6)
6/ 1	52.8 (127.1)	20.4 (36.7)
6/23	53.6 (128.5)	18.5 (33.3)
7/18	45.5 (113.8)	18.3 (33.0)
8/25	44.0 (111.2)	15.9 (28.6)
9/30	35.3 (95.6)	13.6 (24.4)
10/ 1	38.4 (101.2)	14.1 (25.3)
10/20	30.9 (87.5)	13.8 (24.9)
11/ 8	32.8 (91.0)	12.5 (22.4)
11/15	30.9 (87.6)	10.9 (19.5)
11/20	26.7 (80.1)	11.1 (19.9)
12/22	20.8 (69.5)	9.4 (16.9)
1/13/2010	13.3 (55.9)	8.7 (15.7)
1/27	15.1 (59.2)	9.1 (16.4)
2/ 8	17.1 (62.8)	8.9 (16.1)
2/19	19.8 (67.7)	10.1 (18.1)
2/28	21.6 (70.8)	11.1 (20.0)
3/ 5	20.4 (68.8)	11.0 (19.8)
3/23	26.9 (80.3)	11.9 (21.4)

2.5.2 Transverse Temperature Differences

In addition to the vertical temperature differences, the transverse temperature differences were determined from the differences between the highest and lowest temperatures in the top flange, the web, and the bottom flange of the girder. Since the specimen was oriented in an east-west direction, the highest temperatures were recorded on the south-facing surfaces, and the lowest temperatures were on the north-facing surfaces in the web. In the top and bottom flanges, the lowest temperatures were recorded in the middle of the top and bottom flanges.

Figure 2.21 shows the daily transverse temperature changes across the top flange (thermocouples 2, 4, 5, 3, 1). The large transverse temperature differences of 10.6°C (19.1°F) and 10.0°C (18.0°F) were measured on November 8 and 15, 2009, respectively. For the web, Figures 2.22 to 2.24 illustrate the daily transverse temperature changes across the top (thermocouples 22, 6, 23), the middle (thermocouples 20, 7, 21), and bottom (thermocouples 18, 8, 19) of the web, respectively. The transverse temperature difference in the top of the web shown in Figure 2.22 is around 3°C (5.5°F) with no specific variations during the year because of the shadow of the top flange. However, the middle and bottom of the web, which did not have shadow from the top flange in the fall, spring, and winter seasons, exhibited increases in transverse temperature differences as shown in Figures 2.23 and 2.24. The large transverse temperature difference in the middle of the web is 11.4°C (20.4°F) on November 8 and 11.5°C (20.6°F) on November 15, 2009. Similarly, the bottom of the web showed a large transverse temperature difference of 10.6°C (19.2°F) on October 20 and 9.3°C (16.8°F) on November 15, 2009. In addition, Figure 2.25 shows the variation in the daily transverse temperature differences across the bottom flange (thermocouples 14, 10, 9, 11, 15), in which large differences of 21.5°C (38.7°F) and 20.5°C (36.8°F) were measured on October 1 and November 15, 2009, respectively.

Table 2.4 summarizes the large transverse temperature differences in the top flange, the web, and the bottom flange for selected sunny days during the measurements from April 2009 to March 2010. Contrary to the vertical temperature changes, large transverse temperature differences, approximately 10°C (18°F) in the top flange and the web and 20°C (38°F) in the bottom flange, were measured in the late fall and winter during the months of October, November, and December due to high solar radiation on the vertical surface.

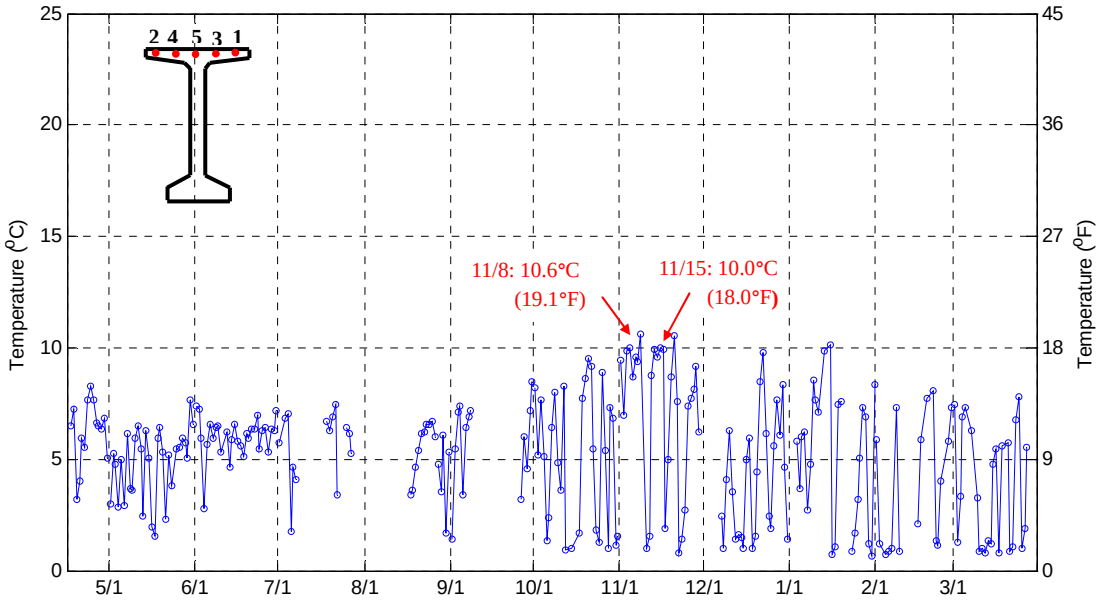

Figure 2.21: Variation in the daily transverse temperature differences in the top flange during the months of April 2009 to March 2010.

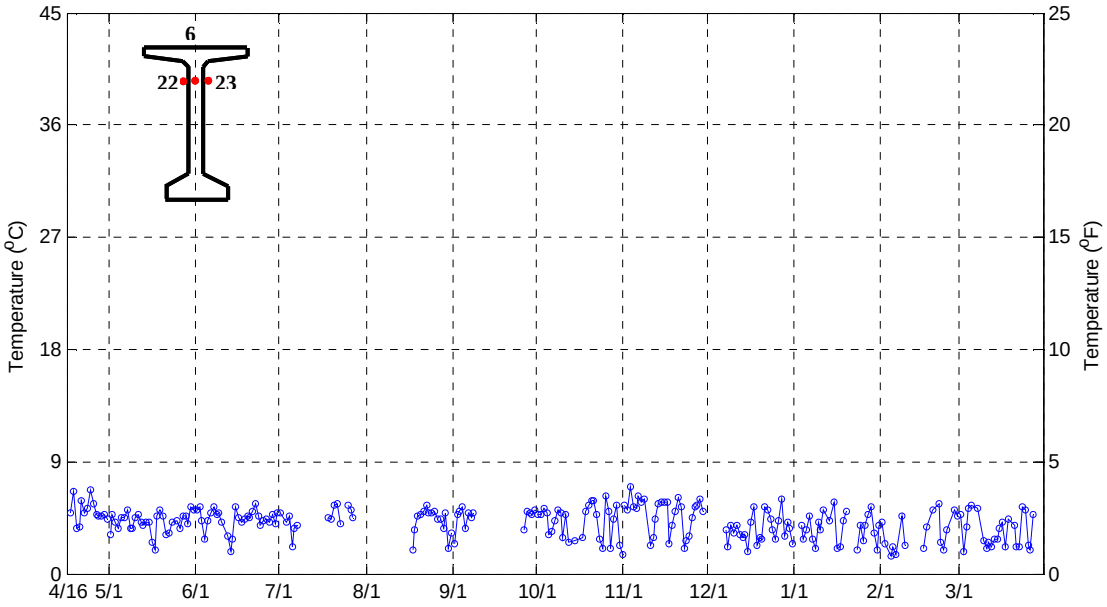

Figure 2.22: Variation in the daily transverse temperature differences in the top of the web during the months of April 2009 to March 2010.

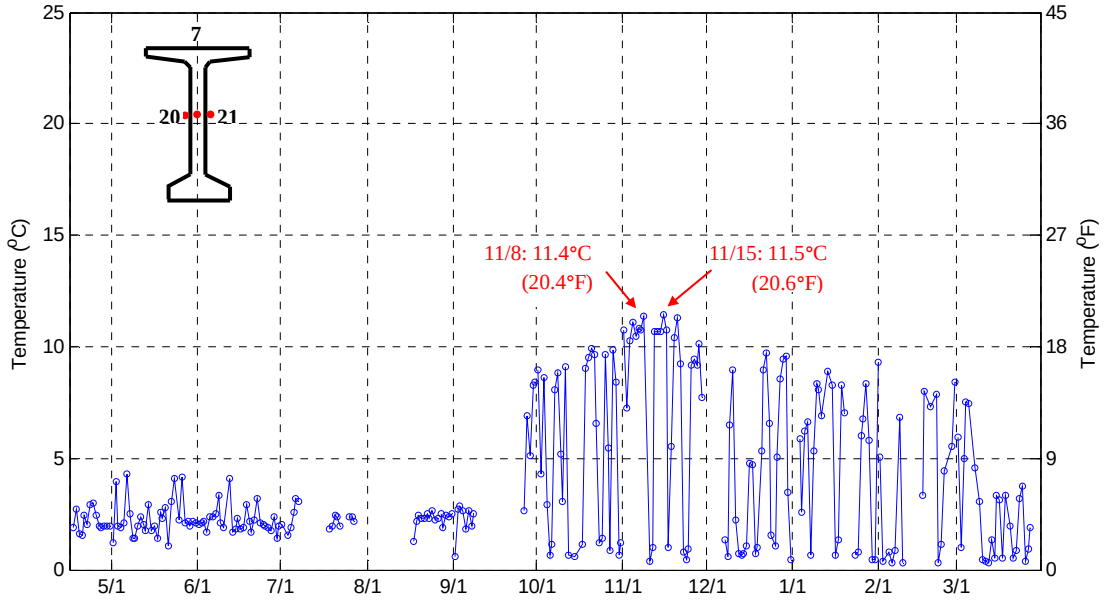

Figure 2.23: Variation in the daily transverse temperature differences in the middle of the web during the months of April 2009 to March 2010.

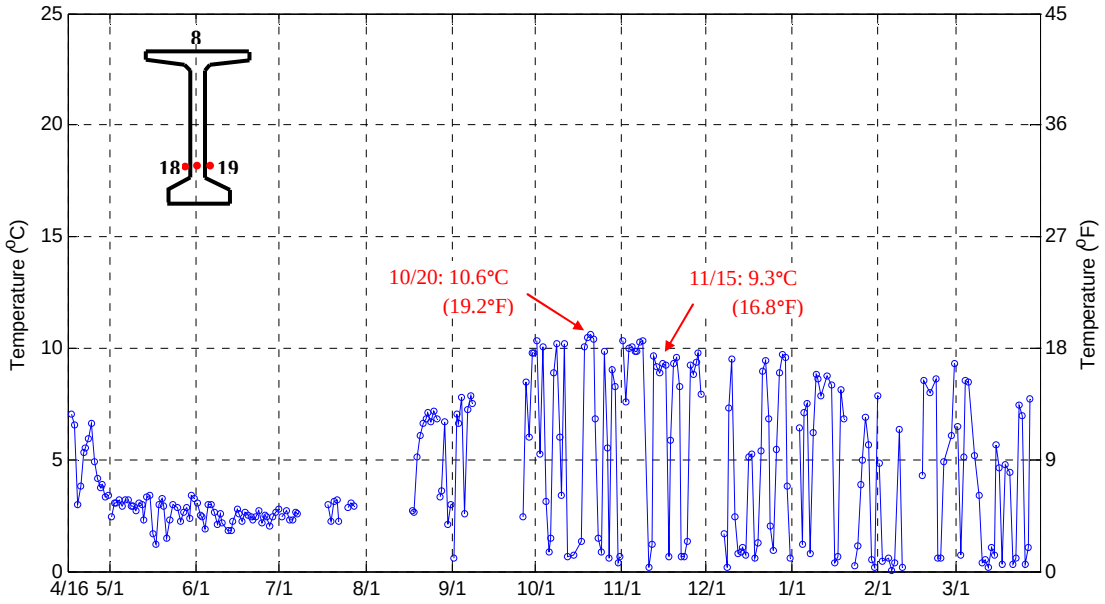

Figure 2.24: Variation in the daily transverse temperature differences in the bottom of the web during the months of April 2009 to March 2010.

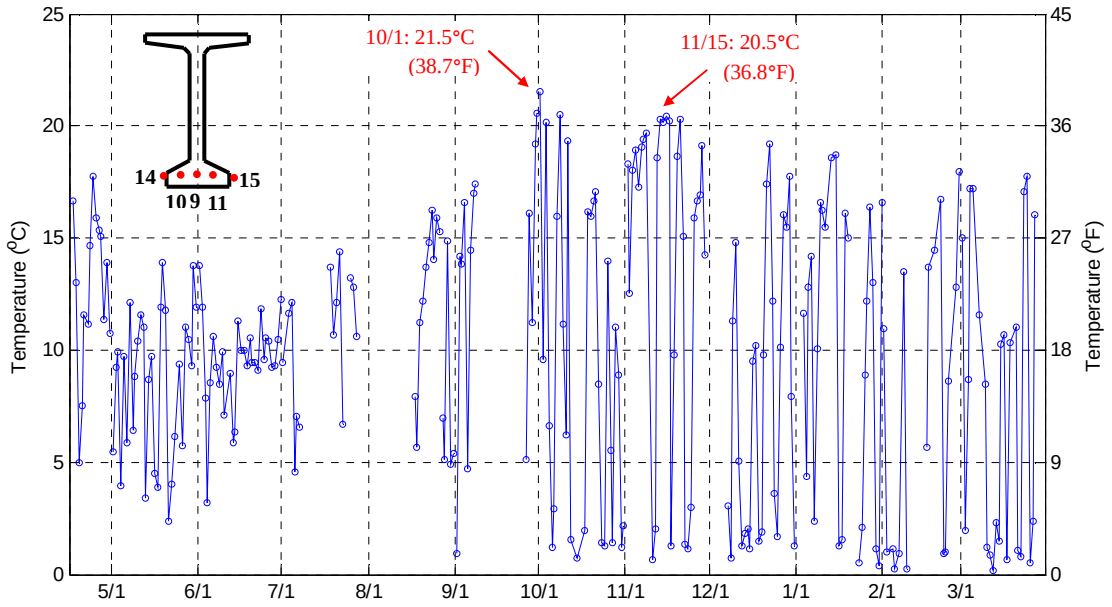

Figure 2.25: Variation in the daily transverse temperature differences in the bottom flange during the months of April 2009 to March 2010.

Table 2.4: The daily transverse temperature differences in the top flange, the web, and the bottom flange for selected sunny days during the months of April 2009 to March 2010.

Dates	Transverse Temperature Differences, °C (°F)				
	Top flange	Top-web	Mid-web	Bottom-web	Bottom flange
4/24/2009	8.3 (14.9)	3.7 (6.7)	3.0 (5.4)	6.7 (12.0)	17.8 (32.0)
5/20	5.3 (9.6)	2.6 (4.6)	2.8 (5.0)	3.0 (5.3)	11.8 (21.2)
5/30	7.6 (13.8)	3.0 (5.4)	2.2 (3.9)	3.4 (6.1)	13.8 (24.8)
6/ 1	7.4 (13.3)	2.8 (5.1)	2.1 (3.7)	3.1 (5.5)	13.8 (24.8)
6/23	7.0 (12.6)	2.6 (4.6)	2.1 (3.8)	2.7 (4.8)	11.9 (21.4)
7/18	6.7 (12.1)	2.5 (4.5)	1.8 (3.2)	3.0 (5.3)	13.7 (24.7)
8/25	6.7 (12.0)	2.8 (5.0)	2.3 (4.1)	7.2 (13.0)	15.9 (28.6)
9/30	8.5 (15.2)	2.9 (5.2)	8.4 (15.2)	9.8 (17.7)	20.6 (37.1)
10/ 1	8.2 (14.8)	2.6 (4.7)	8.9 (16.1)	10.4 (18.6)	21.5 (38.7)
10/20	9.5 (17.1)	3.3 (5.9)	9.9 (17.9)	10.6 (19.2)	16.7 (30.0)
11/ 8	10.6 (19.1)	3.4 (6.0)	11.4 (20.4)	10.3 (18.6)	19.7 (35.4)
11/15	10.0 (18.0)	3.2 (5.8)	11.5 (20.6)	9.3 (16.8)	20.5 (36.8)
11/20	10.5 (19.0)	3.4 (6.2)	11.3 (20.3)	9.6 (17.2)	20.3 (36.5)
12/22	9.8 (17.7)	2.8 (5.1)	9.7 (17.4)	9.4 (17.0)	19.2 (34.6)
1/13/2010	9.8 (17.7)	2.4 (4.2)	8.9 (16.0)	8.8 (15.8)	18.6 (33.5)
1/27	7.3 (13.2)	2.6 (4.7)	8.3 (15.0)	6.9 (12.4)	16.4 (29.5)
2/ 8	7.3 (13.2)	2.6 (4.7)	6.8 (12.3)	6.4 (11.4)	13.5 (24.2)
2/19	7.8 (14.0)	2.9 (5.1)	7.3 (13.1)	8.0 (14.4)	14.5 (26.1)
2/28	7.3 (13.1)	2.6 (4.6)	8.4 (15.1)	9.3 (16.8)	18.0 (32.3)
3/ 5	7.3 (13.1)	3.1 (5.5)	7.5 (13.5)	8.5 (15.2)	17.2 (31.0)
3/23	6.8 (12.2)	3.0 (5.4)	3.2 (5.8)	7.5 (13.4)	17.1 (30.7)

2.6 Variations in Vertical and Transverse Temperature Distributions and Gradients

According to the daily vertical and transverse temperature differences in the girder during the year, the largest vertical temperature difference was recorded in the summer, and it decreased from the summer to the winter. On the other hand, the largest transverse temperature differences occurred in the late fall and the winter and the smallest in the summer. Thus, based on the largest vertical and transverse temperature differences, June 1 and November 15, 2009 were selected as representative days of the largest vertical and transverse temperature distributions, respectively. October 1, which showed large vertical and transverse temperature differences in the fall, was chosen to evaluate the transition of the largest vertical and transverse temperature distributions from the summer to the fall.

2.6.1 Vertical Temperature Distributions and Gradients

Figure 2.26 shows vertical temperature distributions through the depth of the BT-63 section for the three days of June 1, October 1, and November 15, 2009. As noted previously, the temperature magnitude was the highest on June 1 and the smallest on November 15. The highest temperature was measured on the top surface of the top flange (thermocouple 28) and the lowest temperature in the bottom flange (thermocouple 9). In particular, on October 1 and November 15, the temperatures in the girder web exhibited relatively higher increases due to high solar radiation on the vertical surface. Thus, the temperature distribution in the web increased with changes from the summer to the fall. In addition, Figure 2.26 includes temperature distributions, defined by a minimum average temperature of the girder, which would provide the girder with a minimum and a constant temperature distribution over the cross-section. The temperature distributions obtained by the minimum average temperatures shown in Figure 2.26 were nearly constant at around 24°C (74°F) at 6:33 a.m. on June 1 and 15°C (59°F) at 7:05 a.m. on October 1 and 13°C (55°F) at 7:40 a.m. on November 15.

The vertical temperature gradients, defined by subtracting the minimum temperature from the vertical temperature distribution, are presented in Figure 2.27. The representative day of the summer, or June 1, shows a rapid gradient decrease from the top surface and no large gradient in the web. For October 1 and November 15, which show lower temperatures on the top surface, the web temperature gradients increased due to an increase in solar radiation on the vertical surface from the summer to the fall. The vertical temperature differentials, or the temperature difference between the highest and lowest temperatures along the depth of the girder, are 20.4°C (36.7°F) on June 1, 14.1°C (25.3°F) on October 1, and 10.9°C (19.5°F) on November 15, 2009.

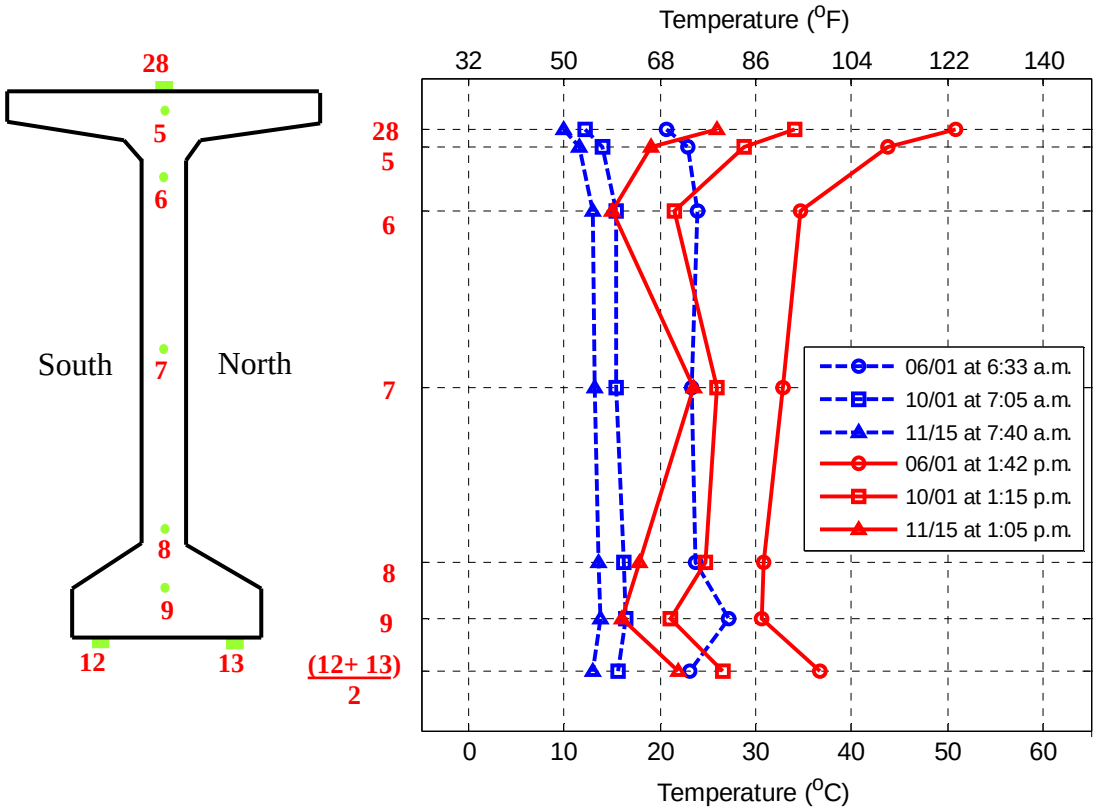

Thermocouple No.		28	5	6	7	8	9	12	13
Temperature, °C (°F) on June 1	6:33 a.m.	20.6 (69.1)	23.0 (73.4)	23.9 (75.0)	23.3 (74.0)	23.8 (74.8)	27.1 (80.7)	23.2 (73.7)	23.2 (73.7)
	1:42 p.m.	50.9 (123.7)	43.8 (110.8)	34.8 (94.6)	32.8 (91.1)	30.8 (87.5)	30.6 (87.0)	39.7 (103.5)	33.8 (92.8)
Temperature, °C (°F) on Oct. 1	7:05 a.m.	12.2 (53.9)	14.0 (57.2)	15.4 (59.7)	15.4 (59.7)	16.2 (61.2)	16.4[a] (61.5)	15.6 (60.1)	15.6 (60.1)
	1:15 p.m.	34.1 (93.4)	28.8 (83.9)	21.4 (70.5)	25.9 (78.6)	24.7 (76.5)	21.0[a] (69.8)	31.7 (89.0)	21.6 (70.9)
Temperature, °C (°F) on Nov. 15	7:40 a.m.	9.9 (49.8)	11.6 (52.9)	12.9 (55.2)	13.1 (55.5)	13.6 (56.6)	13.8[a] (56.9)	13.0 (55.4)	12.9 (55.2)
	1:05 p.m.	25.9 (78.6)	19.0 (66.2)	15.0 (59.0)	23.4 (74.2)	17.9 (64.3)	16.0[a] (60.7)	26.2 (79.1)	17.8 (64.0)

[a] Due to failure of thermocouple 9, the temperature at the location of thermocouple 9 on October 1 and November 15, 2009 were extrapolated using the second-order model (See Appendix A).

Figure 2.26: The vertical temperature distributions on June 1, October 1, and November 15, 2009 in Atlanta, Georgia.

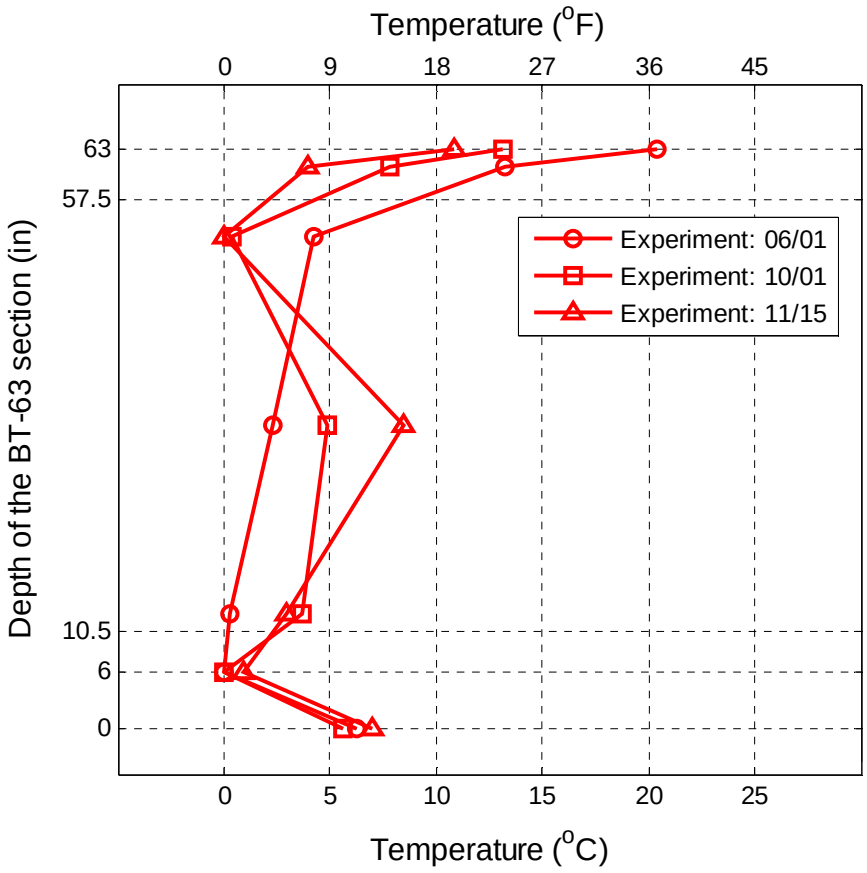

Figure 2.27: The vertical temperature gradients on June 1, October 1, and November 15, 2009 in Atlanta, Georgia.

2.6.2 Transverse Temperature Distributions and Gradients

Figures 2.28 to 2.30 show the transverse temperature distributions across the top flange, the web, and the bottom flange on June 1, October 1, and November 15, 2009. The highest temperature occurred on the south side of the top flange (thermocouple 2), and the lowest temperature occurred in the middle of the top flange (thermocouple 5) as shown in Figure 2.28. Figure 2.29 shows the transverse temperature distributions across the middle of web, in which the south-facing vertical surface exhibited higher temperatures on October 1 and November 15 due to high solar radiation on that surface. Also, the temperature on the vertical surface of the bottom flange on the south side also exhibited higher temperatures on October 1 and November 15 as shown in Figure 2.30.

Furthermore, similar to the vertical temperature distributions in the early morning, Figures 2.28 to 2.30 include transverse temperature distributions defined from the minimum of the average temperatures over the cross-section for the three days. On June 1, the temperature distributions at around 6:30 a.m. were nearly constant at around 21°C (70°F) in the top flange, 23°C (73°F) in the web, and 24°C (75°F) in the bottom flange. The transverse temperature distributions on November 1 were nearly constant at approximately 12°C (54°F) in the top flange, 15°C (59°F) in the web, and 15°C (60°F) in the bottom flange. On November 15, the transverse temperature distributions in the top flange, the web, and the bottom flange were approximately 10°C (50°F), 12°C (54°F), and 13°C (55°F), respectively.

Based on the transverse temperature distributions, the maximum transverse temperature gradients were obtained from subtracting the minimum temperature from the maximum transverse temperature distributions. The transverse temperature gradients in the top flange shown in Figure 2.31 are similar regardless of seasonal changes. Figure 2.32 shows the transverse temperature gradients in the middle of the web, which exhibit larger temperature gradients on October 1 and November 15. Similarly, the transverse temperature gradient of the bottom flange shown in Figure 2.33 also rapidly increases on the south vertical surface on October 1 and November 15 due to high solar radiation on the vertical surface. The largest transverse temperature differentials, calculated by the difference of the highest and lowest temperatures, are 10.0°C (18.0°F) in the top flange, 11.5°C (20.6°F) in the middle of the web, and 20.5°C (36.8°F) in the bottom flange on November 15, 2009.

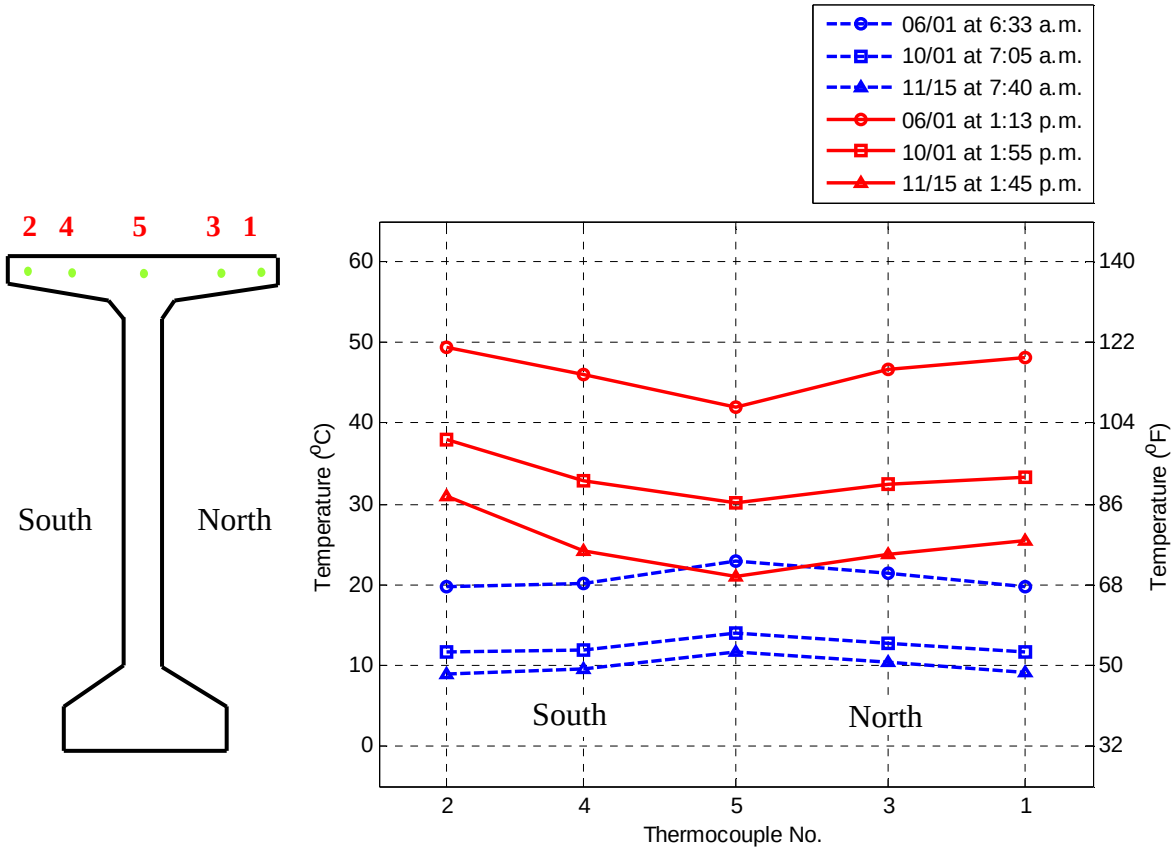

Thermocouple No.		2	4	5	3	1
Temperature, °C (°F) on June 1	6:33 a.m.	19.8 (67.7)	20.2 (68.3)	23.0 (73.4)	21.3 (70.4)	19.8 (67.6)
	1:13 p.m.	49.4 (120.9)	46.0 (114.7)	42.0 (107.6)	46.7 (116.0)	48.1 (118.7)
Temperature, °C (°F) on Oct. 1	7:05 a.m.	11.6 (52.8)	12.0 (53.5)	14.0 (57.2)	12.7 (54.8)	11.6 (53.0)
	1:55 p.m.	38.1 (100.5)	32.8 (91.1)	30.1 (86.2)	32.4 (90.3)	33.4 (92.1)
Temperature, °C (°F) on Nov. 15	7:40 a.m.	8.9 (48.0)	9.6 (49.2)	11.6 (52.9)	10.3 (50.5)	9.0 (48.3)
	1:45 p.m.	31.0 (87.7)	24.3 (75.7)	20.9 (69.7)	23.8 (74.8)	25.4 (77.7)

Figure 2.28: The transverse temperature distributions across the top flange on June 1, October 1, and November 15, 2009 in Atlanta, Georgia.

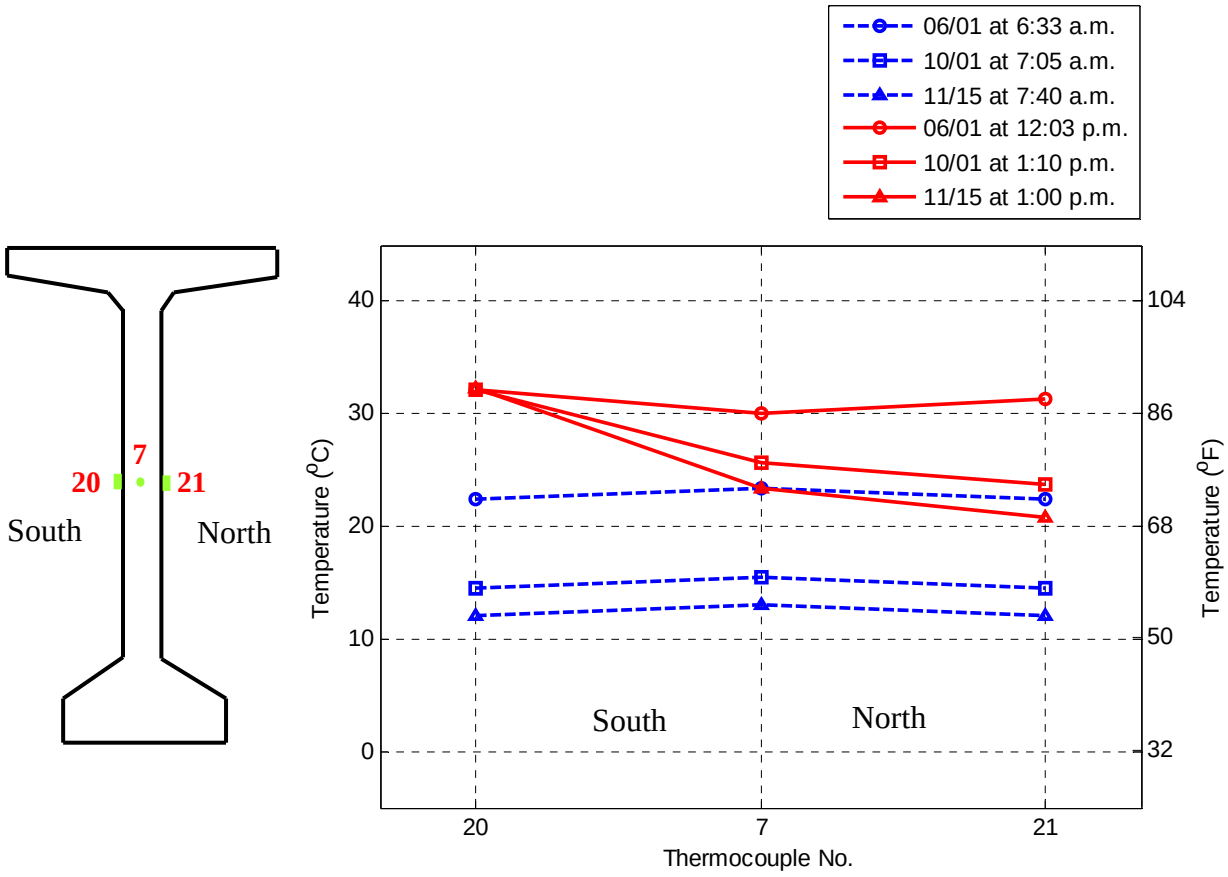

Thermocouple No.		20	7	21
Temperature, °C (°F) on June 1	6:33 a.m.	22.5 (72.5)	23.3 (74.0)	22.4 (72.3)
	12:03 p.m.	32.1 (89.8)	30.1 (86.1)	31.4 (88.4)
Temperature, °C (°F) on Oct. 1	7:05 a.m.	14.5 (58.1)	15.4 (59.7)	14.5 (58.1)
	1:10 p.m.	32.1 (89.8)	25.7 (78.3)	23.7 (74.6)
Temperature, °C (°F) on Nov. 15	7:40 a.m.	12.0 (53.7)	13.1 (55.5)	12.0 (53.6)
	1:00 p.m.	32.3 (90.2)	23.4 (74.0)	20.9 (69.5)

Figure 2.29: The transverse temperature distributions across the middle of the web on June 1, October 1, and November 15, 2009 in Atlanta, Georgia.

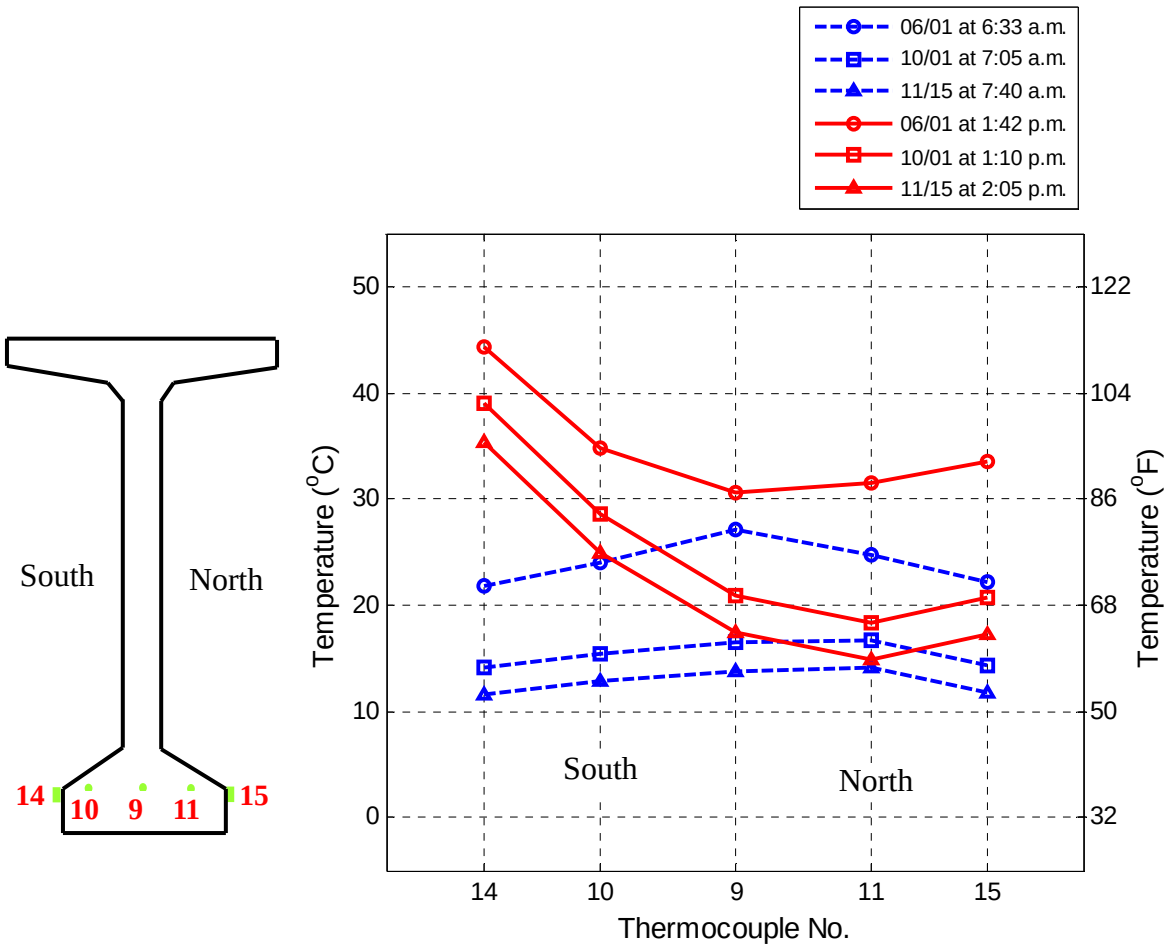

Thermocouple No.		14	10	9	11	15
Temperature, °C (°F) on June 1	6:33 a.m.	21.9 (71.3)	24.0 (75.2)	27.1 (80.7)	24.7 (76.5)	22.1 (71.8)
	1:42 p.m.	44.3 (111.8)	34.7 (94.5)	30.6 (87.0)	31.4 (88.6)	33.5 (92.3)
Temperature, °C (°F) on Oct. 1	7:05 a.m.	14.1 (57.4)	15.4 [a] (59.8)	16.4 [a] (61.5)	16.7 (62.1)	14.4 (57.9)
	1:10 p.m.	39.0 (102.2)	28.5 [a] (83.3)	20.9 [a] (69.5)	18.4 (65.0)	20.6 (69.2)
Temperature, °C (°F) on Nov. 15	7:40 a.m.	11.5 (52.7)	12.9 [a] (55.2)	13.8 [a] (56.9)	14.2 (57.5)	11.8 (53.2)
	2.05 p.m.	35.3 (95.6)	24.9 [a] (76.8)	17.4 [a] (63.3)	14.9 (58.8)	17.3 (63.2)

[a] The temperatures at the thermocouple location 9 and 10 on October 1 and November 15, 2009 were extrapolated using the second-order model (See Appendix A).

Figure 2.30: The transverse temperature distributions across the bottom flange on June 1, October 1, and November 15, 2009 in Atlanta, Georgia.

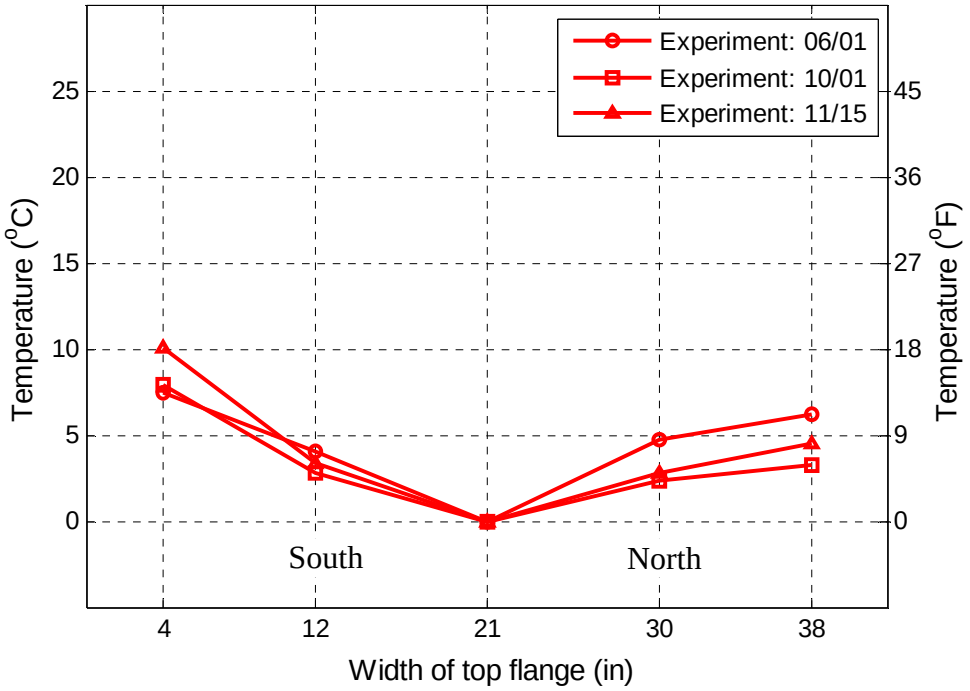

Figure 2.31: The transverse temperature gradients across the top flange on June 1, October 1, and November 15, 2009 in Atlanta, Georgia.

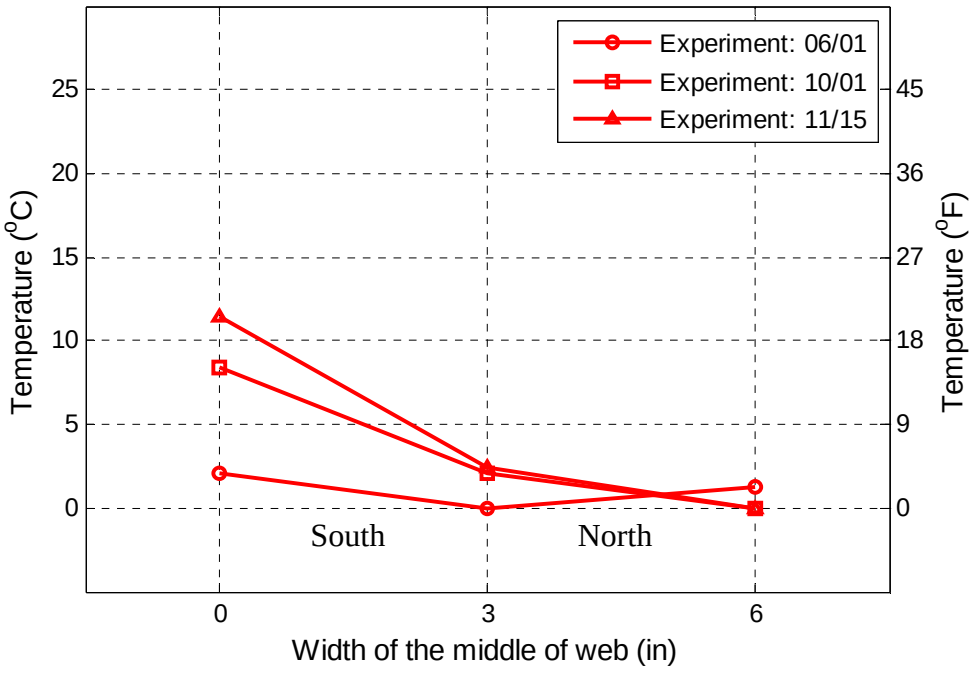

Figure 2.32: The transverse temperature gradients across the middle of the web on June 1, October 1, and November 15, 2009 in Atlanta, Georgia.

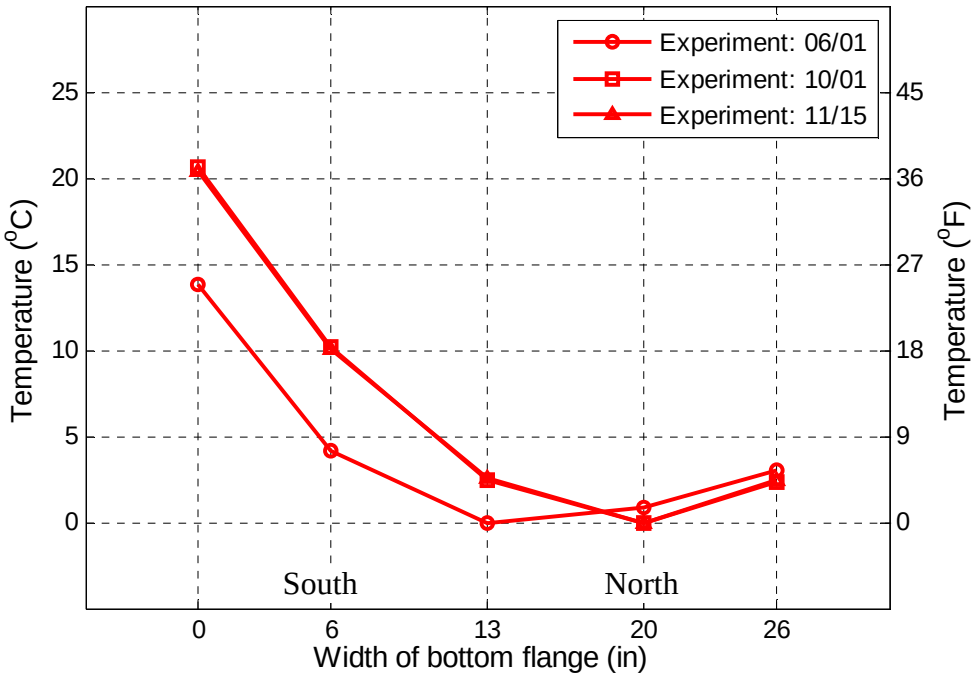

Figure 2.33: The transverse temperature gradients across the bottom flange on June 1, October 1, and November 15, 2009 in Atlanta, Georgia.

CHAPTER 3

FINITE ELEMENT HEAT TRANSFER MODEL

3.1 Introduction

To predict nonlinear temperature distributions in the prestressed concrete bridge girder, a two-dimensional (2D) finite element heat transfer analysis is performed using measured environmental conditions: solar radiation, ambient air temperature, and wind speed. The solar radiation measured on horizontal and vertical planes is applied to the top and vertical surfaces of the girder as a heat source. For inclined surfaces, irradiation is estimated according to the position of the sun, the location of the bridge, the geometry of the girder, and the measured solar radiation on the horizontal surface. The ambient air temperature and wind speed are used to account for heat convection boundary conditions in the heat transfer analysis. The girder temperatures obtained from the heat transfer analysis are then compared with those measured in the experimental study.

3.2 Calculation of Solar Energy on the Inclined Surfaces

Since solar radiation was measured only on a horizontal and vertical surface, the solar radiation incident on other inclined surfaces of the girder was calculated based on the location and geometry of the girder, the position of the sun, and the solar radiation measured on the horizontal surface (Liu and Jordan, 1963):

$$I_T = I_b\left(\frac{\cos\theta}{\cos\theta_z}\right) + I_d\left(\frac{1+\cos\beta}{2}\right) + \rho(I_b + I_d)\left(\frac{1-\cos\beta}{2}\right) \tag{3.1}$$

in which I_T = the total solar radiation on an inclined surface,

I_b = the direct solar radiation, or beam radiation, on a horizontal surface,

I_d = the diffused solar radiation on a horizontal surface,

θ = the incident angle between the beam radiation and the surface normal,

θ_Z = the zenith angle between the line overhead and the line to the sun,

β = the surface angle relative to the horizontal plane, and

ρ = the reflectance value of the ground, 0.2, suggested by Duffie and Beckman (1980), Jansen (1985), and Kouremenos et al. (1987) for surfaces without snow.

The detailed calculation of the solar position, including the solar incident and zenith angles, and the geometrical relationship between the sun and the bridge girder are described in Appendix B.

In Equation (3.1), the calculation of total solar radiation on the inclined surface also requires the separation of the measured total horizontal solar radiation, *I*, into its beam and diffuse components. This study used the following equation presented by Erbs et al. (1982) to compute the fraction of diffuse radiation on a horizontal surface, I_d / I, correlated with the clearness index, k_T.

$$\frac{I_d}{I} = \begin{cases} 1.0 - 0.09k_T & \text{for } k_T < 0.22 \\ 0.9511 - 0.1604k_T + 4.388k_T^2 \\ \qquad -16.638k_T^3 + 12.336k_T^4 & \text{for } 0.22 \le k_T \le 0.80 \\ 0.165 & \text{for } k_T > 0.80 \end{cases} \tag{3.2}$$

The clearness index, k_T, can be predicted using the ratio of the total solar radiation, *I*, to the extraterrestrial solar radiation, I_s, as defined by Liu and Jordan (1960):

$$k_T = \frac{I}{I_s} \tag{3.3}$$

in which $I_s = I_{sc}\left[1+0.033\cos(360n/365)\right]\cos\theta$. The solar constant, I_{sc}, is 1367 W/m^2.

Furthermore, this study accounted for the influence of the shadow on the web of the girder from the overhang of the top flange in the calculation of solar radiation. The shadow distance on the web, *d*, defined by shading plane 1 in Figure 3.1, is given by (Kreith et al., 1978 & Kuehn et al., 1998):

$$d = w_{top}\frac{\tan\alpha_z}{\cos(\gamma_s-\gamma)} \tag{3.4}$$

in which w_{top} = the length of the top flange overhang,

α_s = the solar altitude angle, and

γ_s = the solar azimuth angle.

Since the shadow length may also extend to the inclined bottom flange of the girder, represented as shading plane 2 in Figure 3.1, the equation shown below was developed to calculate the shadow length on the bottom flange:

$$d_T = \frac{(d-h_{web})/w_{bot}}{\cos\beta_T} \tag{3.5}$$

in which h_{web} = the height of the web,

w_{bot} = the width of the bottom flange from the web, and

β_T = the inclined angle of the bottom flange relative to the horizontal plane.

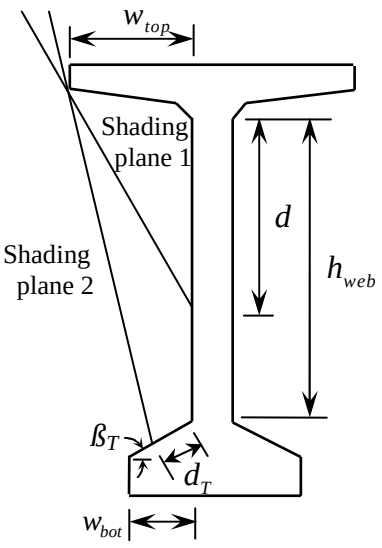

Figure 3.1: The shading of the web and the bottom flange.

For the validation of the solar radiation obtained from the Equation (3.1), Figure 3.2 shows the predicted and measured solar radiation intensity on the vertical surface for two days, June 1 and November 15, 2009. This calculation also includes the influence of the sun position above the east-west direction in the summer. In other words, when the sun is located above the east in the early morning and the west in the late afternoon in the summer, the vertical surface of the girder does not receive direct radiation from the sun. According to Figure 3.2, the differences between the predicted and measured solar radiation exhibit somewhat large values in the early morning and late afternoon. The prediction of the solar radiation was based on the measured solar radiation on the horizontal surface. Thus, these errors, which occurred in the low intensity of solar radiation, might be attributed to temporary clouds which affected the horizontal irradiation in the early morning and late afternoon as shown in Figure 3.2. Compared with the measurements between 10 a.m. and 3 p.m., these errors were less than 38.0 W/m^2 on June 1 and 45.8 W/m^2 on November 15. As the sky was temporarily cloudy and variable even under selectively clear sky conditions, defined as a total cloud cover of less than 10%, the solar radiation predicted at every five minutes from the horizontal irradiation agrees well with the measurements.

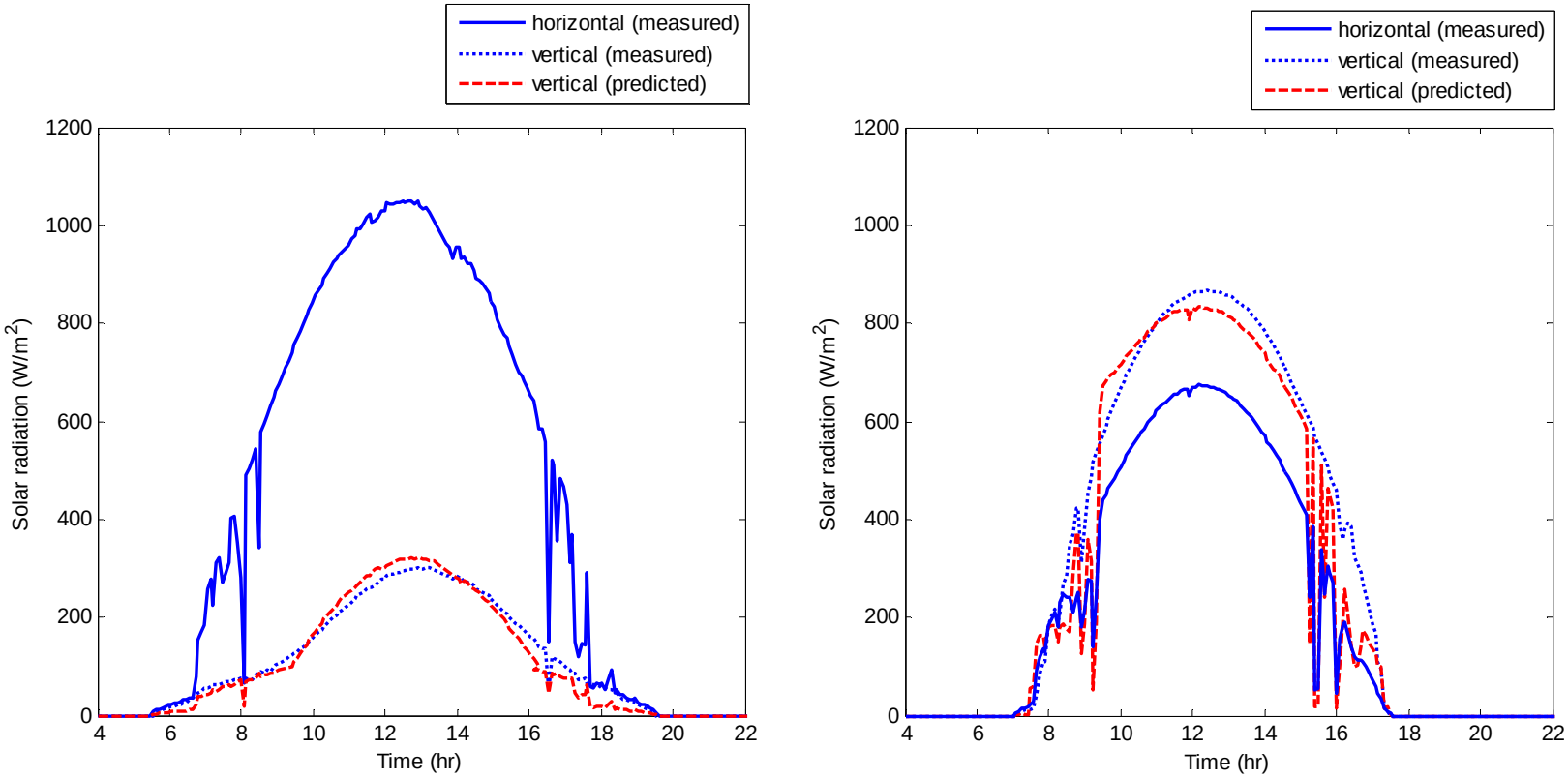

(a) June 1, 2009

(b) November 15, 2009

Figure 3.2: Measured and predicted solar intensity on the vertical surface of the BT-63 girder.

3.3 Transient Heat Transfer Analysis

With an assumption of a constant temperature variation in the longitudinal direction of the girder, the BT-63 section was modeled using a 2D element, DC2D4, in ABAQUS (2008). A total of 584 elements and 699 nodes were used for the cross-section as shown in Figure 3.3. With the finite element model determined, a 2D heat transfer analysis was performed which consisted of four heat transfer phenomena: heat conduction in the concrete, heat convection between the surroundings and the concrete surface, heat irradiation from the sun, and heat radiation to the surroundings. Reflected radiation between the surfaces of the girder was ignored. These heat transfer mechanisms, based on measured environmental boundary conditions, are discussed below in more detail. The initial reference temperature was assumed to be constant over the cross-section based on an average of all the measured temperatures at the start time of the analysis, 12 a.m. For June 1 and November 15, the constant initial temperature was found to be 29.7°C (85.5°F) and 19.3°C (66.7°F), respectively. The standard deviation of the temperatures was 2.01°C (3.62°F) on June 1 and 2.64°C (4.76°F) on November 15 over the cross-section.

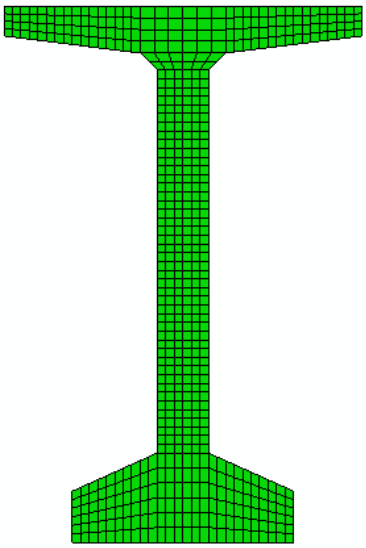

Figure 3.3: Finite element mesh for the heat transfer analysis of the BT-63 section.

3.3.1 Heat Conduction

The heat transfer by conduction, defined as heat transfer between portions of the materials inside the concrete, can be expressed using 2D Fourier equation as a function of time, *t*:

$$k\left(\frac{\partial^2 T}{\partial x^2}+\frac{\partial^2 T}{\partial y^2}\right)=\rho c\frac{\partial T}{\partial t} \tag{3.6}$$

in which T = the temperature of a concrete bridge girder,

k = the thermal conductivity of concrete,

ρ = the density of concrete, and

c = the specific heat capacity of concrete.

The thermal conductivity and the specific heat of concrete were taken as 1.5 W/m·K and 1,000 J/kg·K, respectively, whose values were effectively applied to the thermal analysis of concrete bridge sections under environmental conditions (Branco & Mendes, 1993). Furthermore, since the thermal properties of concrete depend on the current state of concrete such as its composition, density, and moisture content, Chapter 7 discusses the values of the thermal properties of concrete given in several references and evaluate the influence of the thermal properties on temperature distributions in prestressed concrete bridge girders.

3.3.2 Heat Convection

The rate of heat transfer by convection, q_c, is associated with the movement of air particles and temperature differences between ambient air temperature and surface temperature. The heat convection, q_c, was evaluated using Newton's convection law (Williamson, 1967):

$$q_c = h_c(T_s - T_a) \tag{3.7}$$

in which h_c = the convection heat transfer coefficient,

T_s = the concrete surface temperature, and

T_a = the ambient air temperature.

The air temperature, T_a , involved in the analysis was measured from the experiments, and the concrete surface temperature, T_s , was obtained from the predicted temperatures at the previous time step. The convection heat transfer coefficient h_c in W/m$^2\cdot$°K, which mainly depends on the wind speed, was calculated using the following equation (Saetta et al., 1995 & ASHRAE, 2005):

$$h_c = \begin{cases} 5.6 + 4.0v & \text{for } v \le 5 \text{ m/sec} \\ 7.2v^{0.78} & \text{for } v > 5 \text{ m/sec} \end{cases} \tag{3.8}$$

in which v is the wind speed expressed in m/sec and measured by an anemometer in the experiment.

3.3.3 Heat Irradiation and Radiation

The concrete girder mainly gains heat during the day by short-wave radiation and loses the gained heat during the night by long-wave radiation. The heat gains due to the short-wave solar radiation, can be expressed as (Therkeld, 1970)

$$q_s = \alpha I \tag{3.9}$$

in which α = the solar absorptivity, and

I = the total solar radiation reaching the surface of the girder.

The gained heat is emitted from the heated surface to the surrounding atmosphere by long-wave radiation. The amount of the long-wave radiation, as a function of the absolute temperature of the concrete surface and air temperatures, follows the Stefan-Boltzman law (Chapman, 1960).

$$q_r = C_s \varepsilon (T_s^{*4} - T_a^{*4}) \tag{3.10}$$

in which C_s = the Stefan-Boltzman radiation constant (5.669×10^{-8} $W/m^2 \cdot K^4$),

ε = the surface emissivity of concrete,

T_s^* = the absolute temperature of concrete surface, and

T_a^* = the absolute temperature of ambient air.

In the calculation of heat gain and loss, the solar absorptivity of concrete depends on the color, aggregate type, concrete age, and state of weathering (Levinson & Akbari, 2002), and the surface emissivity depends on the material temperature, material color, oxidation level, and amount of polishing (Incropera & Dewitt, 2002). The value of solar absorptivity and surface emissivity used in the study was selected to be 0.50 and 0.85, respectively, based on a previous study on the temperature prediction of concrete pavement (Jeong & Zollinger, 2006). Since heat gain is a main source to yield temperature distributions in the girder, this study also assesses the influence of the solar absorptivity of concrete on the girder temperature distributions in Chapter 7.

3.4 Analytical Results

In the experimental study during the months of April 2009 to March 2010, the largest vertical and transverse temperature distributions were measured on June 1 and November 15, 2009, respectively. Therefore, the finite element heat transfer analysis utilized the environmental conditions measured on the both days to determine the

temperature distributions of the girder. For the validation of the finite element analysis, the predicted temperature variations were compared with the measurements.

3.4.1 Vertical and Transverse Temperature Variations

Girder temperatures obtained from the heat transfer analysis are compared with the measurements along the vertical and lateral directions of the BT-63 section. The measurements showed that the highest temperature in the vertical temperature distribution was on the top surface and the lowest temperature in the bottom flange. Thus, the predicted temperature variations are compared with the measurements at the locations of thermocouples 28, 7, and 13 along the depth of the girder. Figures 3.4 and 3.5 show the variations in the predicted and measured temperatures at the thermocouple locations on June 1 and November 15, 2009, respectively. The predicted vertical temperature variations are in good agreement with the measurements. Figures 3.4 and 3.5 also indicate that with changes from the summer to the winter, vertical temperature magnitudes and differences decrease; conversely, the web temperature (thermocouple 7) increases due to its exposure to high solar radiation incident on the vertical surface in the winter.

In addition to vertical temperature variations, Figures 3.6 and 3.7 show the predicted and measured transverse temperature variations in the top flange, the web, and the bottom flange on June 1 and November 15, 2009, respectively. The highest temperature in the top flange was measured on the south end of the top flange (thermocouple 2) while the lowest temperature was measured in the middle of the top flange (thermocouple 5). In the web, the south-facing surface (thermocouple 20) exhibited the highest value, and the north-facing surface (thermocouple 21) showed the lowest value. Similarly, for the bottom flange, the highest temperature was measured on the south vertical face (thermocouple 14) and the lowest temperature inside the north of the bottom flange (thermocouple 11). Thus, this study compared the predicted and

measured temperatures at the locations of thermocouples 2 and 5 for the top flange, 20 and 21 for the web, and 14 and 11 for the bottom flange, as shown in Figures 3.6 and 3.7. The predicted temperatures are in good agreement with the measurements. In particular, compared with temperature variations on June 1, those on November 15 present larger transverse temperature differences due to high solar radiation on the vertical surface.

Furthermore, this study evaluated absolute average errors between the predicted and measured temperatures at all the sensors. The average absolute error, AAE, is calculated using the following equation (Carino & Tank, 1992):

$$\text{AAE} = \frac{\sum(|\bar{y}-y|)}{n} \tag{3.11}$$

in which $\bar{y}$ = the predicted temperature,

y = the measured temperature, and

n = the total number of the measured or predicted points.

Table 3.1 shows the calculated average absolute errors, which range from 0.3°C (0.6°F) to 2.6°C (4.6°F) on June 1 and from 0.6°C (1.2°F) to 2.0°C (3.6°F) on November 15. The maximum absolute error, MAE, between the predicted and measured temperatures at each sensor location is also shown in Table 3.1. The largest MAE is 4.3°C (7.7°F) in the middle of the top flange (thermocouple 5) on June 1 and 5.4°C (9.7°F) on the south-facing vertical surface of the web (thermocouple 18) on November 15. Therefore, the magnitudes and the variations of the predicted temperatures match well with the measured values.

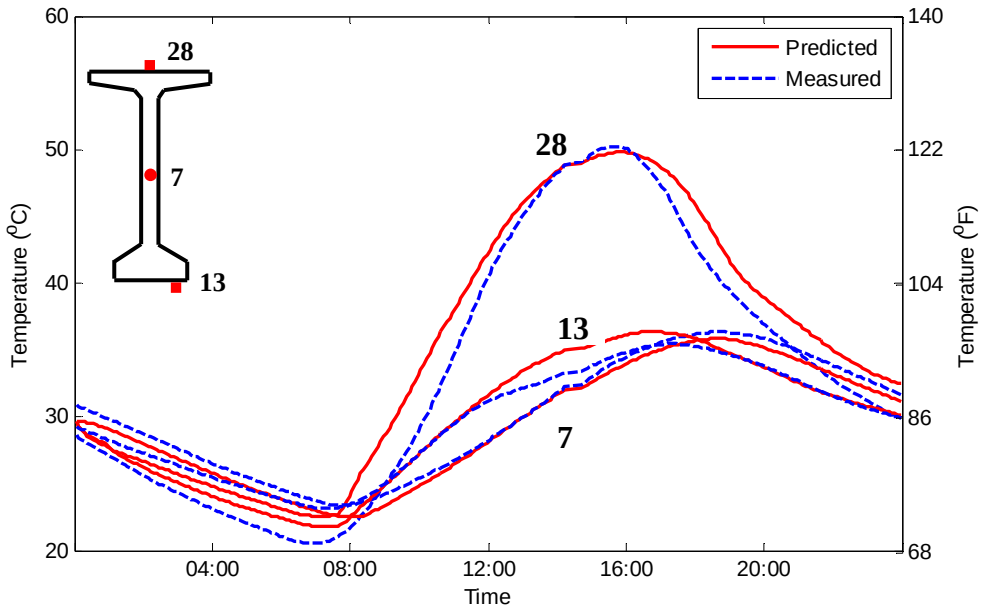

Figure 3.4: Predicted and measured temperature variations at the thermocouple locations along the depth of the BT-63 section on June 1, 2009.

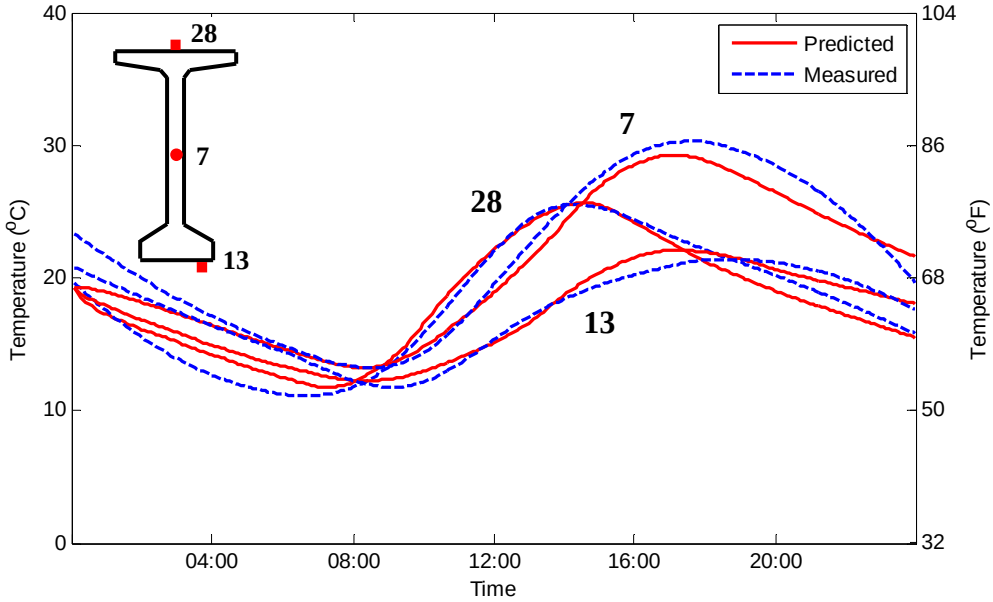

Figure 3.5: Predicted and measured temperature variations at the thermocouple locations along the depth of the BT-63 section on November 15, 2009.

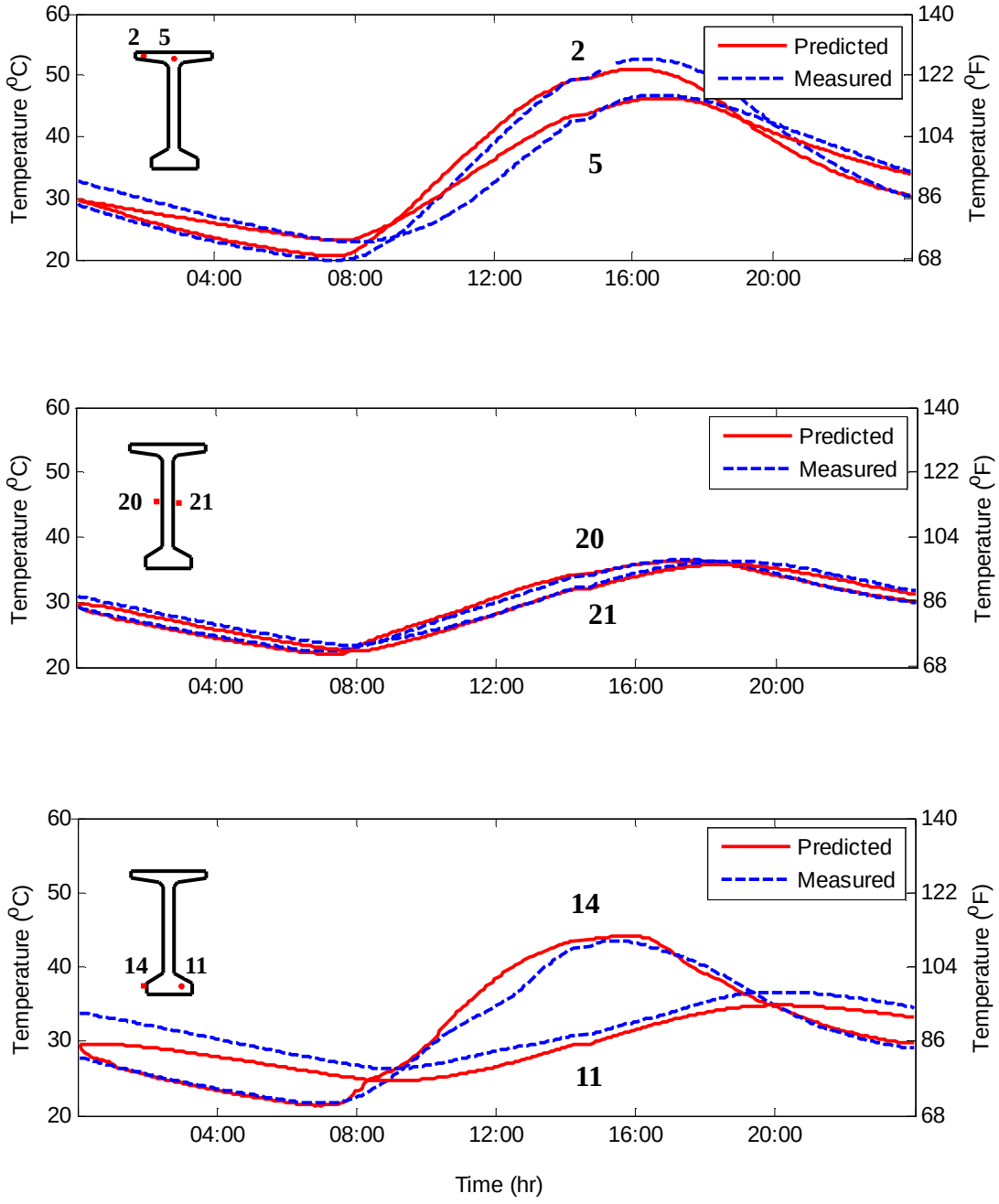

Figure 3.6: Predicted and measured temperature variations at the thermocouple locations across the top flange, the web, and the bottom flange on June 1, 2009.

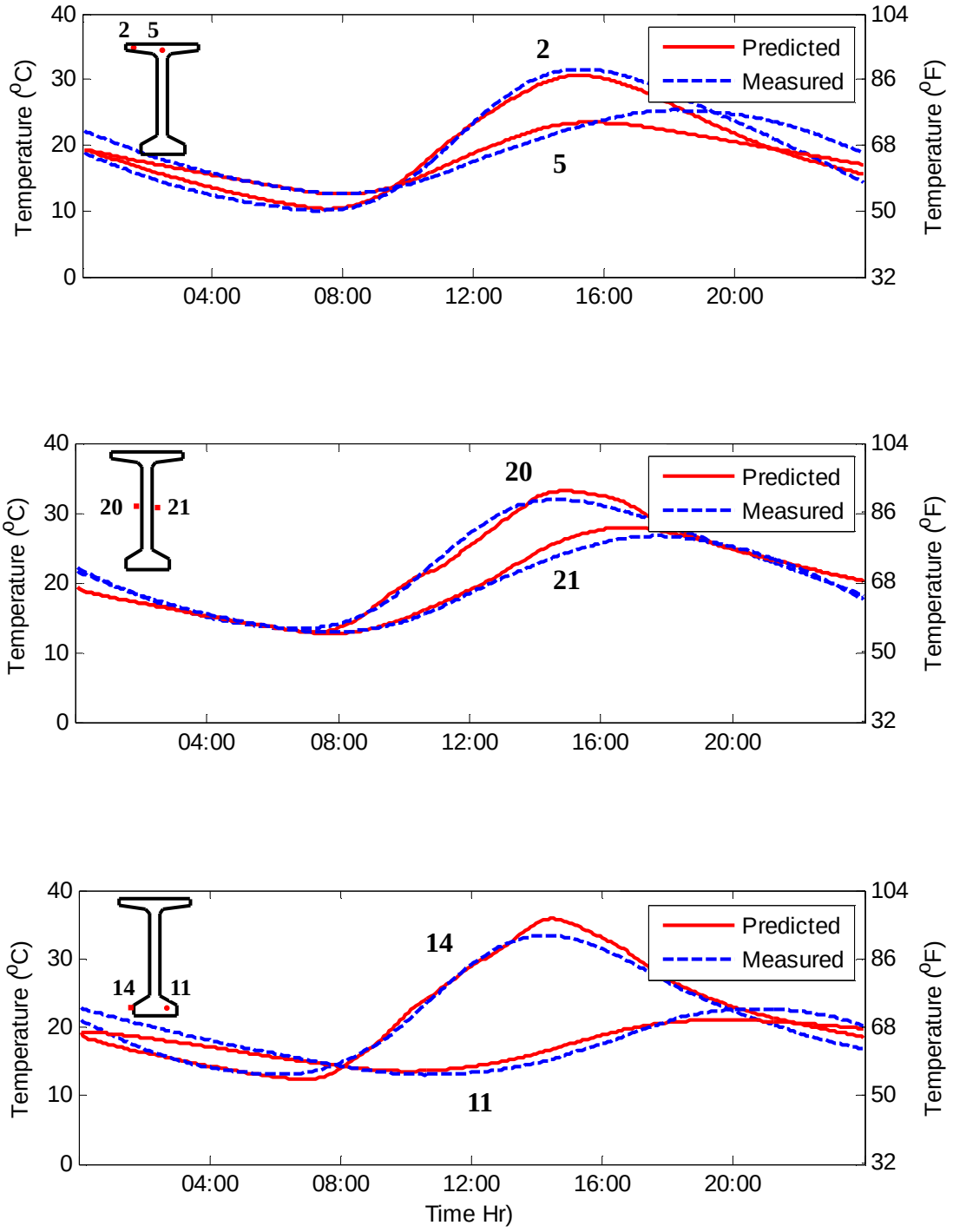

Figure 3.7: Predicted and measured temperature variations at the thermocouple locations across the top flange, the web, and the bottom flange on November 15, 2009.

Table 3.1: Average absolute errors between the predicted and measured temperatures at each sensor location on June 1 and November 15, 2009.

Location	Sensor No.	June 1		November 15	
		AAE, °C (°F)	MAE, °C (°F)	AAE, °C (°F)	MAE, °C (°F)
Top flange	1	1.0 (1.7)	2.2 (3.9)	0.6 (1.2)	1.4 (2.5)
	2	1.4 (2.6)	3.3 (5.9)	1.0 (1.7)	2.0 (3.6)
	3	0.8 (1.4)	2.0 (3.6)	0.8 (1.5)	2.6 (4.7)
	4	1.5 (2.7)	4.0 (7.1)	1.1 (1.9)	2.4 (4.4)
	5	1.5 (2.7)	4.3 (7.7)	1.5 (2.8)	4.2 (7.6)
	24	0.9 (1.7)	2.8 (5.0)	0.7 (1.3)	2.3 (4.1)
	25	0.7 (1.2)	1.8 (3.2)	0.8 (1.5)	2.1 (3.8)
	26	2.6 (4.6)	4.0 (7.1)	1.8 (3.2)	3.3 (6.0)
	27	2.3 (4.1)	4.1 (7.3)	1.3 (2.4)	2.8 (5.0)
	28	1.9 (3.4)	4.2 (7.6)	0.7 (1.3)	1.6 (2.9)
Web	6	1.2 (2.1)	3.3 (6.0)	1.3 (2.3)	3.8 (6.8)
	7	0.6 (1.0)	1.2 (2.2)	1.0 (1.8)	4.0 (7.2)
	8	0.3 (0.6)	0.9 (1.7)	0.8 (1.5)	3.8 (6.8)
	18	0.5 (0.8)	1.6 (2.8)	2.0 (3.6)	5.4 (9.7)
	19	0.7 (1.2)	2.6 (4.6)	0.8 (1.5)	2.6 (4.8)
	20	0.3 (0.6)	0.9 (1.5)	0.8 (1.4)	2.9 (5.3)
	21	0.5 (0.8)	1.5 (2.7)	0.8 (1.4)	2.5 (4.9)
	22	1.3 (2.3)	2.9 (5.2)	1.4 (2.6)	3.5 (6.3)
	23	1.4 (2.5)	3.3 (6.0)	1.6 (3.0)	3.7 (6.7)
Bottom flange	9 [a]	1.9 (3.4)	4.2 (7.5)	-	-
	10 [a]	0.6 (1.0)	1.8 (3.2)	-	-
	11	0.7 (1.2)	1.6 (3.0)	1.1 (1.9)	3.5 (6.2)
	12	1.1 (2.0)	2.9 (5.2)	1.4 (2.4)	3.0 (5.5)
	13	0.7 (1.3)	1.7 (3.0)	0.8 (1.5)	1.8 (3.3)
	14	0.8 (1.5)	3.9 (6.9)	0.9 (1.6)	2.5 (4.4)
	15	0.8 (1.4)	2.2 (4.0)	1.3 (2.4)	4.0 (7.2)
	16	2.7 (4.9)	3.4 (6.1)	0.7 (1.2)	3.1 (5.5)
	17	0.7 (1.2)	2.4 (4.4)	0.9 (1.6)	2.7 (4.9)

[a] The temperatures at thermocouples 9 and 10 were not measured on November 15.

3.4.2 Vertical and Transverse Temperature Differences

This section evaluates maximum vertical and transverse temperature differences predicted by the heat transfer analysis and obtained from the experiments. The vertical temperature difference was studied along the depth of the BT-63 section (thermocouples 28, 5, 6, 7, 8, 9, 12, and 13), and the transverse temperature differences were studied across the top flange (thermocouples 2, 4, 5, 3, and 1), the web (thermocouples 20, 7, and 21), and the bottom flange (thermocouples 14, 10, 9, 11, and 15). The predicted and measured values for the differences and occurrence times are summarized in Tables 3.2 and 3.3 for June 1 and November 15, 2009, respectively.

The maximum vertical temperature differences predicted from the heat transfer analysis were 19.6°C (35.3°F) and 10.1°C (18.2°F), and those obtained from the measurements were 20.4°C (36.7°F) and 10.9°C (19.5°F) on June 1 and November 15, 2009, respectively. Thus, the differences between the predicted and measured values are only 0.8°C (1.4°F) on June 1 and 0.4°C (0.7°F) on November 15, 2009. The predicted occurrence times, 1:42 p.m. on June 1 and 1:35 p.m. on November 15, were also in good agreement with the measured times, 1:42 p.m. and 1:05 p.m., respectively.

Tables 3.2 and 3.3 also show the maximum transverse temperature differences across the top flange, the web, and the bottom flange. The predicted values differed from the measurements by less than 1.6°C (2.8°F) on June 1 and 1.3°C (2.2°F) on November 15, 2009. The occurrence times were also predicted within the difference of 34 minutes on June 1 and 45 minutes on November 15, 2009. For concrete with a low value of thermal conductivity, the time lags less than 45 minutes could be negligible. As a result, the magnitudes and the times of the maximum vertical and transverse temperature differences predicted by the heat transfer analysis agree well with those obtained from the experiments.

Table 3.2: Comparison between the predicted and measured maximum vertical and transverse temperature differences on June 1, 2009.

Temperature difference		Prediction		Measurement		Difference °C (°F)	Lag time (min.)
		Magnitude, °C (°F)	Time	Magnitude, °C (°F)	Time		
Vertical		19.6 (35.3)	13:42	20.4 (36.7)	13:42	0.8 (1.4)	0
Transverse	Top flange	5.8 (10.5)	13:42	7.4 (13.3)	13:13	1.6 (2.8)	29
	Middle of web	2.7 (4.9)	12:03	2.1 (3.7)	12:03	0.6 (1.2)	0
	Bottom flange	14.6 (26.2)	13:08	13.8 (24.8)	13:42	0.8 (1.4)	34

Table 3.3: Comparison between the predicted and measured maximum vertical and transverse temperature differences on November 15, 2009.

Temperature difference		Prediction		Measurement		Difference °C (°F)	Lag time (min.)
		Magnitude, °C (°F)	Time	Magnitude, °C (°F)	Time		
Vertical		10.1 (18.2)	13:35	10.9 (19.5)	13:05	0.8 (1.3)	30
Transverse	Top flange	9.6 (17.3)	13:50	10.0 (18.0)	13:45	0.4 (0.7)	5
	Middle of web	10.2 (18.4)	13:45	11.5 (20.6)	13:00	1.3 (2.2)	45
	Bottom flange	20.8 (37.4)	14:20	20.5 (36.8)	14:05	0.3 (0.6)	15

3.4.3 Vertical and Transverse Temperature Distributions

Based on the maximum vertical and transverse temperature differences, the vertical and transverse temperature distributions were evaluated at the thermocouple locations. The contour plots of the temperatures obtained from the heat transfer analysis for June 1 and November 15, 2009 are presented in Figures 3.8 and 3.9, respectively. The temperature contours shown in Figure 3.8(a) and Figure 3.9(a) were selected from the minimum average temperature over the cross-section during the day. The minimum

temperatures were nearly constant at around 22°C (72°F) on June 1 and 12°C (54°F) on November 15, 2009 over the cross-section, even though a little lower in the top flange and a little higher inside the bottom flange. Figure 3.8(b) and Figure 3.9(b) show the temperature contours at 1:42 p.m. on June 1 and at 1:35 p.m. on November 15, 2009, on which the maximum vertical and transverse temperature differences were observed, respectively.

In addition, Figure 3.10 compares the predicted and measured maximum vertical temperature distributions at the thermocouple locations along the depth of the BT-63 section for June 1 and November 15, 2009. Compared with the measured temperatures, the predicted values differed only by a maximum of 3.5°C (6.4°F) on June 1 and 1.4°C (2.4°F) on November 15 on the northern bottom surface of the bottom flange (thermocouple 12). The difference at the location of thermocouple 12 might be the result of solar radiation reflection or heat radiating from the ground. The shapes of the predicted maximum vertical temperature distributions on June 1 and November 15 are also in very good agreement with those of the measurement.

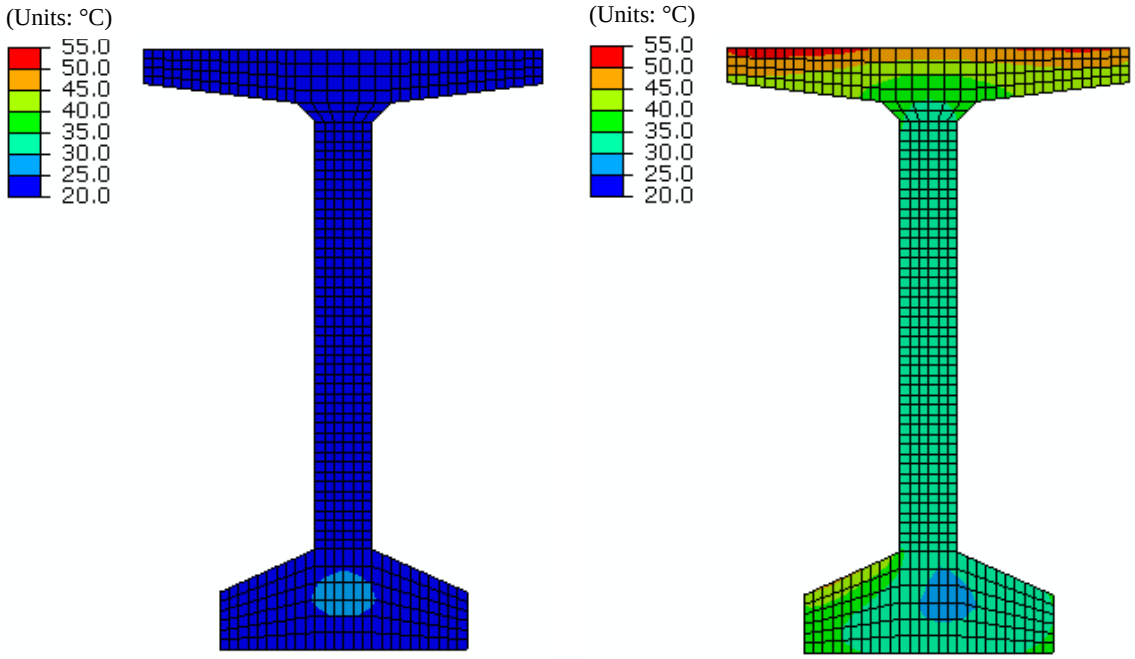

(a) 6:28 a.m. (b) 1:42 p.m.

Figure 3.8: The temperature contour plots of the BT-63 section on June 1, 2009.

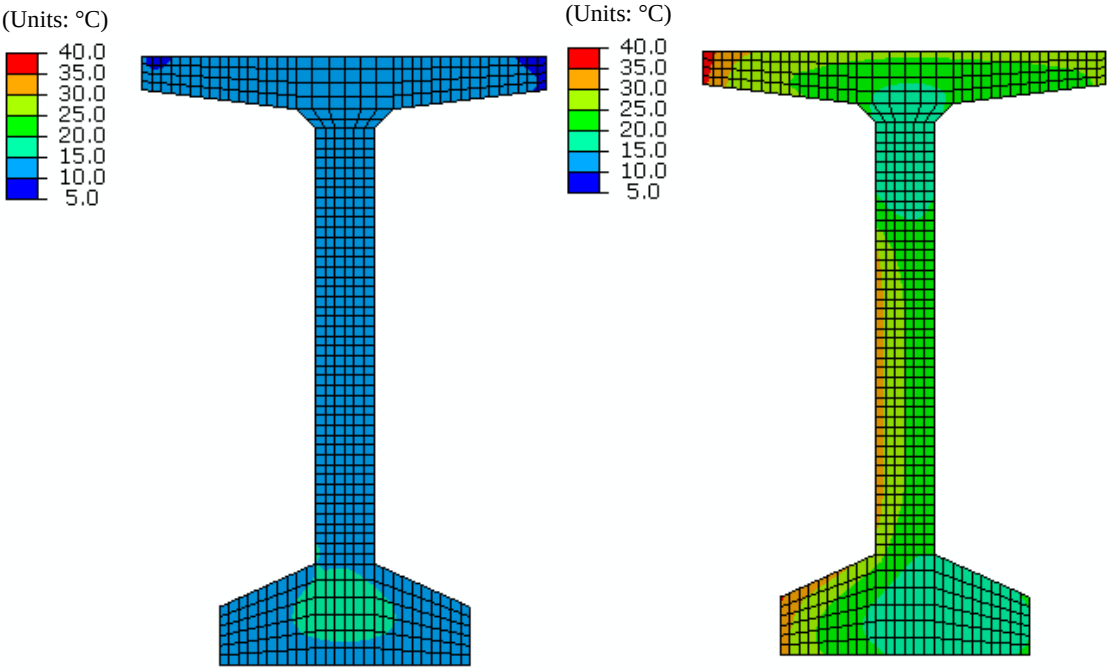

(a) 7:35 a.m. (b) 1:35 p.m.

Figure 3.9: The temperature contour plots of the BT-63 section on November 15, 2009.

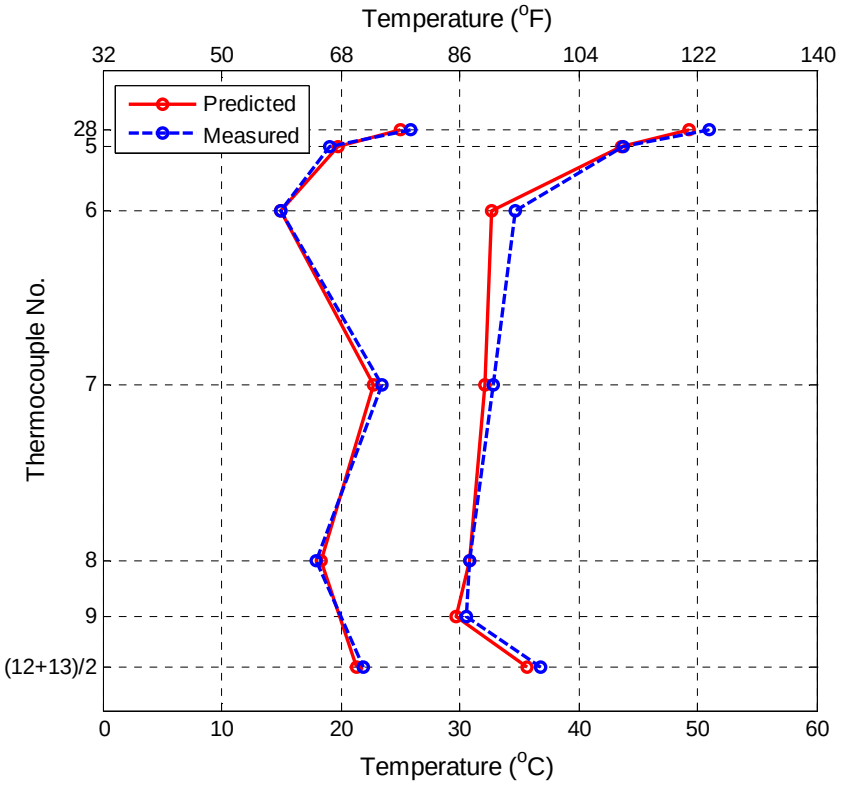

Thermocouple No.	June 1			November 15		
	Predicted °C (°F)	Measured °C (°F)	Difference °C (°F)	Predicted °C (°F)	Measured °C (°F)	Difference °C (°F)
28	49.3 (120.8)	50.9 (123.7)	1.6 (2.9)	25.1 (77.1)	25.9 (78.6)	0.8 (1.5)
5	43.7 (110.6)	43.8 (110.8)	0.1(0.2)	19.8 (67.6)	19.0 (66.2)	0.8 (1.4)
6	32.7 (90.9)	34.8 (94.6)	2.1 (3.7)	15.0 (58.9)	15.0 (59.0)	0.0 (0.1)
7	32.1 (89.9)	32.8 (91.1)	0.7 (1.2)	22.8 (73.0)	23.4 (74.2)	0..6 (1.2)
8	30.8 (87.4)	30.8 (87.5)	0.0 (0.1)	18.4 (65.1)	17.9 (64.3)	0.5 (0.8)
9 [a]	29.7 (85.4)	30.6 (87.0)	0.9 (1.6)	-	-	-
12	36.2 (97.1)	39.7 (103.5)	3.5 (6.4)	24.8 (76.7)	26.2 (79.1)	1.4 (2.4)
13	35.1 (95.1)	33.8 (92.8)	1.3 (2.3)	17.8 (64.0)	17.8 (64.0)	0.0 (0.0)

[a] The temperatures, missed at the thermocouple 9 due to a poor connection to data-logging system on November 15, were not available for the comparison.

Figure 3.10: Predicted and measured maximum vertical temperature distributions at sensor locations along the depth of the BT-63 section on June 1 and November 15, 2009.

In addition to vertical temperature distributions, Figures 3.11 to 3.13 show the predicted and measured transverse temperature distributions across the top flange, the middle of the web, and the bottom flange at the sensor locations, respectively. Across the top flange, a maximum difference of 1.7°C (3.0°F) on June 1 and 2.3°C (4.1°F) on November 15 occurred at the middle (thermocouple 5) and the south end (thermocouple 2) of the top flange, respectively. The middle of the web showed a maximum difference of 0.8°C (1.5°F) on June 1 and 0.7°C (1.4°F) on November 15 on the north vertical surface of the web flange (thermocouple 21). For the transverse temperature distribution of the bottom flange, a maximum temperature difference of 1.8°C (3.3°F) occurred on the north-facing vertical surface of the bottom flange (thermocouple 15) on June 1 and November 15, 2009. Thus, all the temperatures predicted from the heat transfer analysis match well with those measured across the top flange, the web, and the bottom flange. The shapes of the transverse temperature distributions predicted from the heat transfer analysis were also close to those obtained from the experimental study.

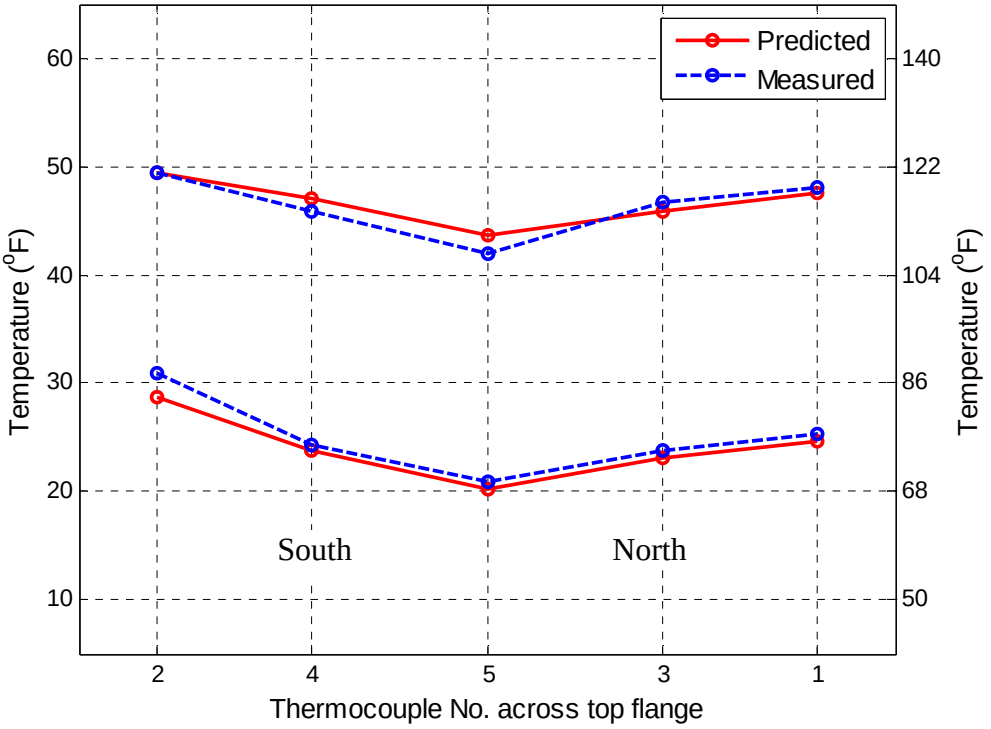

Thermocouple No.	June 1			November 15		
	Predicted °C (°F)	Measured °C (°F)	Difference °C (°F)	Predicted °C (°F)	Measured °C (°F)	Difference °C (°F)
2	49.5 (121.1)	49.4 (120.9)	0.1 (0.2)	28.7 (83.6)	31.0 (87.7)	2.3 (4.1)
4	47.0 (116.6)	46.0 (114.7)	1.0 (1.9)	23.8 (74.9)	24.3 (75.7)	0.5 (0.8)
5	43.7 (110.6)	42.0 (107.6)	1.7 (3.0)	20.1 (68.3)	20.9 (69.7)	0.8 (1.4)
3	45.8 (114.5)	46.7 (116.0)	0.9 (1.5)	23.1 (73.6)	23.8 (74.8)	0.7 (1.2)
1	47.6 (117.6)	48.1 (118.7)	0.5 (1.1)	24.6 (76.3)	25.4 (77.7)	0.8 (1.4)

Figure 3.11: Predicted and measured maximum transverse temperature distributions at sensor location across the top flange on June 1 and November 15, 2009.

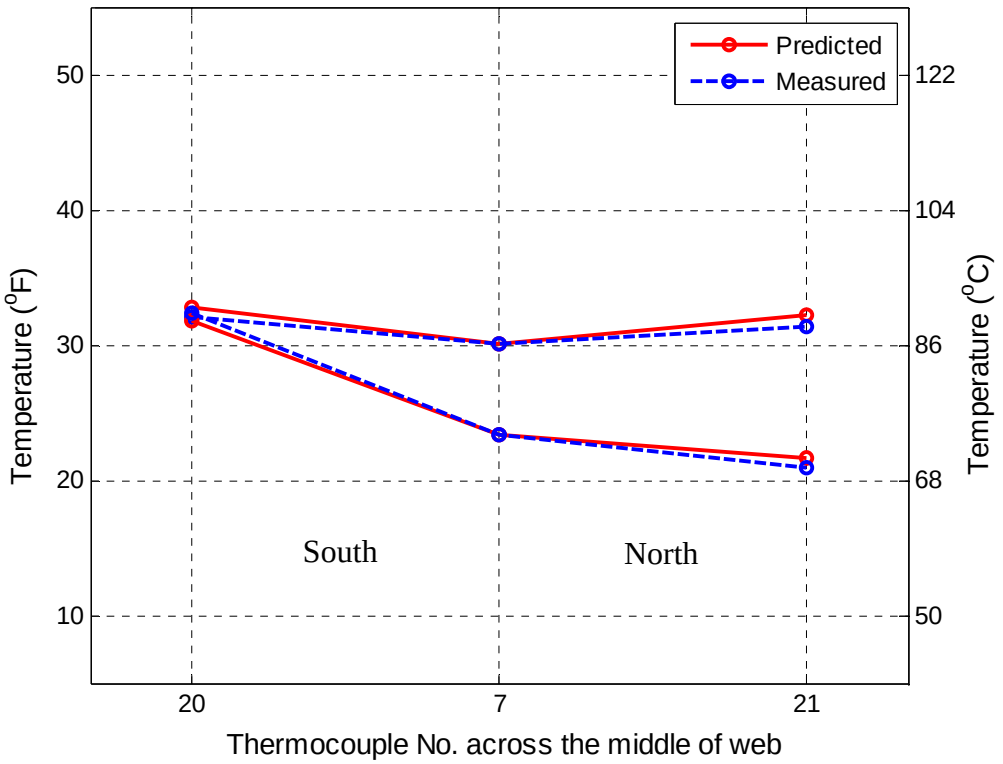

Thermocouple No.	June 1			November 15		
	Predicted °C (°F)	Measured °C (°F)	Difference °C (°F)	Predicted °C (°F)	Measured °C (°F)	Difference °C (°F)
20	32.7 (90.9)	32.1 (89.8)	0.6 (1.1)	31.8 (89.3)	32.3 (90.2)	0.5 (0.9)
7	30.0 (86.1)	30.1 (86.1)	0.1 (0.0)	23.3 (74.0)	23.4 (74.0)	0.1 (0.0)
21	32.2 (89.9)	31.4 (88.4)	0.8 (1.5)	21.6 (70.9)	20.9 (69.5)	0.7 (1.4)

Figure 3.12: Predicted and measured maximum transverse temperature distributions at sensor location across the middle of the web on June 1 and November 15, 2009.

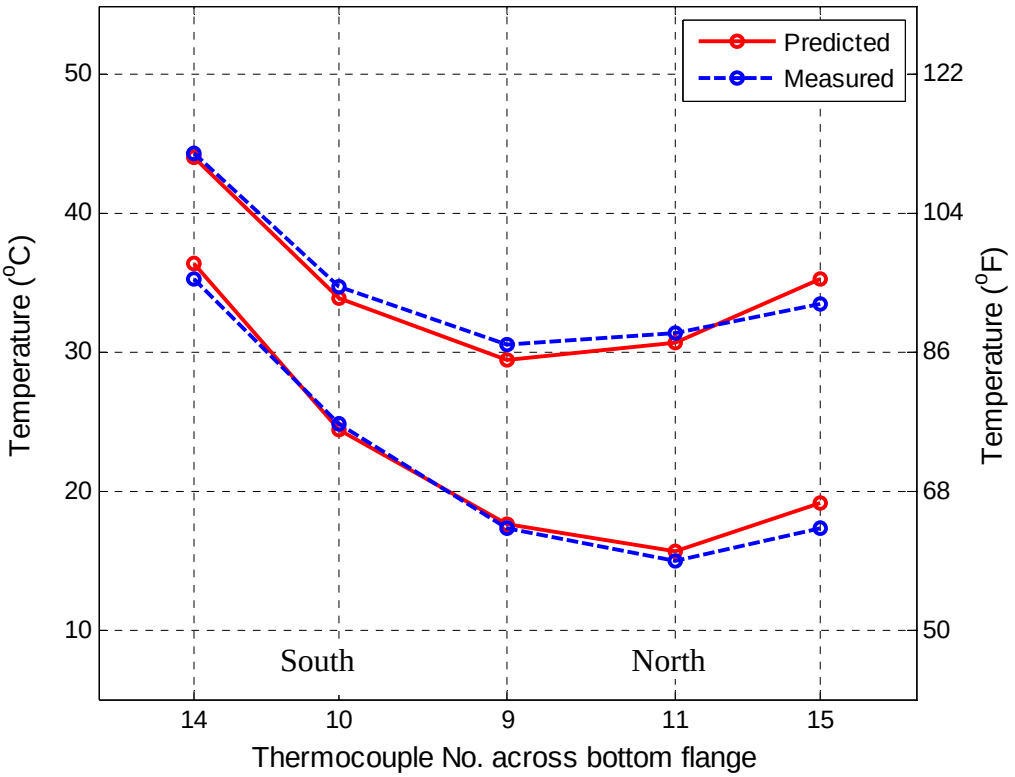

Thermocouple No.	June 1			November 15		
	Predicted °C (°F)	Measured °C (°F)	Difference °C (°F)	Predicted °C (°F)	Measured °C (°F)	Difference °C (°F)
14	44.0 (111.2)	44.3 (111.8)	0.3 (0.6)	36.4 (97.5)	35.3 (95.6)	1.1 (1.9)
10	33.9 (93.1)	34.7 (94.5)	0.8 (1.4)	24.5 (76.1)	24.9 (76.8) [a]	0.4 (0.7)
9	29.5 (85.0)	30.6 (87.0)	1.1 (2.0)	17.6 (63.7)	17.4 (63.3) [a]	0.2 (0.4)
11	30.7 (87.3)	31.4 (88.6)	0.7 (1.3)	15.6 (60.1)	14.9 (58.8)	0.7 (1.3)
15	35.3 (95.6)	33.5 (92.3)	1.8 (3.3)	19.1 (66.5)	17.3 (63.2)	1.8 (3.3)

[a] The temperatures at the thermocouple location 9 and 10 on November 15, 2009 were extrapolated using the second-order equation (See Appendix A).

Figure 3.13: Predicted and measured maximum transverse temperature distributions at sensor location across the bottom flange on June 1 and November 15, 2009.

CHAPTER 4

THERMAL RESPONSE ANALYSIS

4.1 Introduction

In order to evaluate the thermal response of the prestressed concrete bridge girder caused by the temperature distributions, the girder temperatures obtained from the two-dimensional (2D) heat transfer analysis are transferred to a three-dimensional (3D) finite element model with a constant temperature variation along the longitudinal direction of the girder. The 3D thermal response analysis is then performed to examine thermal movements in the vertical and transverse directions and thermal stresses in concrete and prestressing strands. From the experimental data taken from April 2009 to March 2010, June 1 and November 15, 2009 were selected as representative days for the largest vertical and transverse temperature gradients.

4.2 3D Finite Element Model

A simply supported prestressed concrete 100-foot long BT-63 girder was selected for the analytical study. For the thermal response analysis of the girder, a 3D finite element model that includes the prestressing forces was created. Elastomeric bearings pads and dowel bars, by which the prestressed concrete girder is supported, are modeled as simply supported conditions. The nonlinear behavior of the elastomeric bearing pads will be investigated in Chapter 6.

4.2.1 The Model of Concrete Girder and Prestressing Strands

The BT-63 girder was designed to be 100 feet long with a total of 12 straight strands 0.5 inches in diameter. The four strands in the top flange were each prestressed to 10,700 pounds, and the eight strands in the bottom flange were each prestressed to 35,000

pounds each in the bottom flange. Figure 4.1 depicts the arrangement of the prestressing strands over the cross-section of the BT-63 girder.

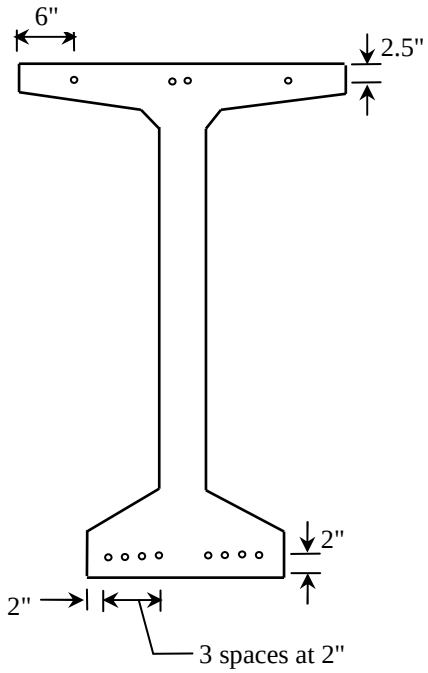

Figure 4.1: The arrangement of the prestressing strands in the BT-63 girder.

The 100-foot long BT-63 girder was modeled with a linear solid element C3D8 in ABAQUS (2008). The cross-section of the girder is composed of 584 elements and 699 nodes, the same as was used in the heat transfer analysis, and extended to 100 feet by an increment of 2 inches per element in the longitudinal direction of the girder. Thus, a total of 350,400 elements and 420,099 nodes were used to model the 100-foot long girder. In addition, the prestressing strands in the top and bottom flanges of the girder were modeled with a 3D two-node truss element T3D2 in ABAQUS (2008) and defined as embedded elements in the solid concrete elements. The embedded element technique used in this study constrains the translational degrees of freedom of the embedded elements, or truss elements, to the interpolated values of the corresponding degrees of freedom of the host element, or solid elements.

Figure 4.2 shows the 3D finite element model of the concrete girder and prestressing strands for the thermal response analysis of the 100-foot long BT-63 girder. The prestressing forces were defined as initial stress conditions and applied uniformly along the strand. The values of the initial stresses, assigned to the top and bottom strands, were 69.9 ksi and 228.8 ksi, respectively, calculated by dividing the prestressing forces by a nominal area of the strand. The vertical and longitudinal non-prestressed steel reinforcements were neglected in this study.

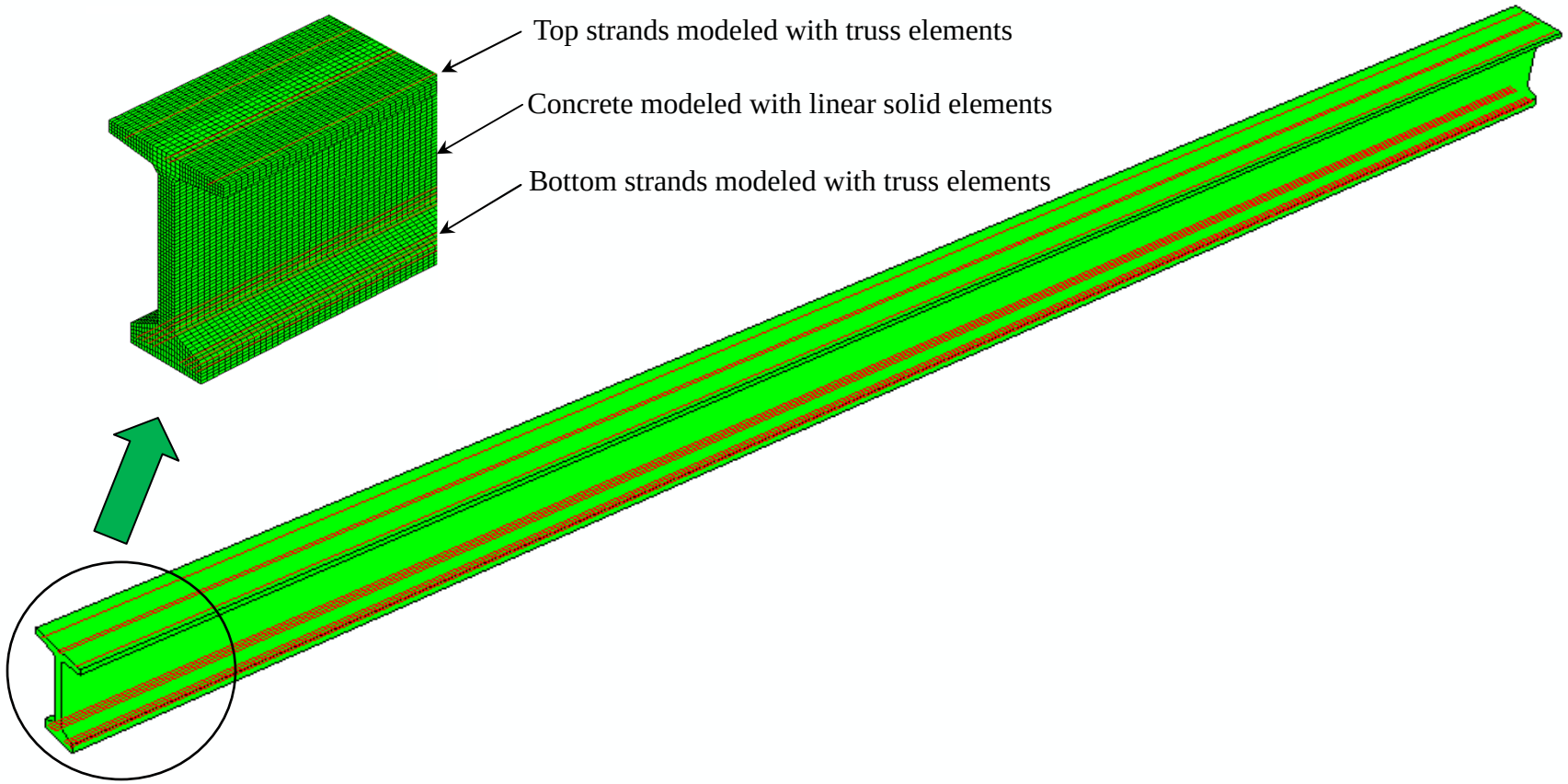

Figure 4.2: The 3D finite element model of the 100-foot long BT-63 girder for the thermal response analysis.

4.2.2 Support Boundary Conditions

Prestressed concrete bridge girders are generally supported by steel-reinforced elastomeric bearing pads. In the middle of the pads, the Georgia Department of Transportation (GDOT) manual states that the elastomeric bearing pads include a 3-inch diameter hole for a smooth dowel bar that provides lateral resistance to the girder. GDOT also specifies that the width of the pad be at least 2 inches narrower on each side than the nominal width of the bottom flange of Type-III and larger prestressed concrete beams. The length of the pad, which is not specified in the GDOT manual, was assumed to be 10 inches according to the *Structures Design Guidelines* (1997) of the Florida Department of Transportation (FDOT). Indeed, the elastomeric bearing pads of Type-V and larger prestressed concrete beams have been commonly designed to be 10 inches long in Georgia. Thus, the size of the elastomeric bearing pad for the BT-63 girder is determined to be 10 inches long, 20 inches wide, and a 3-inch diameter hole in the middle as shown in Figure 4.3. The hole of the bearing pad at the other end of the girder is slotted for the free longitudinal expansion of the girder.

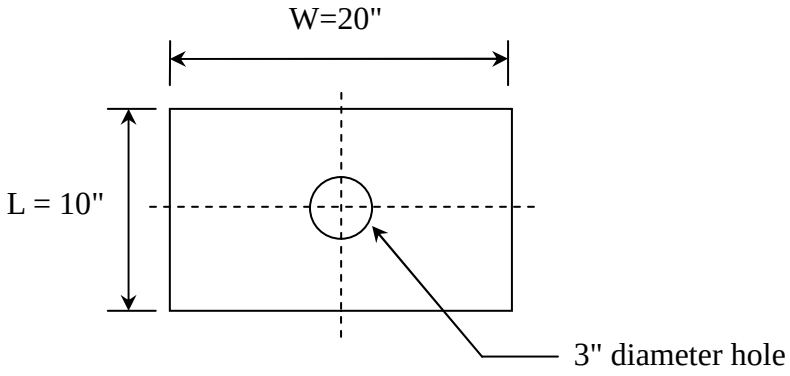

Figure 4.3: The dimensions of the steel-reinforced elastomeric bearing pad.

The bearing pads were modeled as vertical restraints over the area of the bearing pads. The lateral and longitudinal restraints provided by the dowel bars, located in the

middle of the girder at the both ends, were also defined as shown in Figure 4.4. The arrows shown in Figure 4.4 represent the restrained directions due to the bearing pads and the dowel bars. As shown in Figure 4.4(b), the slotted hole at the other end of the girder provides only lateral resistance to the girder.

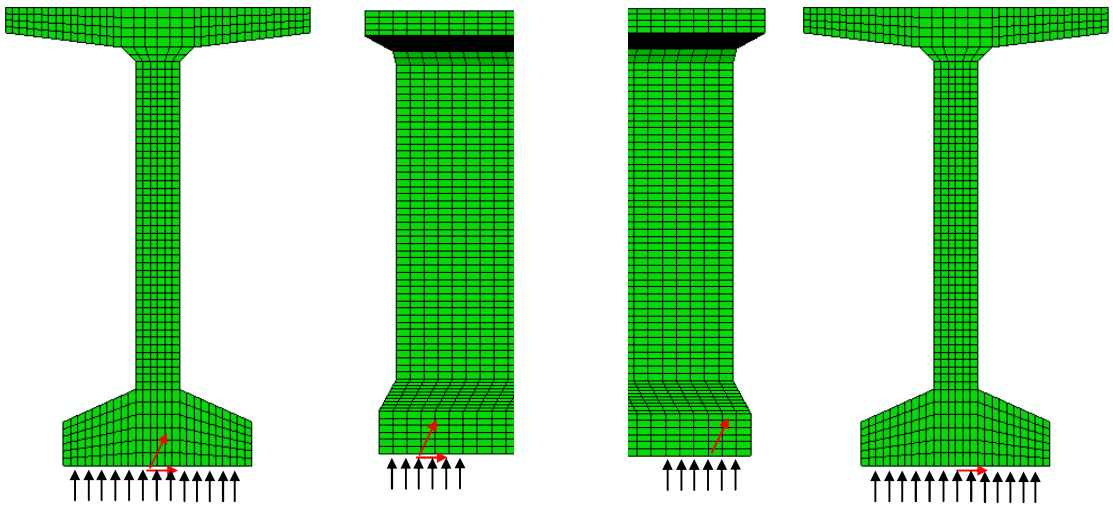

(a) One end of the girder (b) Other end of the girder

Figure 4.4: The support boundary conditions of the BT-63 girder used in this study.

4.2.3 Concrete and Prestressing Strand Material Properties

Based on the concrete compressive strength of 9 ksi obtained from three 6-inch and 12-inch cylinder tests at 28 days of age under standard laboratory conditions, the modulus of elasticity of the high-strength concrete, defined as more than 6 ksi compressive strength, was calculated using the following equation (ACI Committee 435, 1995):

$$E_c = \left(40,000\sqrt{f_c^{'}} + 10^6\right) \cdot \left(\frac{\omega_c}{145}\right)^{1.5} \tag{4.1}$$

in which E_c = the modulus elastic of concrete in psi,

$f_c^{'}$ = the compressive strength of concrete in psi, and

ω_c = the density of concrete in lb/ft^3.

The density of concrete in Equation (4.1) was assumed to be 150 lb/ft^3 for normal-weight concrete. The coefficient of the thermal expansion of concrete was taken as 12×10^{-6} /°C, or 6×10^{-6} /°F (AASHTO, 2007). Table 4.1 summarizes the material property values of the high-strength concrete used for the 3D thermal response analysis. Since the maximum tensile stresses of concrete due to thermal effects do not exceed the allowable tensile stress of concrete, $6\sqrt{f_c'}$, the concrete materials used in the thermal response analysis are modeled to be linear elastic.

Table 4.1: The material properties of concrete for the thermal response analysis.

Property	Density, ω_c (lb/in^3)	Modulus of Elasticity, E_c (psi)	Poisson's Ratio, υ	Coefficient of Thermal Expansion, α (/°C)
Concrete	0.0868	5,044,862	0.2	12×10^{-6}

For the Grade 270 low relaxation prestressing strands, the geometrical and material properties of the strands are defined from the *PCI Bridge Design Manual* (2003). Table 4.2 presents the cross-section area and material properties, including the coefficient of the thermal expansion of the strands. The value of the thermal expansion is 12×10^{-6} /°C, the same as that of the concrete thermal expansion. The design strength of the Grade 270 strands has an ultimate strength of 270 ksi and a yield strength of 245 ksi as shown in Table 4.2. The stress and strain equation for the Grade 270 low-relaxation strands given in the PCI manual (2003) follows:

$$f_{ps} = 270 - \left(\frac{0.04}{\varepsilon_{ps} - 0.007} \right) \tag{4.2}$$

in which f_{ps} = the stress of the strand in ksi, and

ε_{ps} = the strain of the strand after its yielding strain 0.0086.

Table 4.2: The material properties of strands for the thermal response analysis.

Nominal area (in^2)	Modulus of Elasticity, E_{ps} (psi)	Yield Strength (psi)	Ultimate Strength (psi)	Coefficient of Thermal Expansion, α (/°C)
0.153	28,500,000	245,000	270,000	12×10^{-6}

Furthermore, to model the behavior of the prestressing strands after the yielding strength of 245 ksi, this study idealized the stress and strain relationship of the strands as an elastic perfectly plastic material as shown in Figure 4.5.

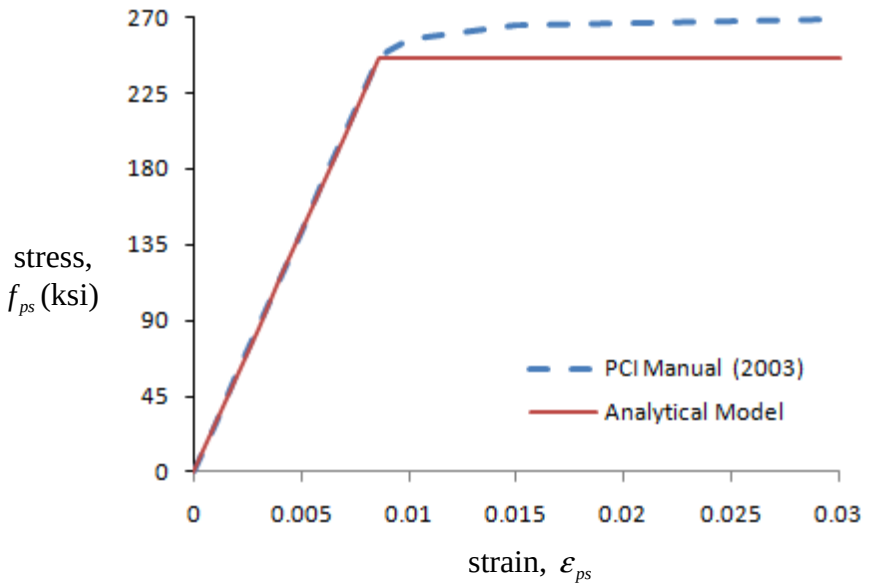

Figure 4.5: The stress and strain diagram of the Grade 270 low-relaxation strands.

4.3 Thermal Response Analysis

To investigate the thermal behavior of the prestressed concrete bridge girder, the temperature distributions obtained from the 2D heat transfer analysis for June 1 and November 15, 2009 were transferred to the 3D finite element model with a constant temperature variation along the length of the girder. A thermal response analysis was then performed at a time step interval of 25 minutes in order to reduce computing time and storage requirements instead of 5-minute intervals used in the 2D heat transfer analysis.

4.3.1 Sequence Analysis Procedures

The thermal response analysis consists of two linear sequential analyses. The first analysis is a static analysis due to initial stress conditions that account for the effects of prestressing forces applied to the top and bottom flanges of the girder. The camber and stresses at the end of the first analysis provide the initial conditions for the start of the thermal stress analysis. The 3D thermal stress analysis employed the girder temperatures obtained from the heat transfer analysis as sequential thermal loads. Since the heat transfer analysis was carried out on a 2D cross-section of the BT-63 girder, temperature variations along the girder were assumed to be constant. The process of the thermal response analysis is shown in Figure 4.6. In addition, this study analyzed the behavior of the girder due to only temperatures without the prestressing forces.

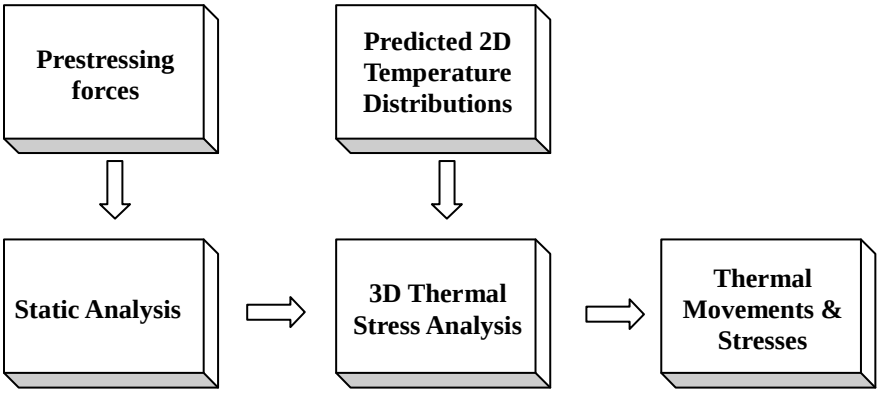

Figure 4.6: Overview of the thermal response analysis process.

4.3.2 Thermal Movements

Table 4.3 summarizes the maximum vertical and transverse thermal movements obtained from the 3D finite element thermal stress analyses on June 1 and November 15, 2009. Since a larger vertical temperature gradient was measured on June 1, the vertical movement of 0.29 inches was larger on June 1 than that on November 15 which was 0.12 inches. On the other hand, larger transverse thermal movements, 0.54 to 0.57 inches, occurred on November 15 because of the larger transverse temperature gradient. Table 4.3 also indicates little difference in the transverse thermal movements between the top flange, the web, and the bottom flange.

Figures 4.7 and 4.8 show variations in the vertical thermal movements of the BT-63 girder at mid-span on June 1 and November 15. Figure 4.7 represents the vertical movements due to only changes in temperatures, and Figure 4.8 includes the effect of prestressing forces on the vertical thermal movements. Figure 4.7(a) shows that the vertical thermal displacement decreases to -0.04 inches during the night and increases to 0.25 inches during the day with increases in solar radiation and air temperature on June 1. Thus, the total vertical thermal movement is 0.29 inches on June 1. For November 15, on which a smaller vertical gradient was measured due to lower solar radiation on the

horizontal surface, the total vertical thermal movement was only 0.12 inches. The prestressing forces, which produced an initial camber of 0.41 inches, increased the vertical thermal movements by the initial camber, as shown in Figure 4.8.

For transverse thermal movements, Figure 4.9 presents variations in the transverse thermal movements on the top, the middle, and the bottom of the BT-63 girder on June 1 and November 15, 2009. Larger transverse movements were observed on November 15 due to the larger transverse temperature gradients. The maximum transverse displacement was 0.57 inches on November 15 and 0.27 inches on June 1 at around 2:30 p.m. As illustrated in Table 4.3, Figure 4.9 also indicates that the transverse thermal movements along the depth of the girder were similar. In addition, Figures 4.10 and 4.11 show the contours of the vertical and transverse thermal displacements at 2:48 p.m. on June 1 and at 2:30 p.m. on November 15, 2009, when the maximum vertical and transverse thermal movements were observed, respectively.

Table 4.3: The maximum thermal movements of the BT-63 girder on June 1 and November 15, 2009.

(Units: inches)

Dates	Vertical movements	Transverse movements		
		Top flange	Web	Bottom flange
June 1, 2009	0.29	0.26	0.26	0.27
December 15, 2009	0.12	0.54	0.56	0.57

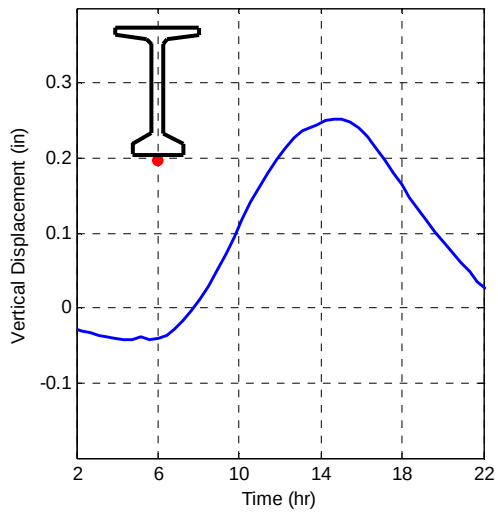

(a) June 1, 2009

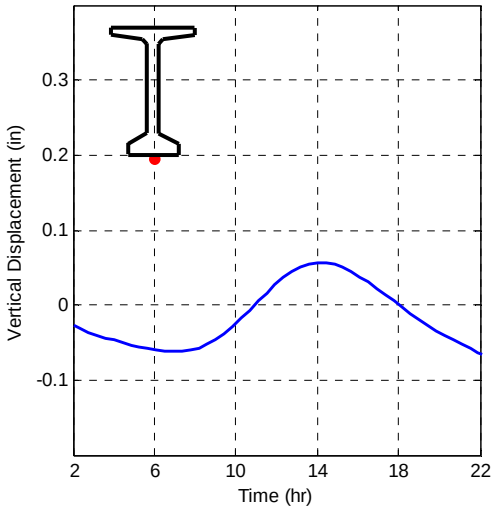

(b) November 15, 2009

Figure 4.7: The vertical movements of the BT-63 girder due to temperatures on June 1 and November 15, 2009.

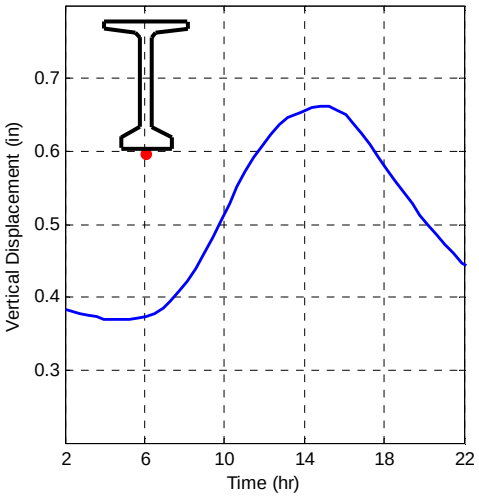

(b) June 1, 2009

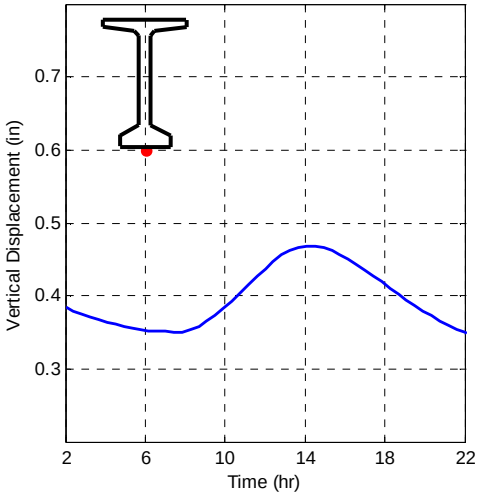

(b) November 15, 2009

Figure 4.8: The vertical movements of the BT-63 girder due to prestressing forces and temperatures on June 1 and November 15, 2009.

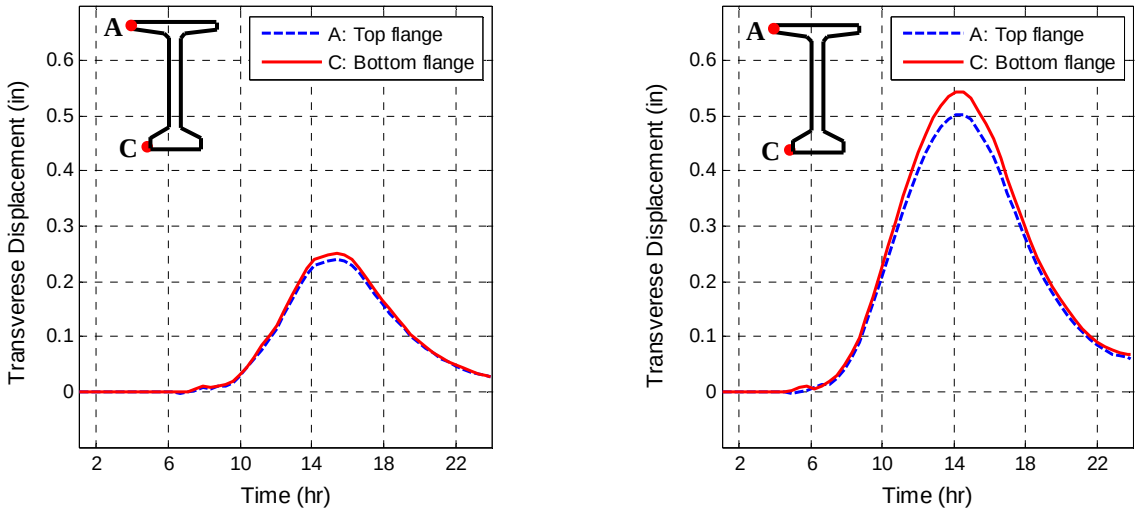

(a) June 1, 2009 (b) November 15, 2009

Figure 4.9: The transverse thermal movements of the BT-63 girder on June 1 and November 15, 2009.

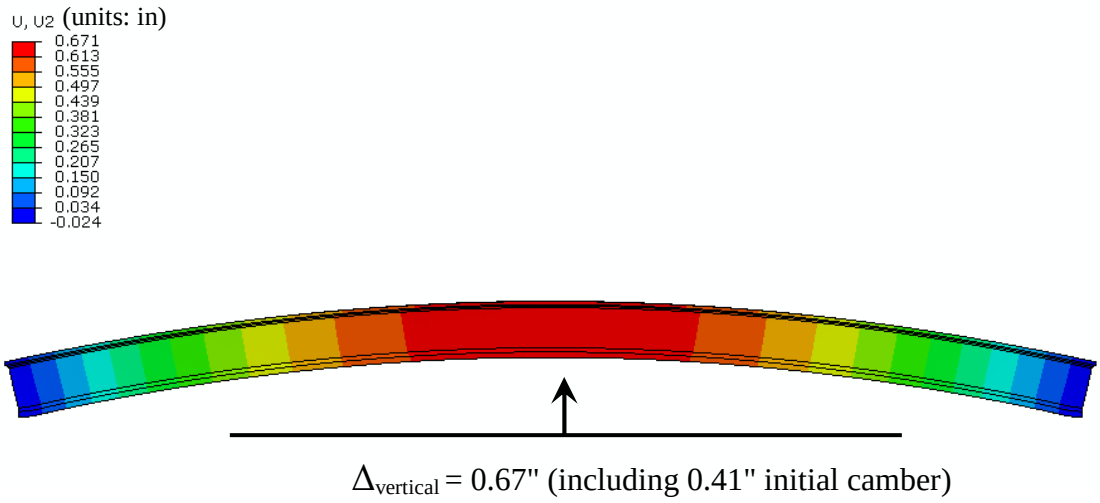

(a) Vertical displacement

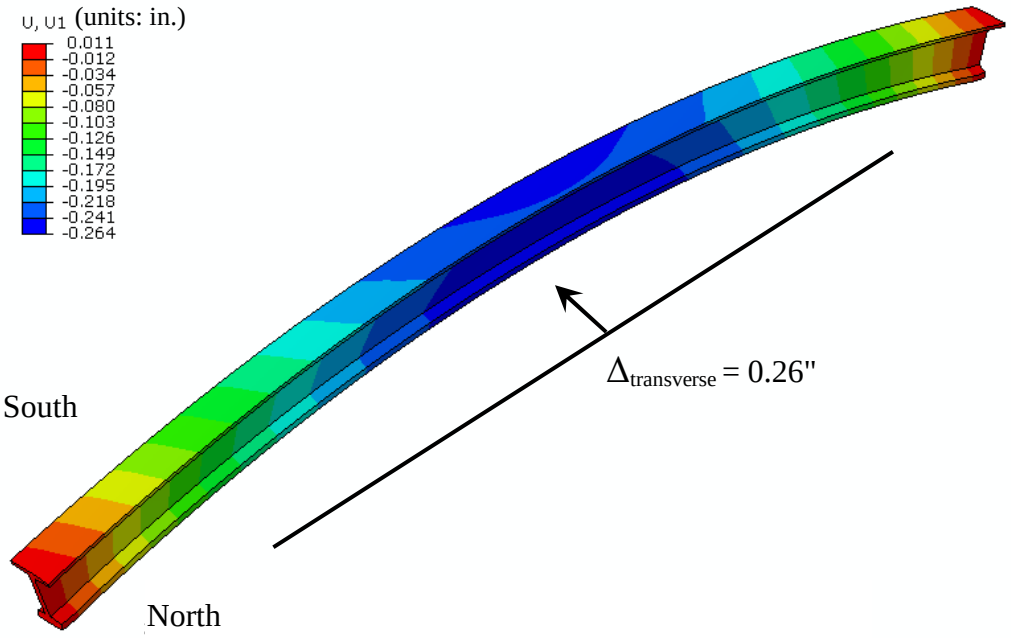

(b) Transverse displacement

Figure 4.10: The displacement contours of the prestressed concrete BT-63 girder at 2:48 p.m. on June 1, 2009 (Scale factor = 100).

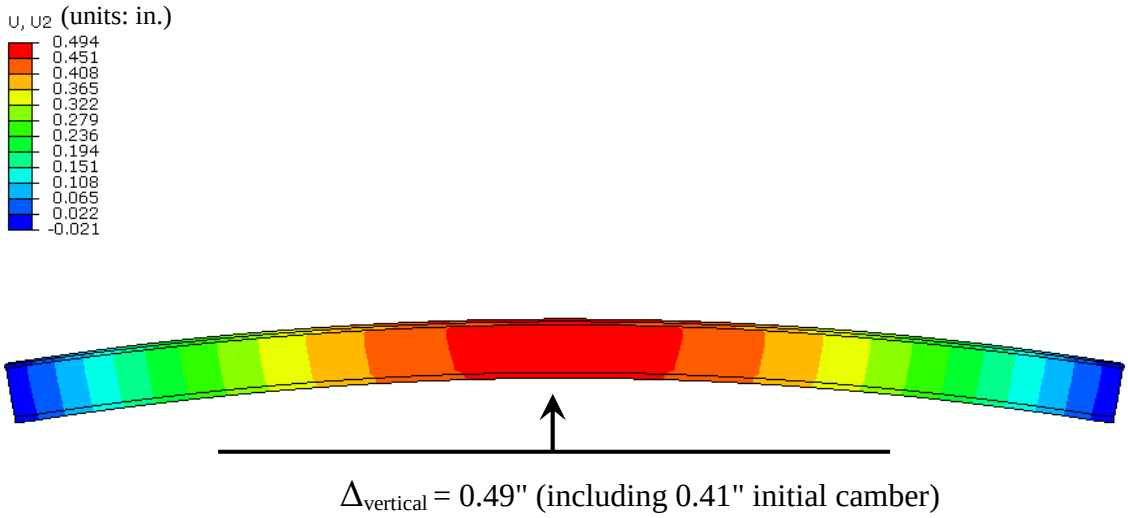

(a) Vertical displacement

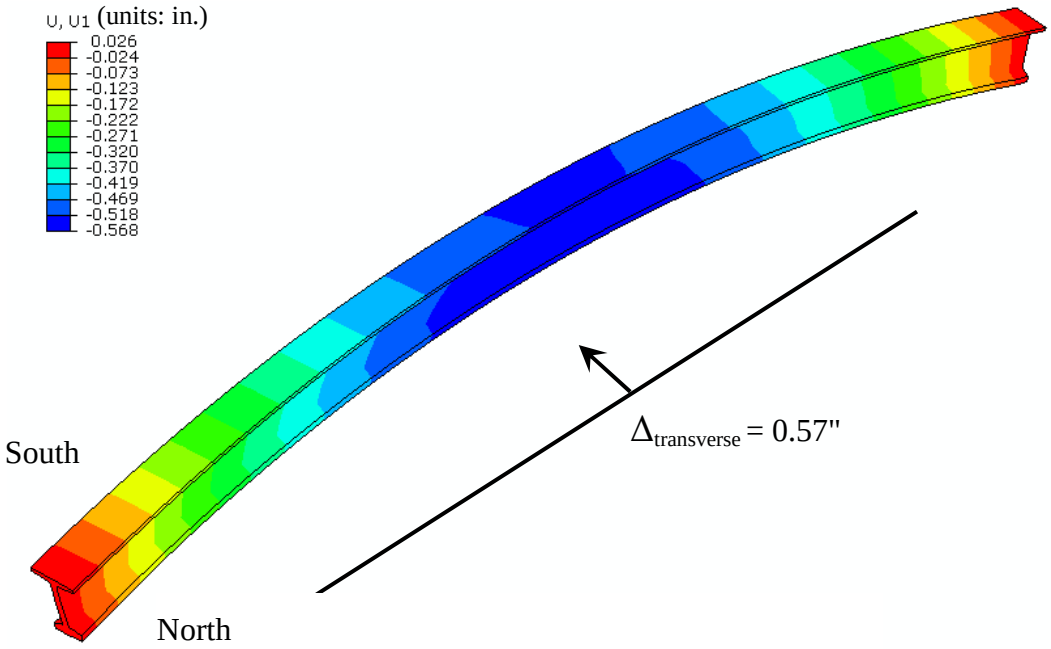

(b) Transverse displacement

Figure 4.11: The displacement contours of the prestressed concrete BT-63 girder at 2:30 p.m. on November 15, 2009 (Scale factor = 100).

4.3.3 Thermal Stresses

Figure 4.12 illustrates the strain differences between the final linear strains and the thermal strains based on the largest vertical temperature distributions on June 1 and November 15. The dashed lines in Figure 4.12 represent the free thermal strains due to nonlinear vertical temperature gradients, and the arrows in Figure 4.12 represent the strain differences, which result in self-equilibrating stresses. With an increase in the vertical temperature gradient due to high solar radiation on the top surface, as shown in Figure 4.12(a), the top and bottom flanges of the bridge girder show high compressive stresses, and the web shows tensile stresses. On November 15, when a large temperature gradient is observed in the web due to high solar radiation on the vertical surface, the web exhibits compressive stresses shown in Figure 4.12(b).

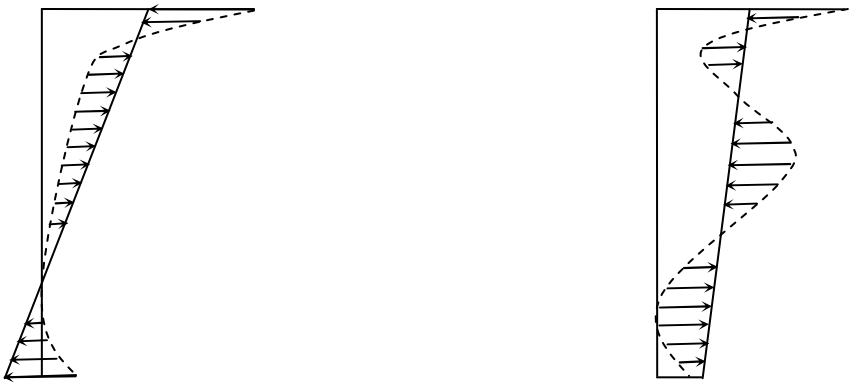

(a) June 1 (b) November 15

Figure 4.12: Strain differences that result in self-equilibrating stresses based on the largest vertical temperature gradients measured on June 1 and November 15, 2009.

Figures 4.13 and 4.14 show variations in the longitudinal stresses of concrete on the top and bottom surfaces of the BT-63 girder on June 1 and November 15, 2009. As the vertical temperature gradient increases during the day, compressive stresses on the

top surface increase up to 460 psi at around 1 p.m. on June 1 and 150 psi at around 12 p.m. on November 15, as shown in Figure 4.13. The higher increase in the compressive stress on June 1 is due to the larger vertical temperature gradient. The influence of prestressing forces applied to the top and bottom flanges of the girder is shown in Figure 4.14. Concrete stresses were shifted to the compressive stresses of about 810 psi on the top surface and 80 psi on the bottom surface due to the prestressing forces.

In addition, variations in the longitudinal stresses of concrete on the top, middle, and bottom of the web are shown in Figures 4.15 and 4.16. On June 1, when vertical and transverse temperature gradients were almost constant in the web, the variations in the concrete stresses were under tensile stresses, which increased to approximately 270 psi on top of the web at around 2:30 p.m., as shown in Figure 4.15(a). For November 15, Figure 4.15(b) presents the maximum compressive stresses of around 470 psi in the middle and 270 psi on the bottom of the web at around 1:30 p.m. because of both the large vertical and transverse temperature gradients in the web. Similar to the top and bottom concrete stresses shown in Figure 4.14, Figure 4.16 shows the initial compressive stresses produced by the prestressing forces, which shift the stresses of the web to a compression of around 200 psi on the top, 430 psi in the middle, and 660 psi on the bottom of the web.

In addition, Figures 4.17 and 4.18 illustrate the variations in the maximum principal stresses of concrete due to prestressing forces and temperatures. When larger vertical thermal movements were observed on June 1, the top surface showed higher tensile stresses than those of the web as shown in Figure 4.17(a) and 4.18(a). On November 15, Figures 4.17(b) and 4.18(b) exhibited higher increases in tensile stresses on the top of the web than those on the top surface.

For the stresses of the strands, Figures 4.19 and 4.20 present the stress variations with changes in temperatures in the top and bottom flanges, respectively. The variation in the stress of the top strand due to temperature variations ranges from 67 to 74 ksi on

June 1 and 67 to 72 ksi on November 15, shown in Figure 4.19. The strand stress in the middle of the bottom flange shown in Figure 4.20 varies from 222 to 226 ksi on June 1 and 223 to 226 ksi on November 15. Therefore, the changes in the stresses of the strands due to temperatures were about 5% in the top flange and 3% in the bottom flange with no specific differences between June 1 and November 15.

Figures 4.20 and 4.21 show the longitudinal stress contours when the highest tensile stresses of 64 and 110 psi were found on the top of the web at 2:22 p.m. on June 1 and at 2:55 p.m. on November 15, 2009, respectively. The maximum principal stress contours of the BT-63 girder at 2:22 p.m. on June 1 and at 2:55 p.m. on November 15 2009 were also presented in Figures 4.22 and 4.23. As noted in Figures 4.20 and 4.21, the highest tensile stresses, 64 psi on June 1 and 110 psi on November 15, were observed on the top of the web. The maximum principal stresses in the girder were within the tensile stresses of 0 to 50 psi, which were less than the allowable tensile stress of concrete, 569 psi.

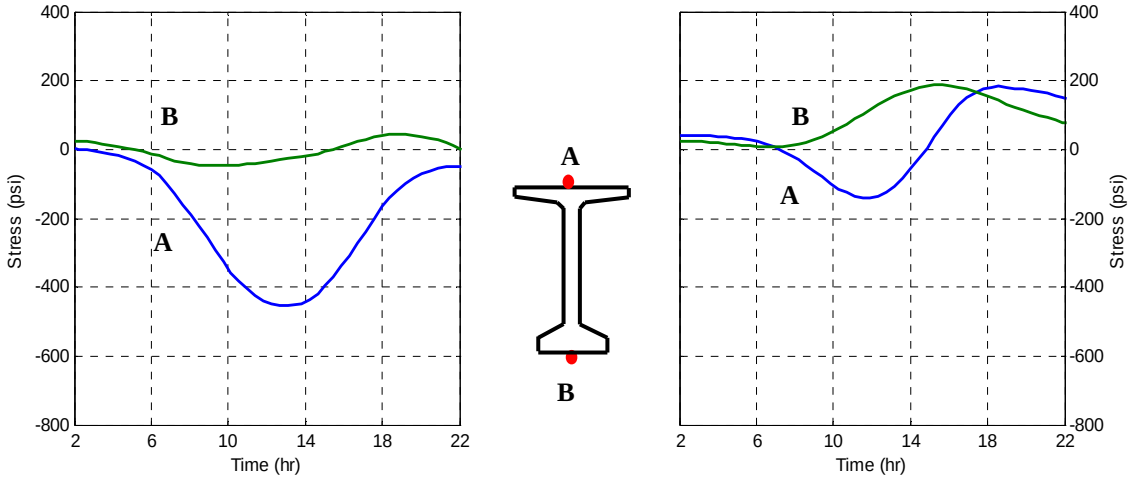

(a) June 1, 2009 (b) November 15, 2009

Figure 4.13: Variations in the longitudinal stresses of concrete on the top and bottom surfaces at mid-span due to temperatures on June 1 and November 15, 2009.

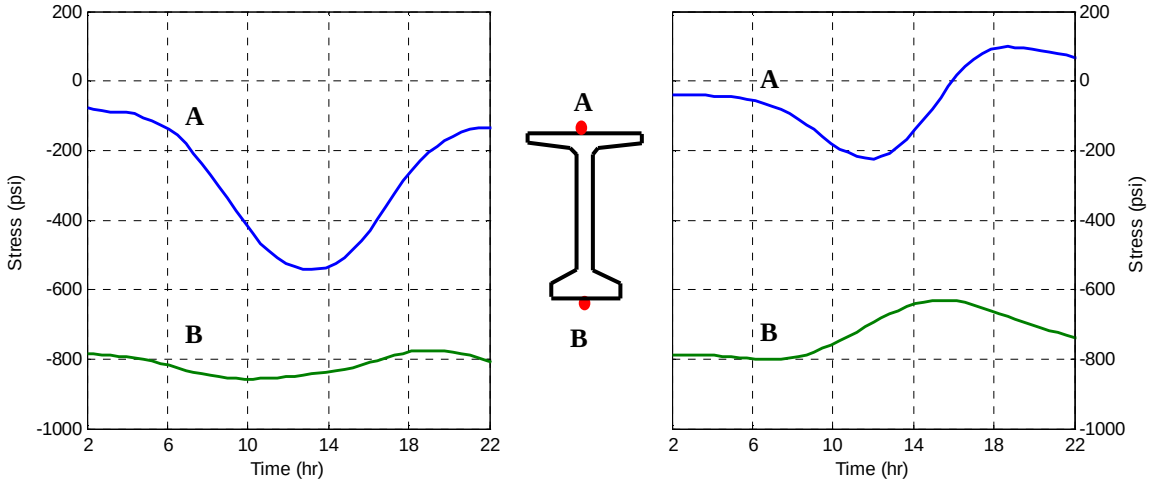

(a) June 1, 2009 (b) November 15, 2009

Figure 4.14: Variations in the longitudinal stresses of concrete on the top and bottom surfaces at mid-span due to prestressing forces and temperatures on June 1 and November 15, 2009.

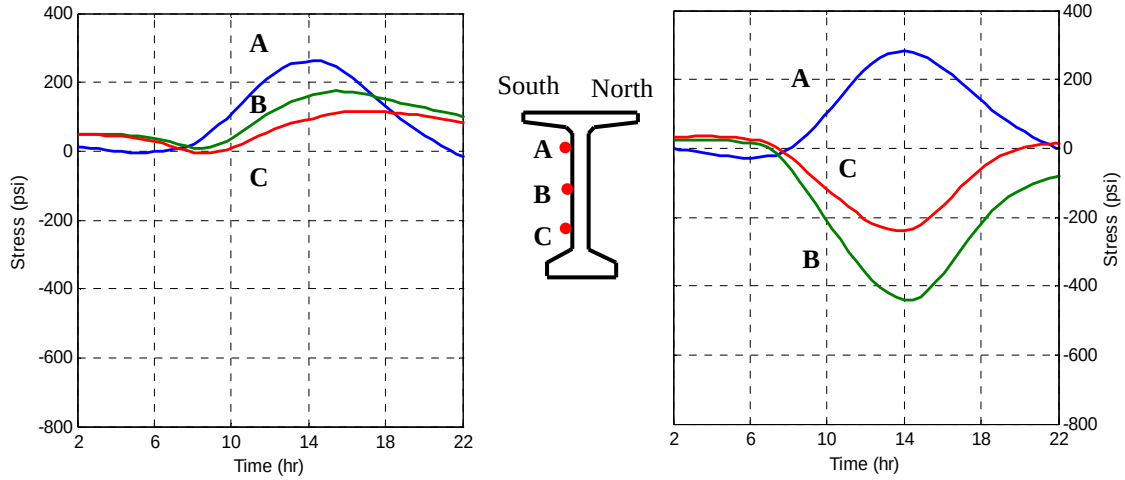

(a) June 1, 2009 (b) November 15, 2009

Figure 4.15: Variations in the longitudinal stresses of concrete on the top, the middle, and the bottom of the web at mid-span due to temperatures on June 1 and November 15, 2009.

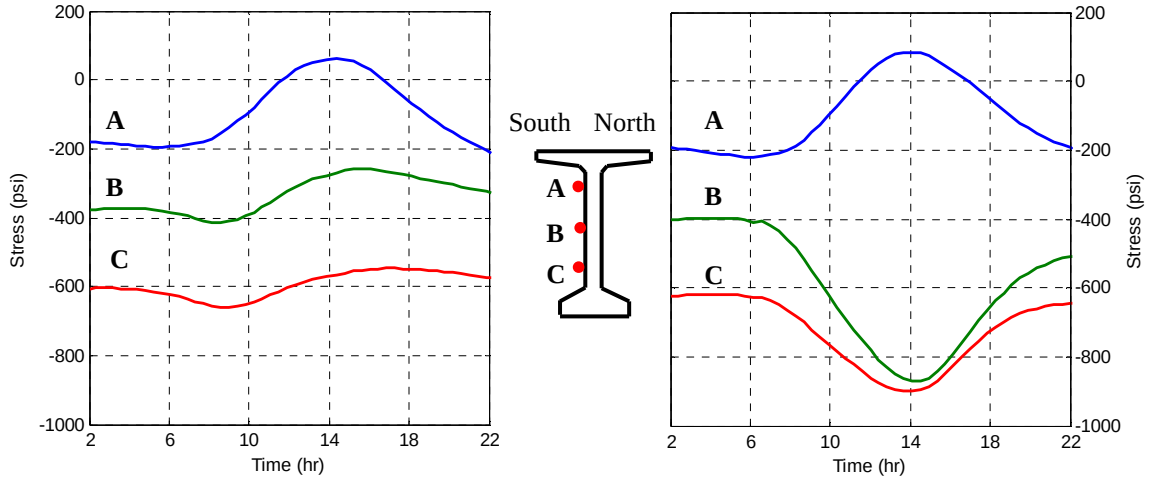

(a) June 1, 2009 (b) November 15, 2009

Figure 4.16: Variations in the longitudinal stresses of concrete on the top, the middle, and the bottom of the web at mid-span due to prestressing forces and temperatures on June 1 and November 15, 2009.

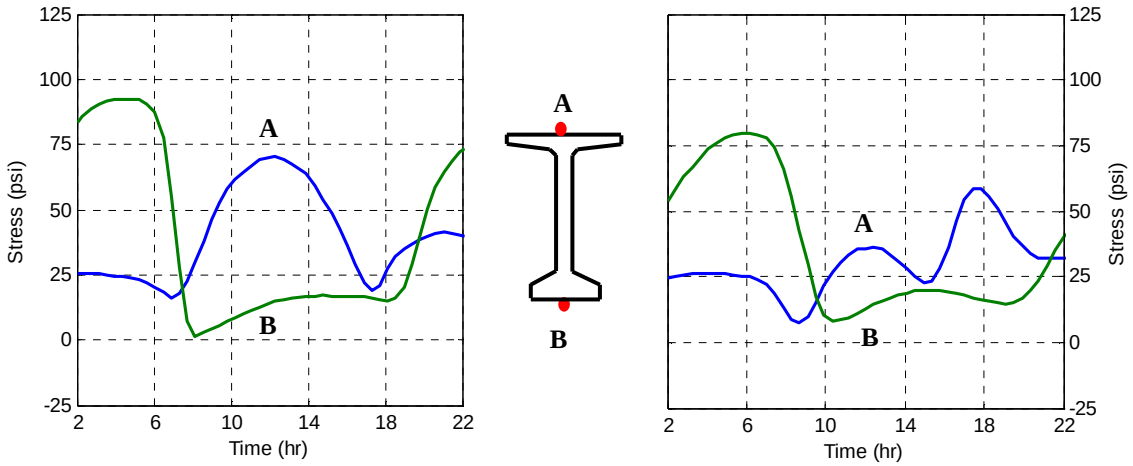

(a) June 1, 2009 (b) November 15, 2009

Figure 4.17: Variations in the maximum principal stresses of concrete on the top and bottom surfaces at mid-span due to prestressing forces and temperatures on June 1 and November 15, 2009.

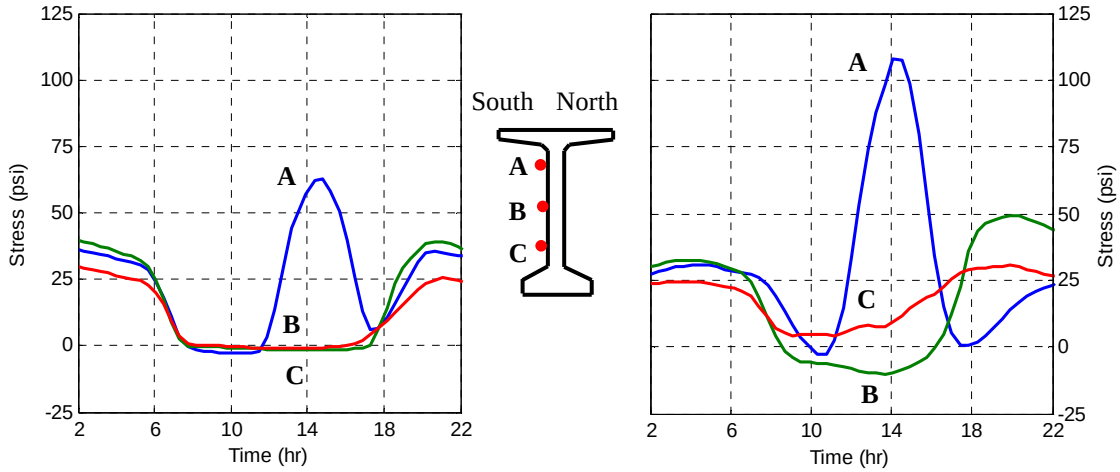

(a) June 1, 2009 (b) November 15, 2009

Figure 4.18: Variations in the maximum principal stresses of concrete on the top, the middle, and the bottom of the web at mid-span due to prestressing forces and temperatures on June 1 and November 15, 2009.

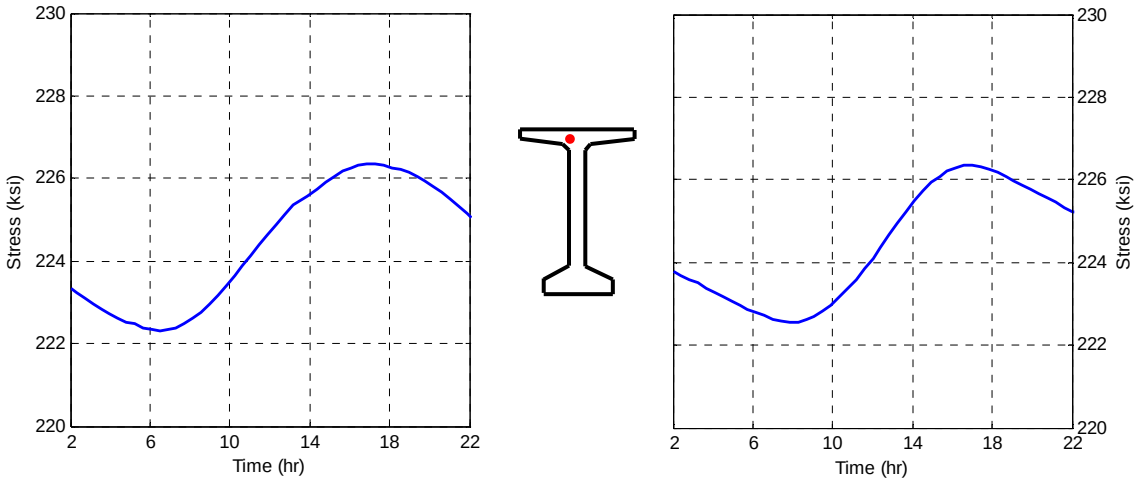

(a) June 1, 2009 (b) November 15, 2009

Figure 4.19: Variations in the stresses of a top strand at mid-span due to temperatures on June 1 and November 15, 2009.

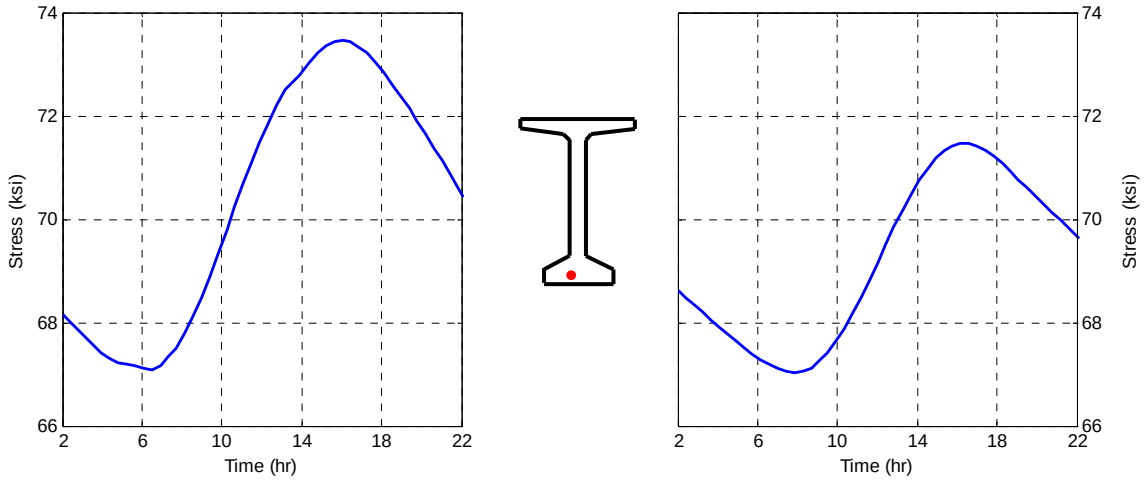

(a) June 1, 2009 (b) November 15, 2009

Figure 4.20: Variations in the stresses of a bottom strand at mid-span due to temperatures on June 1 and November 15, 2009.

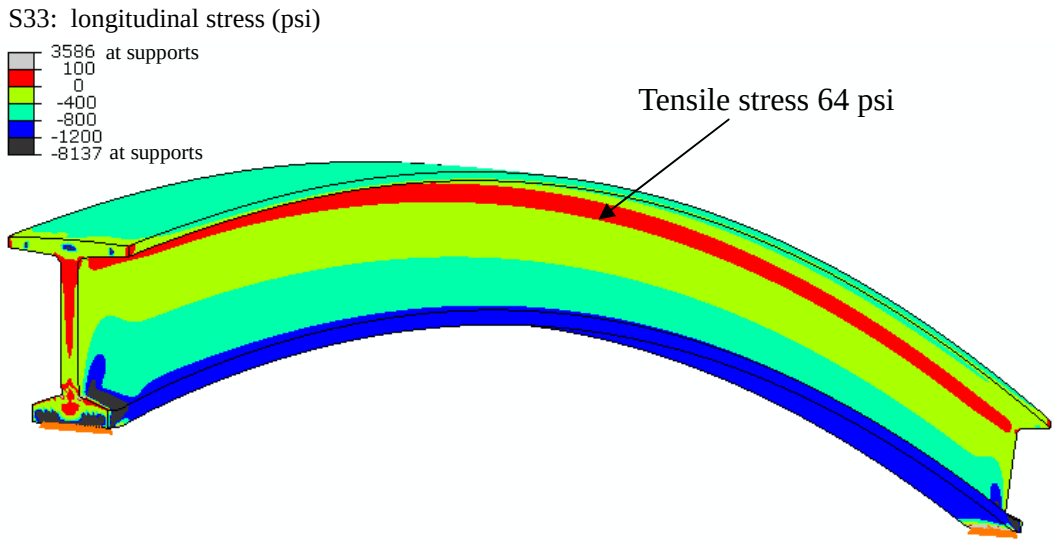

Figure 4.21: The longitudinal stress (S33) contours of the prestressed concrete BT-63 girder s at 2:22 p.m. on June 1, 2009 (Scale factor = 100).

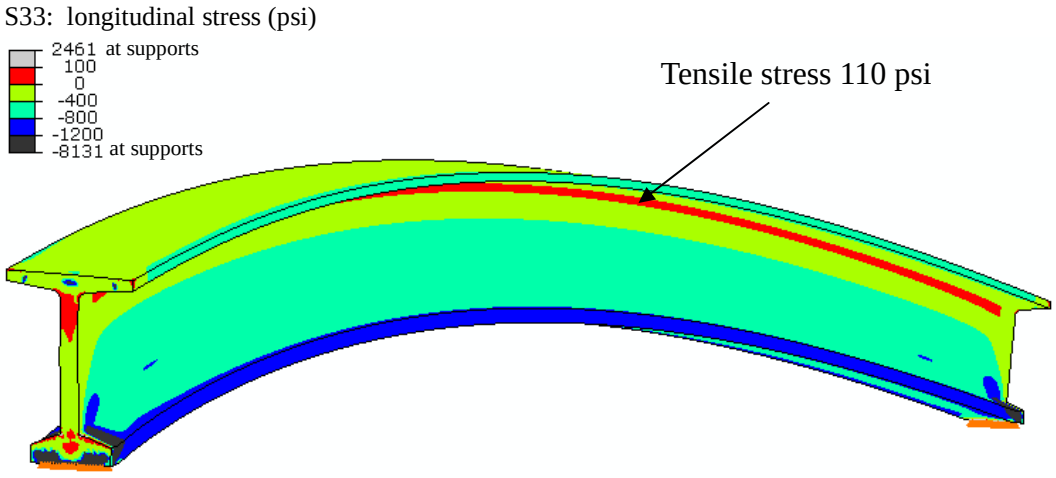

Figure 4.22: The longitudinal stress (S33) contours of the prestressed concrete BT-63 girder s at 2:55 p.m. on November 15, 2009 (Scale factor = 100).

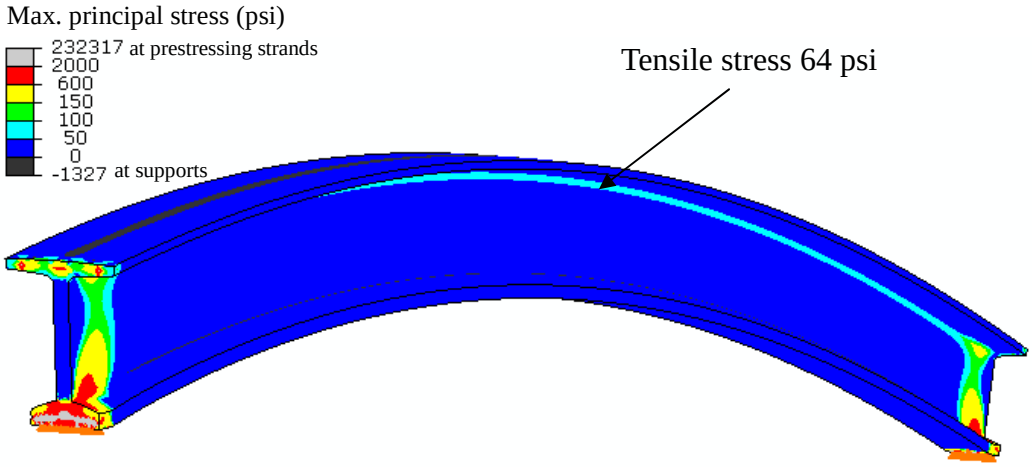

Figure 4.23: The maximum principal stress contours of the prestressed concrete BT-63 girder s at 2:22 p.m. on June 1, 2009 (Scale factor = 100).

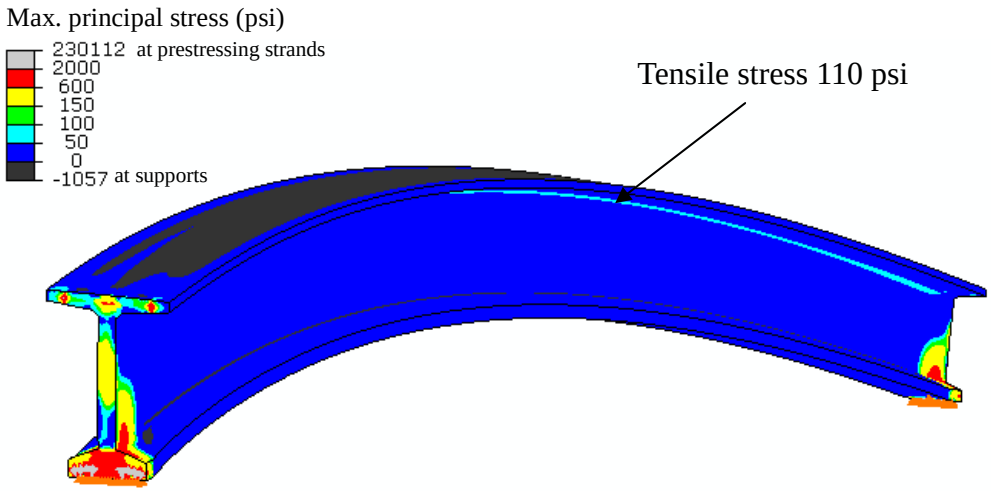

Figure 4.24: The maximum principal stress contours of the prestressed concrete BT-63 girder s at 2:55 p.m. on November 15, 2009 (Scale factor = 100).

CHAPTER 5

DESIGN THERMAL GRADIENTS IN PRESTRESSED CONCRETE BRIDGE GIRDERS

5.1 Introduction

For the thermal design of concrete and prestressed concrete bridge superstructures, the *AASHTO LRFD Bridge Design Specifications* (2007) provide a vertical temperature gradient obtained from average daily solar radiation and normal daily maximum and minimum temperatures for the months of June and July. However, no specific study on expected extreme environmental conditions that could cause maximum temperature gradients in the vertical and transverse directions over a cross-section of the bridge girder has been carried out. Furthermore, no guideline or recommendation on the transverse temperature gradient is provided in the AASHTO specifications.

Based on experimental investigations into the thermal effects in a prestressed concrete girder, extremes in seasonal daily environmental conditions was determined from the National Solar Radiation Data Base (NSRDB) and the National Climatic Data Center (NCDC). Using the extreme environmental conditions, the two-dimensional (2D) finite element heat transfer analyses were performed to determine seasonal extremes in vertical and transverse temperature distributions and gradients in AASHTO-PCI standard girder sections. The influence of bridge orientations on the temperature distributions was also examined. Finally, maximum vertical and transverse temperature gradients were computed for eight cities in the United States.

5.2 Extreme Seasonal Daily Environmental Conditions

An experimental study was carried out on environmental thermal effects on a BT-63 bridge girder segment from April 2009 to March 2010. Based on the relationships

between the environmental conditions and the largest vertical and transverse temperature differentials, the NSRDB and NCDC data, which contain the 30-year (from 1961 to 1990) monthly average daily solar radiation and daily climatic values, respectively, were evaluated for seasonal extremes in daily environmental conditions assuming no wind.

5.2.1 Solar Radiation

According to the experimental investigations presented in Chapter 2, the largest vertical temperature differentials, 18°C (23°F) to 21°C (38°F), were measured during the months of May, June, and July while the largest transverse temperature differentials, around 11°C (20°F) in the top flange and the web and 21°C (38°F) in the bottom flange, were measured in the late fall and the winter during the months of October, November, and December. When these vertical and transverse temperature differentials were measured, the daily solar radiation calculated from the measurements ranged from 28 to 30 MJ/m^2 in the summer and 13 to 20 MJ/m^2 in the late fall and the winter. The NSRDB also showed similar ranges of daily solar radiation, 28.6 to 29.4 MJ/m^2 in May, June, and July and 11.9 to 17.7 MJ/m^2 in October, November, and December under clear sky conditions. Table 5.1 presents the monthly average solar radiation extracted from the NSRDB data and calculated from the measurements from April 2009 to March 2010 in Atlanta, Georgia. The daily solar radiation under global conditions shown in Table 5.1 was calculated for the entire days of the month, and the daily solar radiation under clear conditions was obtained for the clear days of the month defied as a total cloud cover of less than 10%.

In particular, for June 1, on which the largest vertical temperature differential of 20.4°C (36.7°F) was measured, the daily solar radiation was 28.8 MJ/m^2 which was very close to the NSRDB value of 29.4 MJ/m^2 under clear sky conditions in June. When the largest transverse temperature differentials, 10.0°C (18.0°F) in the top flange, 11.5°C (20.6°F) in the middle of the web, and 20.5°C (36.8°F) in the bottom flange, were

measured on November 15, the daily solar radiation of 14.7 MJ/m^2 was also close to the NSRDB value of 13.6 MJ/m^2 under clear sky conditions for November.

Thus, for extreme daily solar radiation in the summer and the winter, this study selected the values of June and December, 29.4 and 11.9 MJ/m^2, respectively, from the NSRDB under clear sky conditions. In addition, this study included the daily solar radiation of March and September, 21.9 and 22.4 MJ/m^2, respectively, for the spring and the fall. The measured daily solar radiation under clear sky conditions was 21.3, 27.3, 21.2, and 11.6 MJ/m^2 in March, June, September, and December, respectively. The differences between the measurements and the NSRDB are less than 2 MJ/m^2 (7%).

Table 5.1: Monthly average solar radiation on a horizontal surface extracted from the NSRDB data and measured during the months of April 2009 to March 2010.

(Units: MJ/m^2·day)

Months		Jan	Feb	Mar	Apr	May	June	July	Aug	Sep	Oct	Nov	Dec
NSRDB	Global	9.3	12.3	16.1	20.3	22.4	23.2	22.1	20.5	17.5	14.5	10.6	8.5
	Clear Sky	13.3	17.0	21.9	26.3	28.7	29.4	28.6	26.2	22.4	17.7	13.6	11.9
Current Study	Global	8.8	8.7	12.3	18.0	16.6	22.7	21.7	18.0	15.1	10.2	11.5	6.1
	Clear Sky	13.0	13.9	21.4	27.3	29.5	27.3	26.3	23.1	21.2	18.3	14.9	11.6

5.2.2 Air Temperature

For expected daily extremes in air temperature, the NCDC data pertaining to the average daily maximum and minimum temperatures and the record daily maximum and minimum temperatures were investigated. The average daily maximum and minimum temperatures are arithmetic averages computed by summing the monthly values for the period of 1961 to 1990 and dividing by thirty. The record daily maximum and minimum temperatures were obtained from the entire record period of 1930 to 1990. Table 5.2

shows the average daily maximum and minimum temperatures and the record daily maximum and minimum temperatures extracted from the NCDC data for the Atlanta Hartsfield Airport station, approximately 10 miles away from the experimental site, and measured at five-minute intervals in Atlanta, Georgia from April 2009 to March 2010.

For June 1 when the largest vertical temperature differentials were measured, the daily maximum temperature was 33.3°C (91.9°F), and the daily minimum temperature was 18.8°C (65.8°F). Compared with the NCDC data for June shown in Table 5.2, the measured daily minimum temperature of 18.8°C (65.8°F) was in good agreement with the average daily temperature of 19.0°C (66.2°F). The measured daily maximum temperature of 33.3°C (91.9°F) was close to both the average daily maximum temperature and the record daily maximum temperature of the NCDC data, 29.9°C (85.8°F) and 38.3°C (100.9°F) for the month of June, respectively. However, since the average daily maximum temperature was somewhat lower than the measured daily maximum temperature, the record daily maximum temperature was selected as an extreme daily maximum temperature.

When the largest transverse temperature differential was measured on November 15, the daily maximum and minimum temperatures were 22.5°C (72.5°F) and 9.3°C (48.8°F). The NCDC data showed the record daily maximum temperature of 28.9°C (84.0°F), the average daily maximum temperature of 17.4°C (63.3°F), and the average minimum temperature of 6.0°C (42.8°F) in November as shown in Table 5.2. Similar to the extreme daily temperature conditions in the summer, the average daily minimum temperature was close to the measured daily minimum temperature, and the record daily maximum temperature was close to the measured daily maximum temperature.

Therefore, this study chose the record daily maximum temperature and the average daily minimum temperature of the 30-year monthly NCDC data as the daily maximum and minimum temperatures for four seasons: March, June, September, and

December were defined as representative months of the spring, the summer, the fall, and the winter, respectively.

Table 5.2: Monthly average daily air temperatures extracted from the NCDC data and measured during the months of April 2009 to March 2010.

(Units: °C)

Months		Jan	Feb	Mar	Apr	May	June	July	Aug	Sep	Oct	Nov	Dec
NCDC	Average Max.	10.2	12.8	17.9	22.6	26.4	29.9	31.1	30.6	27.7	22.6	17.4	12.2
	Average Min.	-0.3	1.4	5.8	10.1	14.8	19.0	20.8	20.6	17.5	11.1	6.0	1.7
	Record Max.	26.1	26.7	29.4	33.9	35.0	38.3	40.6	38.9	36.7	35.0	28.9	26.1
	Record Min.	-22.2	-15.0	-12.2	-3.3	2.8	7.8	11.7	12.8	2.2	-2.2	-16.1	-17.8
Current Study	Average Max.	7.5	8.1	15.7	27.6	27.4	34.1	31.7	29.6	27.3	21.2	18.3	9.9
	Average Min.	-1.2	0.5	6.6	13.1	17.0	21.0	20.2	20.3	16.4	11.2	6.2	1.3
	Record Max.	17.2	18.6	25.6	32.7	34.0	37.8	35.1	32.3	31.4	30.4	23.9	19.6
	Record Min.	-10.0	-5.0	-0.9	6.3	9.5	16.5	17.3	17.6	10.0	2.2	1.7	-2.8

(Units: °F)

Months		Jan	Feb	Mar	Apr	May	June	July	Aug	Sep	Oct	Nov	Dec
NCDC	Average Max.	50.4	55.0	64.2	72.7	79.5	85.8	88.0	87.1	81.9	72.7	63.3	54.0
	Average Min.	31.5	34.5	42.4	50.2	58.6	66.2	69.4	69.1	63.5	52.0	42.8	35.1
	Record Max.	79.0	80.1	84.9	93.0	95.0	100.9	105.1	102.0	98.1	95.0	84.0	79.0
	Record Min.	-8.0	5.0	10.0	26.1	37.0	46.0	53.1	55.0	36.0	28.0	3.0	0.0
Current Study	Average Max.	45.4	46.5	60.3	81.7	81.3	93.4	89.1	85.3	81.1	70.2	64.9	49.8
	Average Min.	29.8	32.9	43.9	55.6	62.6	69.8	68.4	68.5	61.5	52.2	43.2	34.3
	Record Max.	63.0	65.4	78.1	90.9	93.2	100.0	95.2	90.1	88.5	86.7	75.0	67.3
	Record Min.	14.0	23.0	30.3	43.3	49.1	61.7	63.1	63.7	50.0	36.0	35.1	27.0

5.2.3 Wind Speed

For another environmental factor of wind speed, when large vertical and transverse temperature differentials were measured, daily average wind speed calculated by integrating the measurement data using the trapezoidal numerical method and dividing the integration by the total measuring time was within 1 m/sec (2.2 mph) with no specific seasonal variations. The recorded maximum wind speed, or the highest wind speed from the measured wind speed data, was less than 5 m/sec (11.2 mph) on the days when the large vertical and/or transverse temperature differentials were recorded. In particular, for June 1, on which the largest vertical temperature differential was measured, the daily average wind speed was 0.4 m/sec (0.9 mph), and the maximum wind speed was 2.8 m/sec (6.3mph). For November 15, 2009, on which the largest transverse temperature differential was measured, the daily average wind speed was 0.3 m/sec (0.7 mph), and the maximum wind speed was 2.4 m/sec (5.4 mph). Therefore, in this study, the effect of wind speed on temperature variations in bridge girders was disregarded.

5.3 Hourly Variations in Seasonal Environmental Conditions

This section examined variations in the daily environmental conditions determined from the NSRDB for daily solar radiation and from the NCDC for daily maximum and minimum air temperatures with respect to the time of day. Since climatic data provided by weather stations are generally on a daily basis, a study that analyzes the distributions of daily environmental parameters over the length of day is necessary.

For the day length of each season, this study selected the 21st of March, June, September, and December. June 21 and December 21 have the longest and shortest days during the year while the days of March 21 and September 21 are representative days of the spring and the fall. Figure 5.1 shows the variations in sunrise and sunset times during the year and the day lengths calculated from the sunrise and sunset times. The longest day length of the year is 14.24 hours from 5:32 a.m. to 7:46 p.m. on June 21, and the

shortest day length is 9.76 hours from 7:43 a.m. to 5:28 p.m. on December 21 in Atlanta, Georgia. For March 21 and September 21 in Atlanta, Georgia, the lengths of the days are similar; 11.96 hours from 6:46 a.m. to 6:44 p.m. and 11.98 hours from 6:31 a.m. to 6:30 p.m., respectively. In addition, Figure 5.3 illustrates the variations in solar altitude at solar noon during the year in Atlanta, Georgia. The highest and lowest altitudes of the sun are 79.7° and 32.8° on June 21 and December 21, respectively. The solar noon altitude angles on March 21 and September 21 are approximately 56°.

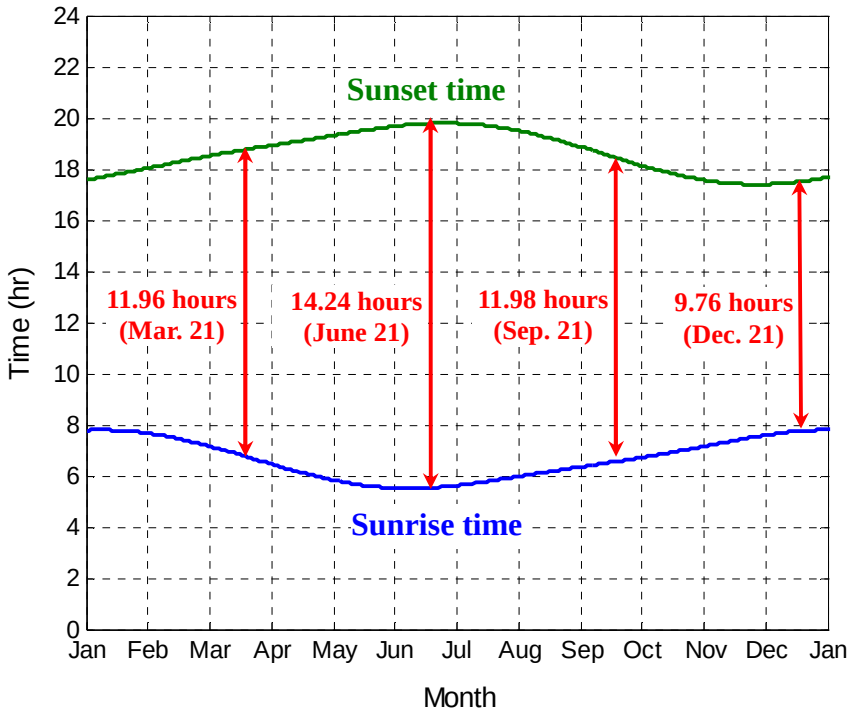

Figure 5.1: The variation in the length of day during the year in Atlanta, Georgia.

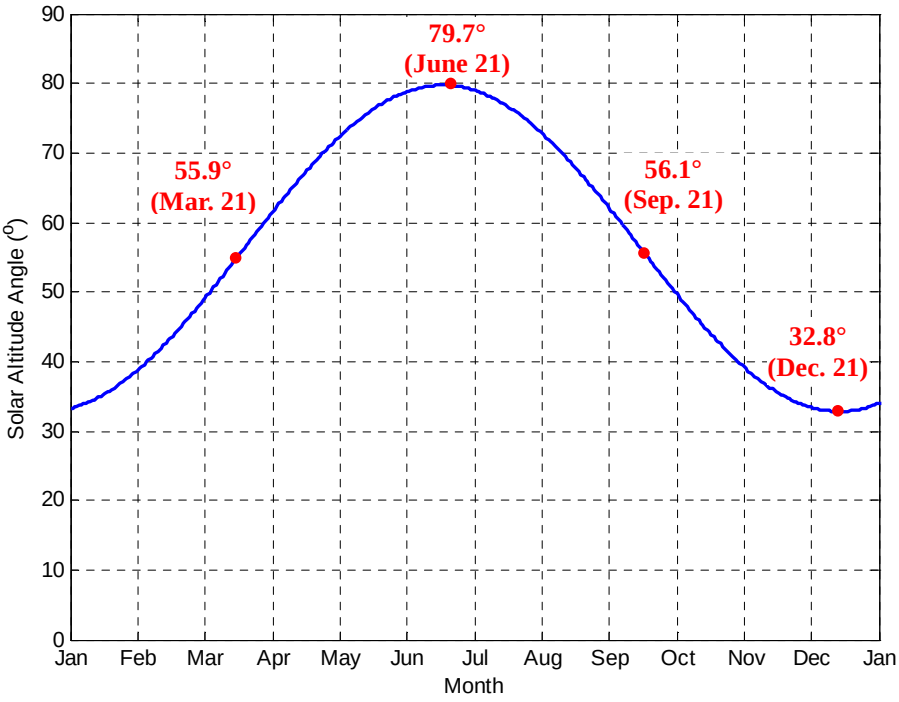

Figure 5.2: The variation in the solar altitude at solar noon during the year in Atlanta, Georgia.

5.3.1 Solar Radiation

For the variation in daily solar radiation with respect to the time of day, the Liu and Jordan (1960) and the Gloyne (1972) equations were evaluated. The Liu and Jordan (1960) equation calculates the temporal variation in solar radiation as a function of the solar hour angle for the period of sunrise to sunset:

$$I(t) = H\frac{\pi}{24}(a + b\cdot\cos w)\cdot\left(\frac{\cos w - \cos w_s}{\sin w_s - w_s\cos w_s}\right) \tag{5.1}$$

in which $I(t)$ = the solar radiation as a function of time t,

H = the daily total solar radiation,

w = the solar hour angle at a time of t,

w_s = the solar hour angle at sunrise,

$a = 0.4090 + 0.5016\sin(w_s - 1.047)$, and

$b = 0.6609 - 0.4767\sin(w_s - 1.047)$.

The Gloyne (1972) equation, a sinusoidal function based on the length of day, is expressed as

$$I(t) = \frac{2H}{T}\sin^2\left(\frac{\pi t}{T}\right) \tag{5.2}$$

in which $I(t)$ = the solar radiation as a function of time *t*, and

T = the daily length in hours.

To evaluate the effectiveness of the two equations on the variation in daily solar radiation over the length of a day, this study compared the predicted solar radiation with the measurements on a horizontal surface for June 1, October 1, and November 15, 2009, on which the largest vertical and transverse temperature differentials were measured. Figure 5.3 shows the solar radiation on a horizontal surface measured every five minutes and the predicted hourly solar radiation using the two equations for the three days noted above. According to Figure 5.3, the Liu and Jordan (1960) equation provides a better correlation with the measurements while the Gloyne (1972) equation exhibits a little time lag, or time shift. Thus, the Liu and Jordan (1960) equation was used for the prediction of variations in solar radiation incident on the horizontal surface of prestressed concrete bridge girders over time.

Furthermore, the measurements of solar radiation incident on the vertical surface were compared with those of the predictions using the Liu and Jordan (1960) equation. The solar radiation incident on the horizontal and vertical surfaces was measured at five-minute intervals. The prediction of solar radiation incident on the vertical surface was

based on the location and geometry of the girder, the position of the sun, and the horizontal solar radiation obtained from the Liu and Jordan (1960) equation. Figure 5.4 shows the predicted and measured solar radiation on the vertical surface for June 1, October 1, and November 15, 2009. The hourly vertical solar radiation predicted using the horizontal solar radiation obtained from the Liu and Jordan (1960) equation also matches well with the measurements for the three days. These results show that the Liu and Jordan (1960) equation can effectively predict variations in solar radiation on the horizontal and inclined surfaces of the bridge girders from given daily solar radiation under clear sky conditions.

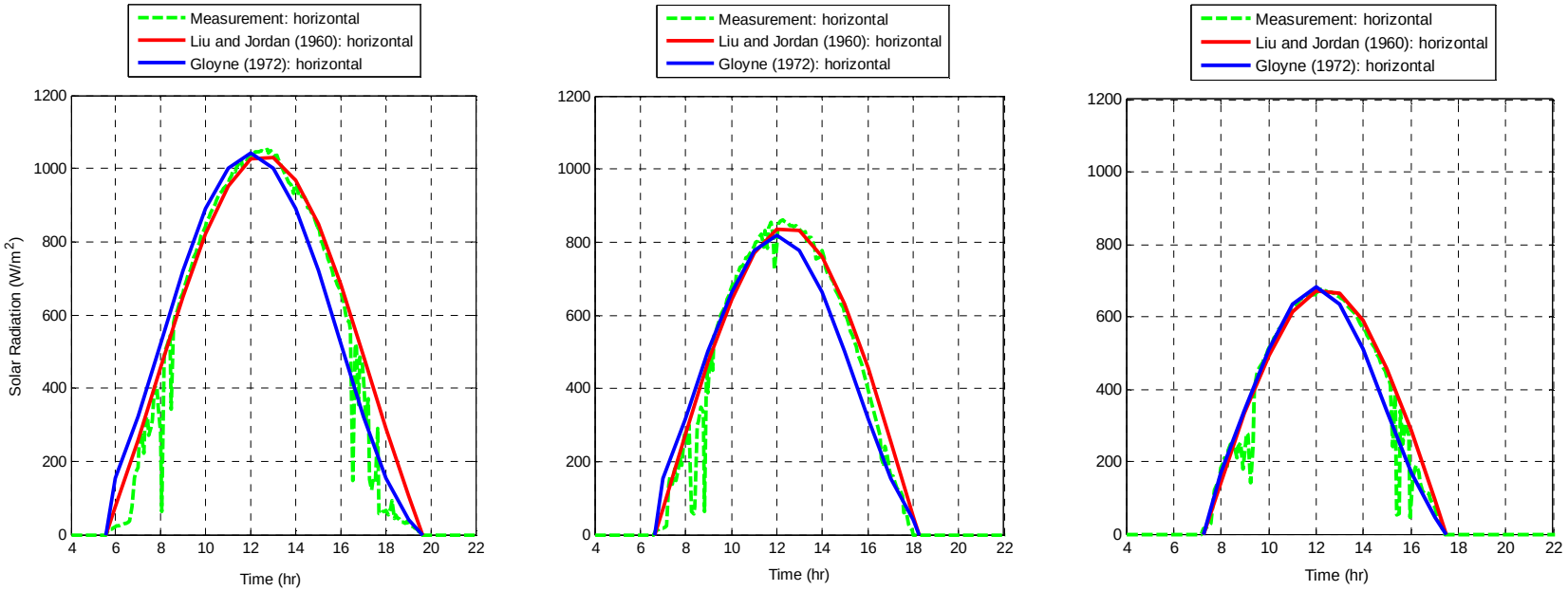

(a) June 1 (b) October 1 (c) November 15

Figure 5.3: Comparison of the solar radiation measured on a horizontal surface every five minutes and the predicted hourly solar radiation for June 1, October 1, and November 15, 2009.

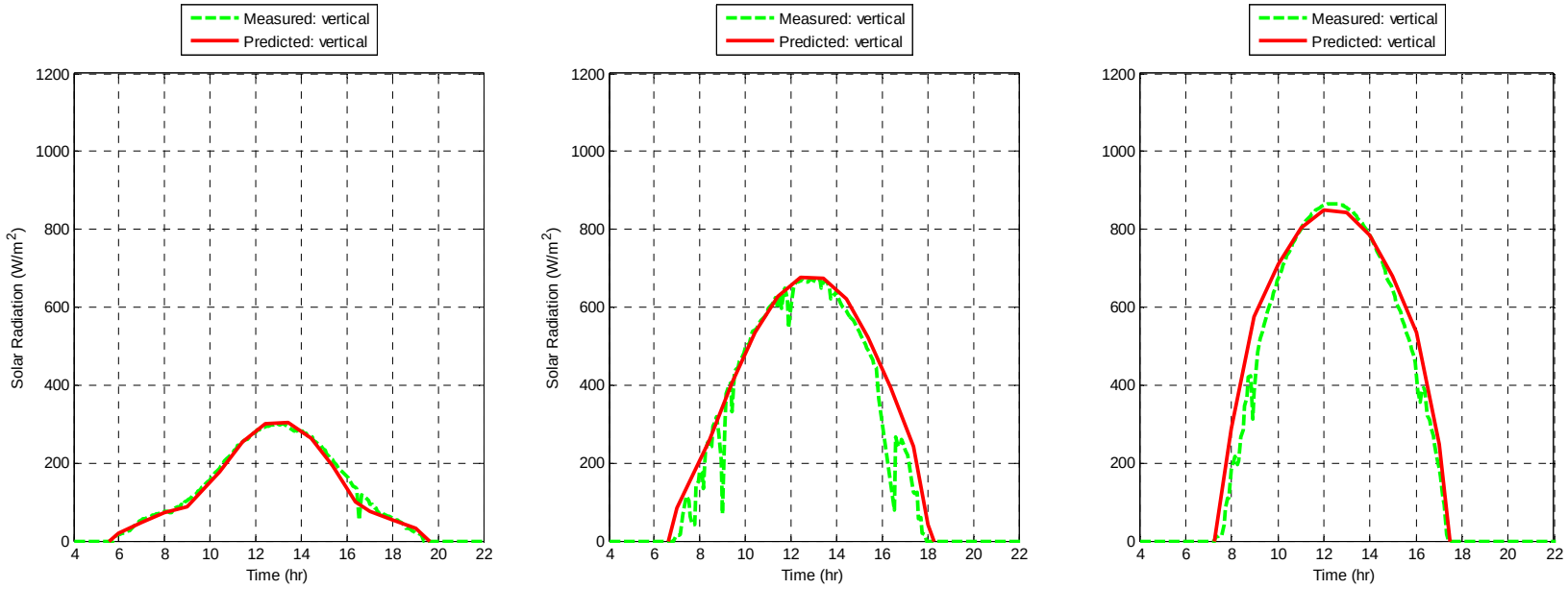

(a) June 1 (b) October 1 (c) November 15

Figure 5.4: Comparison of the solar radiation measured on a vertical surface every five minutes and the predicted hourly solar radiation for June 1, October 1, and November 15, 2009.

5.3.2 Air Temperature

In addition to solar radiation, the air temperature also affects the variation in the temperature distributions of bridge girders. Thus, to determine the variation in air temperature with respect to the time of day, this study evaluated the commonly-used Kreith and Kreider (1978) and the Agullo et al. (1996) equations. The Kreith and Kreider (1978) equation is expressed as a sinusoidal equation:

$$T_{air}(t) = \frac{1}{2}(T_{\max} + T_{\min}) + \frac{1}{2}(T_{\max} - T_{\min}) \cdot \sin\left[(t-9)\frac{\pi}{12}\right] \tag{5.3}$$

in which $T_{air}(t)$ = the air temperature as a function of time t,

$T_{\max}$ = the daily maximum air temperature, and

$T_{\min}$ = the daily minimum air temperature.

The Agullo et al. (1996) suggested a bi-sinusoidal equation based on the magnitudes of the daily minimum and maximum temperatures, $T_{\min}$ and $T_{\max}$, respectively, and the occurrence times of the daily minimum and maximum temperatures, $h_{\min}$ and $h_{\max}$, respectively:

$$T_{air}(t) = \begin{cases} \frac{1}{2}(T_{\max} + T_{\min}) + \frac{1}{2}(T_{\max} - T_{\min}) \cdot \sin\left[2\pi\frac{t-b_1}{2b_2}\right] & , \quad T_{\min} \le t \le T_{\max} \\ \frac{1}{2}(T_{\max} + T_{\min}) + \frac{1}{2}(T_{\max} - T_{\min}) \cdot \sin\left[2\pi\frac{t+12-b_1-b_2}{2(24-b_2)}\right] & , \quad \text{otherwise} \end{cases} \tag{5.4}$$

in which $b_1 = (h_{\max} + h_{\min}) / 2$, and $b_2 = h_{\max} - h_{\min}$.

Variations in air temperature predicted by the two equations were compared with those measured on June 1, October 1, and November 15, 2005. On June 1 and November 15, the largest vertical and transverse temperature differentials were measured. For the evaluation of these equations in the spring and fall conditions, this study also included October 1, when seasonally large vertical and transverse temperature differentials were observed. Figure 5.5 shows the variations in air temperature predicted hourly from the Kreith and Kreider (1978) and the Agullo et al. (1996) equations and the measured data for the three days. The daily maximum and minimum temperatures and the occurrence times of those temperatures employed in the models to predict variations in air temperature were taken from the measurements.

According to Figure 5.5, the Kreith & Kreider (1978) equation provides somewhat better correlations with the measurements on June 1 and October 1 while the Agullo et al. (1996) equation provides better agreement with the measurements on November 15. This difference might be attributed to the variability in air temperature such as the magnitude of daily temperature variance, the occurrence times of daily maximum and minimum temperatures, and instant changes in the weather condition. In this study, the Kreith & Kreider (1978) equation was selected for the variations in air temperature with respect to the time of day because the temperature variations predicted from the Kreith & Kreider (1978) equation showed higher temperatures during the morning. In addition, the Kreith & Kreider (1978) equation can predict temperature variations simply from daily maximum and minimum air temperatures while the Agullo et al. (1996) equation requires both the magnitudes and the times of daily minimum and maximum temperatures.

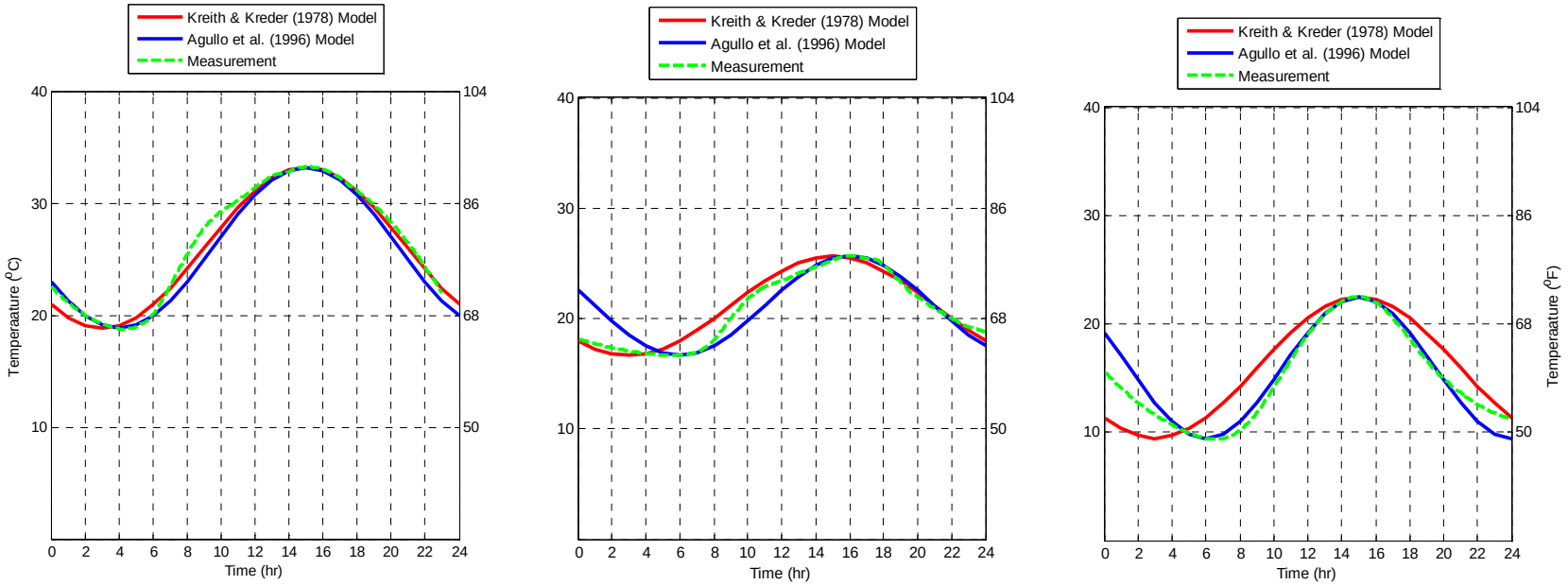

(a) June 1 (b) October 1 (c) November 15

Figure 5.5: Comparison of the air temperature measured every five minutes and the predicted hourly air temperature for June 1, October 1, and November 15, 2009.

5.4 Extreme Seasonal Girder Temperature Variations

With the determined extremes in seasonal environmental conditions in Atlanta, Georgia, this section investigated seasonal extremes in vertical and transverse temperature distributions and differentials in AASHTO-PCI standard girder sections using the 2D heat transfer analysis presented in Chapter 3. Four AASHTO-PCI sections were selected to evaluate the variations in temperature on the AASHTO-PCI sections.

5.4.1 Finite Element Transient Heat Transfer Analysis

The AASHTO-PCI standard girder sections are composed of six I-beams and three bulb-tees. According to the relative lengths of the top and bottom flanges, the six I-beams are also divided into four I-beams having smaller top flanges and two I-beams having wider top flanges. The length of the top flange of the three bulb-tees is longer than that of the bottom flange. Based on the shapes and sizes of the AASHTO-PCI sections, this study selected the smallest and largest sections, Type-I and Type-IV sections, respectively, among the four I-beams with smaller top flanges. For the sections with wider top flanges, the BT-63 section, which is the median of the depths of the three bulb-tee sections, and the Type-V section, which is the same depth of 63 inches, were selected. The thickness of the Type-V section is thicker than that of the BT-63 section. Figure 5.6 shows the cross-sections of the four selected AASHTO-PCI standard girder sections.

The finite element meshes of these four sections for heat transfer analyses are illustrated in Figure 5.7. The size of the element was determined to be approximately one inch long according to a temperature conversion test. Thus, Type-I section was modeled with 342 elements and 266 nodes, Type-IV section with 696 elements and 780 nodes, Type-V section with 880 elements and 990 nodes, and BT-63 section with 584 elements and 699 nodes. All the models used the four-node DC2D heat transfer element in

ABAQUS. The orientation of the bridge sections was assumed to be the east-west direction, in which maximum transverse temperature differentials would occur.

The thermal material properties of concrete used in these heat transfer analyses were taken as the same values used in Chapter 3. That is, the thermal conductivity of concrete is 1.5 W/m·K, and the specific heat of concrete is 1,000 J/kg·K. The values of the solar absorptivity and the surface emissivity of concrete are 0.50 and 0.85, respectively. The heat transfer boundary conditions involved in this study, such as heat irradiation from the sun and heat radiation from the concrete surface, were described in detail in Chapter 3. The heat transfer analyses started at 12 a.m. with a constant temperature distribution over the cross-section. The constant initial temperature was taken as the air temperature at 12 a.m. calculated from daily maximum and minimum temperatures using Equation (5.3). Then, this study evaluated seasonal variations in vertical and transverse temperature distributions in the four AASHTO-PCI sections. As shown in Figure 5.7, the vertical temperature distributions were defined at selected nodes along the A-A line and transverse temperature distributions along B-B, C-C, and D-D lines for the top flange, the web, and the bottom flange, respectively.

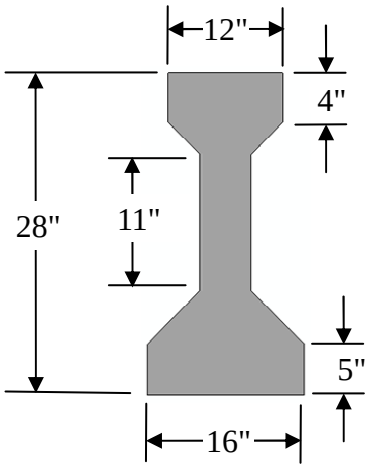

(a) Type-I section

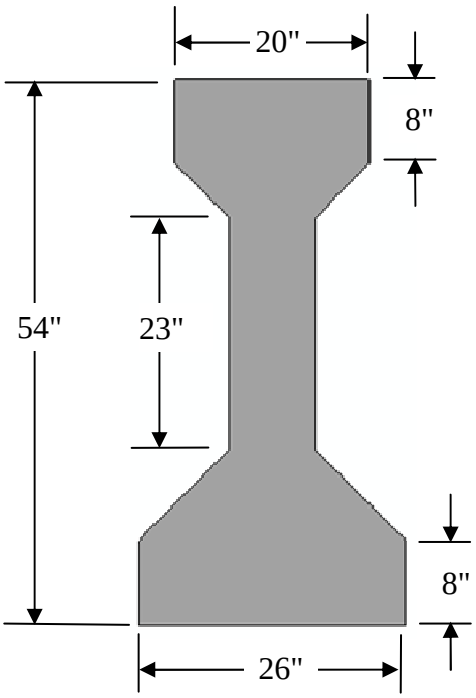

(b) Type-IV section

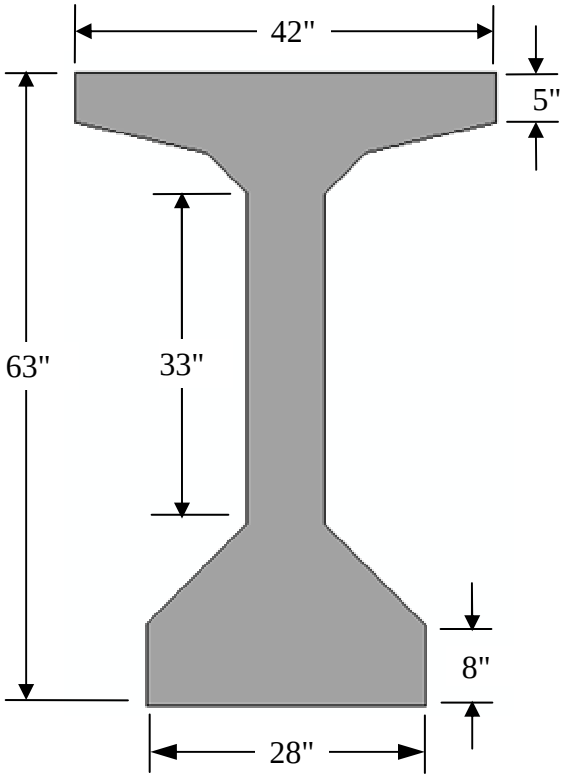

(c) Type-V section

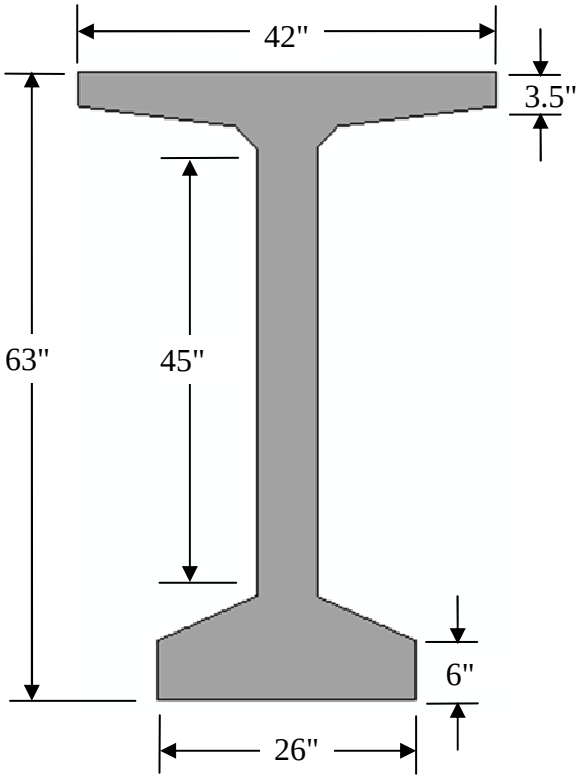

(d) BT-63 section

Figure 5.6: The cross-sections of the AASHTO-PCI standard girder sections.

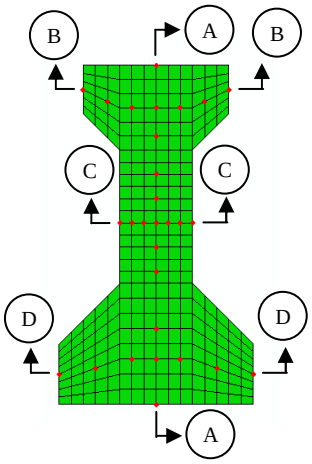

(a) Type-I section

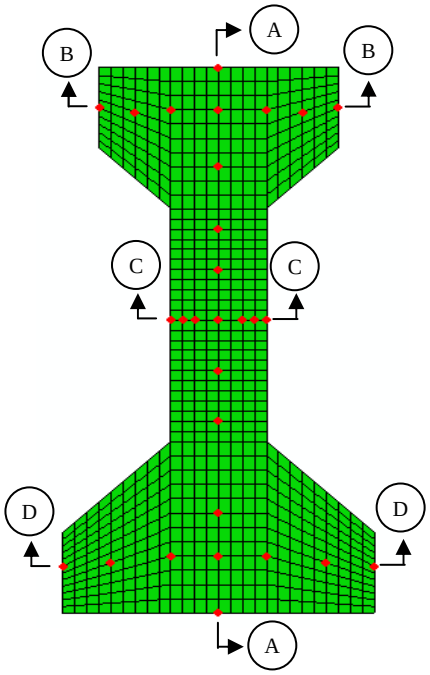

(b) Type-IV section

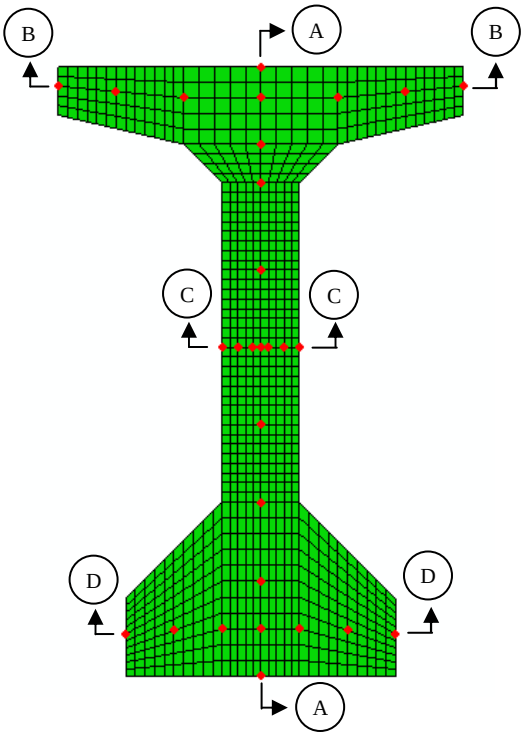

(c) Type-V section

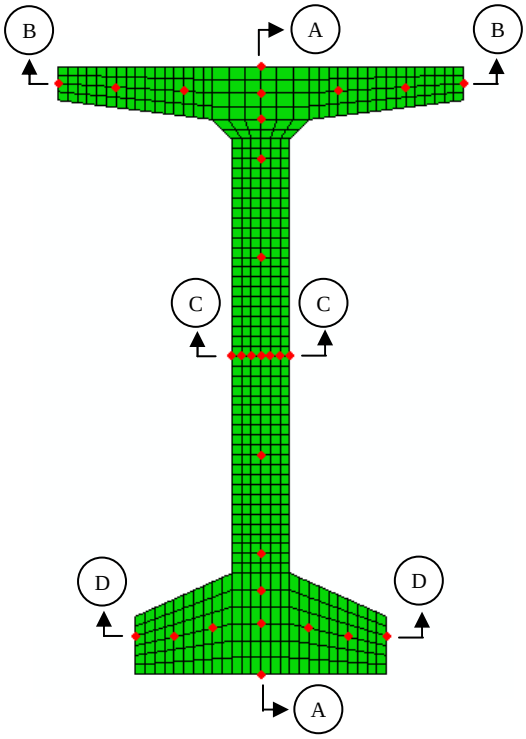

(d) BT-63 section

Figure 5.7: The finite element meshes for the heat transfer analyses and the selected nodes for the vertical and transverse temperature distributions.

5.4.2 Time Interval and Period of the Heat Transfer Analysis

To determine a proper time interval in the heat transfer analysis, this study investigated temperature variations in a BT-63 section for 5-, 15-, 30-, and 60-minute intervals. Environmental conditions involved in this study are extreme summer conditions in Atlanta, Georgia. Daily solar radiation is 29.4 MJ/m^2, and daily maximum and minimum temperatures defined as record daily maximum and average daily minimum temperatures from the NCDC are 38.3°C (100.9°F) and 19.0°C (66.2°F). The 2D heat transfer analyses were performed for a consecutive three-day period, and the influence of time intervals and time periods on temperature variations in the prestressed concrete girder was evaluated.

Figures 5.8 to 5.10 show the temperature variations obtained from the heat transfer analyses of the 5- and 60-minute intervals on the top surface of the top flange, in the middle of the web, and on the bottom surface of the bottom flange, respectively. These figures indicate that heat transfer analysis at the 60-minute interval accurately represents the temperature variations of the prestressed concrete girder. In addition, since concrete with a low value of thermal conductivity responds late to changes in environmental conditions, the study analyzes the time period of heat transfer. Figure 5.11 presents the highest girder temperatures on the top surface, in the web, and on the bottom surface of the BT-63 girder at each analysis period from the heat transfer analysis of the 5-minute interval. All the temperatures exhibit slightly low values on the first day but show approximately the same temperatures on the second and third days. Thus, the 2D heat transfer analysis will be performed hourly for consecutive two days, and the girder temperatures will be determined from the second day result.

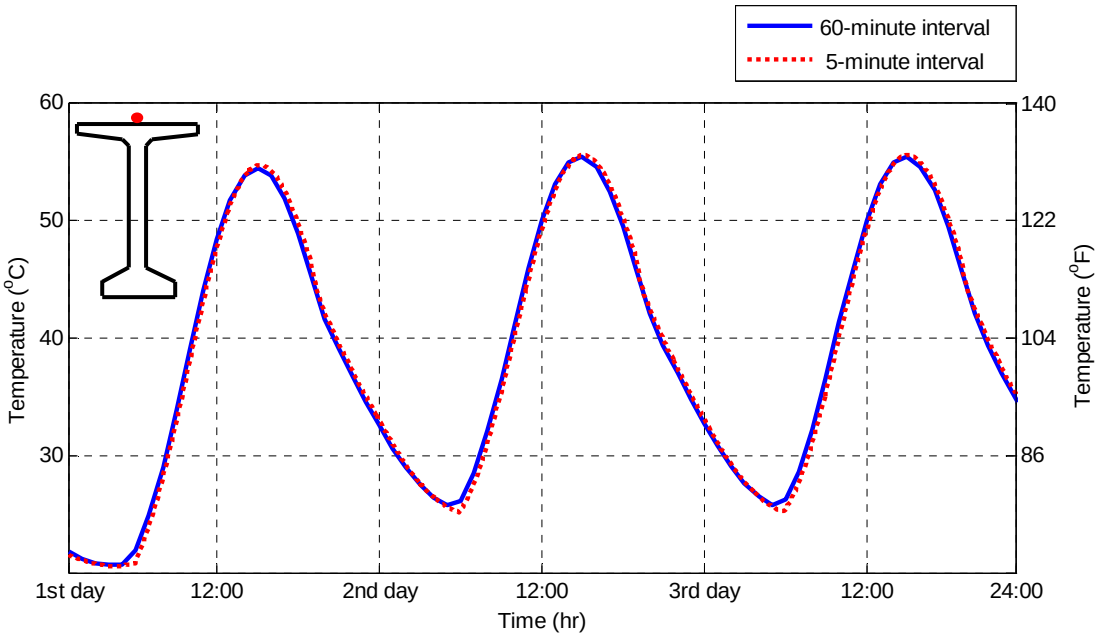

Figure 5.8: Temperature variations on the top surface of the BT-63 girder obtained from the heat transfer analysis using 5- and 60-minute intervals.

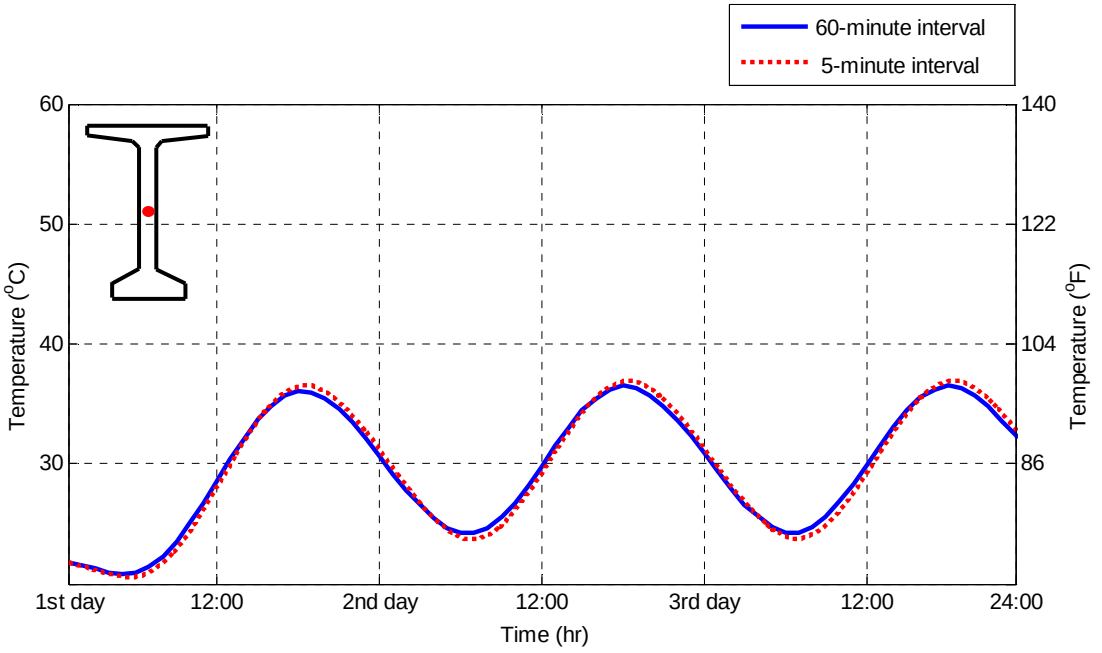

Figure 5.9: Temperature variations in the middle of the BT-63 girder web obtained from the heat transfer analysis using 5- and 60-minute intervals.

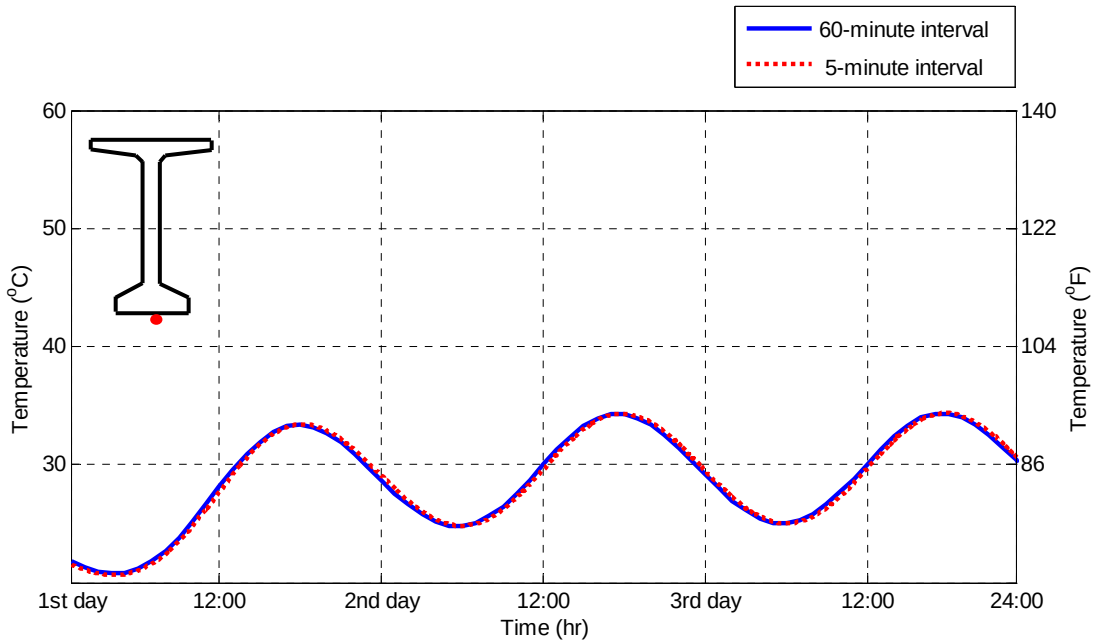

Figure 5.10: Temperature variations on the bottom surface of the BT-63 girder obtained from the heat transfer analysis using 5- and 60-minute intervals.

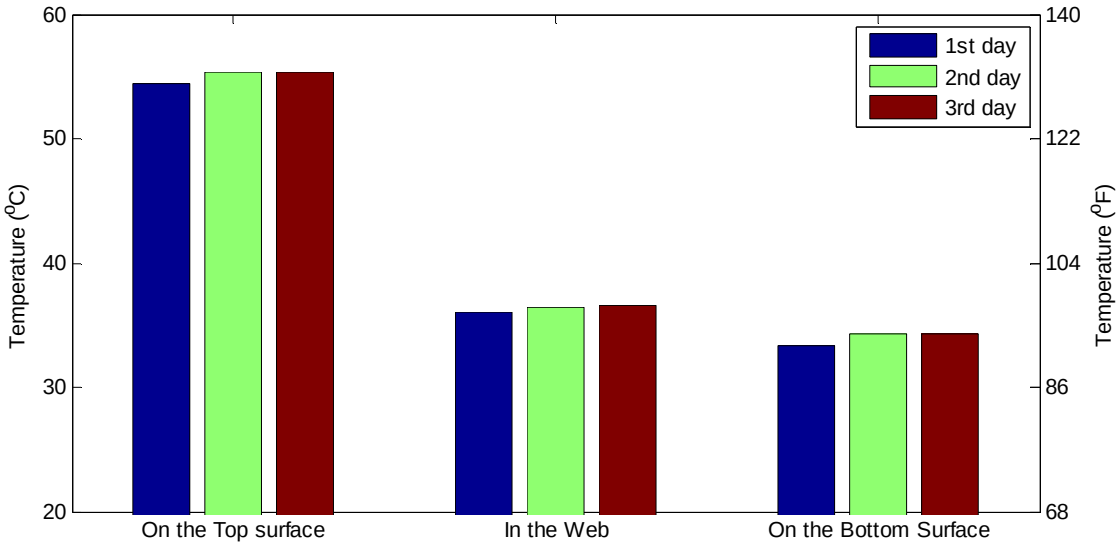

Figure 5.11: The highest temperatures on the top surface, in the middle of the web, and on the bottom surface of the BT-63 girder at each analysis period from the heat transfer analysis using the 60-minute interval.

5.4.3 Seasonal Temperature Differentials

With seasonal changes in environmental conditions, the cross-sections of the prestressed concrete girders experience variations in vertical and transverse temperature differentials. Thus, this study examined the seasonal vertical and transverse temperature changes from the difference between the highest and lowest temperatures in the four selected AASHTO-PCI sections; Type-I, Type-IV, Type-V, and BT-63 sections. Vertical temperatures were studied along the depth of the section (A-A line), and transverse temperatures were studied across the top flange (B-B line), the web (C-C line), and the bottom flange (D-D line).

The highest temperature along the depth of the section, A-A line, was recorded on the top surface of the top flange, and the lowest temperature was recorded in the middle of the bottom flange. For the transverse temperature differentials along the B-B, C-C, and D-D lines, the highest temperatures were recorded on the south end surfaces, and the lowest temperatures were recorded in the middle or northern side of the top flange, the web, and the bottom flange. Tables 5.3 and 5.4 summarize the seasonal largest vertical and transverse temperature differentials in the four sections in Atlanta, Georgia, respectively.

According to Table 5.3, the maximum vertical temperature differentials were 21.8°C (39.3°F) to 26.7°C (48.0°F) in the summer, and the minimum vertical temperature differentials were 11.6°C (20.9°F) to 14.4°C (26.0°F) in the winter. The fall and spring were in the range of 17.8°C (32.1°F) to 21.6°C (38.9°F). Among the four AASHTO-PCI sections in the summer, Type-V section showed the maximum differential of 26.7°C (48.0°F), Type-IV and BT-63 sections 24.6°C (44.3°F) and 24.5°C (44.1°F), respectively, and Type-I section the minimum differential of 21.8°C (39.3°F). Thus, the deeper Type-IV, Type-V and BT-63 sections exhibited larger vertical temperature differentials.

Table 5.4 shows the largest transverse temperature differentials in the top flange, the web, and the bottom flange of the four AASHTO-PCI sections for four seasons. The

transverse temperature differentials were the maximum in the winter and the minimum in the summer. The maximum transverse temperature differentials of the four sections, which occurred in the winter, were 16.6°C (29.9°F) to 20.1°C (36.1°F) in the top flange, 13.3°C (23.9°F) to 16.4°C (29.4°F) in the web, and 21.5°C (38.7°F) to 25.6°C (46.1°F) in the bottom flange. The spring and the fall showed transitions in the transverse temperature differentials from the maximum in the winter to the minimum in the summer. The influence of the shadow on the transverse temperature differentials in the web was also shown in the fall and the spring. While the transverse differentials of Type-I and Type-IV sections in the web were 10.4°C (18.7°F) to 12.6°C (22.7°F), those of Type-V and BT-63 sections were 3.7°C (6.6°F) and 5.7°C (10.3°F) because of the shadow on the web from the long top flange. As a result, the transverse temperature differentials were larger in the wider Type-IV, Type-V, and BT-63 sections.

In addition, Figure 5.12 shows hourly temperature variations in the Type-V section, which showed the maximum vertical temperature differentials among the four AASHTO-PCI sections in Atlanta, Georgia. As mentioned earlier, the highest and lowest temperatures along the depth of the section were recorded on the top surface, denoted as “A” Figure 5.12, and in the bottom flange, denoted as “B” in Figure 5.12, respectively. The seasonal largest vertical temperature differentials of 26.7°C (48.0°F) in the summer, 21.6°C (38.9°F) in the spring, 20.6°C (37.1°F) in the fall, and 14.3°C (25.8°F) in the winter occurred at 2:00 p.m.

Since the maximum transverse temperature differentials were found in the BT-63 section, the hourly variations in transverse temperatures in the top flange, the web, and the bottom flange of the BT-63 section are presented in Figures 5.13 and 5.15, respectively. The “A” and “B”, denoted in Figures 5.13 and 5.15, represent the locations of the highest and lowest temperatures in each transverse temperature variation, respectively. That is, the highest temperatures were observed on the south vertical surfaces of the top flange, the web, and the bottom flange, and the lowest temperatures

were observed in the middle of the top flange and inside the northern side of the web and the bottom flange. The transverse temperature differentials were the maximum in the winter and the minimum in the summer. Because of the shadow of the top flange on the web in the fall and the spring, Figure 5.14(a) and (c) show very small transverse temperature differentials in the web. The occurrence times of the seasonal largest transverse temperature differentials were 1:00 p.m. in the top flange and the web and 2:00 p.m. in the bottom flange.

Table 5.3: Seasonal largest vertical temperature differentials along the depth (A-A) of the four AASHTO-PCI standard girder sections.

AASHTO-PCI Standard Sections	Vertical Temperature Differentials, °C (°F)			
	Spring	Summer	Fall	Winter
Type-I	18.6 (33.6)	21.8 (39.3)	17.8 (32.1)	12.2 (22.0)
Type-IV	21.4 (38.5)	24.6 (44.3)	20.3 (36.6)	14.4 (26.0)
Type-V	21.6 (38.9)	26.7 (48.0)	20.6 (37.1)	14.3 (25.8)
BT-63	19.2 (34.6)	24.5 (44.1)	18.9 (34.1)	11.6 (20.9)

Table 5.4: Seasonal largest transverse temperature differentials in the top flange (B-B), in the web (C-C), and the bottom flange (D-D) of the four AASHTO-PCI standard girder sections.

AASHTO-PCI Standard Sections		Transverse Temperature Differentials, °C (°F)			
		Spring	Summer	Fall	Winter
Type-I	B-B	14.0 (25.2)	8.6 (15.5)	13.2 (23.8)	16.6 (29.9)
	C-C	10.6 (19.0)	3.8 (6.8)	10.4 (18.7)	13.3 (23.9)
	D-D	18.9 (34.0)	12.5 (22.5)	18.2 (32.8)	21.5 (38.7)
Type-IV	B-B	14.4 (25.9)	7.3 (13.2)	13.8 (24.8)	18.9 (34.1)
	C-C	12.6 (22.7)	4.7 (8.5)	12.3 (22.2)	15.8 (28.4)
	D-D	21.3 (38.4)	13.8 (24.8)	20.3 (36.5)	24.6 (44.4)
Type-V	B-B	15.9 (28.6)	8.8 (15.8)	14.7 (26.4)	20.1 (36.1)
	C-C	5.7 (10.3)	5.0 (9.0)	5.2 (9.3)	16.4 (29.4)
	D-D	21.2 (38.2)	12.0 (21.6)	20.2 (36.4)	24.6 (44.2)
BT-63	B-B	16.0 (28.8)	9.0 (16.3)	14.7 (26.5)	19.6 (35.3)
	C-C	4.0 (7.2)	3.8 (6.9)	3.7 (6.6)	13.3 (23.9)
	D-D	23.7 (42.7)	12.0 (21.7)	22.7 (40.9)	25.6 (46.1)

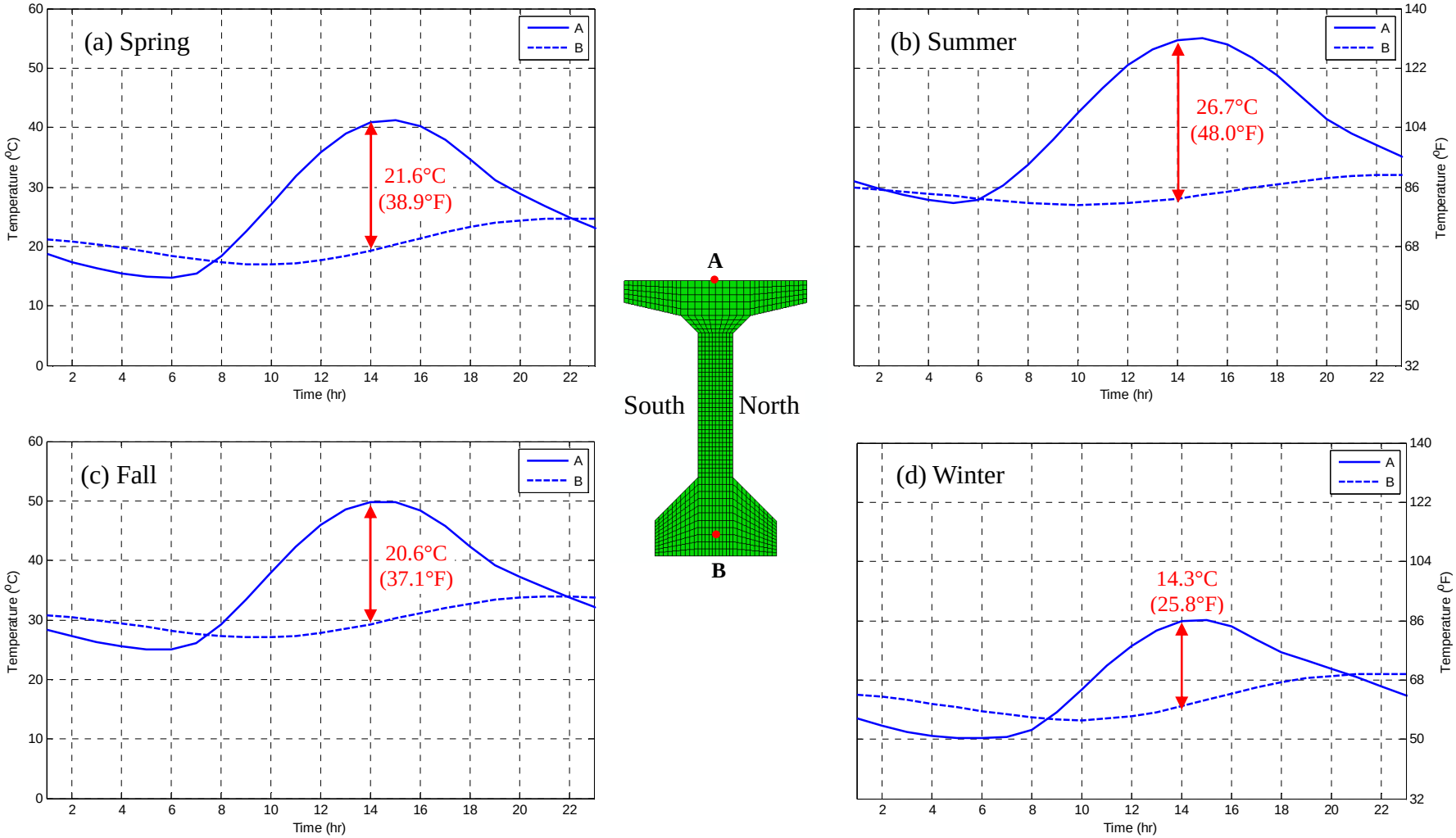

Figure 5.12: Vertical temperature variations along the depth of Type-V section for four seasons in Atlanta, Georgia.

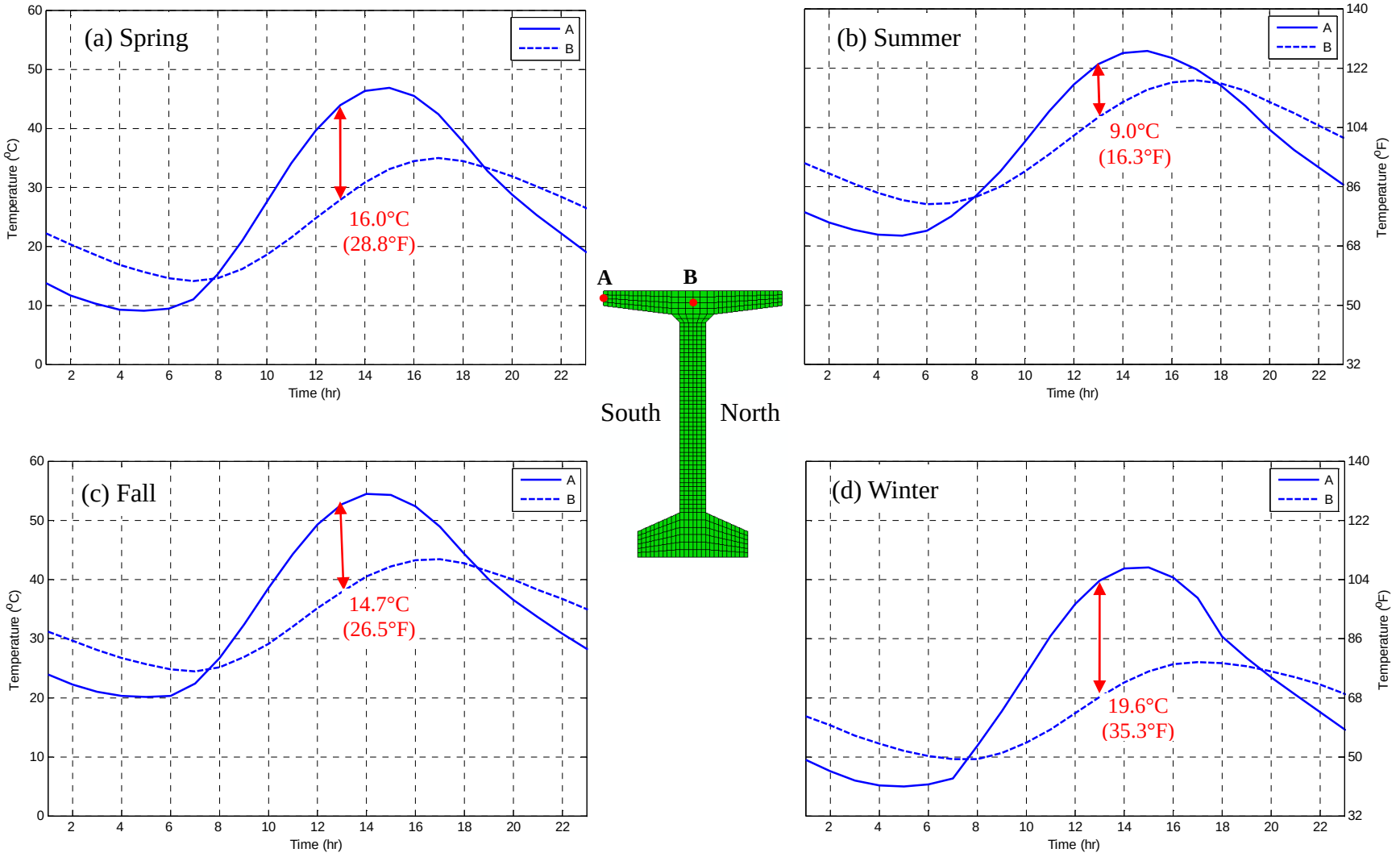

Figure 5.13: Transverse temperature variations in the top flange of BT-63 section for four seasons in Atlanta, Georgia.

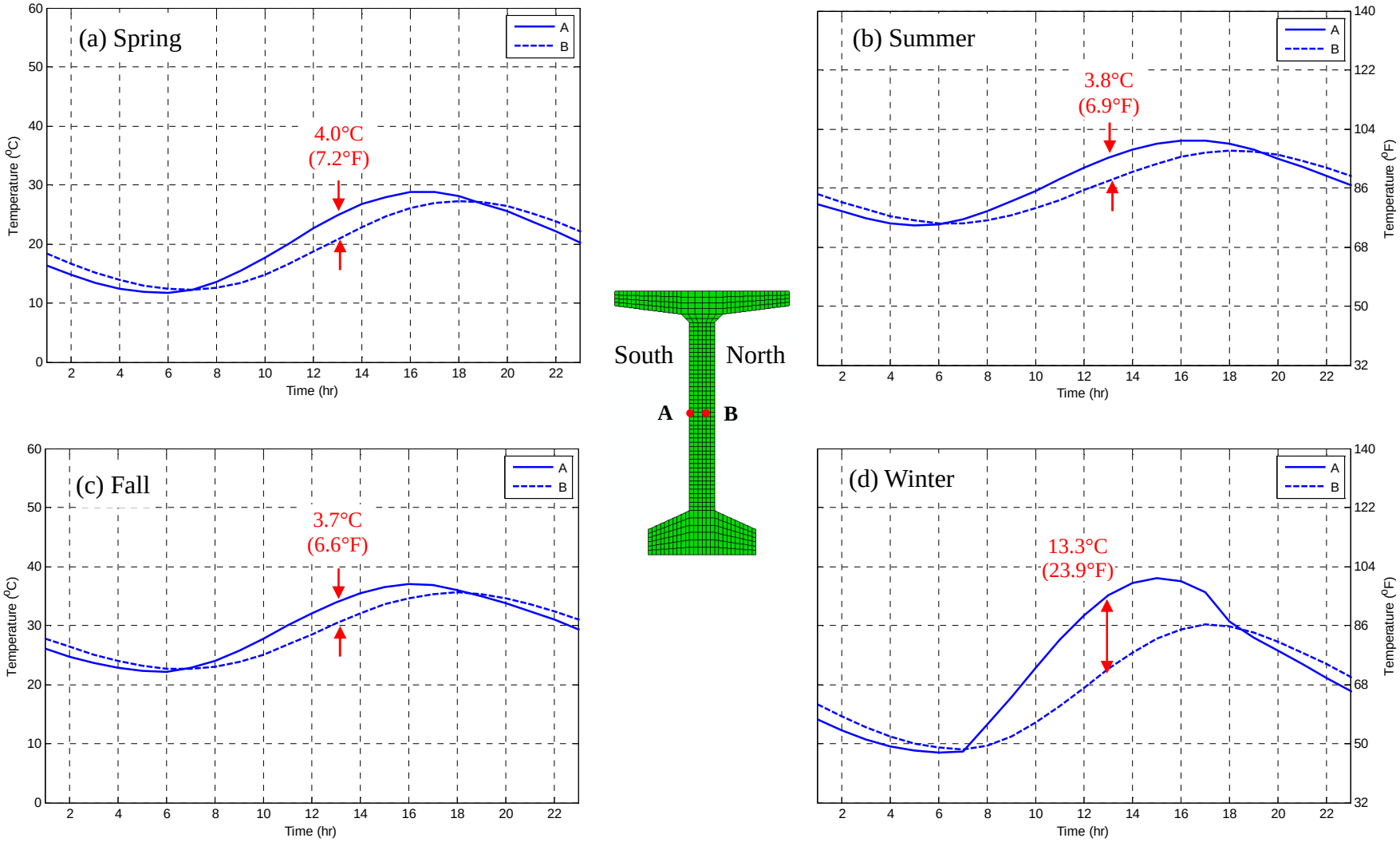

Figure 5.14: Transverse temperature variations in the web of BT-63 section for four seasons in Atlanta, Georgia.

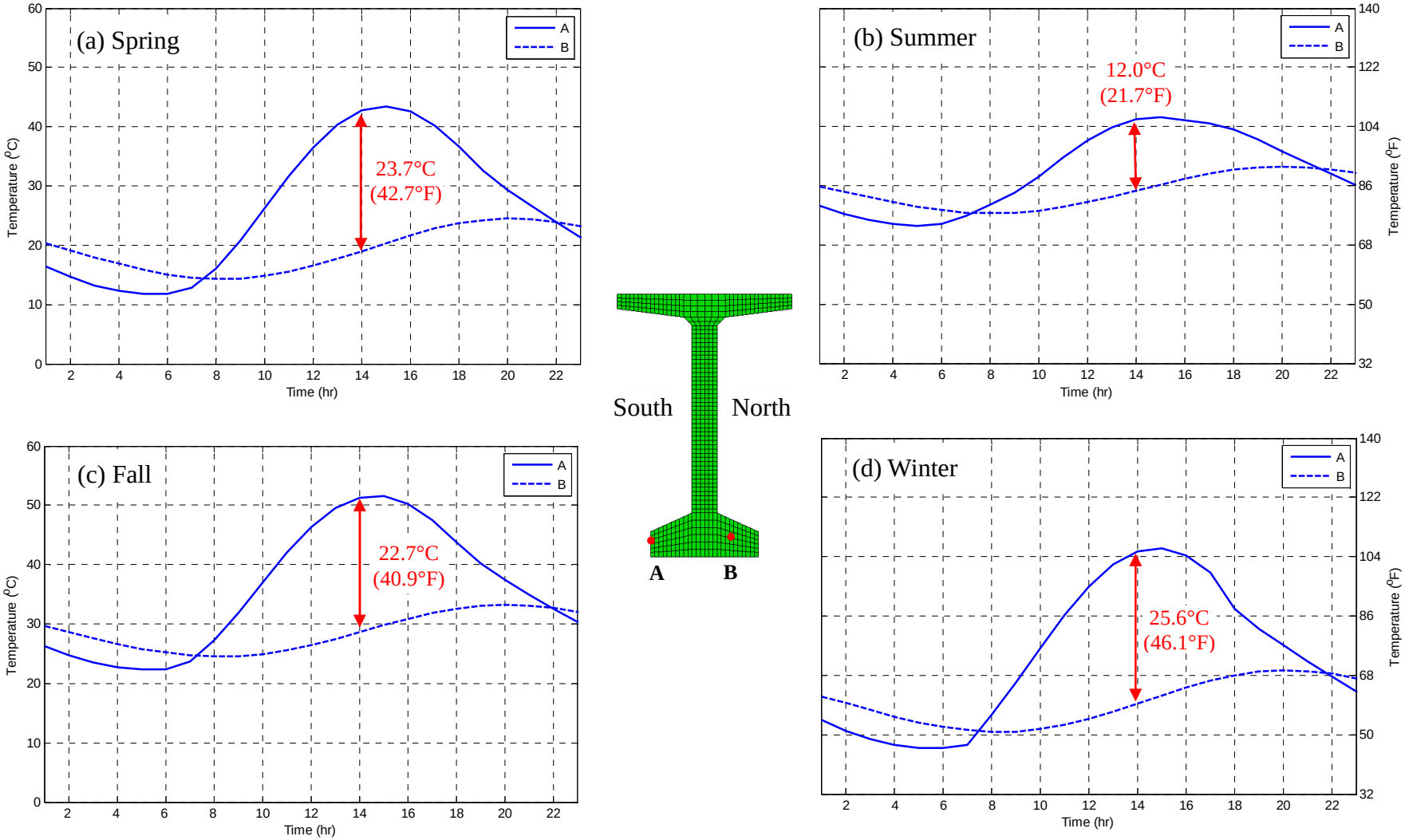

Figure 5.15: Transverse temperature variations in the bottom flange of BT-63 section for four seasons in Atlanta, Georgia.

5.4.4 Seasonal Vertical Temperature Distributions

Based on seasonal largest vertical temperature differentials in Atlanta, Georgia, this study evaluated seasonal maximum vertical temperature distributions along the A-A line for Type-I, Type-IV, Type-V, and BT-63 sections. Figures 5.16 to 5.19 show the seasonal vertical temperature distributions of the four AASHTO-PCI sections. As expected, the magnitudes of the temperatures were the highest in the summer and decreased with decreases in solar radiation and air temperature from the summer to the winter. In the fall, spring, and winter, the vertical temperature distributions showed relatively higher increases in the web due to high solar radiation on the vertical surface. However, for the Type-V and BT-63 sections having wider top flanges, Figures 5.18 and 5.19 exhibit no temperature increases in the top of the web in the fall and the spring because of the shadow on the web from the top flange. The shapes of the seasonal vertical temperature distributions were similar with no specific differences between the four AASHTO-PCI sections.

Figures 5.20 and 5.21 show the seasonal maximum vertical temperature gradients obtained by subtracting the lowest temperature from the maximum vertical temperature distributions for the Type-I and BT-63 sections, respectively. The Type-I section, the smallest section in the AASHTO-PCI sections, showed the minimum vertical temperature differential, and the BT-63 section showed the maximum vertical temperature differential. The vertical temperature gradients obtained from the current study were compared with those given in the AASHTO specifications (AASHTO, 1989 & 2007), which were obtained from solar heating only on the top surface of the bridge deck based on average daily solar radiation for the months of June and July. Therefore, the shapes of the vertical temperature gradients in the summer were similar to those of the AASHTO specifications. The vertical temperature differentials in the summer also agreed well with those of the AASHTO specifications for the small Type-I section. However, for the

deeper BT-63 section, the vertical temperature differentials given in the AASHTO specifications were somewhat smaller. For the other seasons, the vertical temperature gradients of the Type-I and BT-63 sections were different from those of the AASHTO specifications. In the winter, because of the lowest altitude of the sun, or the highest intensity of solar radiation on the vertical surface, largest vertical temperature gradients in the web were found. The fall and the spring with the same solar altitude show very similar vertical temperature gradients, which represent a transition from the summer to the winter or from the winter to the summer. In addition, the influence of the shadow on the vertical temperature gradient in the web was observed in the BT-63 section as shown in Figure 5.21(b).

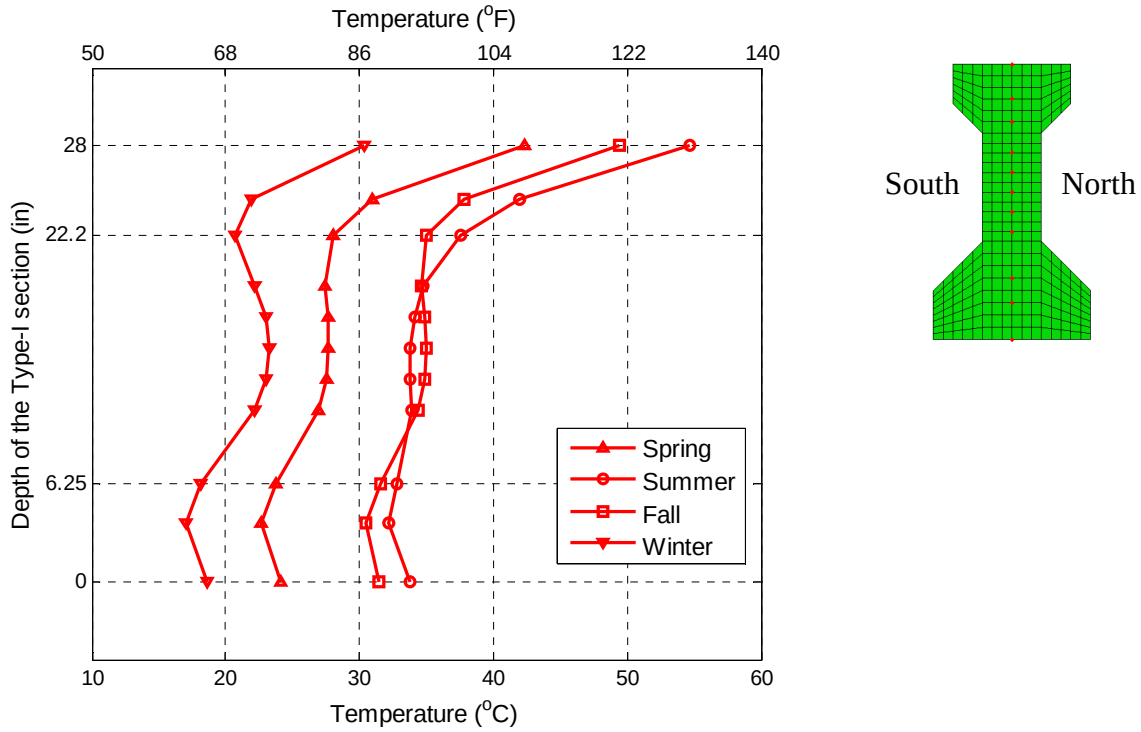

Figure 5.16: The seasonal maximum vertical temperature distributions of Type-I section.

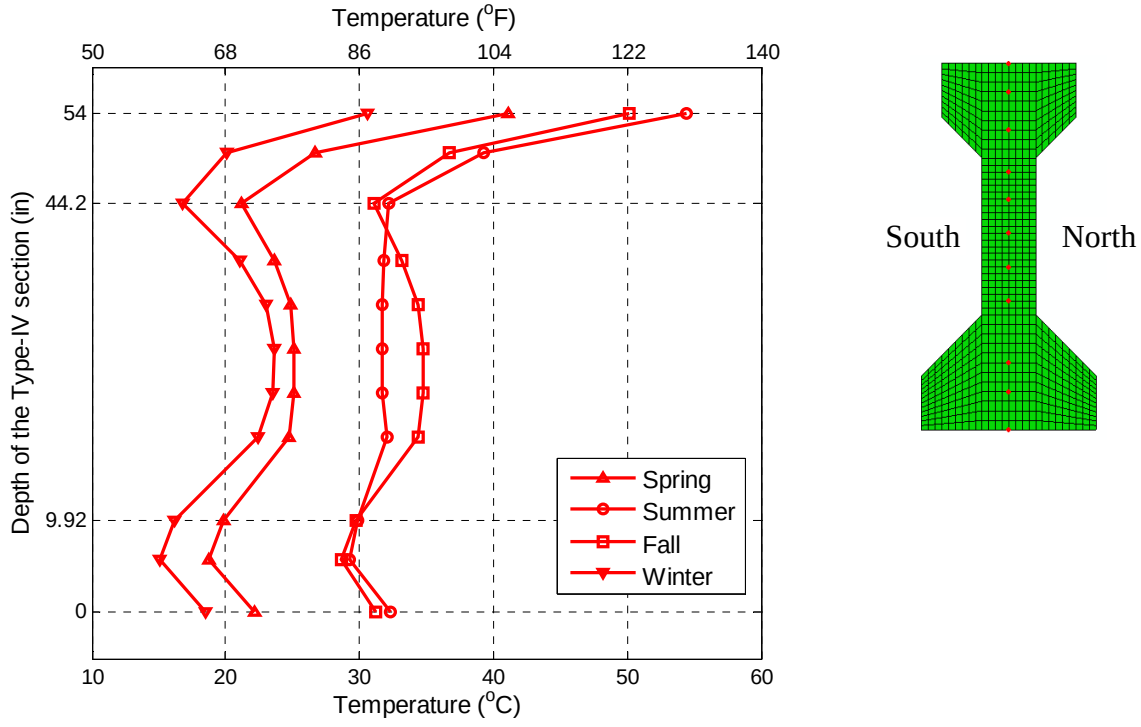

Figure 5.17: The seasonal maximum vertical temperature distributions of Type-IV section.

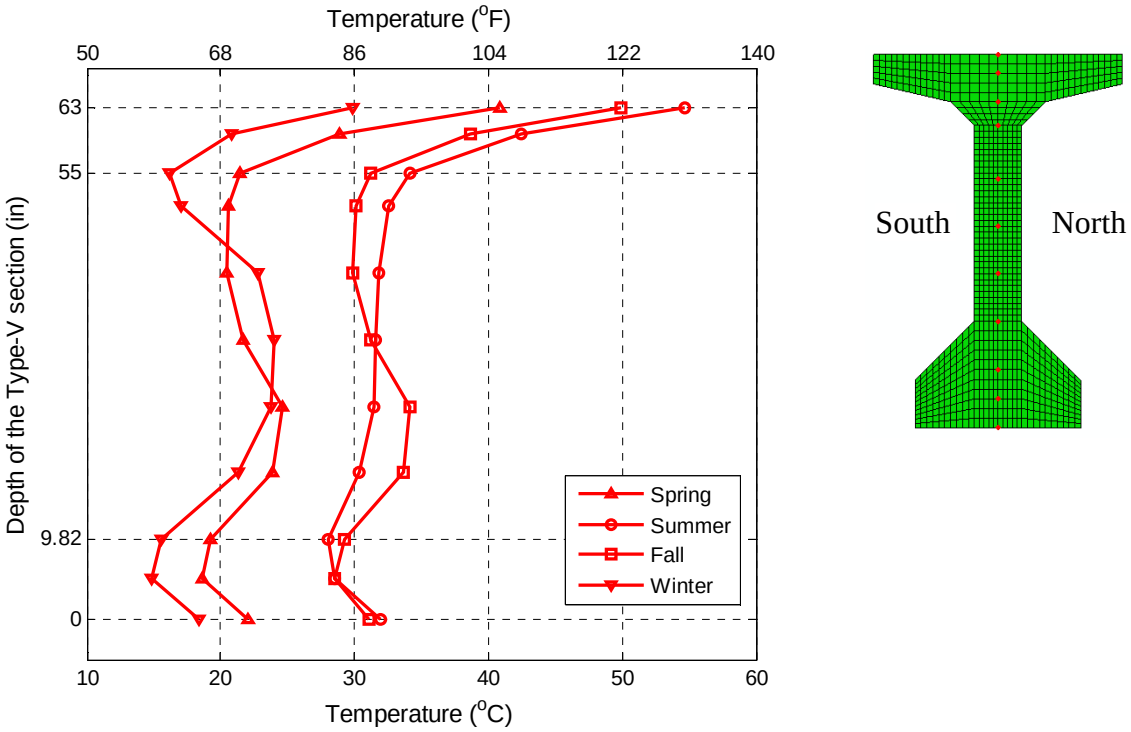

Figure 5.18: The seasonal maximum vertical temperature distributions of Type-V section.

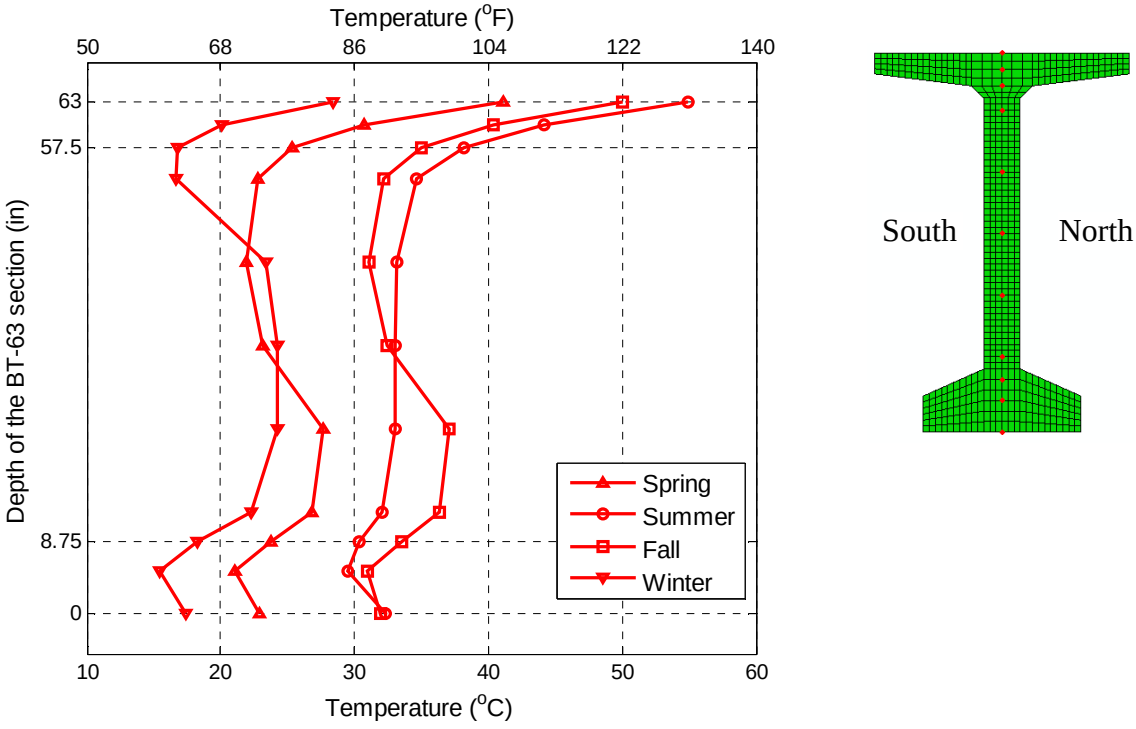

Figure 5.19: The seasonal maximum vertical temperature distributions of BT-63 section.

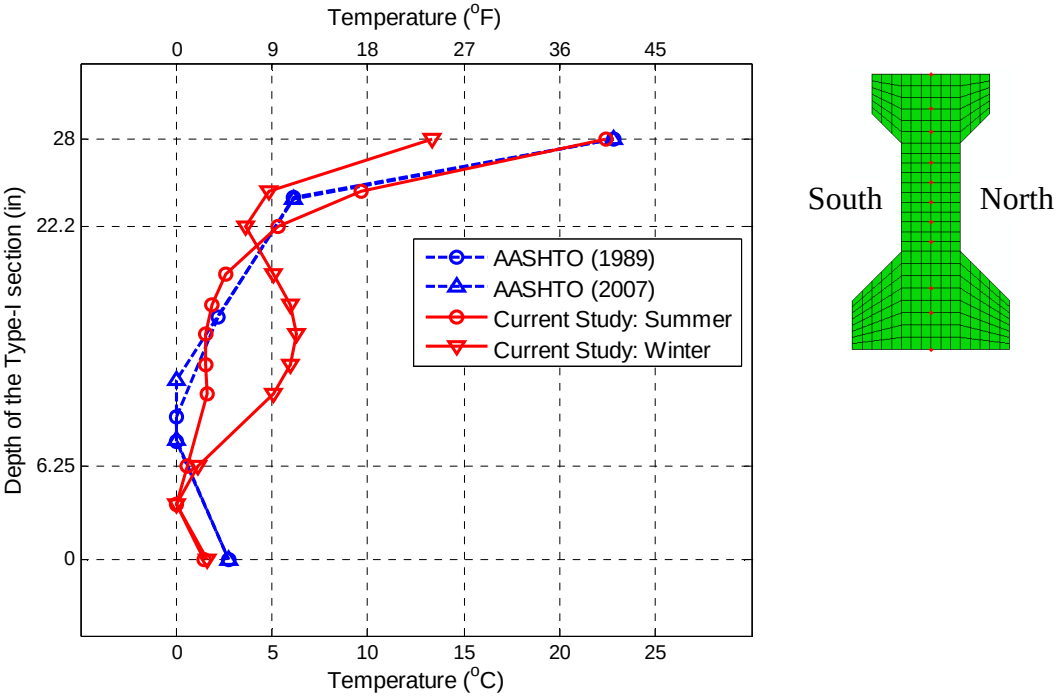

(a) Summer and winter

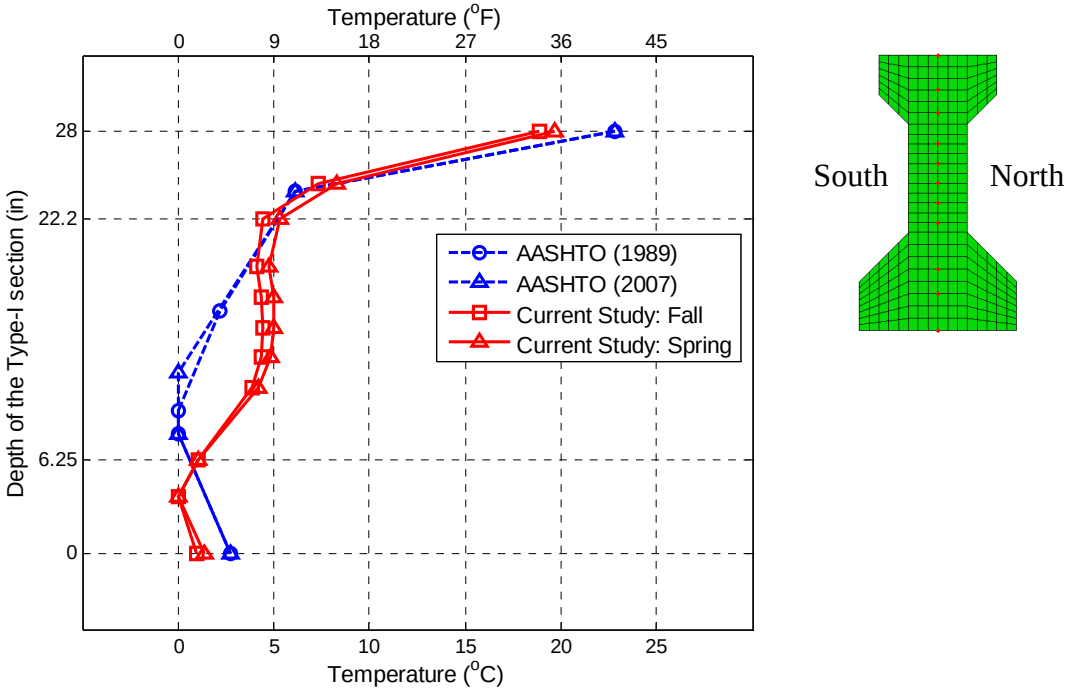

(b) Fall and spring

Figure 5.20: The seasonal maximum vertical temperature gradients of Type-I section.

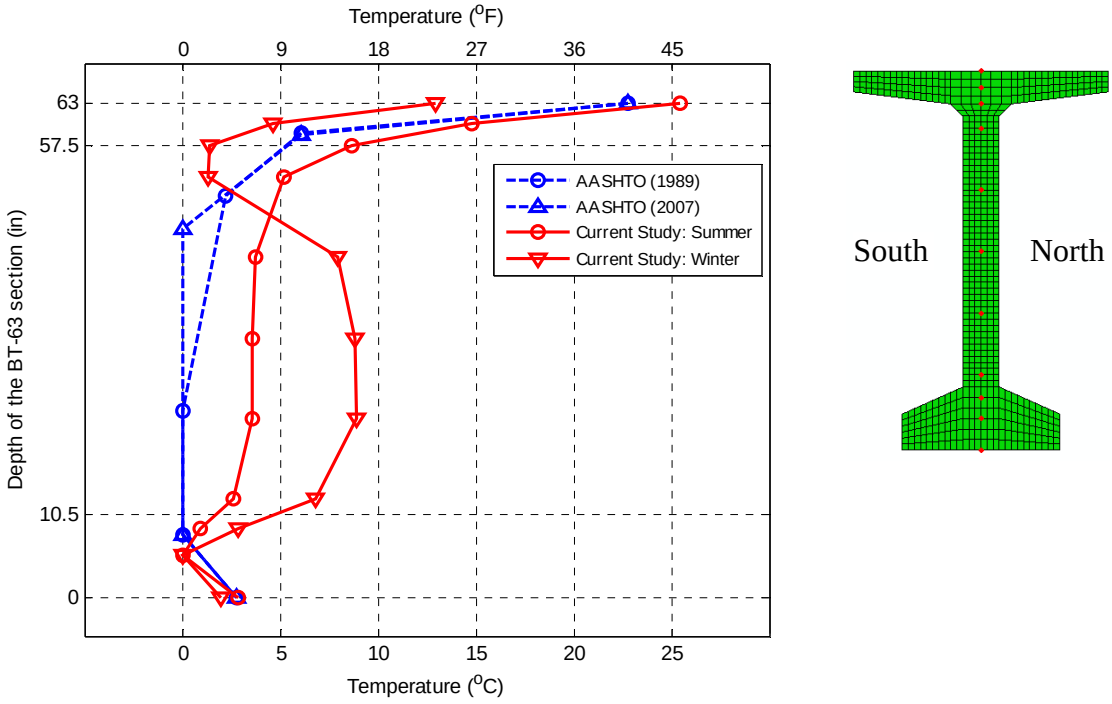

(a) Summer and winter

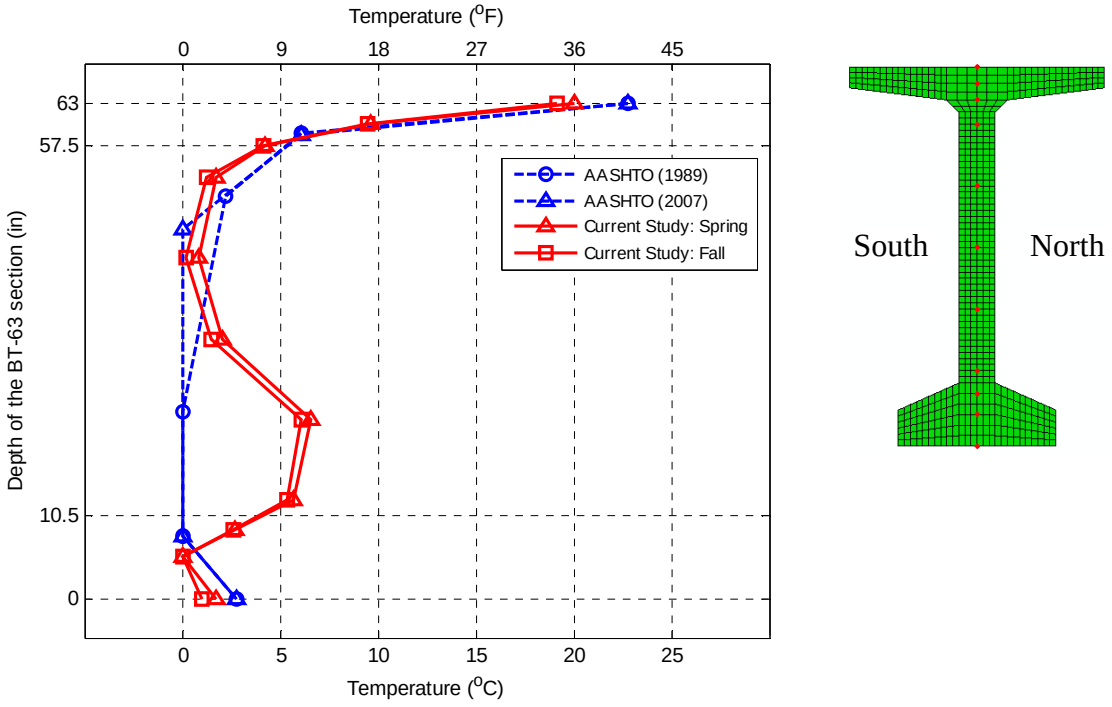

(b) Fall and spring

Figure 5.21: The seasonal maximum vertical temperature gradients of BT-63 section.

5.4.5 Seasonal Transverse Temperature Distributions

This study also investigated seasonal maximum transverse temperature distributions and gradients across the top flange, the web, and the bottom flange of the BT-63 girder, in which the maximum transverse temperature differentials were observed. Figure 5.22 shows the seasonal maximum transverse temperature distributions in the top flange. The highest temperature was found on the south end surface, and the lowest temperature was found in the middle of the top flange. The magnitudes of the temperatures were the highest in the summer, the second highest in the fall, and the smallest in the winter. However, the transverse temperature gradient of the top flange as shown in Figure 5.23 is the largest in the winter, the second largest in the fall and the spring, and the smallest in the summer. The seasonal largest transverse temperature differentials in the top flange obtained from seasonal extreme environmental conditions in Atlanta, Georgia are 19.6°C (35.3°F) in the winter, 16.0°C (28.8°F) and 14.7°C (26.5°F) in the spring and the fall, respectively, and 9.0°C (16.2°F) in the summer.

Figure 5.24 shows the seasonal maximum transverse temperature distributions in the web of the BT-63 section. As expected, the high magnitudes of the temperatures were observed in the summer and the fall. The transverse temperature gradients as shown in Figure 5.25 are the maximum in the winter due to high solar radiation on the vertical surface. In the fall and the spring, unlike the large transverse temperature gradients in the top and bottom flanges, the web exhibited no increases in the transverse gradients due to the shadow on the web. The seasonal largest transverse temperature differentials of the web in Atlanta, Georgia is 13.3°C (23.9°F) in the winter and about 4°C (7°F) in the other seasons.

For the bottom flange, the seasonal maximum transverse temperature distributions and gradients are shown in Figures 5.26 and 5.27, respectively. As mentioned earlier, the magnitudes of the temperatures increased from the winter to the summer. However, in the summer, the temperature magnitudes in the south part of the bottom flange were small

because the shadow of the top flange extended to the bottom flange. Thus, the transverse temperature gradients were the minimum in the summer as shown in Figure 5.27. The seasonal largest transverse temperature differentials of the bottom flange in Atlanta, Georgia are 25.6°C (46.1°F) in the winter, 23.7°C (42.7°F) and 22.7°C (40.9°F) in the fall and spring, respectively, and 12.0°C (21.7°F) in the winter.

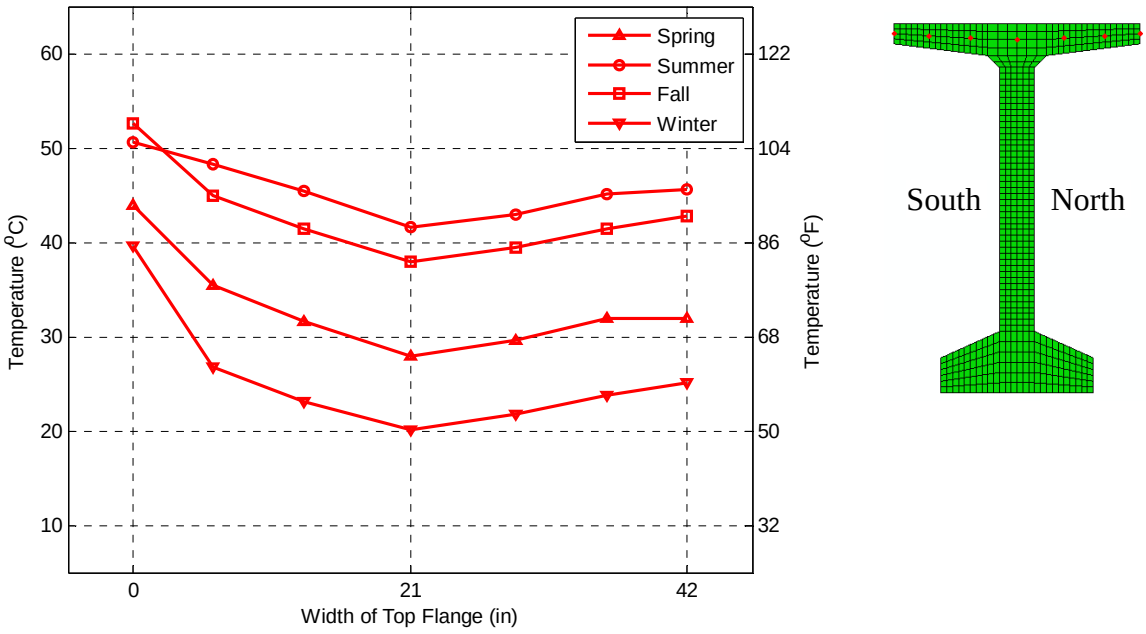

Figure 5.22: Seasonal maximum transverse temperature distributions in the top flange of BT-63 section.

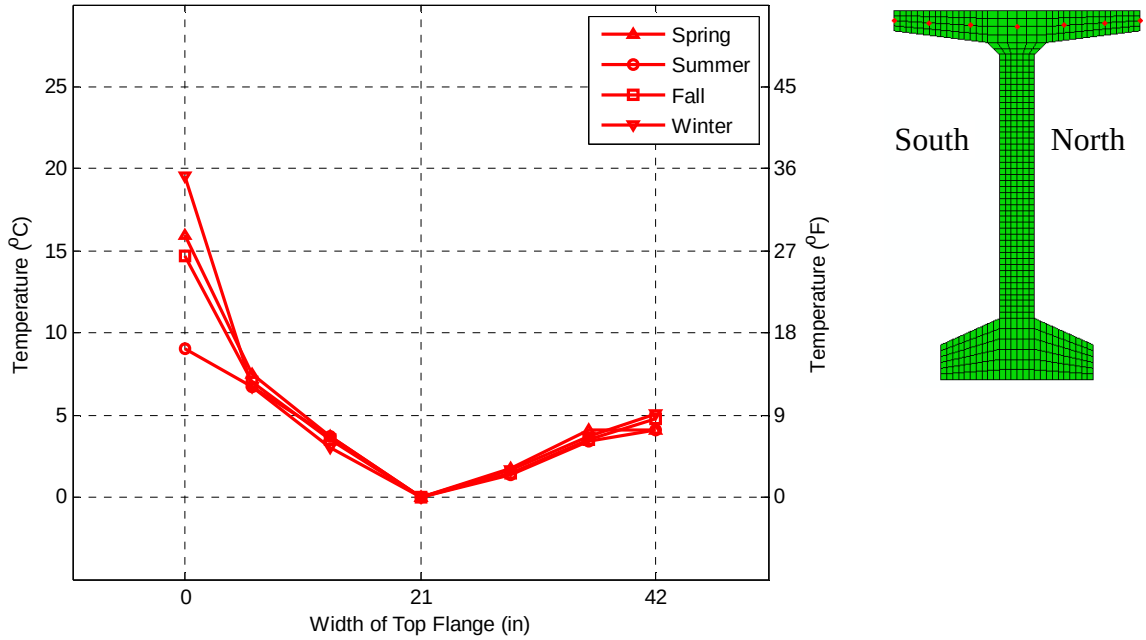

Figure 5.23: Seasonal maximum transverse temperature gradients in the top flange of BT-63 section.

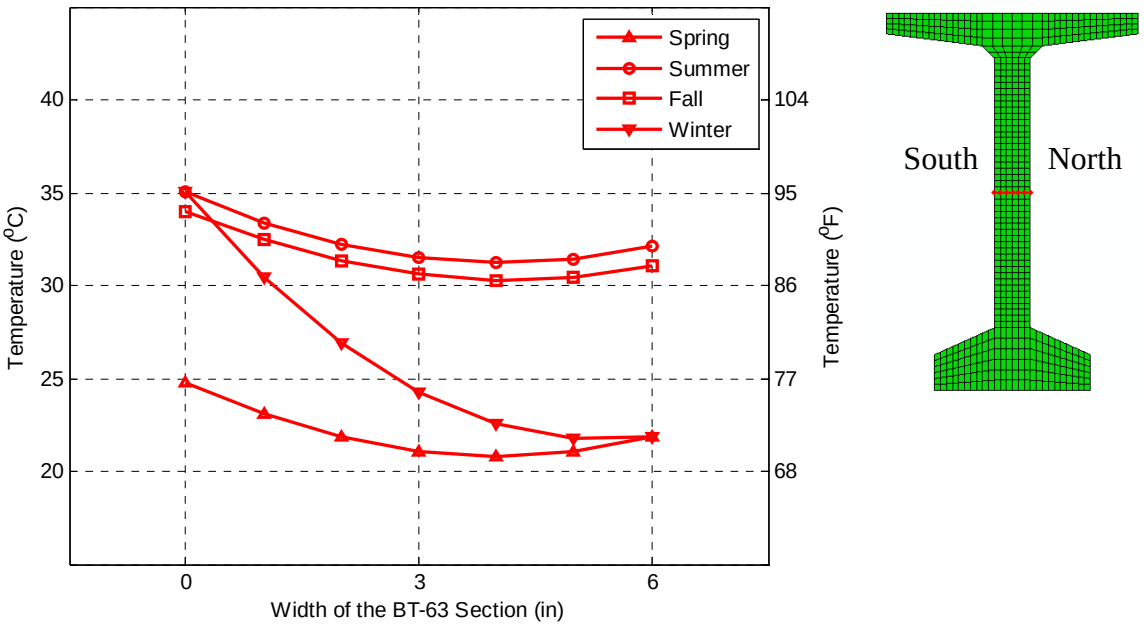

Figure 5.24: Seasonal maximum transverse temperature distributions in the web of BT-63 section.

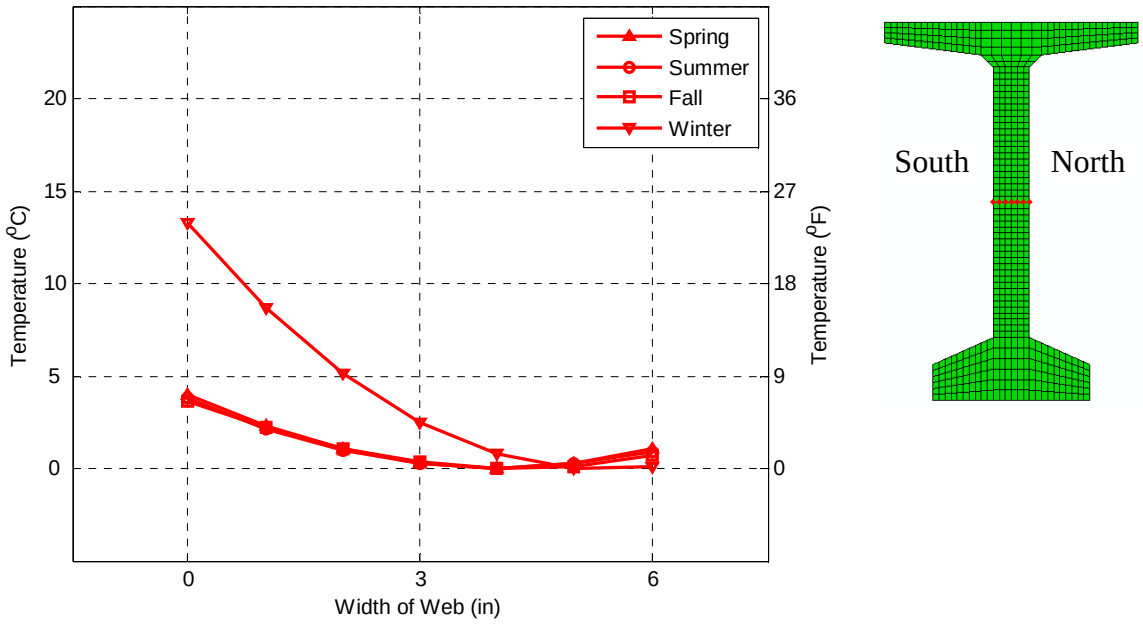

Figure 5.25: Seasonal maximum transverse temperature gradients in the web of BT-63 section.

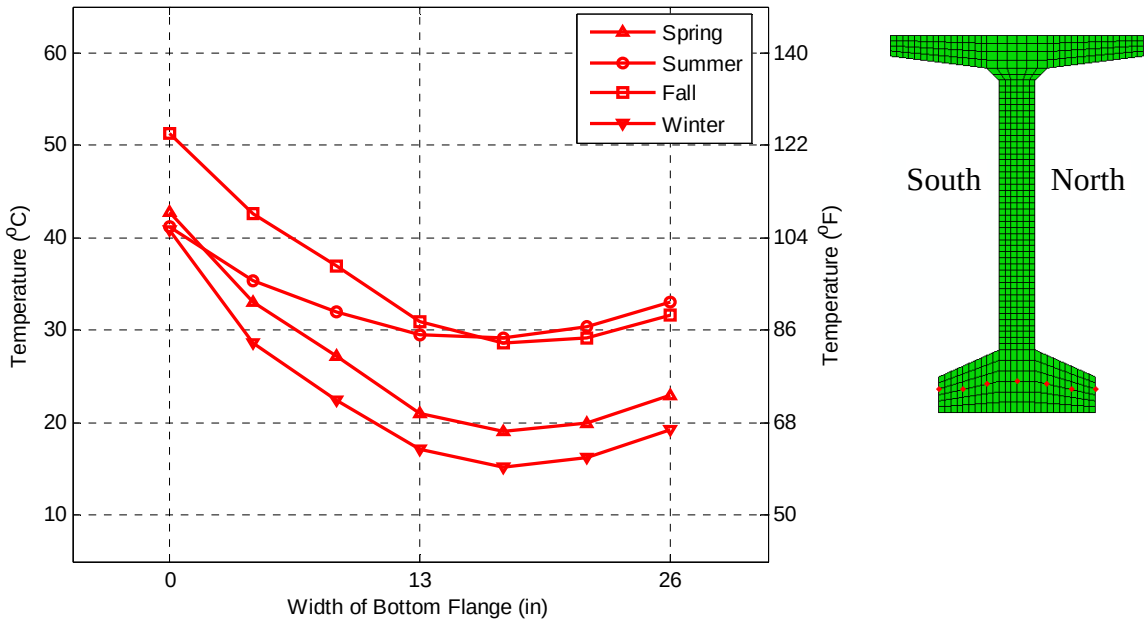

Figure 5.26: Seasonal maximum transverse temperature distributions in the bottom flange of BT-63 section.

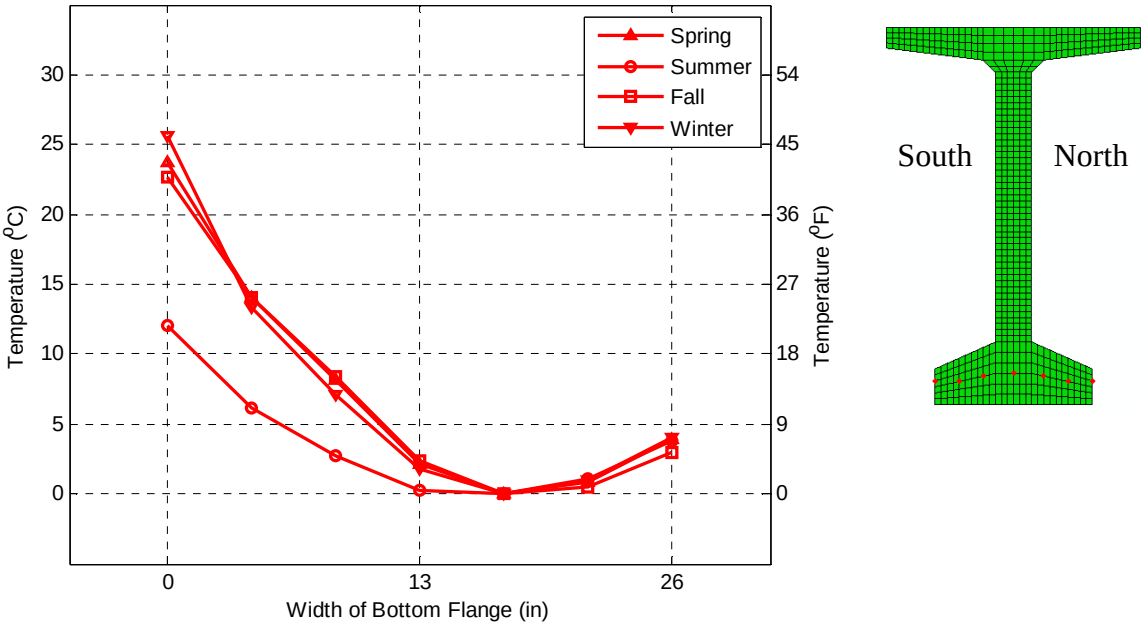

Figure 5.27: Seasonal maximum transverse temperature gradients in the bottom flange of BT-63 section.

5.5 Influences of Bridge Axes on the Temperature Distributions

This study investigated seasonal variations in the vertical and transverse temperature distributions of prestressed concrete bridge girders in an east-west orientation. This orientation was assumed to provide maximum transverse temperature distributions in the bridge girders since only one side of the girders directly receive solar radiation from the sun. Thus, this section evaluated variations in the temperature distributions with changes in bridge orientations using 2D heat transfer analysis. Since the largest vertical and transverse temperature distributions were found in Type-V and BT-63 sections, this analytical study was carried out on these two sections under seasonal extremes in environmental conditions in Atlanta, Georgia. The bridge orientations involved in this study are east-west (E-W), southwest-northeast (SW-NE), south-north (S-N), and southeast-northwest (SE-NW) orientations shown in Figure 5.28.

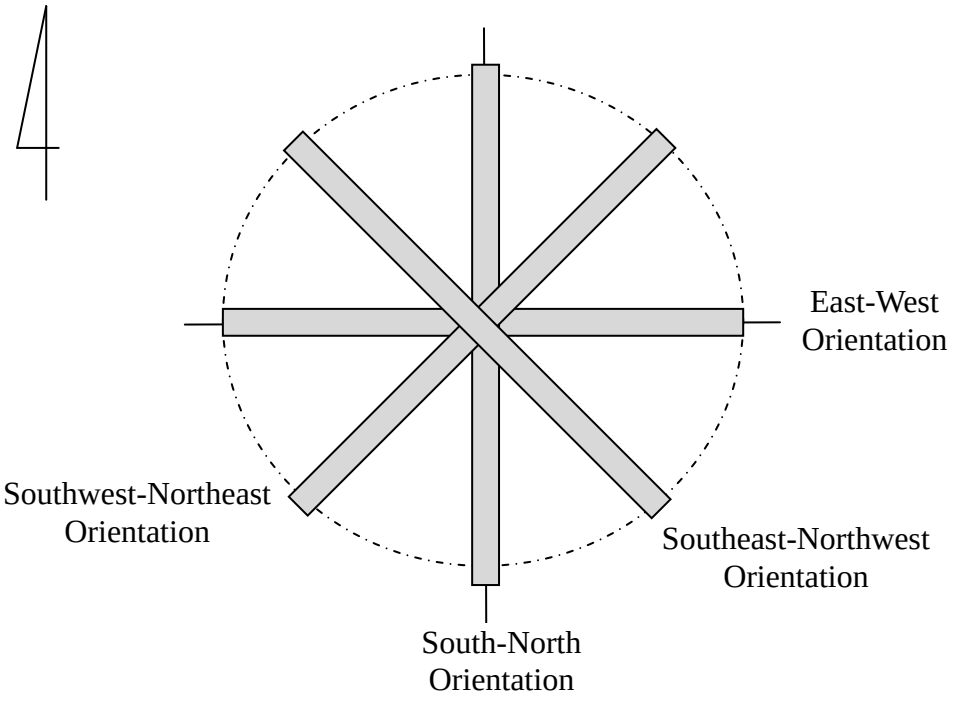

Figure 5.28: Bridge orientations involved in this study.

5.5.1 Vertical Temperature Differentials and Gradients

Tables 5.5 and 5.6 summarize the seasonal largest vertical temperature differentials obtained from the heat transfer analysis in the Type-V and BT-63 sections, respectively, for four bridge orientations. Since vertical temperature variations in the bridge girder mainly depend on the intensity of solar radiation on the top surface of the girder, the vertical temperature differentials were the largest in the summer, the second largest in the fall and spring, and the smallest in the winter. For the same reason, the changes in bridge orientations only slightly affected the vertical temperature differentials. As shown in Tables 5.5 and 5.6, the maximum vertical temperature differentials, 26.7°C (48.0°F) in Type-V section and 24.5°C (44.1°F) in BT-63 section, occurred in the summer and in the E-W orientation. With changes in bridge orientations from the E-W to the SE-NW, variances in the vertical temperature differentials were less than 3.7°C (6.7°F). The occurrence times of the vertical temperature differentials were 2:00 p.m. in all the seasons and orientations.

Based on the maximum vertical temperature differentials which occurred in the summer, Figure 5.29 shows the maximum vertical temperature gradients obtained by subtracting a lowest temperature from the girder temperatures for four bridge orientations. The vertical temperature gradients as shown in Figure 5.29 decreased from the top surface of the top flange to the bottom flange. In particular, the top flange showed a rapid decrease in the vertical temperature gradient. The largest differentials of the vertical gradient were observed in the E-W orientation. With changes in bridge orientations, the values of the vertical differentials slightly changed, and the shapes of the vertical gradients were almost the same.

Figure 5.29 also compared the vertical temperature gradients obtained from the current study and those recommended in the AASHTO specifications (1989, 2007). As discussed in Section 5.4.4, the AASHTO specifications exhibit smaller vertical temperature differentials for the deeper AASHTO-PCI sections, Type-V and BT-63

sections. In addition, while the AASHTO specifications define a minimum temperature, or a zero point of the vertical gradient, in the web or in the bottom of the top flange, this study shows the zero point in the middle of the bottom flange. Thus, for the design of prestressed concrete bridge girders, a simplified vertical temperature gradient was proposed in terms of the locations of the top flange, the web, and the bottom flange of prestressed concrete girders as shown in Figure 5.30. The proposed vertical gradient decreases from the highest temperature on the top surface to the zero temperature in the middle of the bottom flange. The vertical temperature differentials, denoted T_1 and T_2 in Figure 5.30, were determined to be 27°C (49°F) and 5°C (9°F), respectively, based on extreme summer environmental conditions in Atlanta, Georgia.

Table 5.5: Seasonal largest vertical temperature differentials in Type-V section with respect to four bridge orientations.

Bridge Orientations	Vertical Temperature Differentials, °C (°F)			
	Spring	Summer	Fall	Winter
East-West (E-W)	21.6 (38.9) at 2 p.m.	26.7 (48.0) at 2 p.m.	20.6 (37.1) at 2 p.m.	14.3 (25.8) at 2 p.m.
Southwest-Northeast (SW-NE)	21.4 (38.5) at 2 p.m.	24.1 (43.3) at 2 p.m.	20.4 (36.7) at 2 p.m.	14.9 (26.8) at 2 p.m.
South-North (S-N)	22.1 (36.7) at 2 p.m.	23.8 (42.9) at 2 p.m.	23.3 (41.9) at 2 p.m.	17.4 (31.4) at 2 p.m.
Southeast-Northwest (SE-NW)	23.5 (42.4) at 2 p.m.	24.6 (44.3) at 2 p.m.	22.6 (40.6) at 2 p.m.	17.5 (31.6) at 2 p.m.

Table 5.6: Seasonal largest vertical temperature differentials in BT-63 section with respect to four bridge orientations.

Bridge Orientations	Vertical Temperature Differentials, °C (°F)			
	Spring	Summer	Fall	Winter
East-West (E-W)	19.2 (34.6) at 2 p.m.	24.5 (44.1) at 2 p.m.	18.9 (34.1) at 2 p.m.	11.6 (20.9) at 1 p.m.
Southwest-Northeast (SW-NE)	17.8 (32.0) at 2 p.m.	20.8 (37.4) at 2 p.m.	17.3 (31.1) at 2 p.m.	11.0 (19.7) at 2 p.m.
South-North (S-N)	18.9 (34.0) at 2 p.m.	21.0 (37.8) at 2 p.m.	20.4 (36.8) at 2 p.m.	14.8 (26.6) at 2 p.m.
Southeast-Northwest (SE-NW)	21.2 (38.2) at 2 p.m.	22.3 (40.1) at 2 p.m.	20.5 (36.9) at 2 p.m.	15.6 (28.0) at 2 p.m.

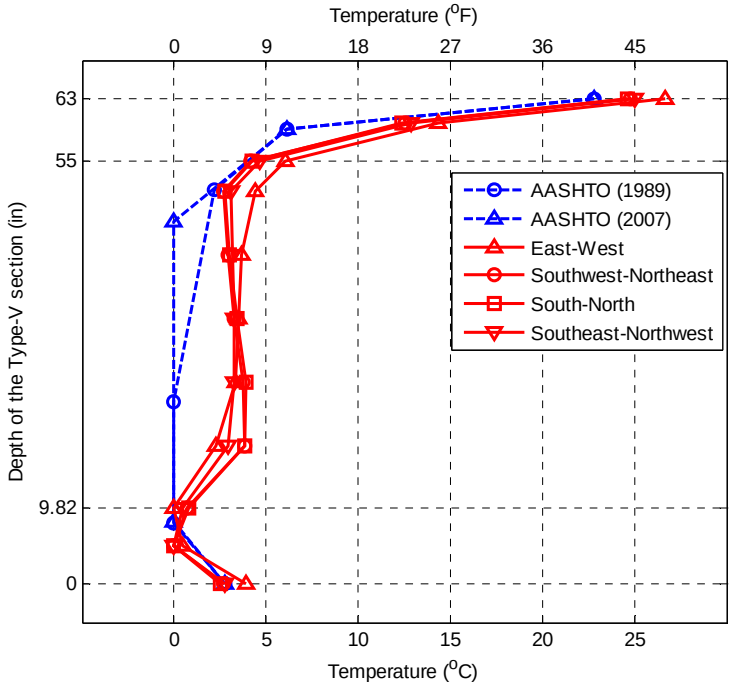

(a) Type-V section

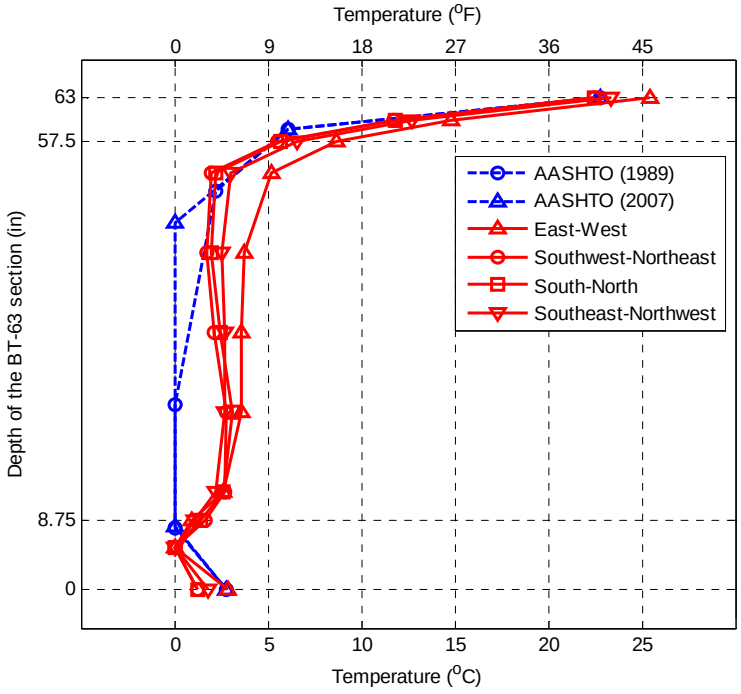

(b) BT-63 section

Figure 5.29: Maximum vertical temperature gradients with respect to four bridge orientations in the summer.

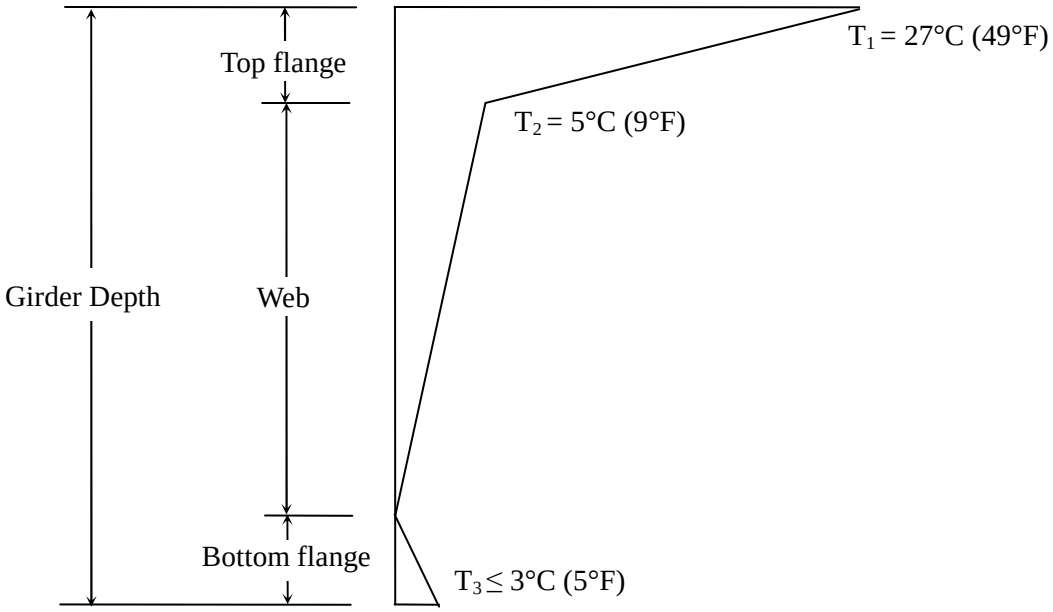

Figure 5.30: A proposed vertical temperature gradient along the depth of prestressed concrete bridge girders.

5.5.2 Transverse Temperature Differentials and Gradients in the Top Flange

In addition, the influence of bridge orientations on transverse temperature differentials in the top flange of prestressed concrete bridge girders was investigated. Since larger transverse temperature differentials were found in the wider Type-V and BT-63 sections, this study evaluated seasonal largest transverse temperature differentials in the top flange of the Type-V and BT-63 sections for each bridge orientation. The maximum transverse temperature differentials were found in the both E-W orientation and the winter; 20.1°C (36.1°F) for Type-V section and 19.6°C (35.3°F) for BT-63 section. In general, large transverse temperature differentials were observed in the E-W and SW-NE orientations, in which bridge girders are more exposed to the sun than the S-N and the SE-NW orientations. With seasonal changes, the transverse temperature

differentials were the largest in the winter because of high solar radiation on the vertical surface.

For the S-N orientation, the transverse temperature differentials of the top flange, shown in Table 5.7 for Type-V section and Table 5.8 for BT-63 section, were similar with no specific seasonal variations. Moreover, the transverse differentials in the winter, even though high solar intensity on the vertical surface, showed smaller values because of smaller time exposed to the sun. The transverse temperature differentials in the SE-NW orientation, in which bridge girders are exposed to the sun for only a couple of hours in the morning, were negligible.

Figure 5.31 also shows the transverse temperature gradients for each orientation in which maximum transverse gradients were observed in the E-W orientation. The transverse gradients increased only in half of the top flange. The gradient in the other side were nearly constant. Therefore, based on the transverse gradients and differentials obtained from extreme winter environmental conditions in Atlanta, Georgian, in the E-W orientation, this study proposed a transverse temperature gradient for the top flange as shown in Figure 5.32. The transverse gradient proposed in this study increases from the middle of the top flange to a maximum differential of 20°C (36°F) at the end of the one side. Temperature T_1 shown in Figure 5.32 was determined to be one-fourth of the maximum temperature differential of 20°C (36°F). The one-fourth temperature, defined as the middle temperature of the transverse gradient, agrees well with the second-order model proposed for transverse temperature distributions in prestressed concrete bridge girders. Between the temperature differentials of T_1, 20°C (36°F), and T_2, 5°C (9°F), shown in Figure 5.32, the transverse temperature gradient was assumed to be linear.

Table 5.7: Seasonal largest transverse temperature differentials in the top flange of Type-V section with respect to four bridge orientations.

Bridge Orientations	Transverse Temperature Differentials: Top Flange, °C (°F)			
	Spring	Summer	Fall	Winter
East-West	15.9 (28.6) at 2 p.m.	8.5 (15.3) at 1 p.m.	14.7 (26.4) at 1 p.m.	20.1 (36.1) at 2 p.m.
Southwest-Northeast	15.9 (28.6) at 12 p.m.	10.5 (18.9) at 11 a.m.	15.0 (27.1) at 11 a.m.	17.6 (31.7) at 12 p.m.
South-North	13.5 (24.3) at 11 a.m.	12.0 (21.6) at 10 a.m.	12.9 (23.3) at 10 a.m.	11.0 (22.4) at 11 a.m.
Southeast-Northwest	7.1 (12.8) at 9 a.m.	9.6 (17.2) at 9 a.m.	6.8 (12.2) at 9 a.m.	2.7 (4.8) at 9 a.m.

Table 5.8: Seasonal largest transverse temperature differentials in the top flange of BT-63 section with respect to four bridge orientations.

Bridge Orientations	Transverse Temperature Differentials: Top Flange, °C (°F)			
	Spring	Summer	Fall	Winter
East-West	16.0 (28.8) at 1 p.m.	9.0 (16.3) at 1 p.m.	14.7 (26.5) at 1 p.m.	19.6 (35.3) at 1 p.m.
Southwest-Northeast	15.8 (28.4) at 12 p.m.	11.0 (19.8) at 11 a.m.	14.7 (26.5) at 11 a.m.	16.6 (29.8) at 12 p.m.
South-North	13.5 (24.4) at 10 a.m.	12.2 (22.0) at 10 a.m.	13.0 (23.4) at 10 a.m.	11.4 (20.5) at 11 a.m.
Southeast-Northwest	7.4 (13.3) at 9 a.m.	9.7 (17.5) at 9 a.m.	7.1 (12.7) at 9 a.m.	3.1 (5.6) at 9 a.m.

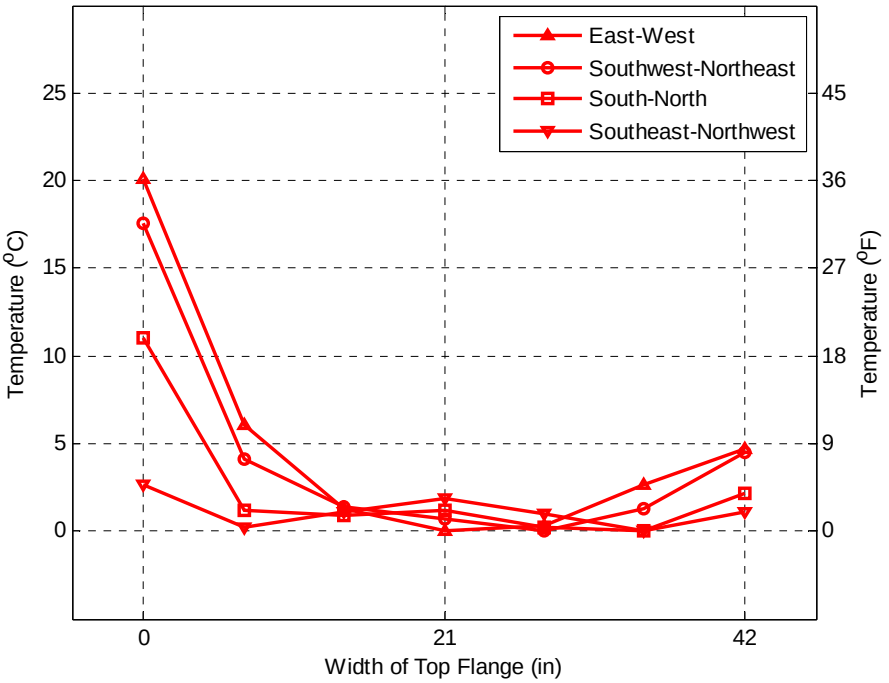

(a) Type-V section

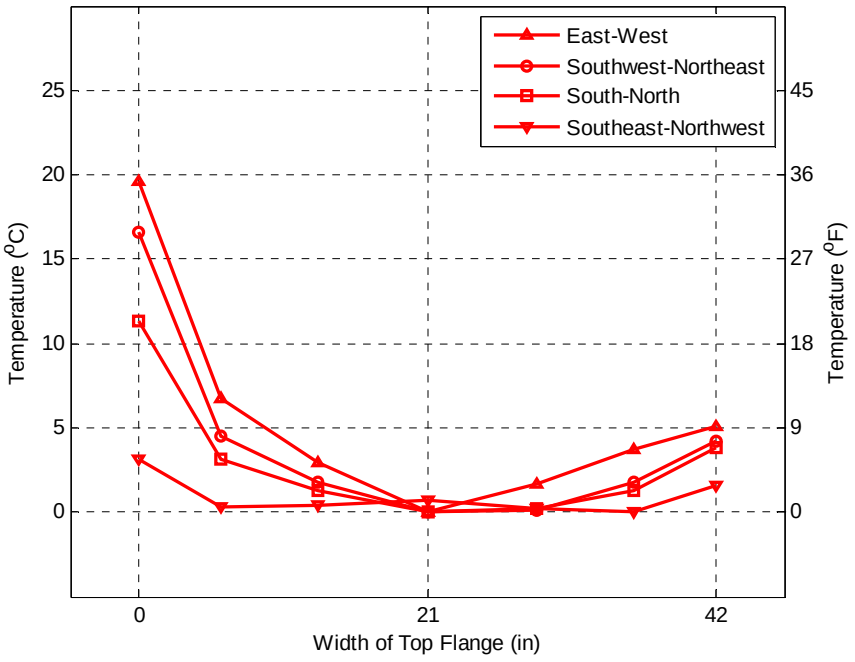

(b) BT-63 section

Figure 5.31: Maximum transverse temperature gradients in the top flange with respect to four bridge orientations in the winter.

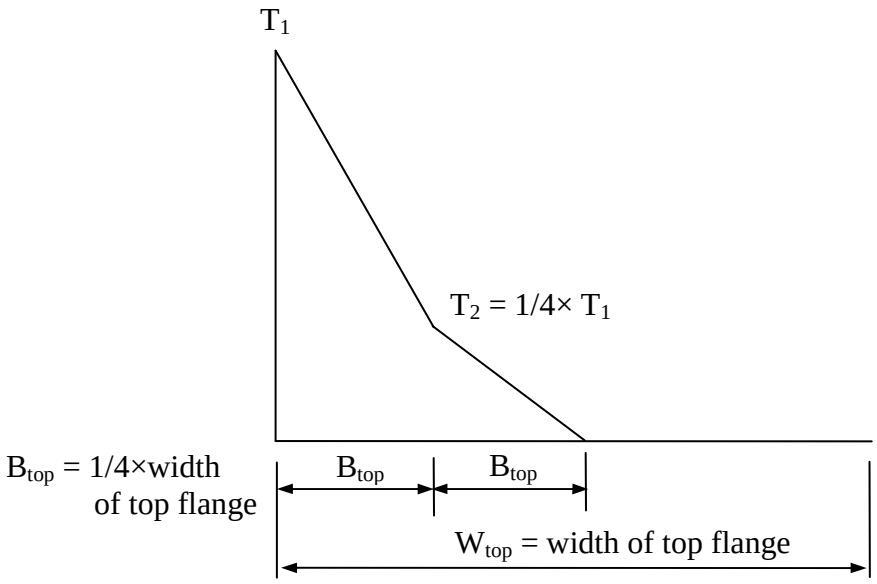

Figure 5.32: A proposed transverse temperature gradient in the top flange of prestressed concrete bridge girders.

5.5.3 Transverse Temperature Differentials and Gradients in the Web

The effects of changes in bridge orientations on transverse temperature differentials in the girder web were also evaluated. Tables 5.9 and 5.10 summarize the seasonal largest transverse temperature differentials in the web of BT-63 and Type-IV sections, respectively, with changes in bridge orientations. Since the web of the bridge girder is more exposed to the sun in an E-W orientation and solar radiation incident on the vertical surface is the highest in the winter, the maximum transverse temperature differentials of 16.4°C (29.4°C) in the Type-V section and 13.2°C (23.9°F) in the BT-63 section occurred in the E-W orientation and in the winter.

For the S-N orientation, the transverse temperature differentials were slightly higher in the fall and the spring with higher solar radiation on the vertical surface and slightly smaller in the winter with less amount of time exposed to the sun. However, in general, the transverse temperature differentials in the S-N orientation were similar in all

the seasons. The SE-NW orientation, as mentioned earlier, represented a slight change in transverse temperature differentials that could be neglected.

The transverse temperature gradients of the web are presented in Figure 5.33 with respect to four bridge orientations for the winter, in which the maximum transverse gradient was found. Similar to the transverse temperature gradient of the top flange, the surface more exposed to the sun experienced a rapid increase in the transverse gradient. The temperatures in the middle of the web were approximately one quarter of the largest temperature, which also provide good agreement with the second-order model of the transverse temperature distribution. Therefore, based on the analytical results obtained from the both E-W orientation and extreme winter environmental conditions in Atlanta, Georgia, this study proposed a transverse temperature gradient across the web of prestressed concrete bridge girders as shown in Figure 5.34. The maximum surface temperature T_1 was determined to be a maximum differential of 16°C (29°F), and the middle temperature T_2 was determined to be 4°C (7°F), one-fourth of the maximum differential. The temperatures between the temperatures T_1 and T_2 were assumed to be linear.

Table 5.9: Seasonal largest transverse temperature differentials in the web of Type-V section with respect to four bridge orientations.

Bridge Orientations	Transverse Temperature Differentials: Web, °C (°F)			
	Spring	Summer	Fall	Winter
East-West	5.7 (10.3) at 1 p.m.	5.0 (9.0) at 1 p.m.	5.2 (9.3) at 1 p.m.	16.4 (29.4) at 1 p.m.
Southwest-Northeast	13.7 (24.7) at 11 a.m.	9.3 (16.8) at 10 a.m.	13.5 (24.2) at 11 a.m.	14.8 (26.7) at 11 a.m.
South-North	12.6 (22.7) at 10 a.m.	11.8 (21.3) at 9 a.m.	12.6 (22.7) at 9 a.m.	10.2 (18.3) at 10 a.m.
Southeast-Northwest	6.5 (11.8) at 8 a.m.	9.8 (17.7) at 9 a.m.	6.8 (12.2) at 8 a.m.	2.1 (3.8) at 8 a.m.

Table 5.10: Seasonal largest transverse temperature differentials in the web of BT-63 section with respect to four bridge orientations.

Bridge Orientations	Transverse Temperature Differentials: Web, °C (°F)			
	Spring	Summer	Fall	Winter
East-West	4.0 (7.2) at 1 p.m.	3.8 (6.9) at 1 p.m.	3.7 (6.6) at 1 p.m.	13.3 (23.9) at 1 p.m.
Southwest-Northeast	11.7 (21.0) at 11 a.m.	8.1 (14.5) at 10 a.m.	11.8 (21.2) at 10 a.m.	12.7 (22.9) at 11 a.m.
South-North	11.0 (19.8) at 9 a.m.	10.5 (18.8) at 9 a.m.	11.3 (20.4) at 9 a.m.	8.9 (16.0) at 10 a.m.
Southeast-Northwest	6.0 (10.9) at 8 a.m.	8.6 (15.5) at 8 a.m.	6.2 (11.2) at 8 a.m.	2.1 (3.7) at 8 a.m.

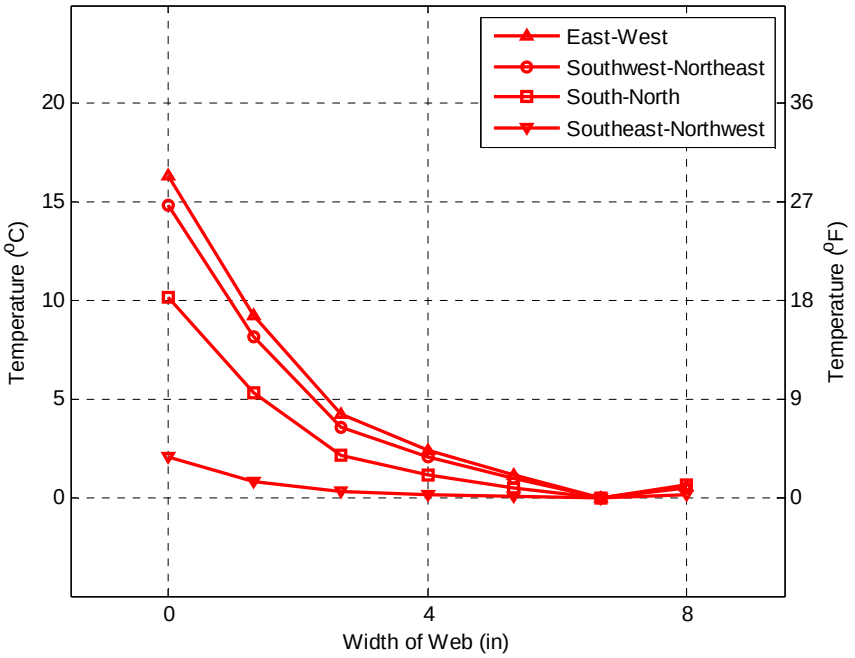

(a) Type-V section

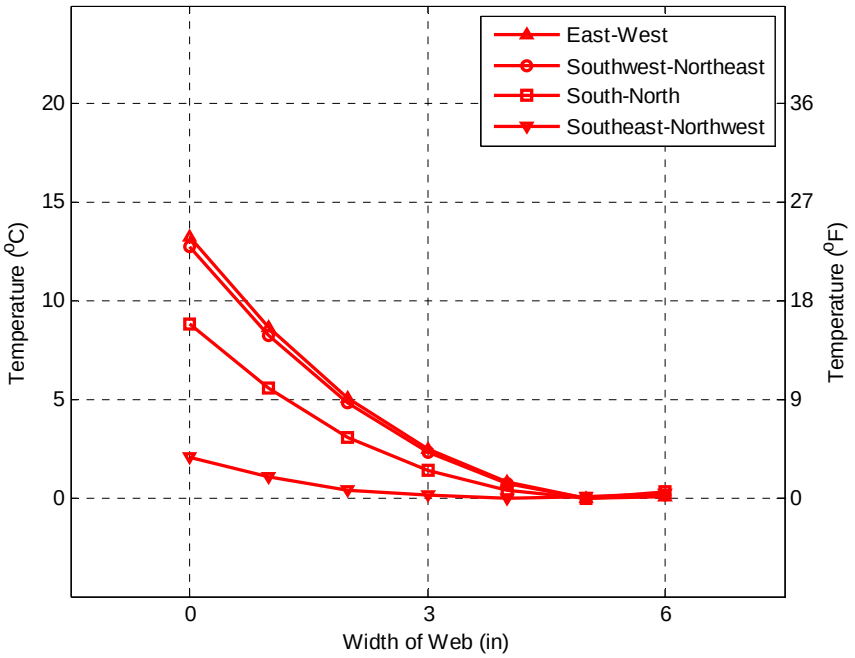

(b) BT-63 section

Figure 5.33: Maximum transverse temperature gradients in the web with respect to four bridge orientations in the winter.

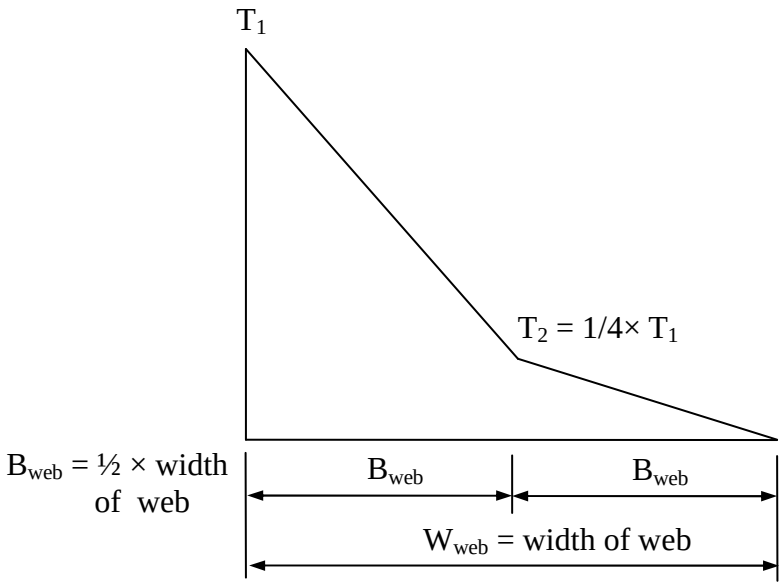

Figure 5.34: A transverse temperature gradient in the web of prestressed concrete bridge girders.

5.5.4 Transverse Temperature Differentials and Gradients in the Bottom Flange

For the bottom flange, Tables 5.11 and 5.12 show the seasonal largest transverse temperature differentials of Type-V and BT-63 sections for the four bridge orientations. As discussed previously, the E-W and SW-NE orientations in the winter yield maximum transverse temperature differentials of 24.6°C (44.2°F) in the Type-V section and 25.6°C (46.1°F) in the BT-63 section. The S-N orientation presents nearly similar transverse differentials in all the seasons except for the winter, which showed a little smaller value due to smaller hours exposed to the sun. The SE-NW orientation, in which bridge girders receive solar radiation directly from the sun for only a few hours, presented the smallest transverse differentials in the bottom flange. In particular, in the winter, the bridge girders in the SE-NW orientation are much less exposed to the sun, so the transverse differentials shown in Tables 5.11 and 5.12 are negligible.

Figure 5.35 shows the transverse temperature gradients in the bottom flange of the Type-V and BT-63 sections for the four bridge orientations in the winter. As mentioned

earlier, large transverse gradients occurred in the E-W and SW-NE orientations. The minimum temperature of the transverse gradient, or a zero point of the gradient, was observed at around one fourth of the width of the bottom flange as shown in Figure 5.35. Based on the maximum transverse gradients obtained in the E-W orientation and in the extreme winter environmental condition in Atlanta, Georgia, Figure 5.36 shows a transverse temperature gradient for the bottom flange of prestressed concrete bridge girders. The maximum differential of T_1 was determined to be 26°C (47°F), and the temperatures of T_2 and T_3 were determined to be 12°C (21°F) and 3°C (5F), respectively. The transverse temperature gradient of the bottom flange proposed in this study also matched well the second-order model of the transverse temperature distribution.

Table 5.11: Seasonal largest transverse temperature differentials in the bottom flange of Type-V section with respect to four bridge orientations.

Bridge Orientations	Transverse Temperature Differentials: Bottom Flange, °C (°F)			
	Spring	Summer	Fall	Winter
East-West	21.2 (38.2) at 2 p.m.	12.0 (21.6) at 2 p.m.	20.2 (36.4) at 2 p.m.	24.6 (44.2) at 2 p.m.
Southwest-Northeast	20.1 (36.3) at 12 p.m.	14.8 (26.6) at 12 p.m.	19.4 (34.8) at 12 p.m.	20.7 (37.3) at 1 p.m.
South-North	17.1 (30.8) at 11 a.m.	16.5 (29.7) at 11 a.m.	14.8 (26.6) at 10 a.m.	12.0 (21.7) at 11 a.m.
Southeast-Northwest	9.2 (16.6) at 10 a.m.	12.4 (22.4) at 9 a.m.	8.6 (15.5) at 10 a.m.	3.4 (6.2) at 10 a.m.

Table 5.12: Seasonal largest transverse temperature differentials in the bottom flange of BT-63 section with respect to four bridge orientations.

Bridge Orientations	Transverse Temperature Differentials: Bottom Flange, °C (°F)			
	Spring	Summer	Fall	Winter
East-West	23.7 (42.7) at 2 p.m.	12.0 (21.7) at 2 p.m.	22.7 (40.9) at 2 p.m.	25.6 (46.1) at 2 p.m.
Southwest-Northeast	22.4 (40.4) at 12 p.m.	17.7 (31.9) at 12 p.m.	21.6 (38.8) at 12 p.m.	22.1 (39.8) at 12 p.m.
South-North	18.9 (33.9) at 11 a.m.	18.8 (33.8) at 11 a.m.	14.4 (25.9) at 10 a.m.	12.0 (21.6) at 11 a.m.
Southeast-Northwest	10.8 (19.4) at 10 a.m.	14.1 (25.3) at 9 a.m.	10.3 (18.6) at 10 a.m.	3.9 (7.0) at 10 a.m.

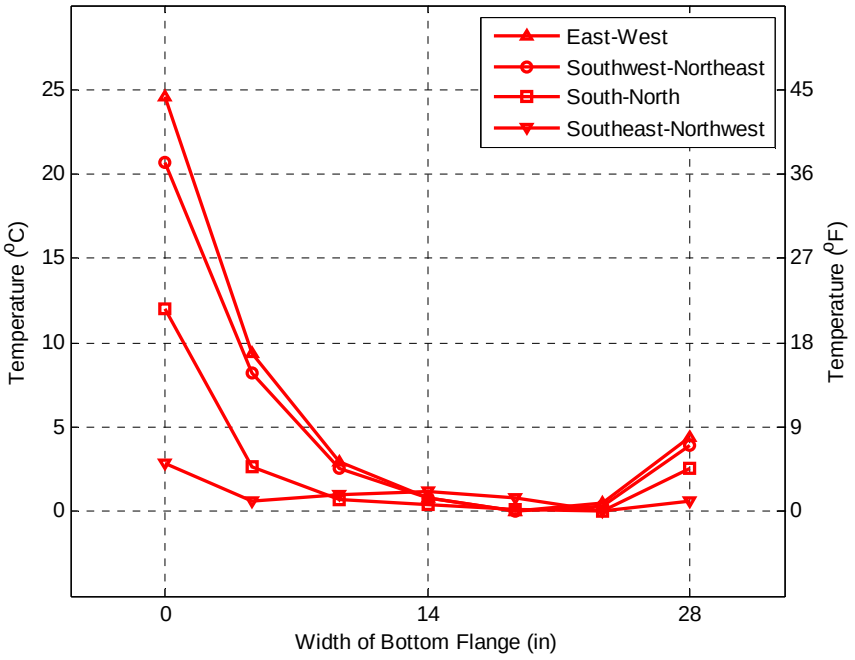

(a) Type-V section

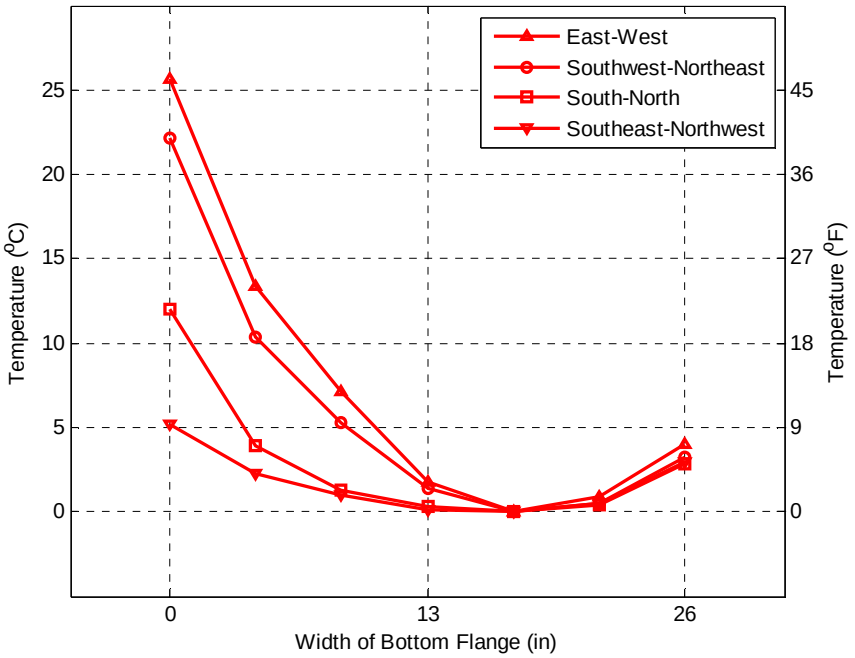

(b) BT-63 section

Figure 5.35: Maximum transverse temperature gradients in the bottom flange with respect to four bridge orientations in the winter.

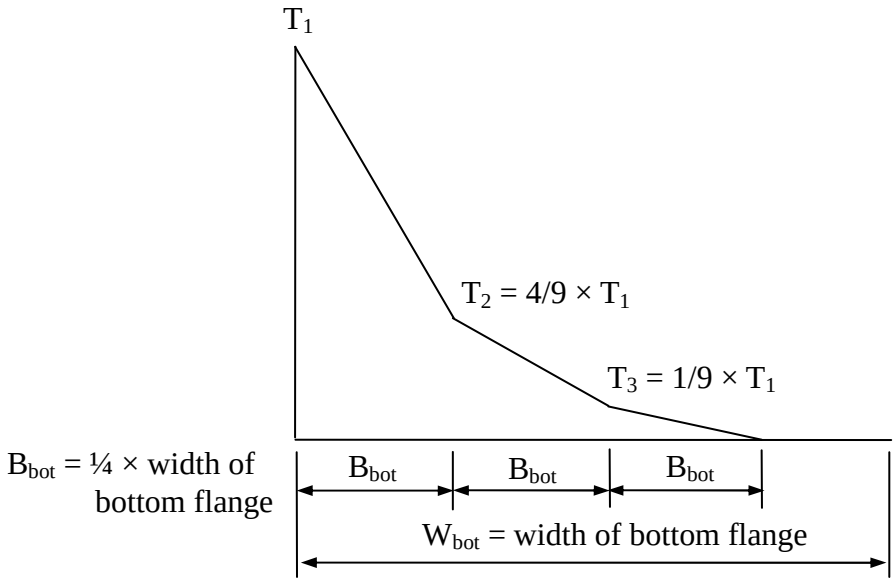

Figure 5.36: A transverse temperature gradient in the bottom flange of prestressed concrete bridge girders.

5.6 Thermal Differentials at Selected Cities in the United States

The vertical and transverse temperature differentials suggested in this study were based on extreme environmental conditions in Atlanta, Georgia. Thus, this section further evaluates extreme summer and winter environmental conditions in the United States. As mentioned previously, the summer and the winter are based on the months of June and December. The extreme environmental conditions were applied to the 2D finite element heat transfer analysis, and the vertical and transverse temperature differentials were investigated.

5.6.1 Extreme Environmental Conditions in the United States

The experimental data taken from April 2009 to March 2010 showed that when the large vertical and transverse temperature differentials were measured, daily solar radiation showed a good correlation with the NSRDB 30-year (from 1961 to 1990)

monthly average daily solar radiation under clear sky conditions. Daily maximum and minimum temperatures correlated well with the record daily maximum temperature and the average daily minimum temperature of the NCDC climatic data, respectively.

In addition, with seasonal changes from the summer to the winter, the largest vertical temperature differential was observed in the summer and the largest transverse temperature differential in the winter. Thus, for the months of June and December, representative months of the summer and the winter, this study explored the NSRDB and NCDC data at a total of 235 cities and selected eight cities involving extreme environmental conditions such as the highest daily solar radiation, the highest record daily maximum temperature, and the largest daily temperature variance. Table 5.13 shows the environmental conditions extracted from the NSRDB and the NCDC for the eight cities. For June, the highest daily solar radiation in the United States was 32.5 MJ/m^2 in Alamosa, Colorado, and the highest record daily maximum temperature was 50.0°C (122°F) in Phoenix, Arizona. The largest daily temperature variance of 32.3°C (58.3°F) was found in Medford, Oregon. In addition, Atlanta, Georgia, was included in the current study. Similarly, in the winter, the highest daily solar radiation of 18.4 MJ/m^2 was observed in Hilo, Hawaii, and the highest record daily maximum temperature of 34.4°C (94°F), was observed in Brownsville, Texas. Caribou, Maine, and Annette, Alaska, which have extremely cold environmental conditions in the winter, were also included. Figure 5.37 illustrates the cities involving extremes in environmental conditions in the summer and the winter in the United States.

The determined extreme daily environmental conditions shown in Table 5.13 were hourly distributed over the length of the days; June 21 for the summer and December 21 for the winter. The days of June 21 and December 21, representative days of the summer and the winter, have the longest and shortest days of the year. For variations in daily solar radiation with respect to the time of the day, the Liu and Jordan (1960) equation was used to calculate hourly solar radiation incident on the surfaces of the girders. Variations

in daily air temperature were obtained from the Kreith and Kreider (1978) equation. The effect of wind speed on the maximum temperature differentials was disregarded.

Table 5.13: Extremes in summer and winter environmental conditions for the eight cities in the United States.

Cities	Seasons [b]	Daily Solar Radiation, MJ/m^2	Record Daily Maximum, °C (°F)	Average Daily Minimum, °C (°F)	Daily Variance [a], °C (°F)
Alamosa, CO (37.45°N, 105.87°W)	Summer	32.5	33.8 (93)	5.0 (41.0)	28.8 (52.0)
	Winter	11.2	16.1 (61)	-18.1 (-0.5)	34.2 (61.5)
Phoenix, AZ (33.43°N, 1112.02°W)	Summer	31.3	50.0 (122)	22.7 (72.9)	27.3 (49.1)
	Winter	12.3	31.1 (88)	5.4 (41.8)	25.7 (46.2)
Medford, OR (42.73°N, 122.87°W)	Summer	30.9	42.7 (109)	10.4 (50.7)	32.3 (58.3)
	Winter	7.7	22.2 (72)	- 0.4 (31.2)	22.6 (40.8)
Atlanta, GA (33.65°N, 84.43°W)	Summer	29.4	38.3 (101)	19.0 (66.2)	19.3 (34.8)
	Winter	11.9	26.1 (79)	1.7 (35.0)	24.4 (44.0)
Brownsville, TX (25.90°N, 97.43°W)	Summer	28.5	38.9 (102)	23.8 (74.9)	15.1 (27.1)
	Winter	15.1	34.4 (94)	11.3 (52.4)	23.1 (41.6)
Caribou, ME (46.87°N, 68.02°W)	Summer	30.5	35.6 (96)	9.5 (49.1)	23.8 (46.9)
	Winter	6.2	14.4 (58)	-14.7 (5.5)	29.1 (52.5)
Hilo, HI (19.72°N, 155.07°W)	Summer	29.4	32.2 (90)	19.8 (67.6)	12.4 (22.4)
	Winter	18.4	33.9 (93)	18.2 (64.8)	15.7 (28.2)
Annette, AK (55.03°N, 131.57°W)	Summer	29.9	31.7 (89)	8.8 (47.8)	22.9 (41.2)
	Winter	2.6	16.7 (62)	- 0.3 (31.4)	17.0 (30.6)

[a] The daily variance was the difference between the record daily maximum temperature and the average daily minimum temperatures.

[b] The summer and the winter are based on the months of June and December.

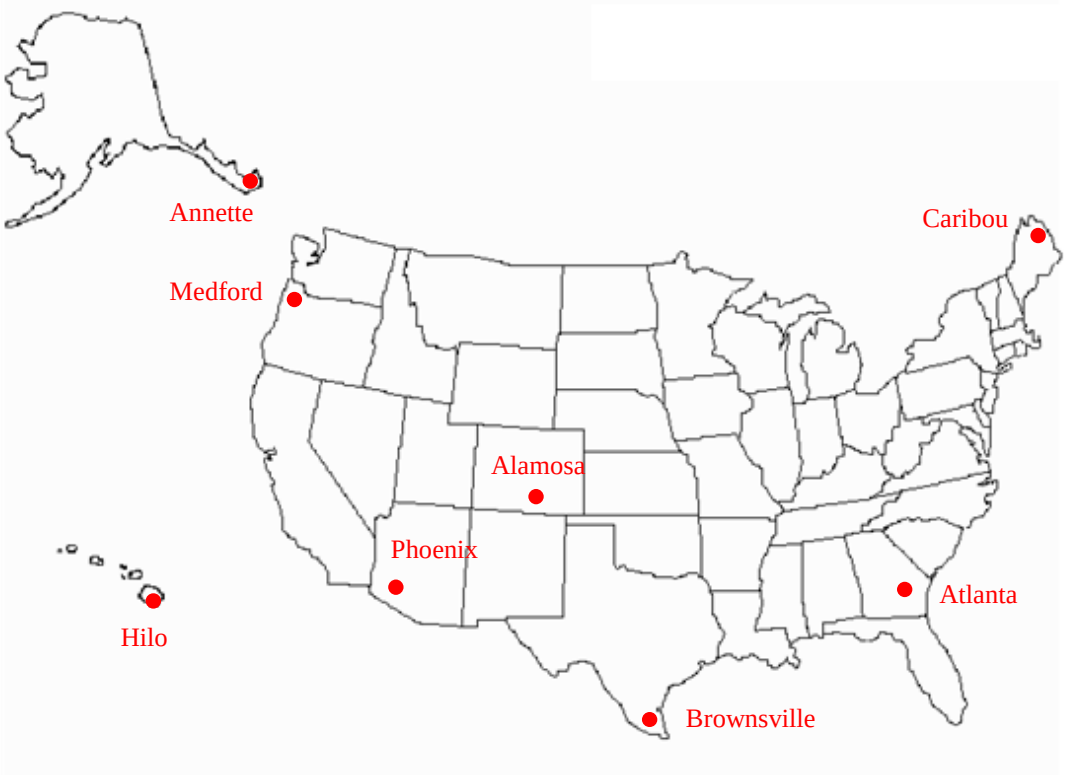

Figure 5.37: Selected cities pertaining to extreme summer and winter environmental conditions in the United States.

5.6.2 Vertical and Transverse Temperature Differentials

With the extreme environmental conditions, the 2D heat transfer analyses were performed to determine maximum vertical and transverse temperature differentials for the eight cities of the United States. With changes in bridge orientations, the E-W orientation provided the largest vertical and transverse temperature differentials in AASHTO-PCI standard sections. Moreover, among the AASHTO-PCI sections, Type-V and BT-63 sections showed larger vertical and transverse differentials than the other AASHTO-PCI sections. Indeed, the Type-V section, a little thicker than the BT-63 section, exhibited somewhat larger vertical and transverse temperature differentials. Therefore, for the Type-V section in the E-W orientation, maximum vertical and transverse temperature differentials were evaluated under extremes environmental conditions in the summer and the winter, respectively, for the eight cities of the United States.

Table 5.14 shows the vertical and transverse temperature differentials obtained from the 2D heat transfer analyses. The vertical temperature differentials were a maximum of 31.1°C (56.0°F) in Alamosa, Colorado, and a minimum of 22.6°C (40.7°F) in Annette, Alaska. In general, the vertical temperature differentials were around 30°C (54°F) in Medford, Oregon, Alamosa, Colorado, and Phoenix, Arizona, located in the Western United States, and around 26°C (47°F) in Brownsville, Texas, Atlanta, Georgia, and Caribou, Main, located in the Eastern United States. The city of Hilo, Hawaii, was 24°C (43°F), and Annette, Alaska, was 23°C (41°F).

The maximum transverse temperature differentials, 24°C (43°F) in the top flange, 19°C (34°F) in the web, and 29°C (52°F) in the bottom flange, also occurred in Alamosa, Colorado. The remaining cities of the continental United States, Phoenix, Arizona, Medford, Oregon, Alamosa, Colorado, Atlanta, Georgia, and Brownsville, Texas, were in the range of 18°C (32°F) to 21°C (38°F) in the top flange, 15°C (27°F) to 17°C (31°F) in the web, and 22°C (40°F) to 25°C (45°F) in the bottom flange. The transverse differentials in Hilo, Hawaii, were 16°C (29°F), 15°C (27°F), and 22°C (40°F) in the top flange, in the web, and in the bottom flange, respectively. Annette, Alaska, showed transverse temperature differentials of 13°C (23°F) in the top flange, 11°C (20°F) in the web, and 15°C (27°F) in the bottom flange.

In conclusion, since both maximum vertical and transverse temperature differentials were observed in Alamosa, Colorado, the vertical thermal differential defined in Atlanta, Georgia, increases from 27°C (49°F) to 31°C (56°F). The T_2, the temperature at the bottom of the top flange shown in Figure 5.30, is the same 5°C (9°F) as defined in Atlanta, Georgia. The transverse temperature differentials increase to 24°C (44°F) for the top flange, 19°C (35°F) for the web, and 29°C (53°F) for the web. Figures 5.38 and 5.39 show the vertical and transverse temperature gradients proposed in this study for the thermal design of prestressed concrete bridge girders in the United States.

Table 5.14: Vertical and transverse temperature differentials for the eight cities of the United States.

Cities	Vertical Differentials, °C (°F)	Transverse Differentials, °C (°F)		
		Top flange	Web	Bottom flange
Alamosa, CO	31.1 (56.0)	24.2 (43.5)	19.2 (34.6)	29.3 (52.7)
Phoenix, AZ	29.6 (53.3)	20.5 (36.9)	16.8 (30.2)	25.3 (45.5)
Medford, OR	29.9 (53.7)	18.3 (33.0)	15.1 (27.1)	22.0 (39.6)
Atlanta, GA	26.7 (48.0)	20.1 (36.1)	16.4 (29.4)	24.6 (44.2)
Brownsville, TX	25.6 (46.0)	18.2 (32.8)	15.2 (27.4)	23.3 (41.9)
Caribou, ME	27.2 (48.9)	20.9 (37.6)	16.9 (30.5)	24.3 (43.7)
Hilo, HI	23.8 (42.9)	16.4 (29.4)	14.6 (26.2)	22.0 (39.5)
Annette, AK	22.6 (40.7)	13.0 (23.4)	10.9 (19.6)	15.0 (27.0)

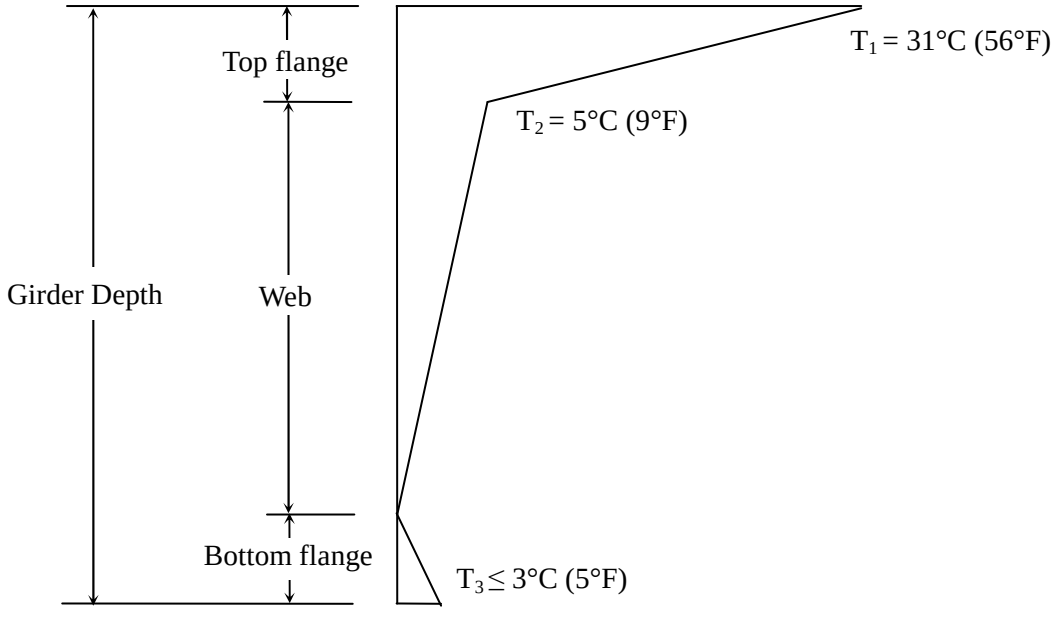

Figure 5.38: The design vertical temperature gradient along the depth of prestressed concrete bridge girders in the United States.

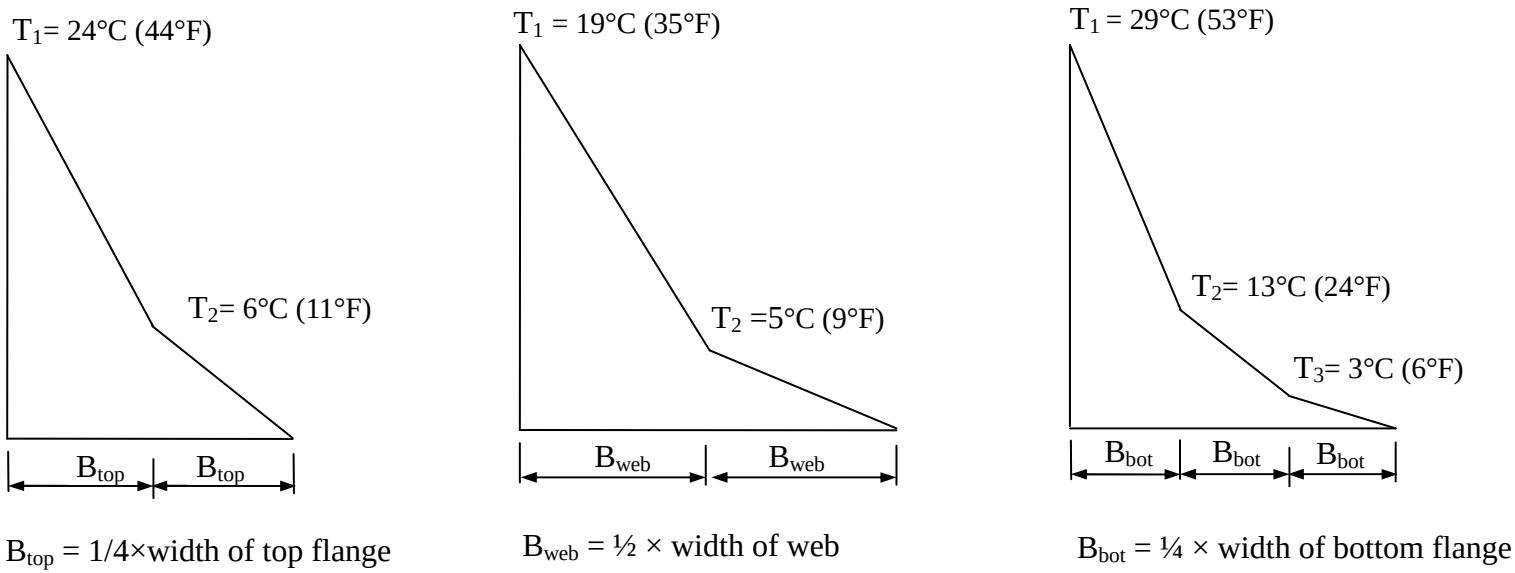

B_{top} = 1/4×width of top flange

B_{web} = ½ × width of web

B_{bot} = ¼ × width of bottom flange

(a) Top flange (b) Web (c) Bottom flange

Figure 5.39: Design transverse temperature gradients of prestressed concrete bridge girders in the United States (Not to scale).

CHAPTER 6

STRUCTURAL BEHAVIOR OF A PRESTRESSED CONCRETE BRIDGE GIRDER DURING CONSTRUCTION

6.1 Introduction

The largest vertical and transverse temperature gradients were found to occur in the deeper and wider cross-sections of the Type-V and BT-63. The BT-63 girder was then selected for further thermal response analyses in an east-west orientation for extreme summer and winter environmental conditions in Atlanta, Georgia. A three-dimensional (3D) nonlinear finite element analysis was performed to evaluate the combined effects of the thermal response, initial imperfections, and support conditions on the behavior of the prestressed concrete girder during construction. Furthermore, a simple beam model was developed for calculating vertical and transverse thermal movements induced by nonlinear temperature gradients for simply supported girders.

6.2 3D Finite Element Thermal Response Analysis

The thermal response analysis is composed of a static analysis and its subsequent thermal stress analysis. The 3D static analysis was first performed to introduce camber and stresses induced by prestressing forces to the girder. The support boundary condition involved in this analysis was defined as a simply supported condition as shown in Figure 4.4. The 3D finite element thermal stress analysis was then performed to determine the thermal response of the girder due to environmental thermal effects. During the analysis, the temperature distributions obtained from the 2D heat transfer analysis were transferred to the 3D finite element model with a constant temperature variation along the length of the girder. Since prestressed concrete girders are generally supported by elastomeric bearing pads, the stiffness of the bearing pads was modeled as nonlinear springs. For

comparison, the simply supported boundary conditions were also included in this analysis. An overview of the 3D thermal response analysis is illustrated in Figure 6.1.

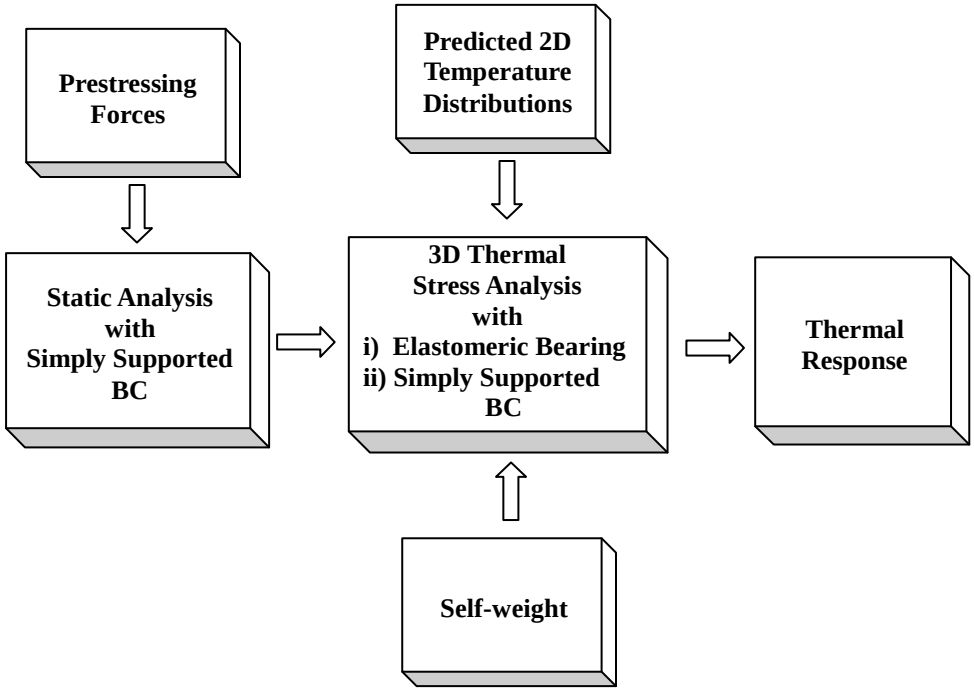

Figure 6.1: Overview of the 3D thermal response analysis process.

6.2.1 Finite Element Model of the Prestressed Concrete BT-63 Girder

For the design span of prestressed concrete bridge girders, Chapter 6 of the *PCI Bridge Design Manual* (2003) provides a preliminary design reference. Figure 6.2 is the preliminary design chart of the BT-63 girder extracted from the *PCI Bridge Design Manual* (2003). According to Figure 6.2, the AASHTO BT-63 girder can be extended to a maximum of 130 feet long using 12-ksi concrete compressive strength, 8-foot girder spacing, and 44 0.6-inch diameter strands. The prestressed concrete BT-63 girder involved in this study was designed to be 100 feet long with 7-ksi concrete compressive strength, 6-foot girder spacing, and 24 prestressing strands as shown in Figure 6.2. All the strands are 0.5-inch diameter special low relaxation strands. The detailed arrangement of the strands is illustrated in Figure 6.3, in which the 4 strands are placed in

the top flange and the 20 strands in the bottom flange. The four strands were stressed to 10,000 pounds each, and all the remaining strands were stressed to 33,818 pounds each. As described in Chapter 4, the prestressing strands were modeled using 3D truss elements, T3D2 in ABAQUS (2008), with 2 inches in length. The 100-foot BT-63 girder was modeled with 350,000 linear solid elements, C3D8 in ABAQUS.

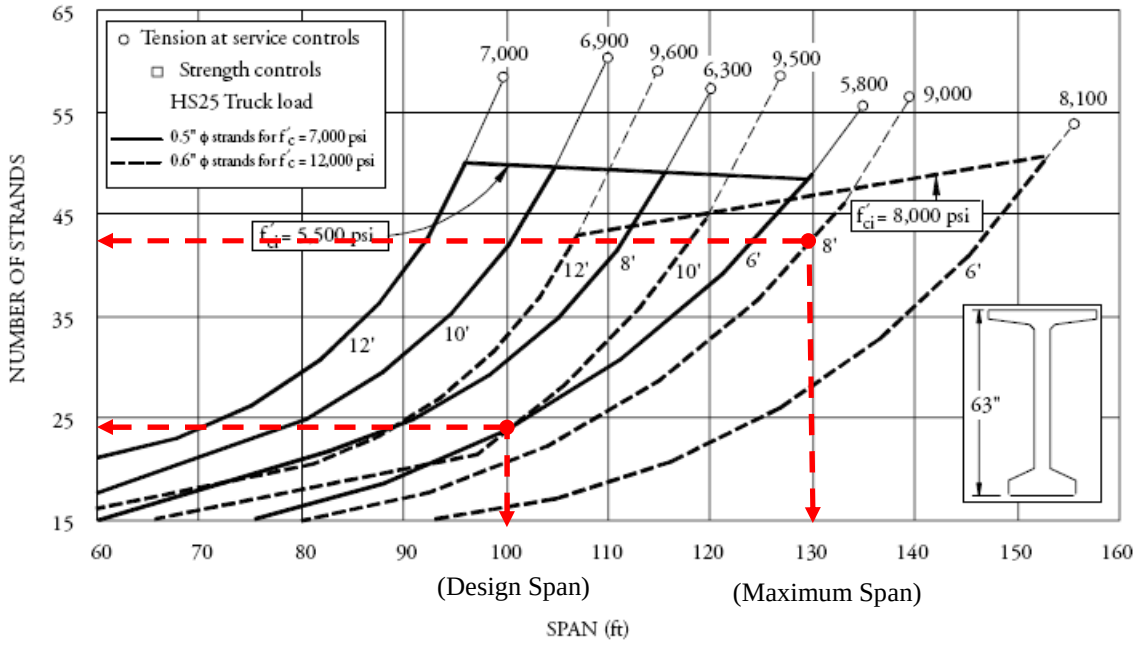

Figure 6.2: The preliminary chart of the AASHTO-PCI Bulb-Tee BT-63 section extracted from the *PCI Bridge Design Manual* (2003).

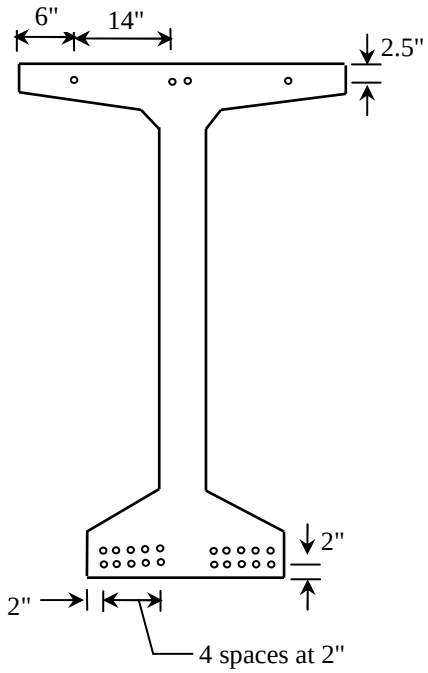

Figure 6.3: The arrangement of the prestressing strands in the BT-63 girder.

The material properties of concrete used in this study are shown in Table 6.1. Since the compressive strength of concrete was defined to be 7 ksi, the modulus of elasticity was calculated using the Equation (4.1) proposed by ACI Committee 435 (1995) for high-strength concrete more than 6 ksi. The density of concrete was assumed to be 150 lb/ft^3 as a normal-weight concrete. The coefficient of thermal expansion, which pertains to the thermal movement of the girder, was taken as 12×10^{-6} /°C, or 6×10^{-6} /°F (AASHTO, 2007) as used in Chapter 4.

The geometry and materials of 0.5-inch diameter low relaxation strands, the same values as used in Chapter 4, were taken from the *PCI Bridge Design Manual* (2003). The design yield strength of the strands is 245 ksi. After the yielding of the strands, or 0.0086 yield strain, the stress and strain relationship was defined to be perfectly plastic. The coefficient of the thermal expansion of the strands was 12×10^{-6} /°C, or 6×10^{-6} /°F.

Table 6.1: Material properties of concrete used in the thermal stress analysis.

Property	Density, ω_c (lb/in^3)	Modulus of elasticity, E_c (psi)	Poisson's ratio, υ	Coefficient of thermal Expansion, α (/°C)
Concrete	0.0868	4,131,130	0.2	12×10^{-6}

6.2.2 Support Conditions

Prestressed concrete bridge girders are generally supported by steel-reinforced elastomeric bearing pads which provide vertical support in compression and minimal horizontal restraint to the girder. However, the support condition of the elastomeric bearing pads could increase the movements of the girder particularly during construction. Thus, in order to account for the influence of the elastomeric bearing pad in the 3D finite element analyses, the effective vertical stiffness of the bearing pad was examined.

Since bridge engineers specify elastomeric bearing pads based on the hardness of the elastomer, the *AASHTO Standard Specifications* (2002) and the *AASHTO LRFD Bridge Design Specifications* (2007) provide the shear modulus of the elastomer, 95 to 130 psi, 130 to 200 psi, and 200 to 300 psi, for a nominal hardness of 50, 60, and 80, respectively. Based on the AASHTO specifications, the *GDOT Bridge and Structures Design Policy Manual* (2005) specifies that "the hardness should be 60 and the shear modulus shall be 130 to 200 psi." Thus, the elastomeric bearing pad involved in this study was based on the hardness of 60 as specified in the GDOT manual.

With the hardness of the elastomeric bearing pad, this study selected the stress and strain curve of a steel-reinforced elastomeric bearing from the *AASHTO LRFD Bridge Design Specifications* (2007) in terms of the shape factor of the bearing pad. For rectangular bearings without holes, the shape factor of one layer of an elastomeric bearing pad, *S*, is calculated using the following equation (AASHTO, 2002 & 2007):

$$S = \frac{LW}{2h_{r\max}(L+W)} \tag{6.1}$$

in which

L = the length of the elastomeric bearing parallel to the longitudinal girder axis,

W = the width of the bearing in the transverse direction, and

$h_{r\max}$ = the thickness of the thickest elastomeric layer in the elastomeric bearing.

Since the GDOT manual requires that the elastomeric bearing pads include a 3-inch diameter hole in the middle of the pads for a smooth dowel bar, the above equation was modified to account for the circular area when calculating the shape factor:

$$S = \frac{LW - (\pi D^2 / 4)}{h_{r\max}\left[2(L+W) + \pi D\right]} \tag{6.2}$$

in which D is the diameter of the hole in the bearing. The slotted hole at one end of the girder was assumed to be circular in the calculation of the shape factor.

For the width of the elastomeric bearing pad, the GDOT (2005) specifies that "the width of the pad shall be at least 2 inches narrower on each side than the nominal width of the bottom flange of Type-III and larger PSC beams." The length of the bearing pad, not specified in the GDOT manual, was based on the FDOT guideline (1997), and the thickness of the pad was taken from one bearing pad used for the BT-63 prestressed concrete girder in Georgia. Thus, the size of the elastomeric bearing pad of the BT-63 girder involved in this study was determined to be 10 inches long, 20 inches wide, and 2-3/8 inches thick with a 3-inch diameter hole in the middle as shown in Figure 6.4. The bearing pad is composed of 3/16-inch thick load plates and 1/4-inch thick covers on the

top and bottom of the bearing pad and three 5/64-inch internal plates equally spaced between load plates. Thus, the elastomer thickness of the outer and inner layers is 0.63 inches, and the shape factor of the steel-reinforced elastomeric bearing pads, calculated using Equation (6.2), is 8.8.

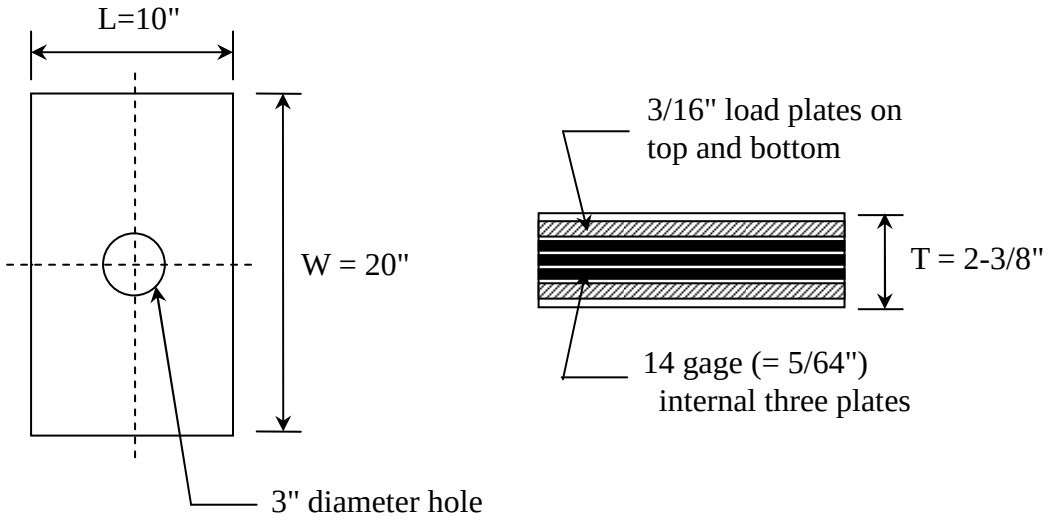

Figure 6.4: The configuration and dimensions of the steel-reinforced elastomeric bearing pad.

From a durometer hardness of 60 and a shape factor of 8.8, the effective compressive stiffness of the bearing pad was calculated using the stress and strain curve of the steel-reinforced elastomeric bearing given in the *AASHTO LRFD Bridge Design Specifications* (2007). Figure 6.5 depicts the stress and strain curves for 60 durometer steel-reinforced elastomeric bearings for various shape factors. For a shape factor of 8.8, the stress and strain curve was defined as a bi-linear relationship with one inflection point denoted as A in Figure 6.5, and the compressive modulus of the bearing pad, E_s, was calculated. The vertical bearing stiffness was then derived as follows:

$$k_y = \frac{E_s A}{H} \tag{6.3}$$

in which A = the area of the bearing pad, and

H = the thickness of the bearing.

The calculated compressive modulus and stiffness of the steel-reinforced elastomeric bearing pad is summarized in Table 6.2. Up to 0.028 compressive strain, or 600 psi compressive stress, the compressive stiffness is 1,741 kips/in, and after that, the compressive stiffness increases to 2,708 kips/in.

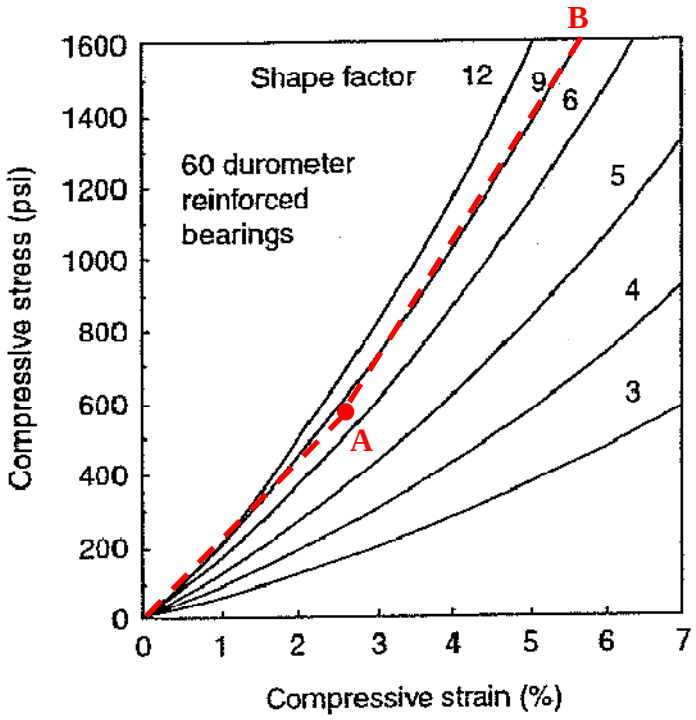

Figure 6.5: The stress and strain curve of the steel-reinforced elastomeric bearing pad extracted from the AASHTO specifications (AASHTO, 2007).

Table 6.2: The shape factor and compressive stiffness of the elastomeric bearing pad determined for the current study.

Shear Factor	Shear Modulus (ksi)	Compressive Modulus (ksi)		Compressive Stiffness (kips/in)	
		O - A	A - B	O - A	A - B
8.8	0.165	21.4	33.3	1,741	2,708

In 2000, Yazdani et al. analyzed the elastomeric bearing stiffness of standard precast prestressed concrete bridge girders using finite element analysis. Yazdani et al. (2000) indicated that the vertical stiffness calculated from the AASHTO specifications was close to that obtained from the finite element analysis. This study also recommended that the effects of the horizontal bearing restraint be ignored in the design of AASHTO precast concrete bridge girders. Thus, the horizontal stiffness of the bearing pad was assumed to be zero in this study. However, the lateral resistance to the girder provided by the dowel bar in the middle of the girder was included in the analyses.

The elastomeric bearing pad was then modeled using a series of nonlinear spring elements, SPRING1 in ABAQUS, which provide restraint only when they are compressed. The compressive stiffness of individual springs was calculated based on the mesh above the pad in the bottom flange of the girder. Thus, the vertical strings were categorized as corner, edge, and center spring elements according to the location of the springs within the bearing surface as shown in Figure 6.6. Table 6.3 presents the compressive stiffness of the spring elements calculated from the appropriate tributary area: k_1 up to 0.028 compressive strain and k_2 for strain greater than 0.028. The force and displacement relationship defined from the compressive stiffness was shown in Figure 6.7. In addition to the nonlinear springs, dowel bars located in the middle of the bearing pads were defined as shown in Figure 6.8, in which the arrows represent the restrained directions due to the dowel bars at the both ends. For comparison purposes, the bearing pads were also modeled as rigid vertical restraints as previously shown in Figure 4.4.

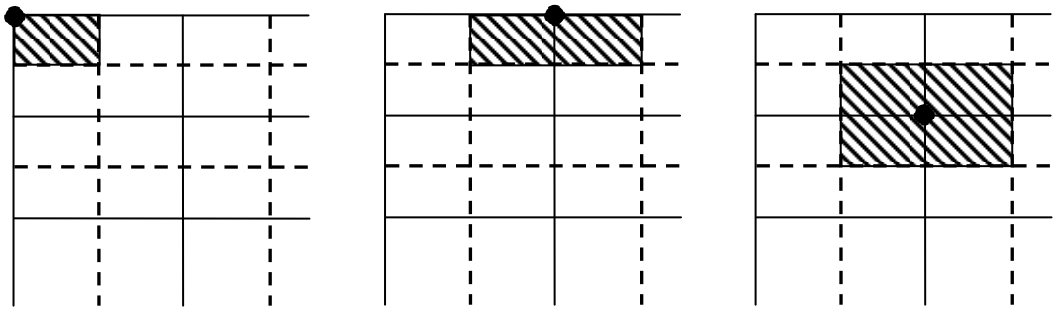

(a) Corner spring (b) Edge spring (c) Center spring

Figure 6.6: The relationships between each spring element and tributary area.

Table 6.3: The vertical compressive stiffness of the spring elements.

Type of Spring Elements	Number of Elements	Spring Stiffness (kip/in)	
		k_1	k_2
Corner springs	4	4.35	6.77
Edge springs	46	8.71	13.54
Center springs	76	17.41	27.08

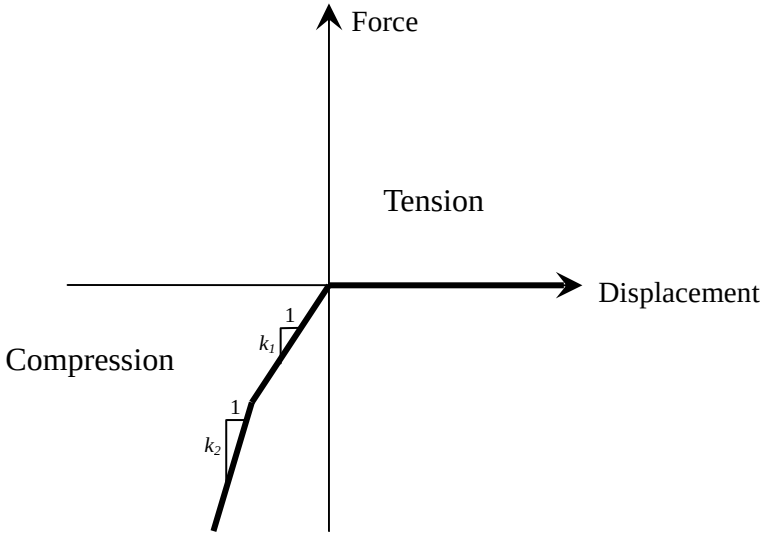

Figure 6.7: The force and displacement relationship of the spring element.

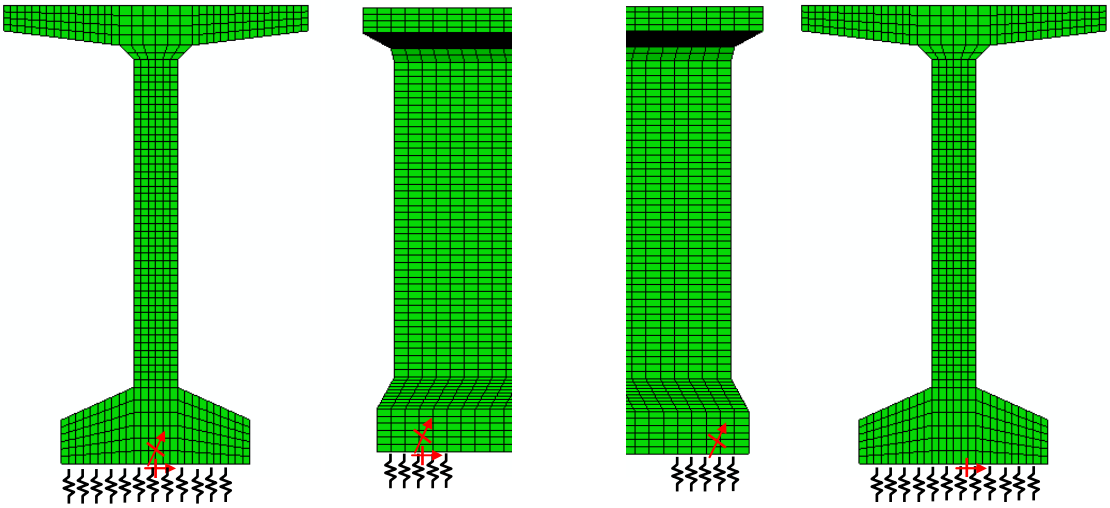

(a) One end of the girder (b) Other end of the girder

Figure 6.8: The support boundary conditions of the BT-63 girder.

6.2.3 Thermal Movements

This section presents the thermal response of the prestressed concrete BT-63 girder obtained from the 3D finite elements analyses. To evaluate the effects of elastomeric bearing pads on the thermal behavior of the girder, the thermal response of the girder obtained with elastomeric bearing pads was compared with the thermal response of the girder with a simply supported boundary condition.

Table 6.4 summarizes the maximum longitudinal, vertical, and transverse thermal movements obtained from the 3D thermal stress analyses in the summer and the winter for the two boundary condition cases. In the elastomeric bearing pad condition, the maximum longitudinal thermal movements were 0.18 inches in the summer and 0.27 inches in the winter. Compared with the simply supported boundary condition, the bearing pad condition exhibited somewhat smaller longitudinal movements.

The maximum vertical thermal movements with elastomeric bearing pads were 0.73 inches in the summer and 0.43 inches in the winter. Compared with the simply supported boundary condition, the elastomeric bearing pads increased the vertical thermal

movements from 0.42 inches to 0.73 inches in the summer and from 0.18 inches to 0.43 inches in the winter. The maximum transverse thermal movements were 0.40 inches in the summer and 0.77 inches in the winter. As expected, there were no differences in the maximum transverse thermal movements between the elastomeric bearing and the simply supported boundary conditions.

Table 6.4: Maximum longitudinal, vertical, and transverse thermal movements at mid-span with the simply supported (SS) and elastomeric bearing (EB) conditions in the summer and the winter.

(Units: inches)

Seasons	Longitudinal		Vertical		Transverse					
	SS	EB	SS	EB	SS			EB		
					Top Flange	Web	Bottom Flange	Top Flange	Web	Bottom Flange
Summer	0.22	0.18	0.42	0.73	0.39	0.39	0.40	0.39	0.39	0.40
Winter	0.30	0.27	0.18	0.43	0.70	0.74	0.77	0.70	0.74	0.77

Figure 6.9 shows variations in the longitudinal thermal movements of the BT-63 girder due to variations in temperatures with the elastomeric bearing pads. For the vertical thermal movements, Figure 6.10 shows hourly variations in the vertical thermal movements of the girder with the elastomeric bearing pad condition. The initial vertical camber induced by the 24 prestressing strands was 1.29 inches, and it decreased to 0.32 inches due to the self-weight of the girder. The environmental thermal effects increased the vertical displacements to 1.05 inches at 3 p.m. in the summer and 0.75 inches at 2 p.m. in the winter.

Variations in the transverse thermal movements of the girder in the elastomeric bearing boundary condition are shown in Figure 6.11. The maximum transverse thermal displacement is 0.40 inches in the summer and 0.77 inches in the winter at 1 p.m.

Contrary to the vertical thermal movements, the winter exhibited larger transverse thermal movements because of higher solar intensity on the vertical surface. The support condition of the elastomeric bearing pads did not affect the transverse thermal movements.

Figures 6.12 and 6.13 show the contours of the maximum vertical and transverse displacements obtained from the 3D thermal stress analyses in the summer and the winter, respectively.

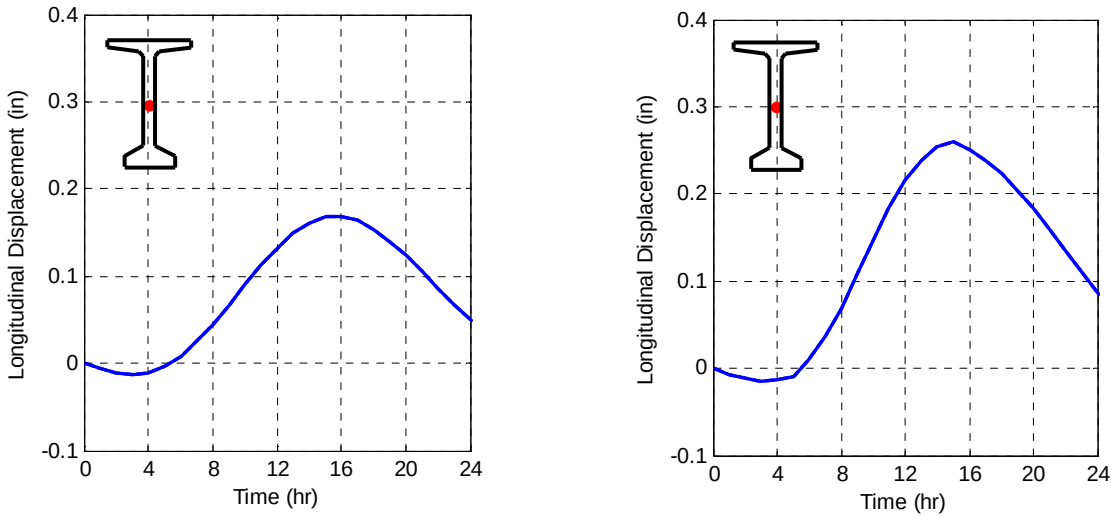

(a) Summer (b) Winter

Figure 6.9: Variations in the longitudinal thermal movements at the end of the prestressed BT-63 girder with the elastomeric bearing condition in the summer and the winter.

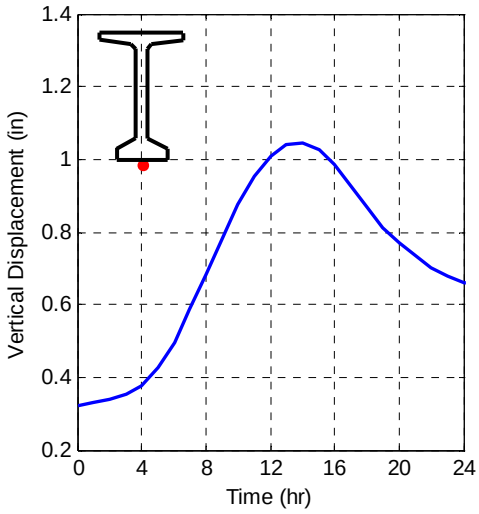

(b) Summer

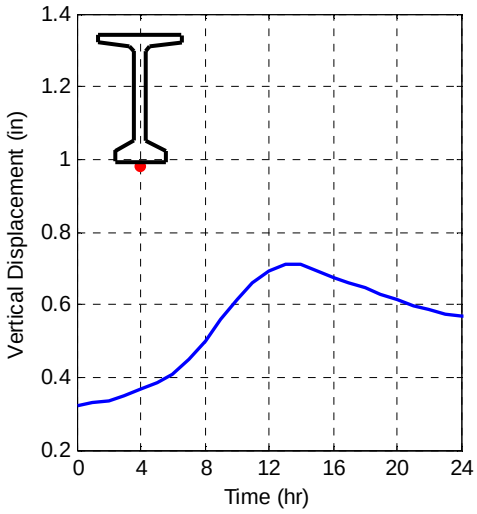

(b) Winter

Figure 6.10: Variations in the vertical thermal movements of the prestressed BT-63 girder at mid-span with the elastomeric bearing condition in the summer and the winter.

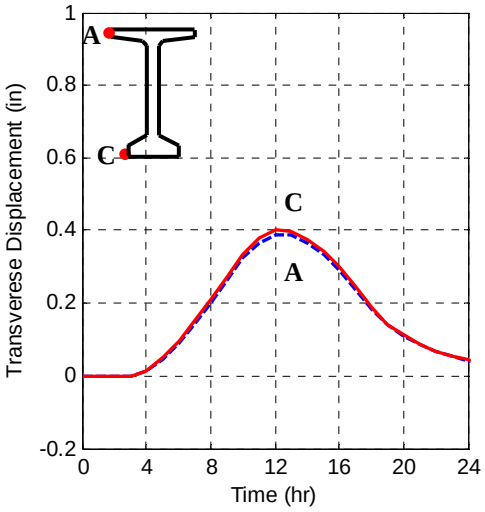

(a) Summer

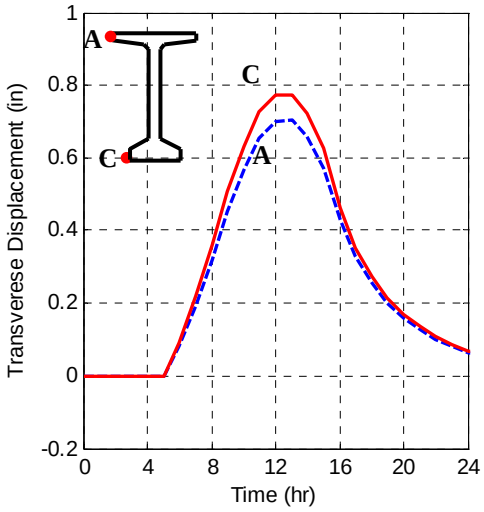

(b) Winter

Figure 6.11: Variations in the transverse thermal movements of the prestressed BT-63 girder at mid-span with the elastomeric bearing condition in the summer and the winter.

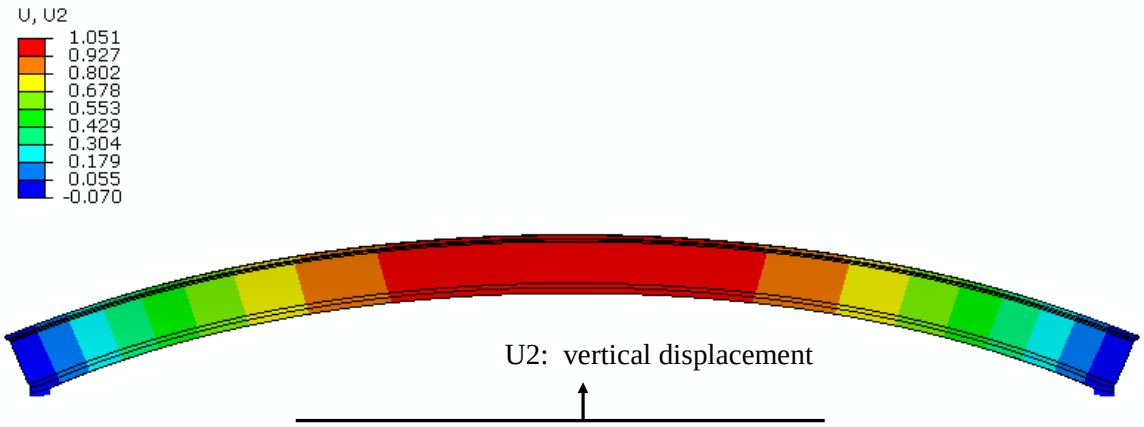

(a) Vertical displacement at 3 p.m. (units: inches)

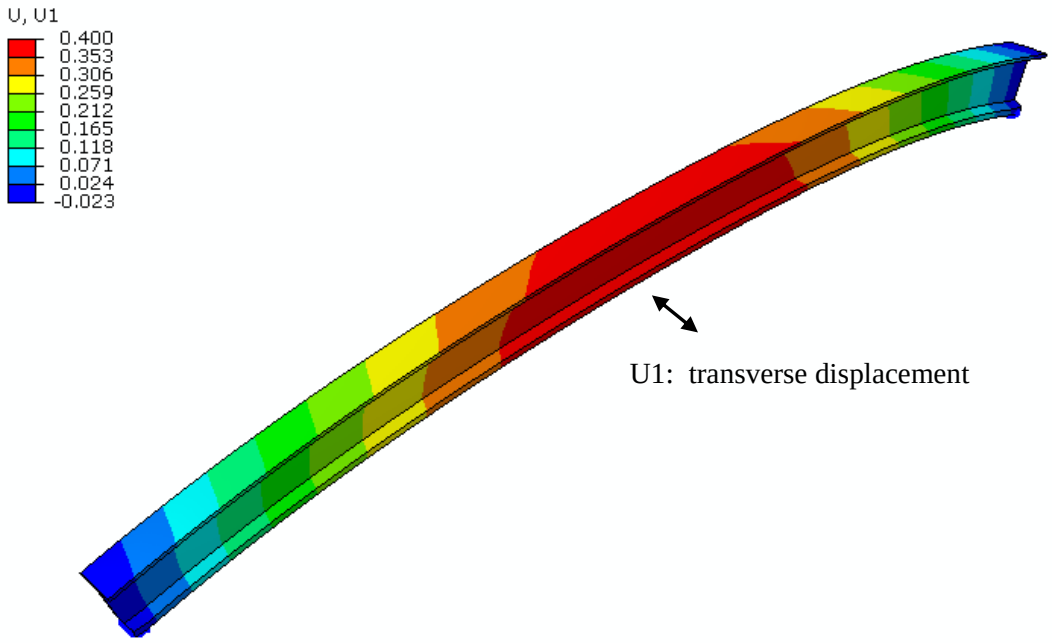

(b) Transverse displacement at 1 p.m. (units: inches)

Figure 6.12: The vertical and transverse displacement contours of the prestressed BT-63 girder supported by the elastomeric bearing pads in the summer (Scale factor =100).

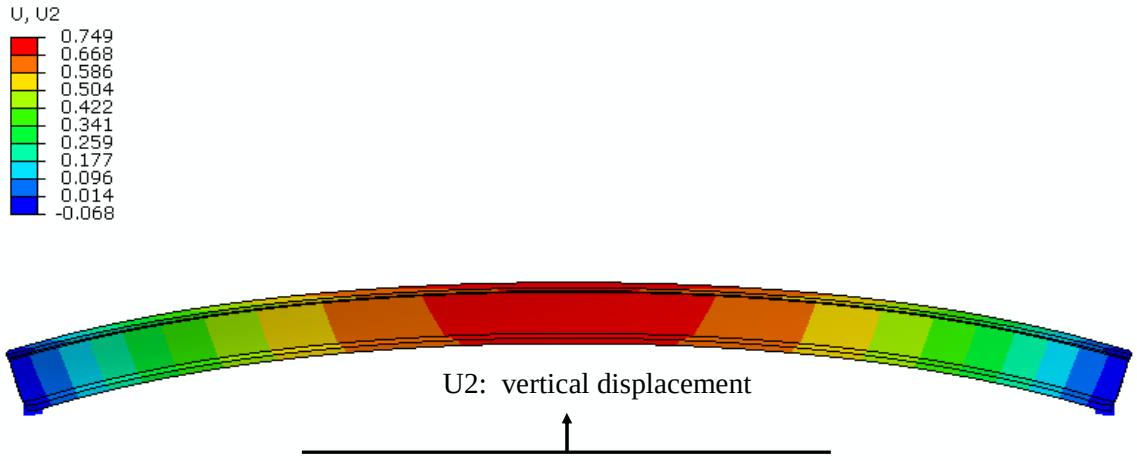

(a) Vertical displacement at 2 p.m. (units: inches)

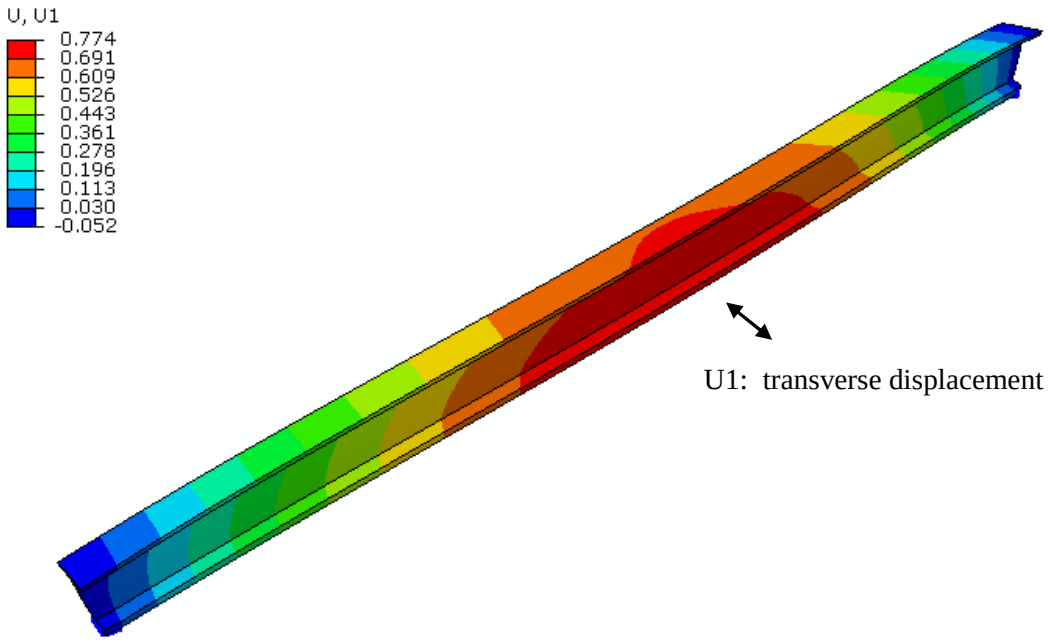

(b) Transverse displacement at 1 p.m. (units: inches)

Figure 6.13: The vertical and transverse displacement contours of the prestressed BT-63 girder supported by the elastomeric bearing pads in the winter (Scale factor =100).

6.2.4 Thermal Stresses

In addition to the thermal movements, Figures 6.14 and 6.15 show variations in the longitudinal thermal stresses on the top and bottom surfaces of the BT-63 girder at mid-span. Concrete compressive stresses due to the prestressing forces and self-weight were about 830 psi on the top surface and 1,100 psi on the bottom surface. With larger vertical temperature gradients in the summer, the compressive stresses increased to about 1,130 psi on the top surface and 1,330 psi on the bottom surface as shown in Figure 6.14(a). In the winter, the compressive stresses on the top and bottom surfaces only slightly changed due to the smallest vertical temperature gradients.

Variations in concrete stresses on the top, the middle, and the bottom of the web are also shown in Figure 6.15. Due to increased vertical and transverse temperature gradients in the web in the winter as discussed in Chapter 4, the middle and bottom of the web showed higher compressive stresses of around 1,480 and 1,640 psi at 1 p.m., respectively, as shown in Figure 6.15(b). The top of the web which is shadowed by the top flange, exhibited little transverse temperature gradient resulting in a decrease in compressive stresses.

Variations in the stresses of the top and bottom strands are shown in Figures 6.15 and 6.16, respectively, for the summer and the winter. The top strand was prestressed to about 65 ksi and the bottom strand to about 208 ksi. The stresses of the top strand reduced to 59 ksi due to the self-weight of the girder, and the stresses of the bottom strand increased to 213 ksi. With changes in temperatures, the tensile stresses of the top strand increased to 69 ksi in the summer and the winter as shown in Figure 6.16. The stresses of the bottom strand shown in Figure 6.17 increased to 216 ksi in the summer and 219 ksi in the winter.

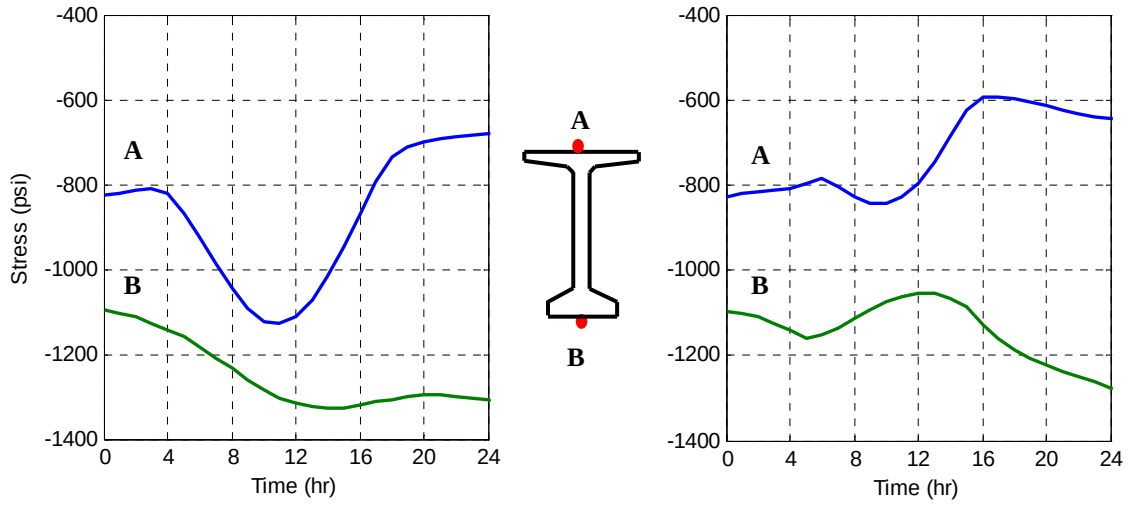

(a) Summer (b) Winter

Figure 6.14: Variations in the longitudinal stresses on the top and bottom surfaces at mid-span in the summer and the winter.

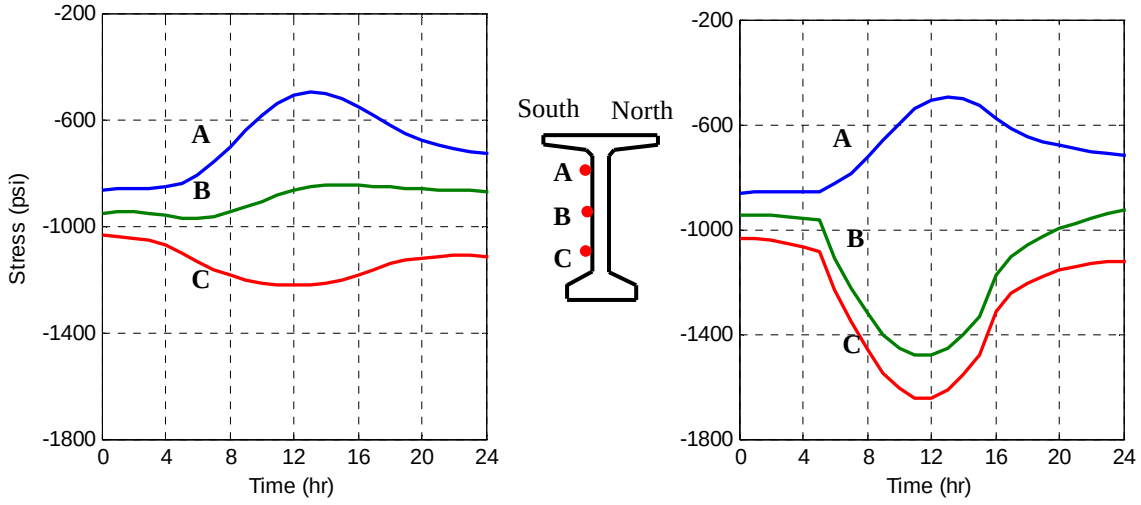

(a) Summer (b) Winter

Figure 6.15: Variations in the longitudinal stresses on the top, the middle, and the bottom of the web at mid-span in the summer and the winter.

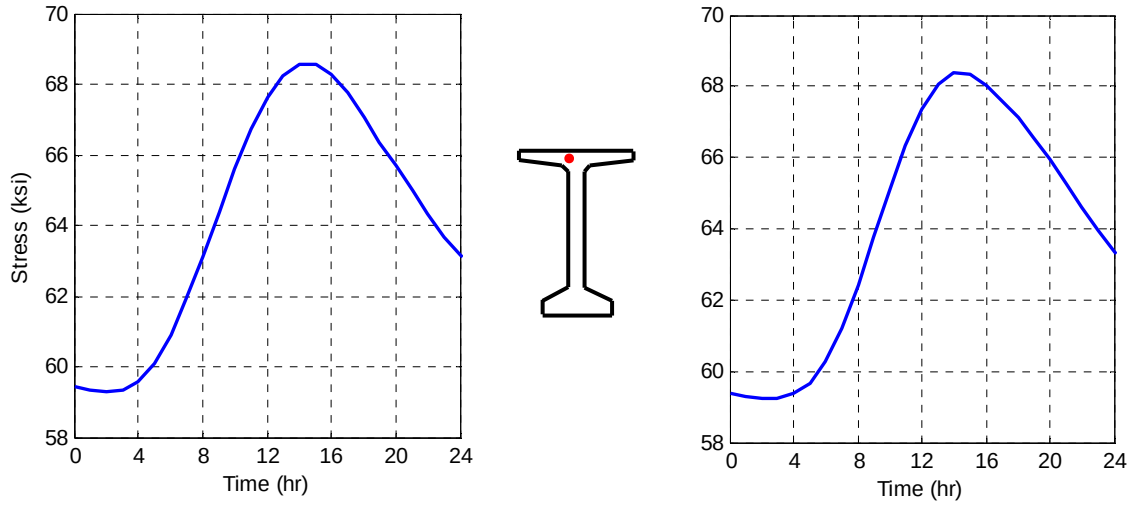

(a) Summer (b) Winter

Figure 6.16: Variations in the stresses of a top strand at mid-span in the summer and the winter.

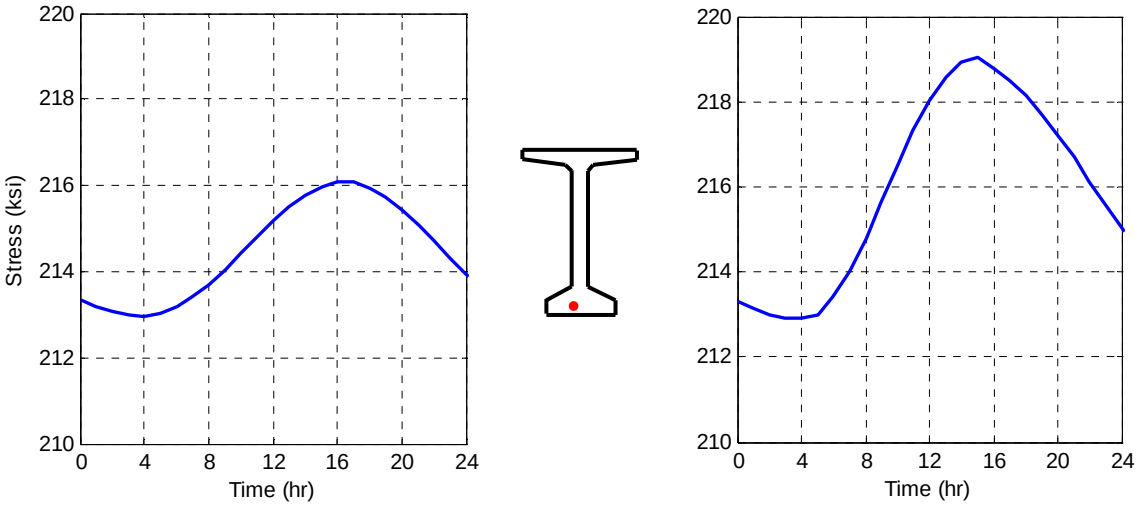

(a) Summer (b) Winter

Figure 6.17: Variations in the stresses of a bottom strand at mid-span in the summer and the winter.

6.3 Behavior of a Prestressed Concrete Girder During Construction

In addition to the environmental thermal effects, fabrication and construction errors are combined to determine the behavior of prestressed concrete bridge girders prior to the placement of cross bracing and the deck slab. The main imperfections considered in this study are initial sweep in the girder and the slope of the bearing supports. The sweep is a lateral deformation from the center of the straight girder at mid-span. The 3D finite element analysis was performed to account for changes in geometry and stress states of the girder due to the initial sweep and support slope. Since the largest transverse thermal movements were observed in the winter, temperature distributions were determined using extreme winter environmental conditions in Atlanta, Georgia.

6.3.1 Procedures of Sequential Analyses

To analyze the combined effects of initial sweep, bearing support slope, and thermal response on the prestressed concrete girder, a 3D finite element analysis procedure was developed which could update the geometry and stresses of the girder in each construction state. The 3D finite element sequential analysis procedure is illustrated in Figure 6.18.

The first static analysis shown in Figure 6.18 is performed to generate the initial sweep in the girder and camber and stresses due to prestressing forces. To define the shape of the initial sweep, the self-weight of the girder was applied in the lateral direction. The magnitude of the initial sweep was specified by scaling the maximum lateral deformation obtained from the static analysis to a target sweep value. The camber and stresses induced by the prestressing forces were obtained from initial stress conditions, 65.4 ksi to the top strands and 222.1 ksi to the bottom strands. Since the sweep and the camber occur prior to the placement of the girder on the bearing supports, the support boundary condition in the first static analysis was assumed to be a simply supported condition as described in Figure 4.4.

The shape and value of the initial sweep and the camber and stresses of the girder obtained from the first static analysis were used to update the geometry and stress states of the girder for the next analysis. The slope of the bearing support was then produced by applying displacement boundary conditions corresponding to the support slope to the upgraded 3D finite element model. Since the support slope is a stress-free behavior, the stress states in the concrete and prestressing strands are the same as those defined in the first static analysis.

Finally, the prestressed concrete girder updated from the previous analyses—the first static analysis for initial sweep in the girder and the effects of prestressing forces and the second static analysis for the support slope of the girder—provided a reference configuration of the next 3D nonlinear finite element analysis. The self-weight of the girder and the winter temperature distributions obtained from the 2D heat transfer analysis were applied to evaluate the behavior of the prestressed concrete girder. This final 3D finite element analysis accounted for the nonlinearity of the geometry and the nonlinear behavior of the elastomeric bearing pads.

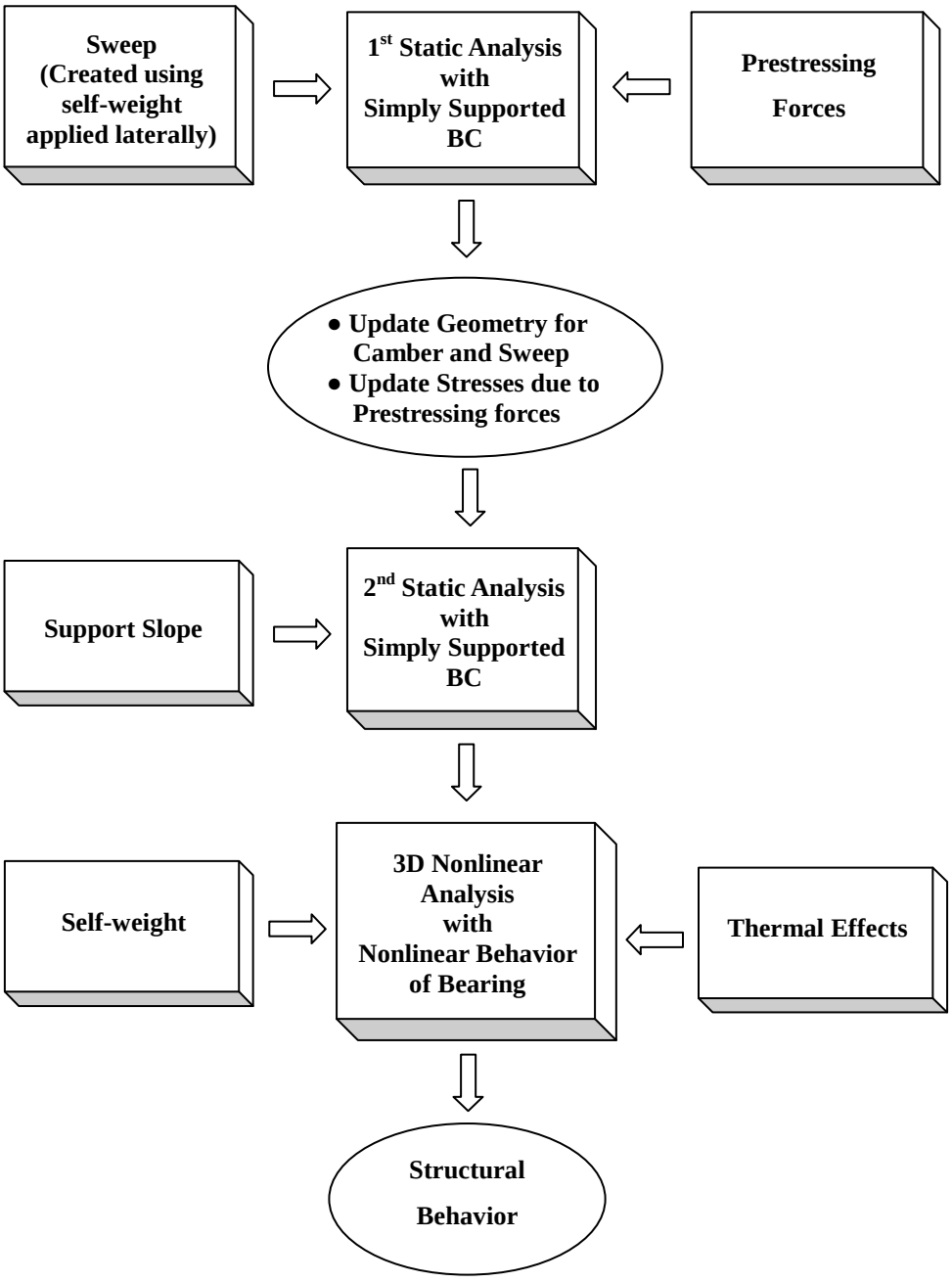

Figure 6.18: Overview of the 3D finite element sequential analysis.

6.3.2 Structural Analyses with Support Slope and Initial Sweep

The effect of support slope on the behavior of the prestressed BT-63 girder was first evaluated with no initial sweep. The support slopes chosen for this study are 0, 2.5, and 5°. The angle of 0° represents a perfectly flat condition between the girder and the supports. The maximum value of support slope of 5° was chosen based on the maximum measured support slope of 0.0079 rad. (4.5°) on the collapsed girders in Arizona (Oesterle et al., 2007). The camber and stresses induced by prestressing forces were included in the analysis. Figure 6.19(a) shows the 3D finite element model upgraded by support slope and prestressing forces. The 3D finite element nonlinear analysis was performed to investigate the behavior of the BT-63 girder due to the self-weight of the girder and thermal effects.

For a support slope of 5° at both ends of the girder, the vertical and transverse responses of the prestressed BT-63 girder were then examined with increases in initial sweep from 1.25 inches to 5.00 inches. An initial sweep of 1.25 inches was selected in accordance with the sweep tolerance of 1/8 inches per 10-foot length of prestressed concrete beams provided in the *PCI Bridge Design Manual* (2003). Figure 6.19(b) shows the 3D finite element models after the changes in the geometry and stress state from initial sweep, support slope, and prestressing forces. The self-weight of the girder and the thermal effects determined from extreme winter environmental conditions in Atlanta, Georgia were applied to the 3D nonlinear finite element models.

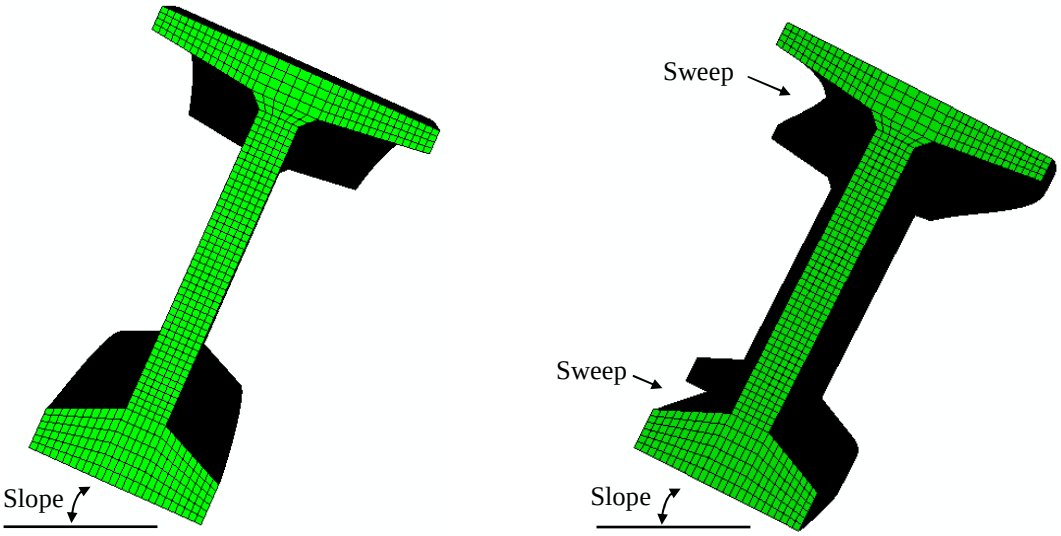

(a) Support slope with no initial sweep (b) Support slope and initial sweep

Figure 6.19: The finite element models after accounting for support slope and initial sweep.

6.3.3 Vertical Behavior of the Prestressed Concrete Girder

Figures 6.20 and 6.21 show variations in the vertical response of the prestressed BT-63 girder at mid-span with increases in support slope and initial sweep. For a geometrically perfect structure, or no initial sweep in the girder, Figure 6.20 exhibits the vertical movements of the girder for the support slopes of 0°, 2.5°, and 5°. As the support slope increased, vertical deformations due to the self-weight also increased. After the girder was installed on the sloped bearing support, it experienced variations in the vertical movements due to the combined thermal effects with the self-weight. However, the increases in the support slope only slightly changed the vertical thermal movements as shown in Figure 6.20.

To evaluate the influence of the initial sweep on the vertical behavior of the girder, Figure 6.21 shows variations in the vertical movements of the girder with increases in initial sweep from 1.25 inches to 5.00 inches. The support slope was kept at a constant 5° during these analyses. For the initial sweep of 4.5 and 5.0 inches, the 3D

nonlinear finite element analyses stopped at 2 p.m. and at 10 a.m., respectively, with error messages of “largest increment of displacement” in the lateral direction at 30,157,001 nodes (located on the top flange at mid-span) and “excessive distortion at a total of 1,398,666 integration points in solid elements.” According to the messages, the excessive distortion was caused by the large increment of lateral displacements which is an indication of a structural instability in the model.

Table 6.5 summarizes the maximum vertical deformations of the girder caused by self-weight and temperature variations with increases in support slope and initial sweep. With increases in the support slope from 0° to 5°, the vertical deformations due to the self-weight increased from 0.96 inches to 1.03 inches, and the maximum vertical thermal deformations decreased from 0.38 inches to 0.33 inches. As the initial sweep increased from 0 to 4.5 inches with a constant support slope of 5°, the vertical deformations also increased from 1.03 inches to 1.07 inches due to the self-weight and decreased from 0.33 inches to 0.27 inches due to the combined thermal effects with the self-weight. Furthermore, the changes in the vertical deformations with increase in support slope and initial sweep are presented in Figure 6.22.

Figure 6.23 illustrates the contours of the vertical displacements obtained from the 3D nonlinear finite element analyses for the prestressed BT-63 girder with an initial sweep of 3.5 inches and a support slope of 5°. The maximum vertical displacements in the end of the top flange were 2.04 inches at mid-section and 1.71 inches at the end of the girder at 3 p.m.

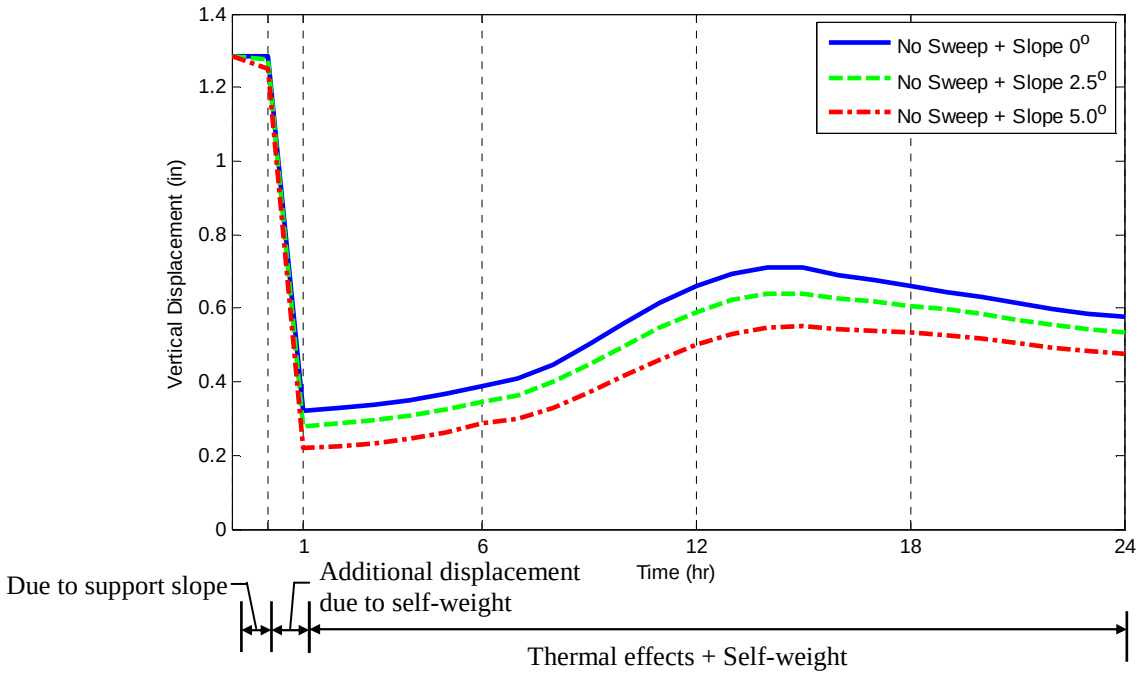

Figure 6.20: Variations in the vertical displacements of the BT-63 girder at mid-span during construction with increases in support slope with no initial sweep.

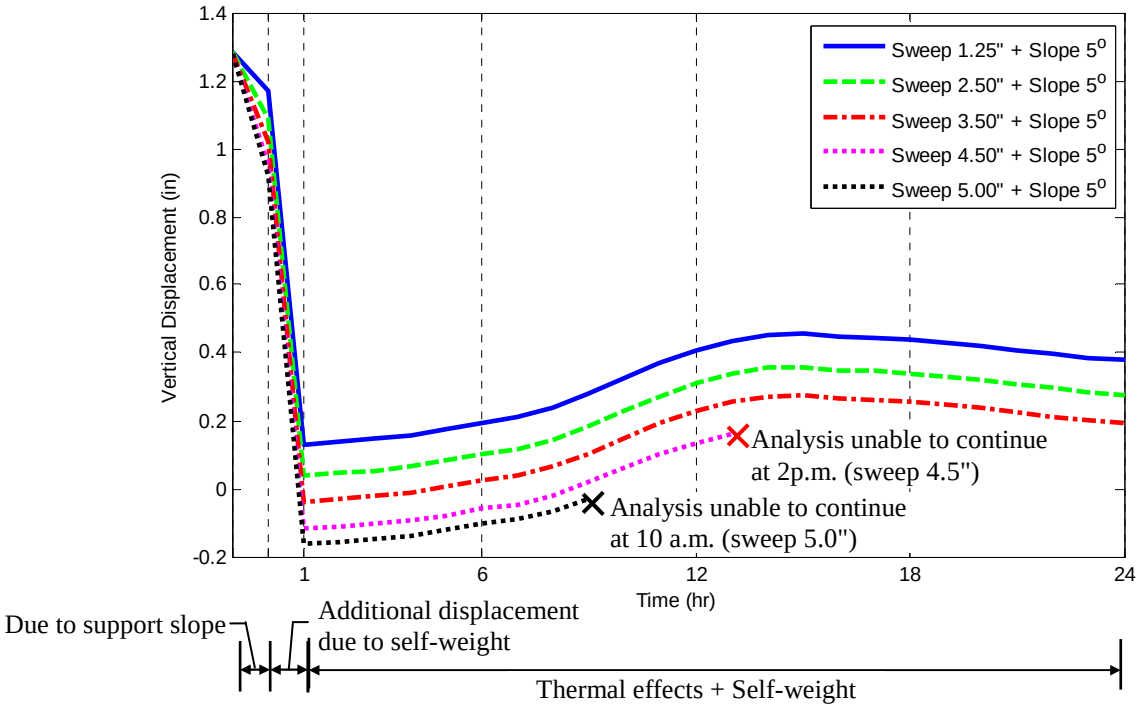

Figure 6.21: Variations in the vertical displacements of the BT-63 girder at mid-span during construction with increases in initial sweep and a support slope of 5°.

Table 6.5: The maximum vertical deformations of the BT-63 girder due to self-weight and thermal effects with increases in initial sweep and support slope.

Initial Sweep (inches)	Support Slope (degrees)	Vertical Deformation (inches)	
		Only self-weight	Thermal effects
0.00"	0.0°	- 0.99	+ 0.38
0.00"	2.5°	- 0.98	+ 0.35
0.00"	5.0°	- 1.03	+ 0.33
1.25"	5.0°	- 1.04	+ 0.32
2.50"	5.0°	- 1.05	+ 0.31
3.50"	5.0°	- 1.06	+ 0.31
4.50"	5.0°	- 1.07	+ 0.27

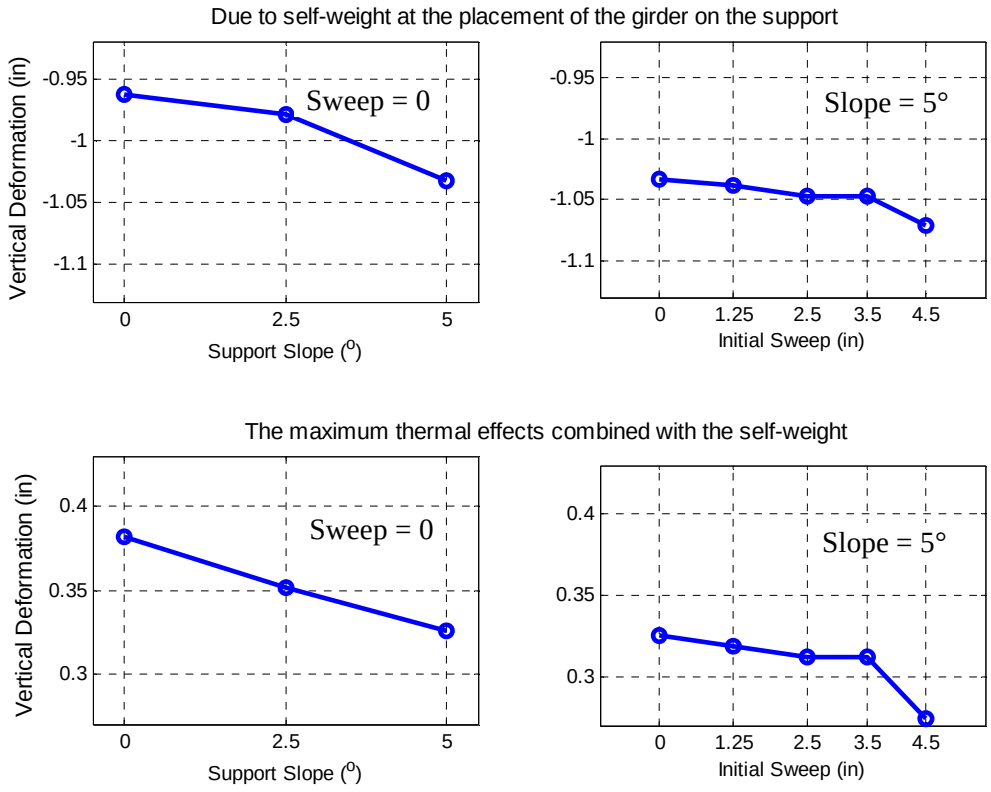

Figure 6.22: Changes in the vertical deformations due to the combined thermal effects and self-weight with increases in initial sweep and support slope.

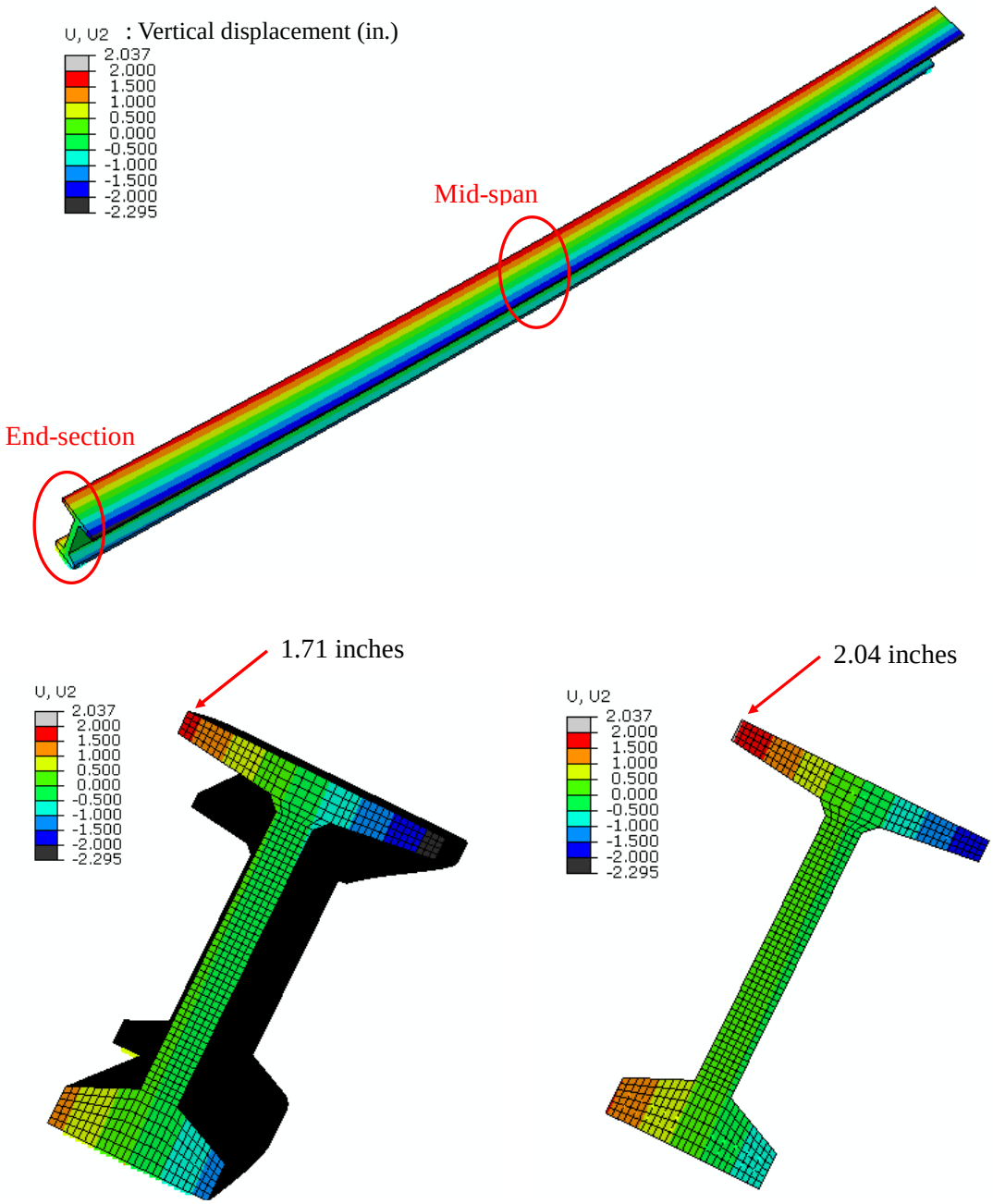

(a) at the end of the girder (b) at the mid-span

Figure 6.23: The contours of the vertical displacements at 3 p.m. obtained from the 3D nonlinear finite element analysis with an initial sweep of 3.5 inches and a support slope of 5° (Scale factor =5).

6.3.4 Transverse Behavior of the Prestressed Concrete Girder

For the transverse response of the prestressed BT-63 girder during construction, Figures 6.24 and 6.25 show variations in the transverse displacements in the middle of the girder web with increases in support slope and initial sweep, respectively. The increases in the support slope as shown in Figure 6.24 increased initially lateral deformations before the girder was subjected to thermal effects. Additional lateral deformations due to the thermal effects only slightly changed with increases in the support slope from of 0° to 5°.

With increases in initial sweep and a constant support slope of 5°, Figure 6.25 shows increases in the transverse deformations at the middle height of the web at mid-span. As mentioned previously, for the prestressed BT-63 girder with an initial sweep of 4.5 inches and 5.0 inches, the 3D nonlinear finite element analyses stopped with error messages of the "largest increment of displacement" in the lateral direction and "excessive distortion" in solid elements. The girder with initial sweep of 4.5 inches and 5.0 inches showed additional lateral deformations of 4.61 inches and 4.75 inches, respectively, immediately after the girder was installed on the sloped bearing support. The combined thermal effects increased the lateral deformations of the girder with the initial sweep of 4.5 and 5.0 inches to 5.69 inches at 1 p.m. and 5.26 inches at 9 p.m., respectively. Therefore, the total lateral displacements including the initial sweep of 4.5 and 5.0 inches at the middle height of the web at mid-span were 10.09 inches and 10.26 inches, respectively, as shown in Figure 6.25. After that, the 3D finite element analyses halted due to a failure of the numerical solution to converge which is an indication of instability of the structure.

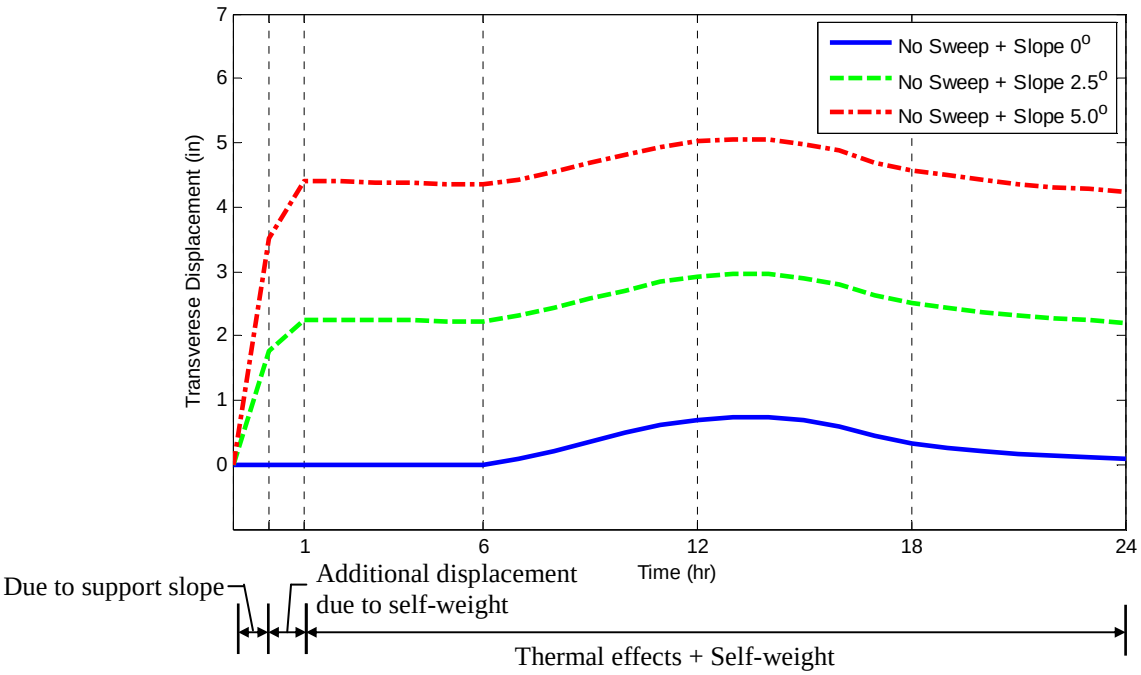

Figure 6.24: Variations in the transverse displacements at mid-height of the girder web during construction with increases in support slope with no initial sweep.

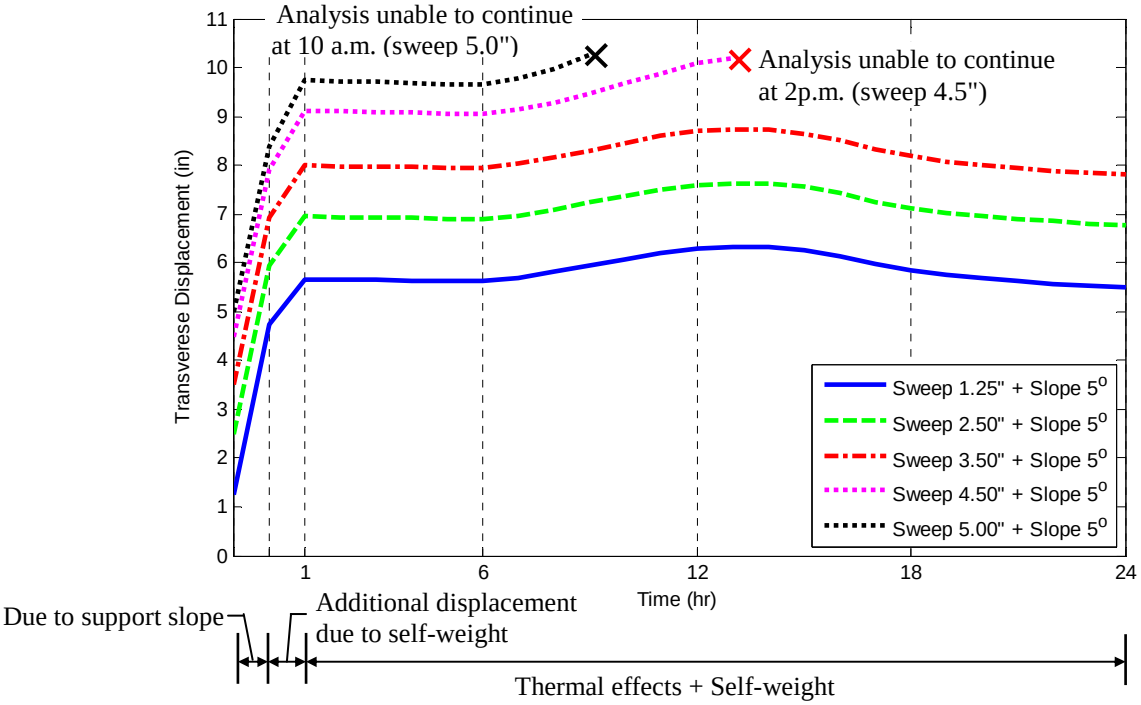

Figure 6.25: Variations in the transverse displacements at mid-height of the girder web during construction with increases in initial sweep and a support slope of 5°.

Table 6.6 summarizes the maximum transverse deformations of the girder at mid-span due to self-weight and thermal effects with increases in support slope and initial sweep. The transverse deformations due to the combined thermal effects increased gradually from 0.74 to 0.81 inches with increases in support slope from 0° to 5° and also increased from 0.81 to 0.92 inches with increases in initial sweep from 0 to 3.5 inches. Figure 6.26 presents the changes in the transverse deformations with increases in support slope and initial sweep.

For the girder with initial sweep of 4.5 inches, Figure 6.27 shows the contour plots of the maximum transverse displacements at the end of the girder and the mid-section at 1 p.m. The maximum transverse displacements, not including the initial lateral sweep, were 8.92 inches in the middle of top flange and 5.70 inches in the middle of the web at mid-span before the lateral instability of the girder occurred due to excessive distortion of the girder.

Table 6.6: The maximum transverse deformations of the BT-63 girder due to self-weight and thermal effects with increases in initial sweep and support slope.

Initial Sweep (inches)	Support Slope (degrees)	Transverse Deformation (inches)	
		Only self-weight	Thermal effects
0.00"	0.0°	0	+ 0.74
0.00"	2.5°	+ 0.45	+ 0.74
0.00"	5.0°	+ 0.90	+ 0.81
1.25"	5.0°	+ 0.94	+ 0.83
2.50"	5.0°	+ 1.00	+ 0.86
3.50"	5.0°	+ 1.07	+ 0.92
4.50"	5.0°	+ 1.20	+ 1.15

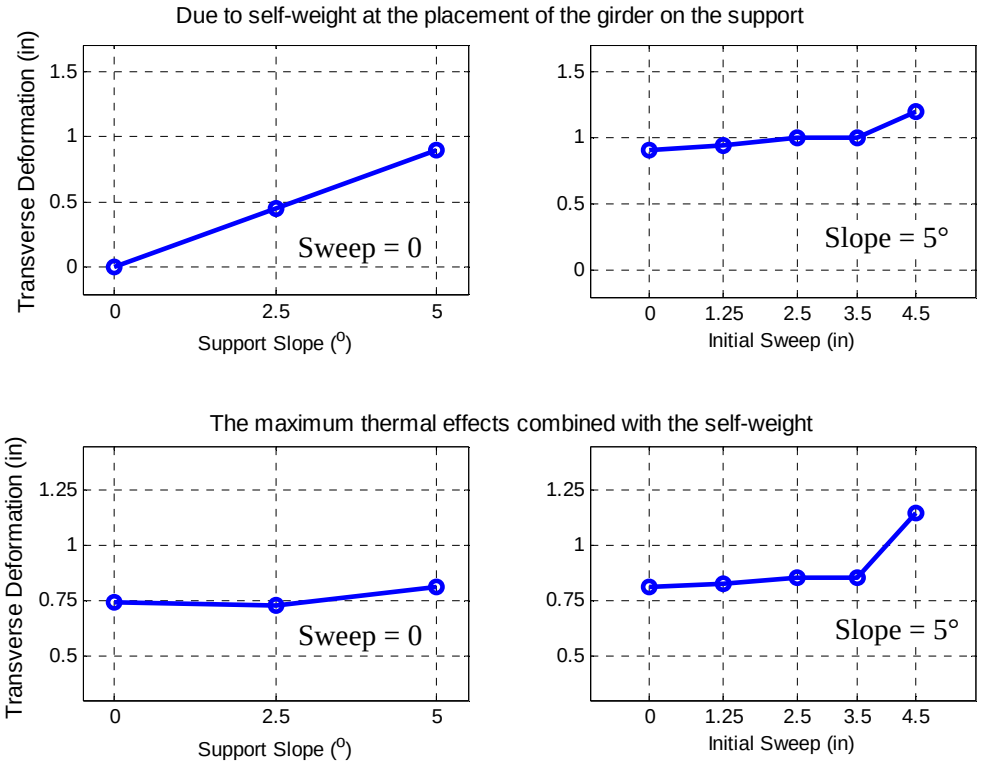

Figure 6.26: Changes in the transverse deformations due to the combined thermal effects and self-weight with increases in initial sweep and support slope.

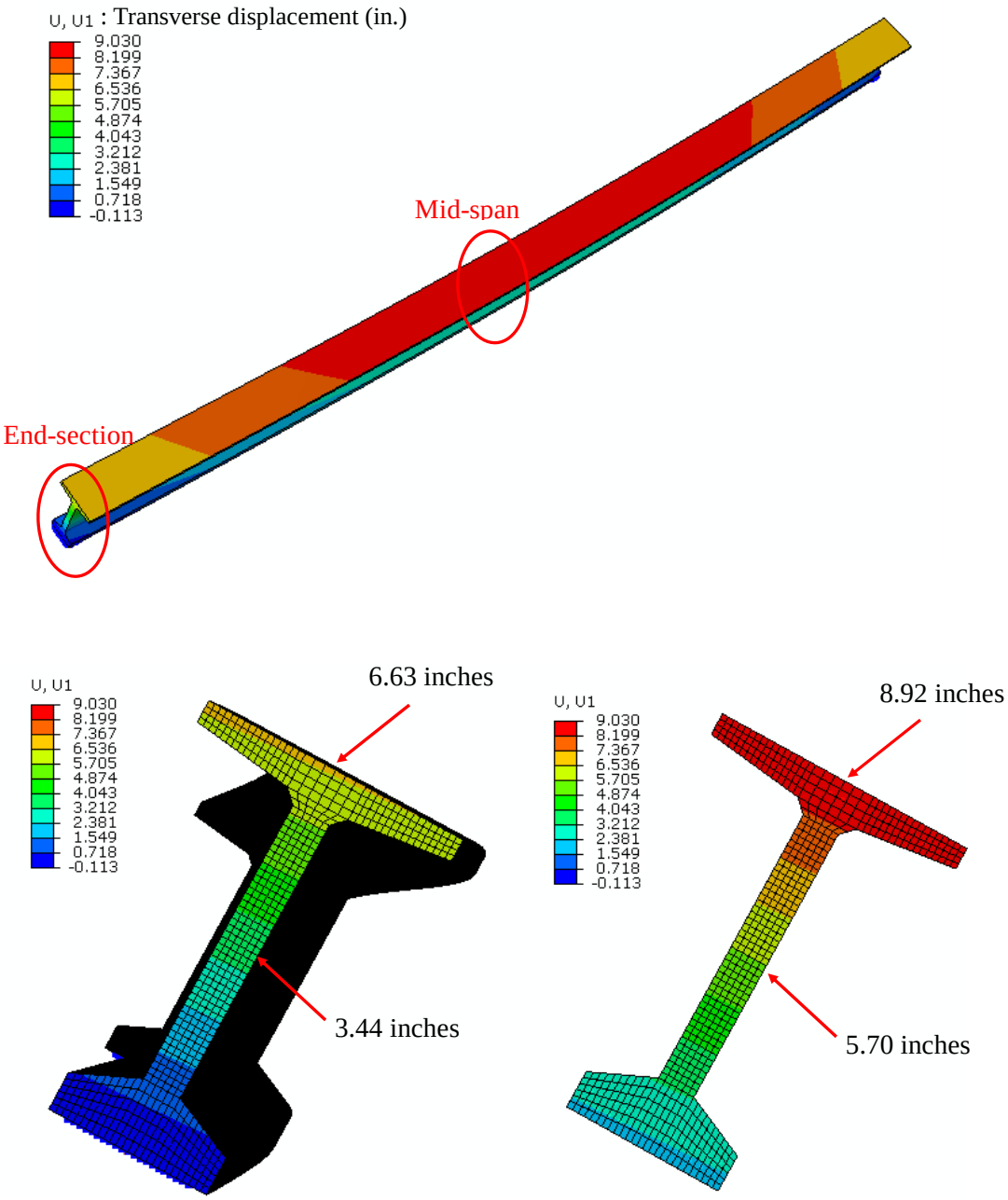

(a) at the end of the girder (b) at the mid-span

Figure 6.27: The contours of the transverse displacements at 1 p.m. obtained from the 3D nonlinear finite element analysis with an initial sweep of 4.5 inches and a support slope of 5° (Scale factor = 5).

6.4 A Simple Beam Model for the Calculation of Thermal Deformations

In order to provide a simplified calculation of the vertical and transverse deformations, a beam model was developed. Thus, the assumptions involved in the development of the beam model are as follows:

(1) The material is homogenous and isotropic.
(2) The material has linear stress-strain relationship.
(3) Plane sections remain plane and perpendicular to the longitudinal axis of the beam during the deformations.
(4) Longitudinal and transverse thermal responses are uncoupled.
(5) The temperature variation is constant along the length of the beam.
(6) Initial sweep, elastomeric bearings, and support slope are neglected.
(7) The beam is simply supported.

6.4.1 Development of the Simple Beam Model

Figure 6.28 illustrates vertical strain distributions along the depth of a prestressed concrete bridge girder caused by a nonlinear vertical temperature gradient. The unrestrained plane section tends to expand in accordance with the vertical temperature gradient as shown in a Figure 6.28(b). The initial thermal strain is

$$\varepsilon_t(y) = \alpha \cdot \Delta T(y) \tag{6.4}$$

in which $\varepsilon_t(y)$ = the free thermal strain at a depth y from the center of the gravity of the cross-section,

$\Delta T(y)$ = the temperature differential at a depth y, and

α = the coefficient of thermal expansion.

However, the initially plane section remains planar according to the Navier-Bernoulli hypothesis. Thus, the final strain profile shown in Figure 6.28(d) must be linear and thus can be expressed by

$$\varepsilon(y) = \varepsilon_o + y \cdot \phi \tag{6.5}$$

in which ε_o = the strain at the center of the gravity of the cross-section, and

ϕ = the curvature of the girder.

The vertical thermal deformation can be obtained by integrating the curvature ϕ over the length of the girder. For a simple span, the vertical deformation at mid-span is

$$\delta_v = \frac{\phi \cdot L^2}{8} \tag{6.6}$$

in which L is the length of the girder.

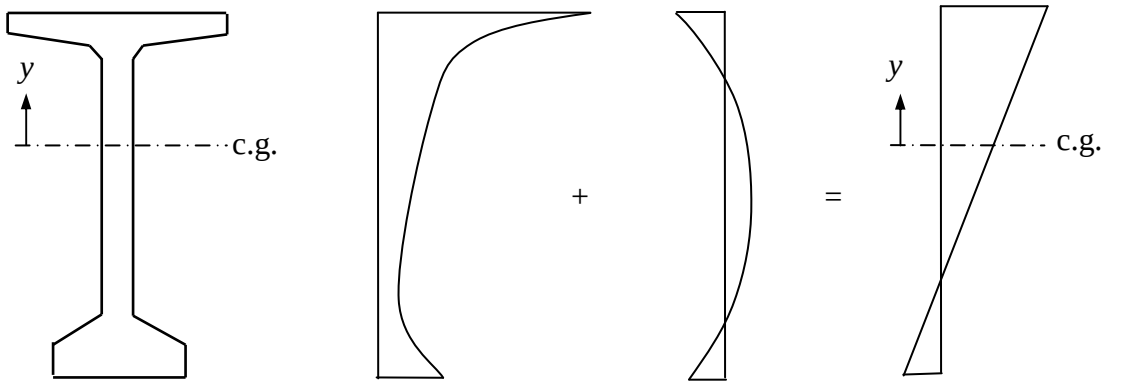

(a) Cross-section (b) Free thermal strain (b) Strain difference inducing self-equilibrating stresses (d) Final linear strain

Figure 6.28: Strain distributions induced by nonlinear vertical temperature distributions in a simply supported prestressed concrete bridge girder.

In order to determine the curvature of the girder, artificial end moments were calculated using the free thermal strains shown in Figure 6.28(b). Figure 6.29 shows a simple beam model that can calculate vertical thermal movements from the artificial moments at the ends of the girder. The end moment M_x is obtained from the nonlinear vertical temperature gradient along the depth of the cross-section as follows:

$$M_x = \int [\sigma(y) \cdot b\,(y) \cdot y]\, dy = \int [E \cdot \alpha \cdot \Delta T(y) \cdot b(y) \cdot y]\, dy \qquad (6.7)$$

in which $\Delta T(y)$ = the vertical temperature differential at a depth *y*,

$b(y)$ = the width of the girder section at a depth *y*, and

E = the concrete modulus of elasticity.

Then, the curvature ϕ_x can be calculated by

$$\phi_x = \frac{M_x}{EI_x} \qquad (6.8)$$

in which I_x = the moment of inertia of the cross-section with respect to the strong *x*-axis.

For the calculation of transverse thermal movements, the artificial end moments shown in Figure 6.30 were determined from the transverse temperature gradients. Since the transverse temperature gradients vary from the top to the bottom flanges, this study defined three transverse temperature gradients using the temperature distributions in the middle of the top flange, in the middle of the web, and in the middle of the bottom flange. Therefore, the total transverse end moments are the summation of the transverse end moments calculated from each transverse temperature gradient:

$$M_y = \int_{top\ flange} [E \cdot \alpha \cdot \Delta T(x) \cdot b(x) \cdot x] dx + \int_{web} [E \cdot \alpha \cdot \Delta T(x) \cdot b(x) \cdot x]\, dx + \int_{bottom\ flange} [E \cdot \alpha \cdot \Delta T(x) \cdot b(x) \cdot x]\, dx \quad (6.9)$$

in which $\Delta T(x)$ = the transverse temperature differential at a width *x*,

$b(x)$ = the depth of the bridge girder at a width *x*, and

E = the concrete modulus of elasticity.

Like to Equation (6.8), the curvature ϕ_y is then calculated using the transverse end moments as follows:

$$\phi_y = \frac{M_y}{EI_y} \quad (6.10)$$

in which I_y = the moment of inertia of the cross-section with respect to the *y*-axis.

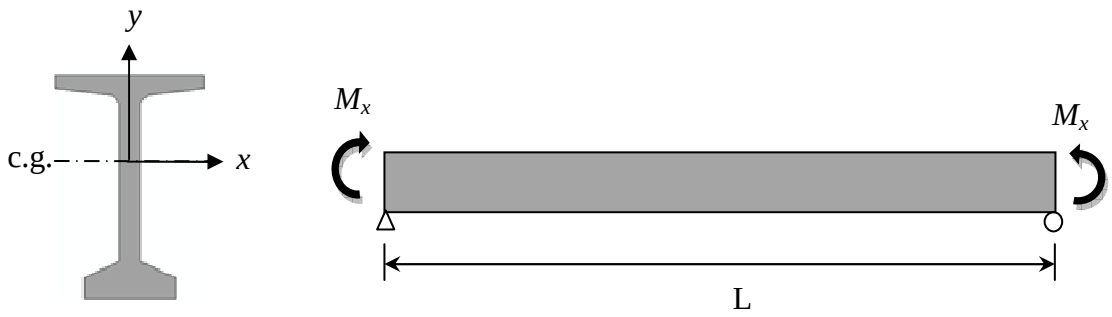

Figure 6.29: A beam model with the end moments for the thermal vertical movements.

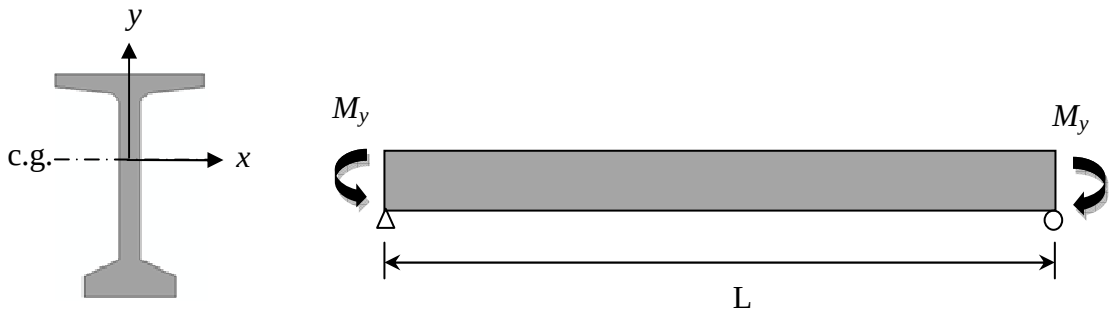

Figure 6.30: A beam model with the end moments for the thermal transverse movements.

6.4.2 Comparison of the Beam Model with the 3D Finite Element Analysis

For the BT-63 girder, which showed the largest vertical and transverse temperature gradients among the chosen AASHTO-PCI standard sections, the proposed beam model was used to calculate vertical and transverse thermal movements from hourly vertical and transverse temperature gradients defined in Chapter 5. The length of the BT-63 girder is 100 feet, and the material properties of concrete are shown in Table 6.1.

To verify the beam model proposed in this study, the thermal movements calculated using the beam model were compared with those obtained from the 3D finite element thermal stress analysis for the same simply supported boundary conditions. The

detailed calculation procedures of the thermal movements using the beam model are described in Appendix C. Figures 6.31 and 6.32 show the predicted vertical and transverse thermal movements for both the beam model and those obtained from the 3D finite element analysis. As can be seen in these figures, the thermal movements calculated from the beam model correlated well with those obtained from the 3D finite element analysis.

Furthermore, this study evaluated the absolute average errors of the thermal movements between the beam model and the 3D finite element analysis. Table 6.7 represents average absolute errors of 0.02 to 0.03 inches in the thermal movements. The maximum absolute errors are in the range of 0.03 to 0.06 inches. In addition, Table 6.8 summarizes the maximum vertical and transverse thermal movements obtained from the beam model and the 3D finite element analysis. The maximum vertical thermal movements calculated using the beam model were 0.54 inches in the summer and 0.20 inches in the winter. The calculated maximum transverse thermal movements were 0.39 inches in the summer and 0.81 inches in the winter. Compared with the results of the 3D finite element analyses, the difference in the maximum vertical and transverse thermal movements were less than 0.03 inches (5.3%).

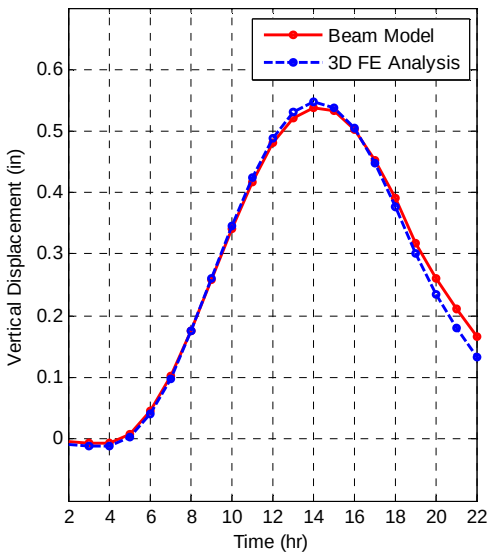

(a) Summer

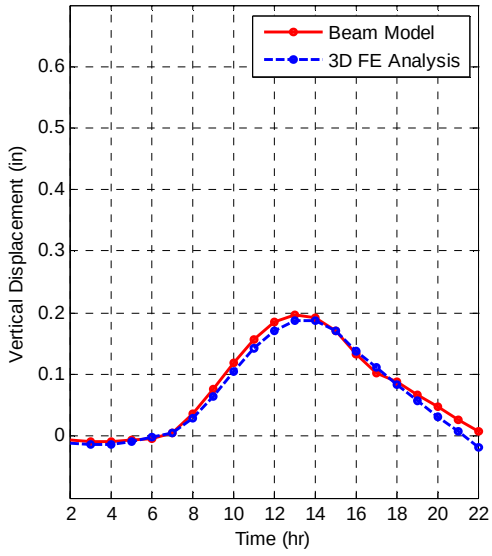

(b) Winter

Figure 6.31: Comparisons of the vertical thermal movements calculated using the beam model with those obtained from the 3D finite element analysis.

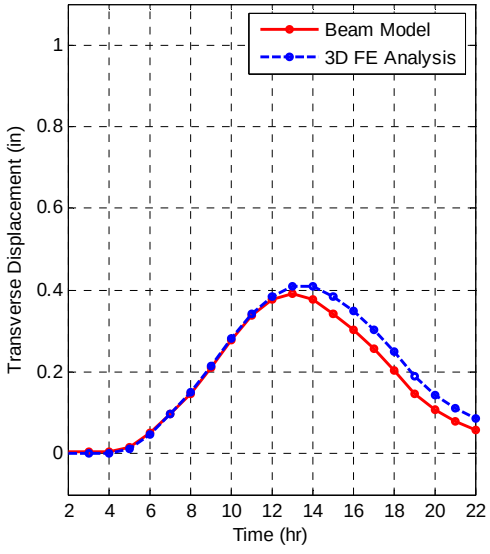

(a) Summer

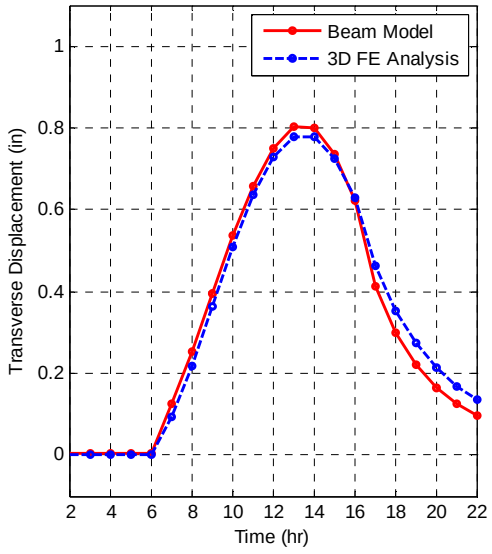

(b) Winter

Figure 6.32: Comparisons of the transverse thermal movements calculated using the beam model with those obtained from the 3D finite element analysis.

Table 6.7: Average absolute errors (AAE) of the vertical and transverse thermal movements between the beam model and the 3D finite element analysis.

(Units: inches)

Seasons	Vertical Thermal Movements		Transverse Thermal Movements	
	AAE	MAE	AAE	MAE
Summer	0.02	0.04	0.02	0.05
Winter	0.02	0.03	0.03	0.06

Table 6.8: Maximum vertical and transverse thermal movements obtained from the beam model and the 3D finite element analysis.

(Units: inches)

Seasons	Maximum Vertical Movements		Maximum Transverse Movements	
	Beam Model	3D FE Analysis	Beam Model	3D FE Analysis
Summer	0.54	0.55	0.39	0.40
Winter	0.20	0.19	0.81	0.78

6.4.3 Thermal Movements of AASHTO-PCI Bridge Girders

Chapter 5 investigated differences in vertical and transverse temperature differentials for four AASHTO-PCI standard girder sections; Type-I, Type-IV, Type-V, and BT-63 sections. Among in the group of four I-beams with smaller top flanges, the smallest Type-V and the largest Type-IV sections were chosen. The Type-V and the BT-63 section which have the same depth of 63 inches were selected from the remaining five sections having wider top flanges. The dimensions and the cross-sections of the four AASHTO-PCI sections are shown in Figure 5.6.

Using the beam model, the thermal movements of the four AASHTO-PCI girders were calculated based on the temperature distributions in Chapter 5, Section 5.4. Table 6.9 summarizes the maximum vertical and transverse thermal movements obtained from

the beam model in terms of the span length of the girders. Since the behavior of the girders mainly depends on the moment of inertia of the cross-sections, the Type-I section, which has the smallest moment of inertia with respect to the strong *x*-axis, has the largest vertical thermal movement. However, the maximum span of the Type-I section is 48 feet which yields maximum vertical thermal movements of 0.27 inches in the summer and maximum transverse thermal movements of 0.15 inches in the winter. For the transverse thermal movements, the Type-IV section which has large transverse temperature differentials and a small moment of inertia with respect to the weak *y*-axis exhibited the largest transverse thermal movements among the four AASHTO-PCI sections. The Type-V and BT-63 sections with the longer top flanges showed similar vertical and transverse thermal movements.

Table 6.9: The maximum vertical and transverse thermal movements of the four AASHTO-PCI standard sections in the summer and the winter.

(Units: $\times 6.94 \times 10^{-9}$ inches)

AASHTO-PCI Standard Sections	I_x, in^4	I_y, in^4	Maximum Vertical Movements [a]		Maximum Transverse Movements [a]		Maximum Span, ft (PCI, 2002)
			Summer	Winter	Summer	Winter	
Type-I	22,750	27,413	$117L^2$	$71L^2$	$53L^2$	$63L^2$	48
Type-IV	260,730	26,724	$39L^2$	$23L^2$	$123\ L^2$	$153\ L^2$	120
Type-V	521,180	66,345	$59L^2$	$26L^2$	$40L^2$	$82L^2$	145
BT-63	392,638	40,521	$55L^2$	$20L^2$	$40L^2$	$83L^2$	130

[a] L is the span of the girder in inches.

CHAPTER 7

INFLUENCES OF THE THERMAL PROPERTIES ON TEMPERATURE DISTRIBUTIONS AND THERMAL BEHAVIOR

7.1 Introduction

The temperature distributions and thermal behavior of concrete and prestressed concrete bridge girders are affected by the thermal properties of concrete as well as the solar absorptivity of the concrete surface. In particular, since concrete is a composite material, the values of the thermal properties of concrete depend on the characteristics of its constituents. Therefore, this study uses two-dimensional (2D) finite element heat transfer analysis to evaluate the influences of the thermal conductivity, the specific heat, and the solar absorptivity of concrete on temperature distributions in a prestressed concrete bridge girder. For the thermal behavior of the girder, the influence of the coefficient of thermal expansion of concrete is evaluated using the three-dimensional (3D) finite element analysis presented in Chapter 6.

7.2 Literature Reviews on the Thermal Properties of Concrete

The exposed surfaces of concrete and prestressed concrete bridge girders receive solar radiation during the day which mainly generates temperature variations and differentials in the bridge girders. The heat transfer inside concrete is dependent on the values of the thermal conductivity, the specific heat, and the solar absorptivity of concrete, which vary with changes in materials and environmental conditions. Thus, previous studies relevant to the variation in the thermal properties of concrete were reviewed.

7.2.1 Thermal Conductivity and Specific Heat

The thermal conductivity and the specific heat of concrete depend on the current state of concrete such as its composition, density, moisture content, and temperature. According to the literature review on the thermal conductivity and the specific heat of concrete, several authors suggested the values of approximately 1.3 to 2.6 W/m·K for the thermal conductivity and 800 to 1,200 J/kg·K for the specific heat of concrete as illustrated in Table 7.1.

For high-strength concrete, VanGreem et al. (1997) performed experimental studies on the thermal conductivity and the specific heat of the high-strength concrete. The thermal conductivity of high-strength concrete, which ranged from 1.7 to 2.6 W/m·K, was similar to that of normal-strength concrete. The value of the specific heat of high-strength concrete was also similar to that of normal-strength concrete in the range of 840 to 1,050 J/kg·K.

Thus, this study performed parametric studies using values of 1.5, 2.0, and 2.5 W/m·K for the thermal conductivity of concrete, and values of 800, 1000, and 1,200 J/kg·K for the specific heat of concrete.

Table 7.1: The thermal conductivity and specific heat of concrete in the literature.

References	Thermal Conductivity, *k* (W/m·K)	Specific Heat, *c* (J/kg·K)
Kreith (1973)	1.21	840
CIBSE Guide (1983)	1.35	820
Elbadry and Ghali (1983)	1.50	960
Hirst (1984)	1.40	960
Duffie and Beckman (1980)	1.73	840
Branco and Mendes (1993)	1.50	1,000
Incropera and DeWitt (2002)	1.4	880
Ghali, Favre, and Elbadry (2002)	1.5 - 2.5	840 – 1,200
ASHRAE Handbook (2005)	1.3 - 2.6	800-1,000

7.2.2 Solar Absorptivity

During the day, the heat gain on the surfaces of concrete structures is highly dependent on the solar absorptivity of concrete which varies according to the color, aggregate type, concrete age, and state of weathering. For the thermal analysis of concrete structures, several authors recommended the solar absorptivity of concrete in the range of 0.50 to 0.80. Table 7.2 summarizes the values of concrete absorptivity in several references. Based on the recommended values in the literature, the parametric study pertaining to the influence of concrete solar absorptivity on girder temperatures was carried out using values for the solar absorptivity of 0.5, 0.6, 0.7, and 0.8.

Table 7.2: The solar absorptivity of concrete in the literature.

References	Solar Absorptivity, α
Anderson (1977)	0.60
Neville (1996)	0.5-0.8
Ghali, Favre, and Elbadry (2002)	0.65–0.80
Incropera and DeWitt (2002)	0.60
ASHRAE Handbook (2005)	0.65-0.80

7.2.3 Thermal Expansion Coefficient

The coefficient of thermal expansion (CTE) is another important material property needed to calculate the thermal stresses and movements. The CTE of concrete depends primarily on the types and the proportions of aggregates. The fineness of cement, the moisture content of concrete, and the age of concrete also affect the CTE of concrete. The *AASHTO LRFD Bridge Design Specifications* (2007) provide ranges of 5.4 to 14.4 × 10^{-6} /°C (3 to 8 × 10^{-6} /°F) for the CTE of normal-density concrete and 7.2 to 10.8 × 10^{-6} /°C (4 to 6 × 10^{-6} /°F) for the CTE of low-density concrete. The Federal Highway Administration (FHWA, 2002) addresses that the CTE of Portland cement concrete ranges from about 7.4 to 13 × 10^{-6} /°C (4.1 to 7.3 × 10^{-6} /°F). Therefore, values

for CTE of 6, 9, and 12 × 10^{-6} / °C were used for the thermal response of a prestressed concrete bridge girder using a 3D thermal stress analysis with temperature distributions determined from the 2D heat transfer analysis.

7.3 Temperature Distributions with the Thermal Properties of Concrete

The 2D finite element heat transfer model presented in Chapter 3 was employed to investigate variations in temperature distributions over the cross-section of the BT-63 girder with changes in the thermal properties of concrete. A summary of the material parameters used for this study are shown below:

(1) The thermal conductivity of concrete: 1.5, 2.0, and 2.5 W/m·K

(2) The specific heat of concrete: 800, 1000, and 1,200 J/kg·K

(3) The solar absorptivity of concrete: 0.5, 0.6, 0.7, and 0.8

Environmental boundary conditions involved in these parametric studies were solar radiation, ambient air temperature, and wind speed measured at five-minute intervals on June 1, 2009, on which the highest girder temperature and the largest vertical temperature differential were measured during the months of April 2009 to March 2010.

7.3.1 Thermal Conductivity of Concrete

To eliminate the effect of finite element sizes on the parametric studies, this study first compared temperature distributions obtained from the model, composed of 584 elements over the BT-63 section, with those from a model which quadrupled the number of finite elements. Figure 7.1 shows the two models meshed using 2D heat transfer DC2D4 elements in ABAQUS (2008); Model A with 584 elements and Model B with 2,336 elements. The width and height of each element were determined to be approximately 1 inch in Model A and 0.5 inches in Model B. Then, the 2D finite element heat transfer analysis was performed using the same 5-minute time steps as used in the experiment.

Figures 7.2 to 7.4 show the vertical temperature distributions of the two finite element models along the depth of the top flange at around 2 p.m. when high girder temperatures and large temperature differentials were observed. The temperature distributions obtained from Model A match well with those obtained from Model B as shown in Figures 7.2 to 7.4. The maximum differences between the two models are only 0.13°C (0.23°F), 0.09°C (0.16°F), and 0.07°C (0.13°F) in the thermal conductivity of 1.5, 2.0, and 2.5 W/m·K, respectively, on the top surface (the location of Node A in the figures) where the highest solar heat flux is applied. Therefore, Model A with 584 elements was used for the subsequent parametric studies on the influence of the thermal properties of concrete in the temperature distributions.

Figure 7.5 compares the temperature distributions obtained from the three thermal conductivity values along the depth of the top flange. The other thermal parameters maintained a constant 1,000 J/kg·K of specific heat and 0.5 of solar absorptivity during the analysis. As thermal conductivity increased from 1.5 to 2.5 W/m·K, the temperature on the top surface decreased by about 2°C (3.6°F), or 4%, due to heat being conducted faster from the top surface. This resulted in an increase of about 1°C (1.8°F) to 2°C (3.6°F), or 2 to 5%, inside the girder. In particular, the temperature at Node C, approximately 1.4 inches below the top surface, represents a base point of the temperature changes.

Figure 7.6 also compares the temperature distributions obtained from the thermal conductivity 1.5, 2.0, and 2.5 W/m·K along the depth of the BT-63 girder. As shown in Figure 7.5, with increases in the thermal conductivity, the temperatures decease on the top surface and increase inside the girder. The results of this parametric study indicate that the thermal conductivity of concrete, in the range of 1.5 to 2.5 W/m·K, only slightly affects the changes in the girder temperatures by about 2°C (3.6°F), or 4%, since no heat is generated inside the girder.

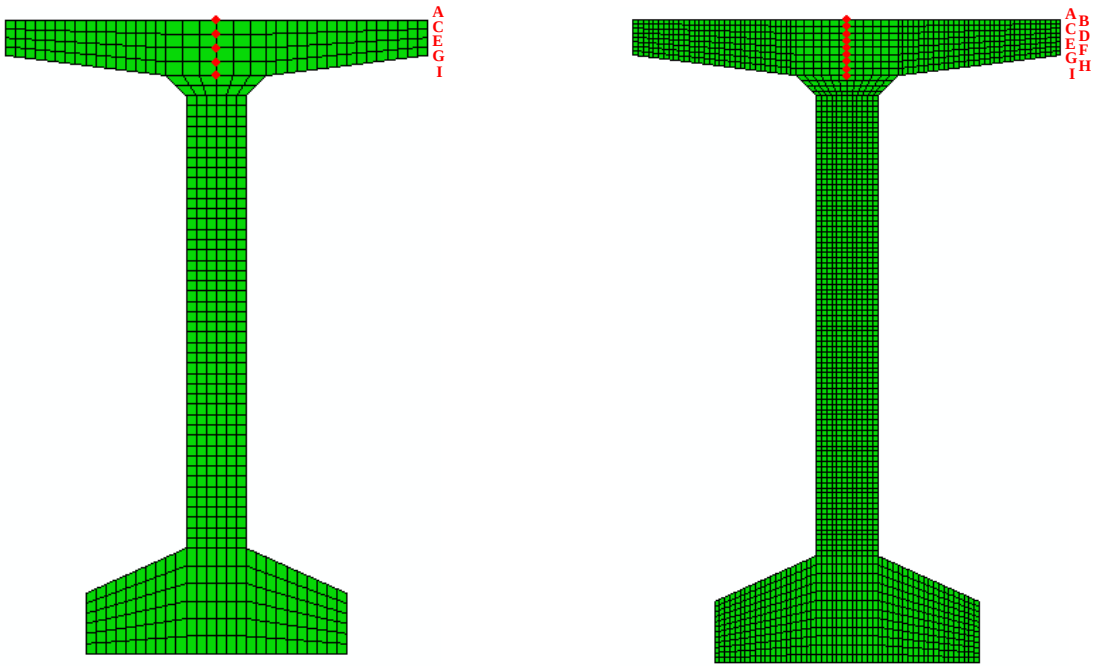

(a) Model A: 584 elements

(b) Model B: 2,336 elements (= 4 × 584 elements)

Figure 7.1: The two finite element models and the nodes selected along the depth of the top flange.

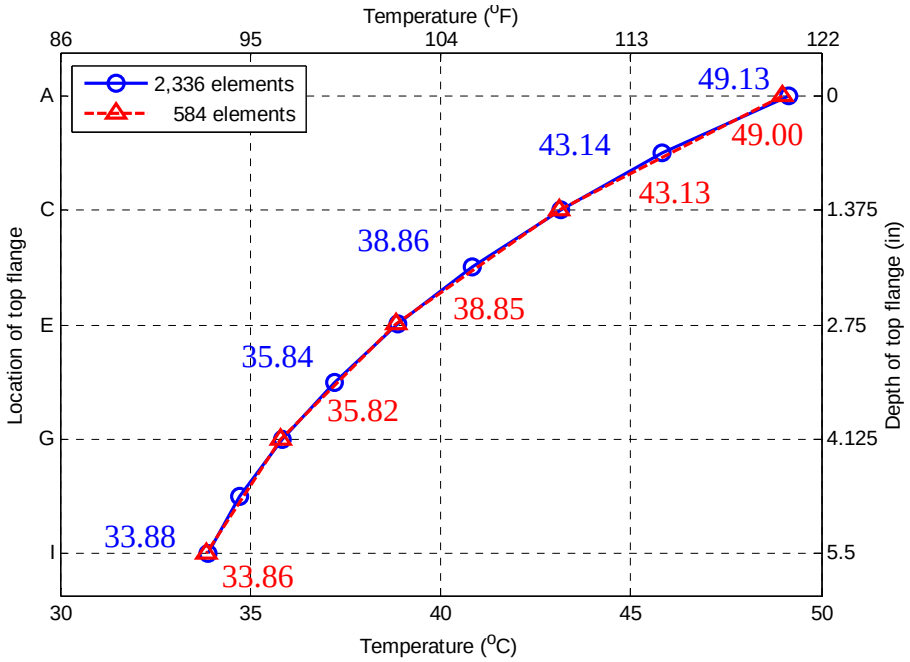

Figure 7.2: The temperature distributions obtained from the thermal conductivity of concrete, k = 1.5 W/m·K, through the depth of the top flange at 2:08 p.m. on June 1, 2009.

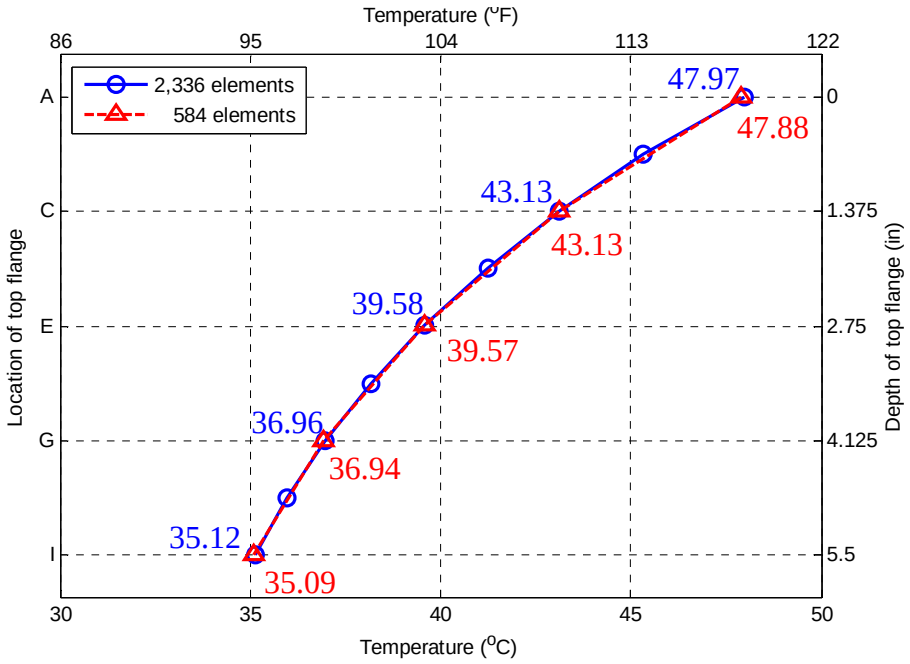

Figure 7.3: The temperature distributions obtained from the thermal conductivity of concrete, k = 2.0 W/m·K, through the depth of the top flange at 2:08 p.m. on June 1, 2009.

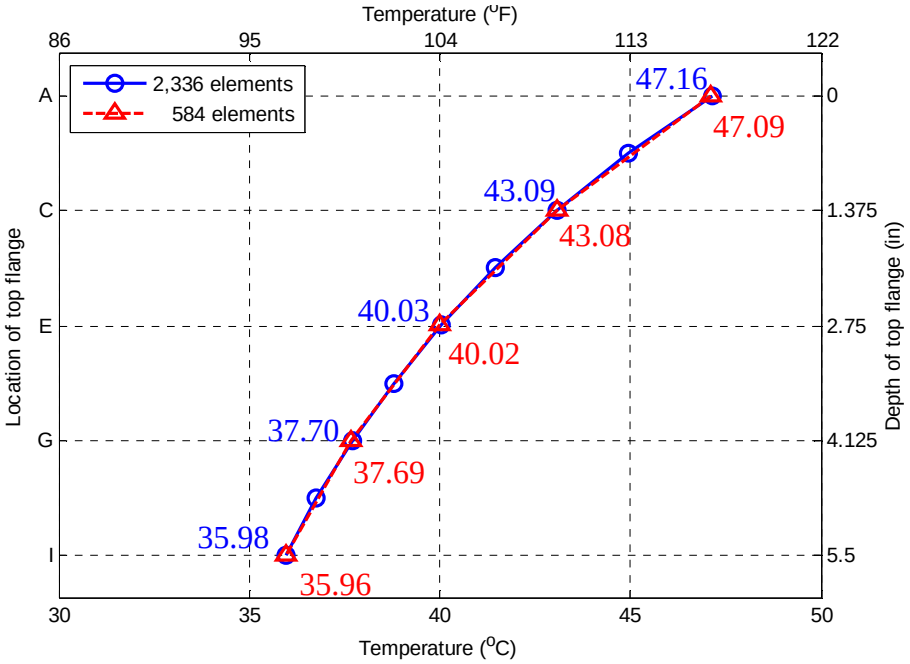

Figure 7.4: The temperature distributions obtained from the thermal conductivity of concrete, k = 2.5 W/m·K, through the depth of the top flange at 2:08 p.m. on June 1, 2009.

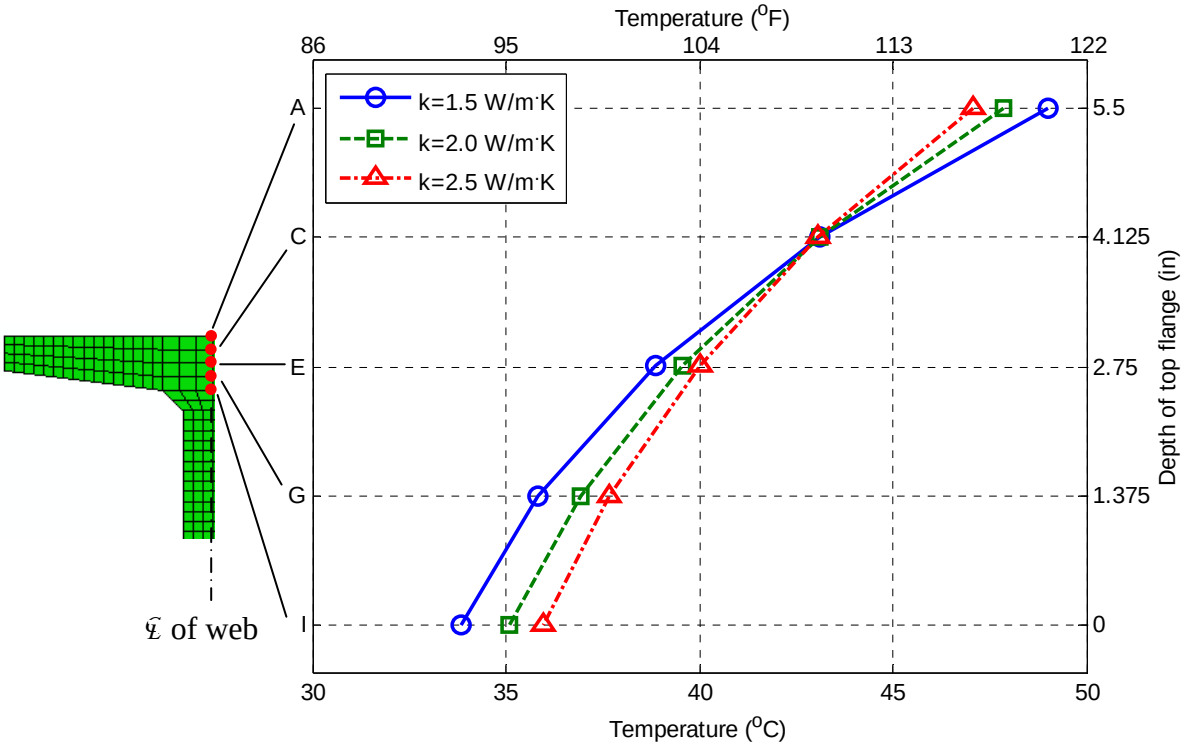

(Units: °C)

Thermal Conductivity, (W/m·K)	Locations				
	A	C	E	G	I
1.5	49.00 (0 %)	43.13 (0 %)	38.85 (0 %)	35.82 (0 %)	33.86 (0 %)
2.0	47.88 (-2.3%)	43.13 (0 %)	39.57 (1.9 %)	36.94 (3.1 %)	35.09 (3.6 %)
2.5	47.09 (-3.9%)	43.08 (-0.1%)	40.02 (3.0 %)	37.69 (5.2 %)	35.96 (6.2 %)

Figure 7.5: Comparisons of the temperature distributions obtained from changes in the thermal conductivity of concrete, k = 1.5, 2.0 and 2.5 W/m·K, through the depth of the top flange at 2:08 p.m. on June 1, 2009.

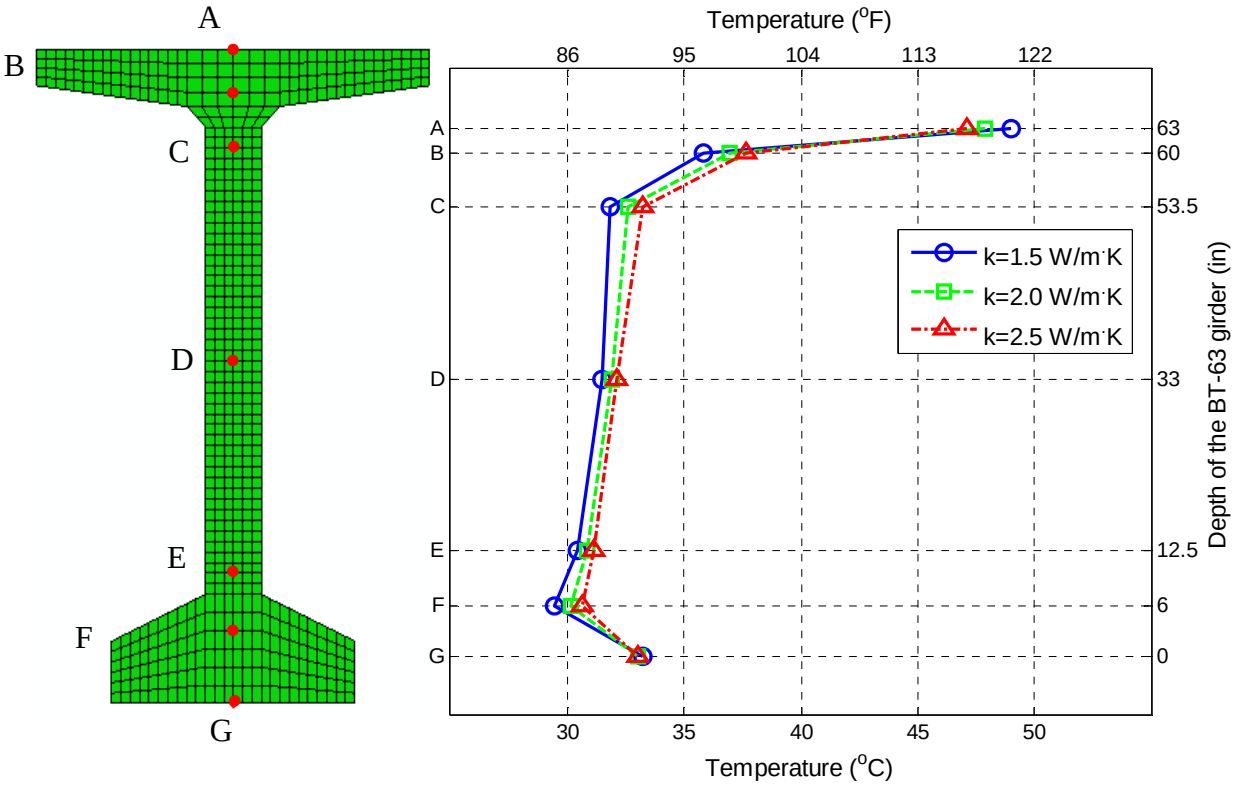

(Units: °C)

Thermal Conductivity, (W/m·K)	Locations						
	A	B	C	D	E	F	G
1.5	49.00 (0 %)	35.82 (0 %)	31.84 (0 %)	31.48 (0 %)	30.41 (0 %)	29.44 (0 %)	33.25 (0 %)
2.0	47.88 (-2.3%)	36.94 (3.1%)	32.63 (2.5%)	31.87 (1.3%)	30.84 (1.4%)	30.13 (2.4%)	33.04 (-0.6%)
2.5	47.09 (-3.9%)	37.69 (5.2%)	33.27 (4.5%)	32.12 (2.0%)	31.15 (2.4%)	30.67 (4.2%)	33.00 (-0.8%)

Figure 7.6: Comparisons of the temperature distributions obtained from changes in the thermal conductivity of concrete, k = 1.5, 2.0 and 2.5 W/m·K, through the depth of the BT-63 girder at 2:08 p.m. on June 1, 2009.

Furthermore, Figures 7.7 to 7.9 show temperature contours obtained at 12:23, 2:42, and 4:27 p.m. on June 1, 2009 from the thermal conductivity of 1.5, 2.0, and 2.5 W/m·K, respectively. The figures represent the main heat flow from the top surface to the bottom flange of the girder due to the solar heating of the top surface over time. The bottom flange exhibits both vertical and transverse heat flows caused by solar radiation incident on the south top and vertical surfaces of the bottom flange. Figures 7.7 to 7.9 also exhibit heat transfer from the highest temperature contours at 12:23 p.m. With increases in thermal conductivity, the temperature contours showed rapid heat flow from the top surface of the girder which resulted in temperature decreases on the top surface and temperature increases inside the girder. The temperature differences between the thermal conductivity of 1.5, 2.0, and 2.5 W/m·K were less than about 2°C (3.5°F).

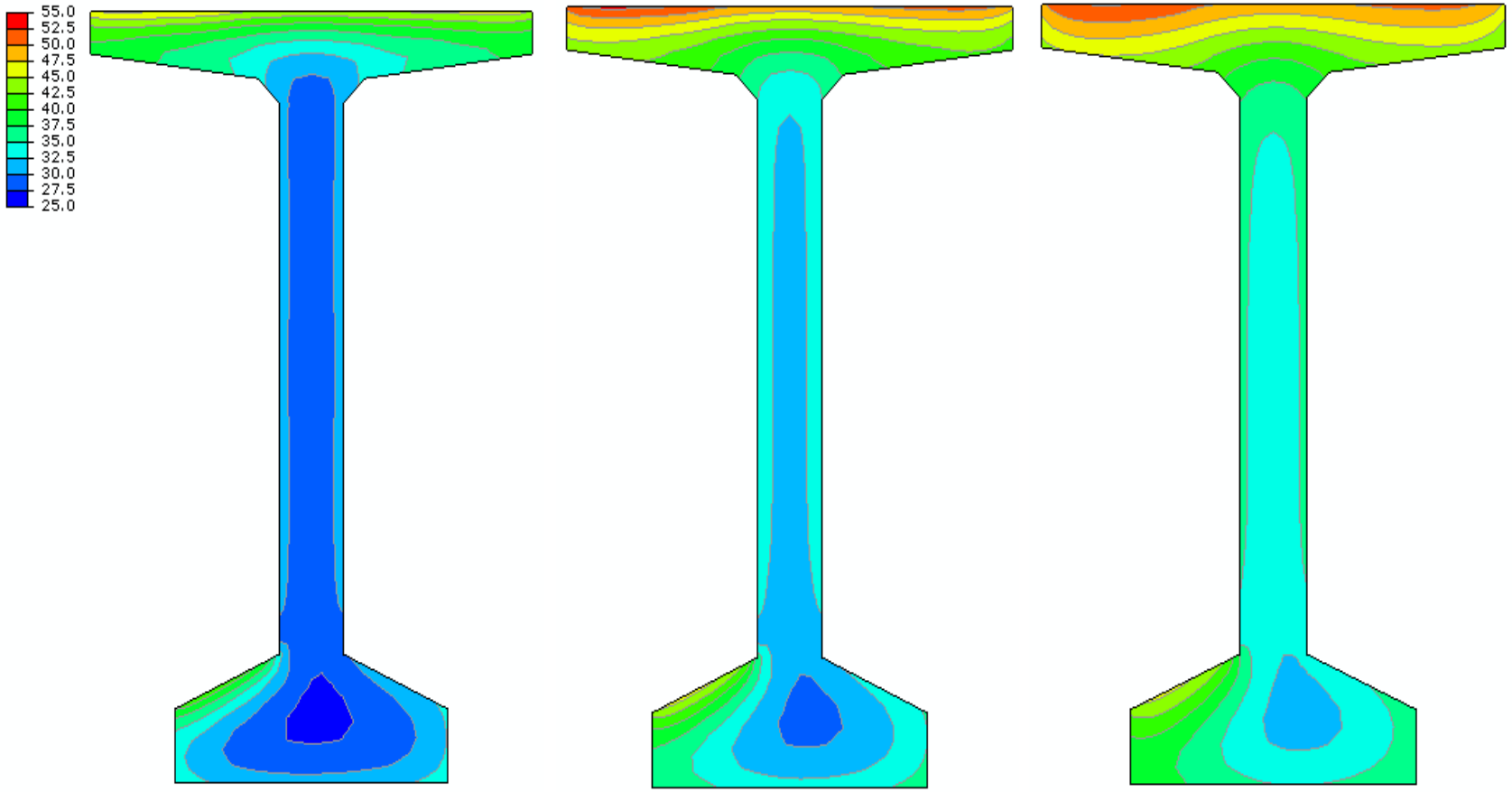

(a) Temperature contour at 12:23 PM (b) Temperature contour at 2:42 PM (c) Temperature contour at 4:27 PM

Figure 7.7: Variations in temperature contours over the cross-section of the BT-63 girder obtained using k = 1.5 W/m·K for the thermal conductivity.

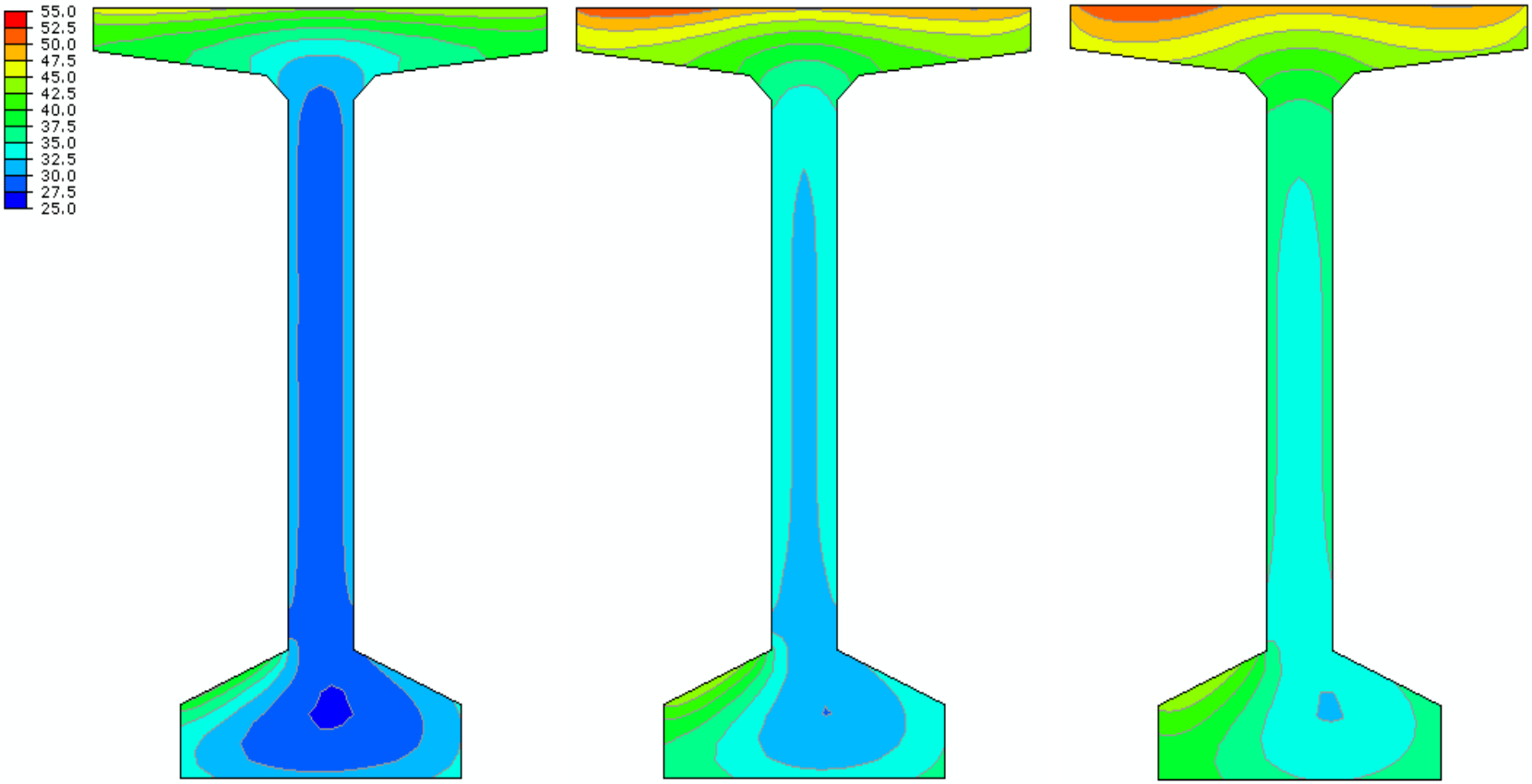

(a) Temperature contour at 12:23 PM (b) Temperature contour at 2:42 PM (c) Temperature contour at 4:27 PM

Figure 7.8: Variations in temperature contours over the cross-section of the BT-63 girder obtained using k = 2.0 W/m·K for the thermal conductivity.

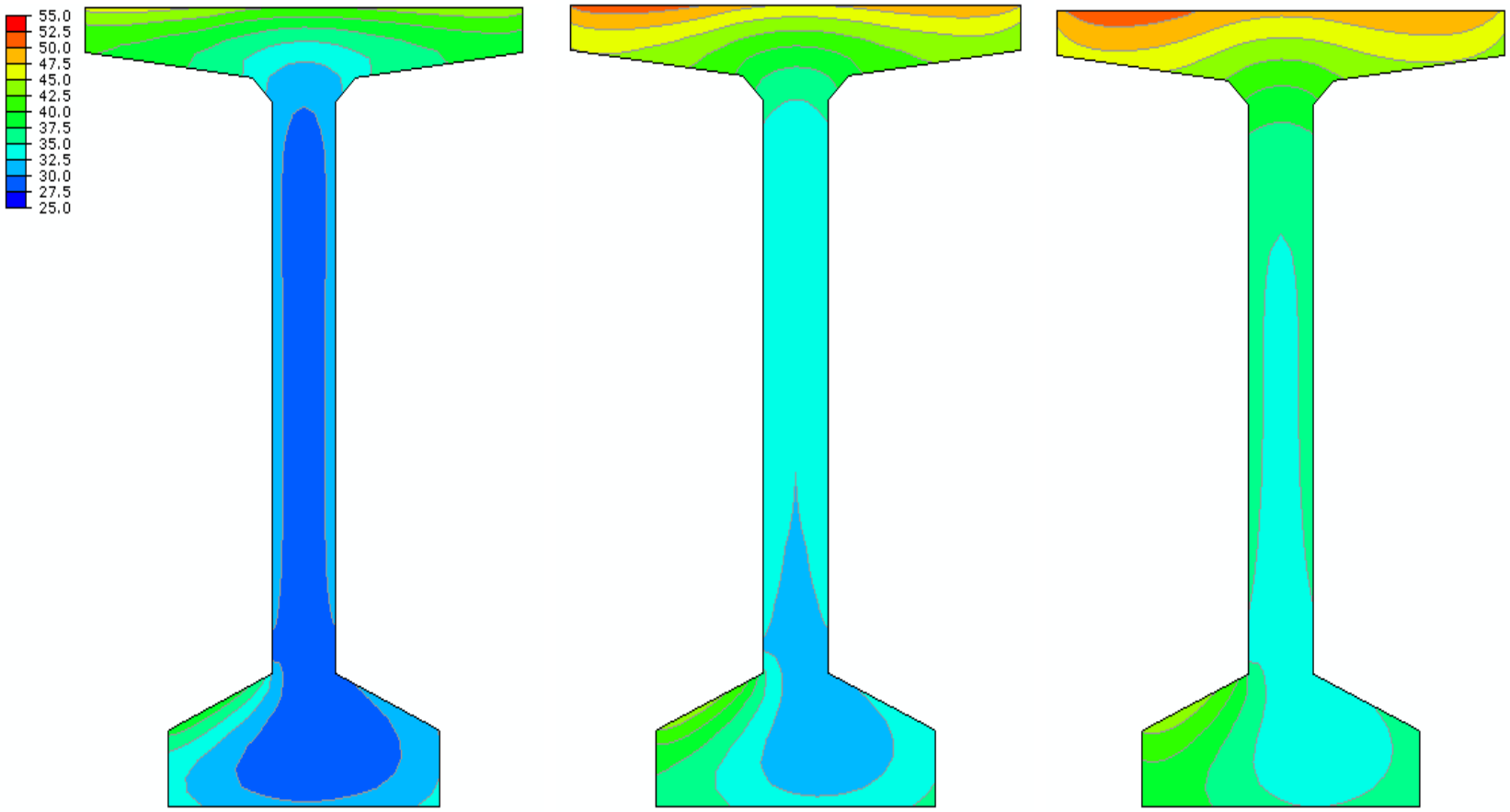

(a) Temperature contour at 12:23 PM (b) Temperature contour at 2:42 PM (c) Temperature contour at 4:27 PM

Figure 7.9: Variations in temperature contours over the cross-section of the BT-63 girder obtained using k = 2.5 W/m·K for the thermal conductivity.

7.3.2 Specific Heat of Concrete

In addition to the thermal conductivity of concrete, the specific heat of concrete also affects temperature distributions in prestressed concrete bridge girders. According to the literature review, the specific heat of concrete ranges from approximately 800 to 1,200 J/kg·K. The values of the specific heat chosen in this study are 800, 1000, and 1200 J/kg·K. The thermal conductivity and the solar absorptivity of concrete maintained the values of 1.5 W/m·K and 0.5, respectively, during the analysis.

Figure 7.10 shows the temperature distributions obtained from the heat transfer analysis of the three specific heat values, 800, 1,000, and 1,200 J/kg·K. In addition, Figure 7.11 presents the vertical temperature distributions along the depth of the BT-63 girder with increases in the specific heat of concrete at 2:08 p.m. when high girder temperatures were measured. Since specific heat capacity is the amount of heat energy required to raise the temperature by one degree per unit mass, the temperatures decreased with increases in the specific heat of concrete. Indeed, as the specific heat of concrete increased from 800 to 1,200 J/kg·K, the girder temperatures decreased by approximately 1°C (1.8°F) to 4°C (7.2°F), or 4 to 10%.

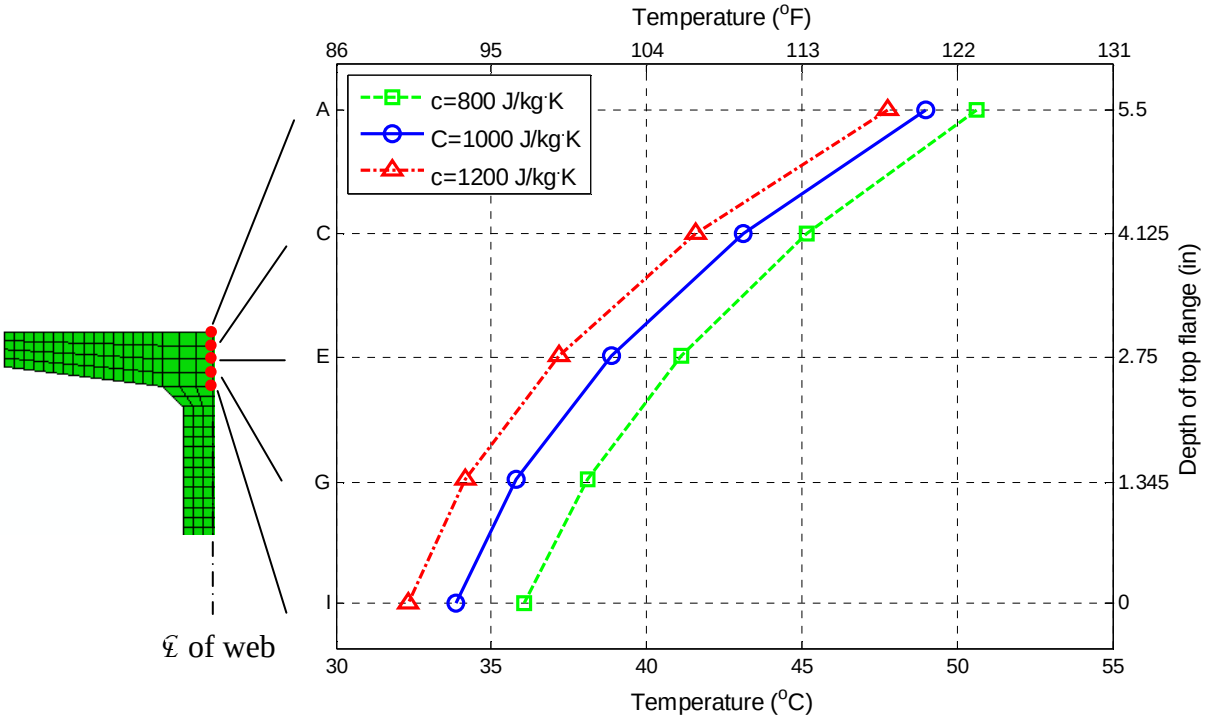

(Units: °C)

Specific Heat, (J/kg·K)	Locations				
	A	C	E	G	I
800	50.64 (0 %)	45.17 (0 %)	41.11 (0 %)	38.12 (0 %)	36.05 (0 %)
1,000	49.00 (-3.2%)	43.13 (-4.5 %)	38.85 (-5.5 %)	35.82 (-6.0 %)	33.86 (-6.1 %)
1,200	47.75 (-5.7%)	41.60 (-7.9%)	37.17 (-9.6 %)	34.16 (-10.4 %)	32.32 (-10.3 %)

Figure 7.10: Comparisons of the temperature distributions obtained from the specific heat of concrete, c = 800, 1000, and 1200 J/kg, through the depth of the top flange at 2:08 p.m. on June 1, 2009.

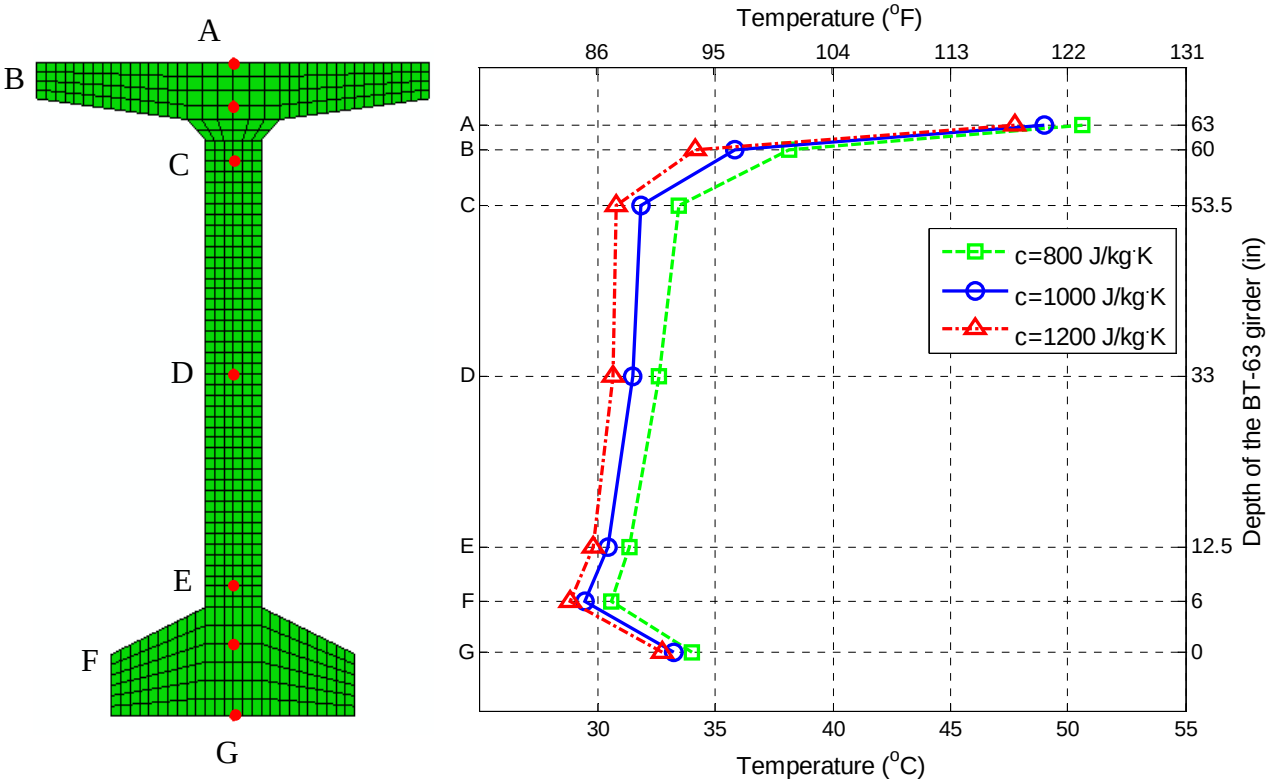

(Units: °C)

Specific Heat, (J/kg·K)	Locations						
	A	B	C	D	E	F	G
800	50.64 (0 %)	38.12 (0 %)	33.42 (0 %)	32.59 (0 %)	31.36 (0 %)	30.54 (0 %)	34.04 (0 %)
1,000	49.00 (-3.2%)	35.82 (-6.0%)	31.84 (-4.7%)	31.48 (-3.4%)	30.41 (-3.0%)	29.44 (-3.6%)	33.25 (-2.3%)
1,200	47.75 (-5.7%)	34.16 (-10.4%)	30.79 (-7.9%)	30.66 (-5.9%)	29.79 (-5.0%)	28.82 (-5.6%)	32.77 (-3.7%)

Figure 7.11: Comparisons of the temperature distributions obtained from the specific heat of concrete, c = 800, 1000, and 1200 J/kg, through the depth of the BT-63 girder at 2:08 p.m. on June 1, 2009.

7.3.3 Solar Absorptivity of Concrete

For concrete exposed to the sun, the solar absorptivity of concrete is the factor used to determine the amount of solar heat flux absorbed by the concrete surface. The values of concrete solar absorptivity used in several studies in the literature are in the range of 0.5 to 0.8 as described in Table 7.2. Thus, with respect to the values 0.5, 0.6, 0.7, and 0.8 of concrete solar absorptivity, variations in temperature distributions along the depth of the BT-63 girder were evaluated. During the analysis, the other thermal properties of concrete maintained constant: 1.5 W/m·K of thermal conductivity and 1,000 J/kg·K of specific heat.

Figures 7.12 and 7.13 show the temperature distributions obtained from the four values of concrete solar absorptivity along the depth of the top flange and along the depth of the girder, respectively. As solar absorptivity increased by 0.1, the temperatures on the top surface increased by about 8%, or 4°C (7.2°F). The temperature increased by 5%, or 1.8°C (3.2°F), in the middle of the top flange (location B); 2.5%, or 0.8°C (1.4°F), in the middle of the web (location D); and 1.2%, or 0.4°C (0.7°F), in the middle of the bottom flange (location F) with increases in solar absorptivity by 0.1. The bottom surface, affected by solar radiation reflection or heat radiating from the ground, showed an increase of 3%, or 1.0°C (1.8°F), with an increase of 0.1 in the solar absorptivity.

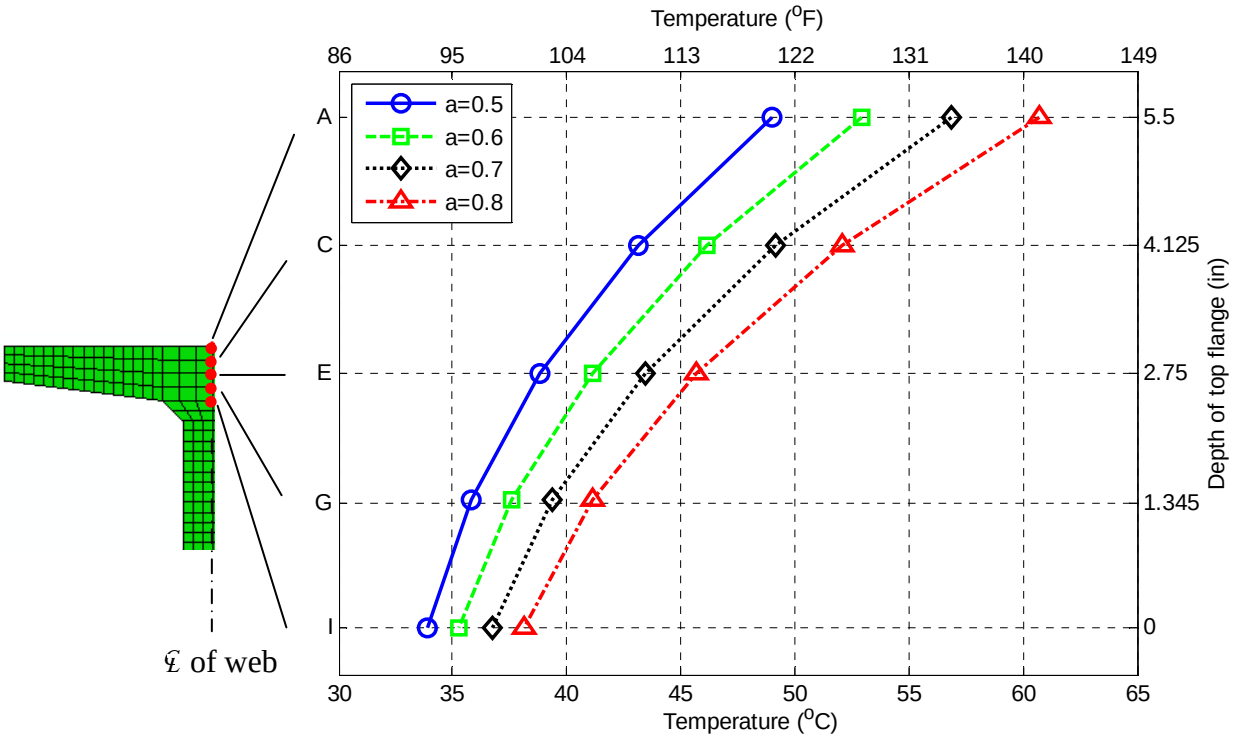

(Units: °C)

Solar Absorptivity	Locations				
	A	C	E	G	I
0.5	49.00 (0 %)	43.13 (0 %)	38.85 (0 %)	35.82 (0 %)	33.86 (0 %)
0.6	52.93 (8.0%)	46.14 (7.0 %)	41.15 (5.9%)	37.61 (5.0%)	35.29 (4.2%)
0.7	56.83 (16.0%)	49.12 (13.9%)	43.44 (11.8%)	39.39 (10.0%)	36.72 (8.4%)
0.8	60.71 (23.9%)	52.08 (20.8%)	45.72 (17.7%)	41.16 (14.9%)	38.14 (12.6%)

Figure 7.12: Comparisons of the temperature distributions obtained from the solar absorptivity of concrete, α = 0.5, 0.6, 0.7, and 0.8, through the depth of the top flange at 2:08 p.m. on June 1, 2009.

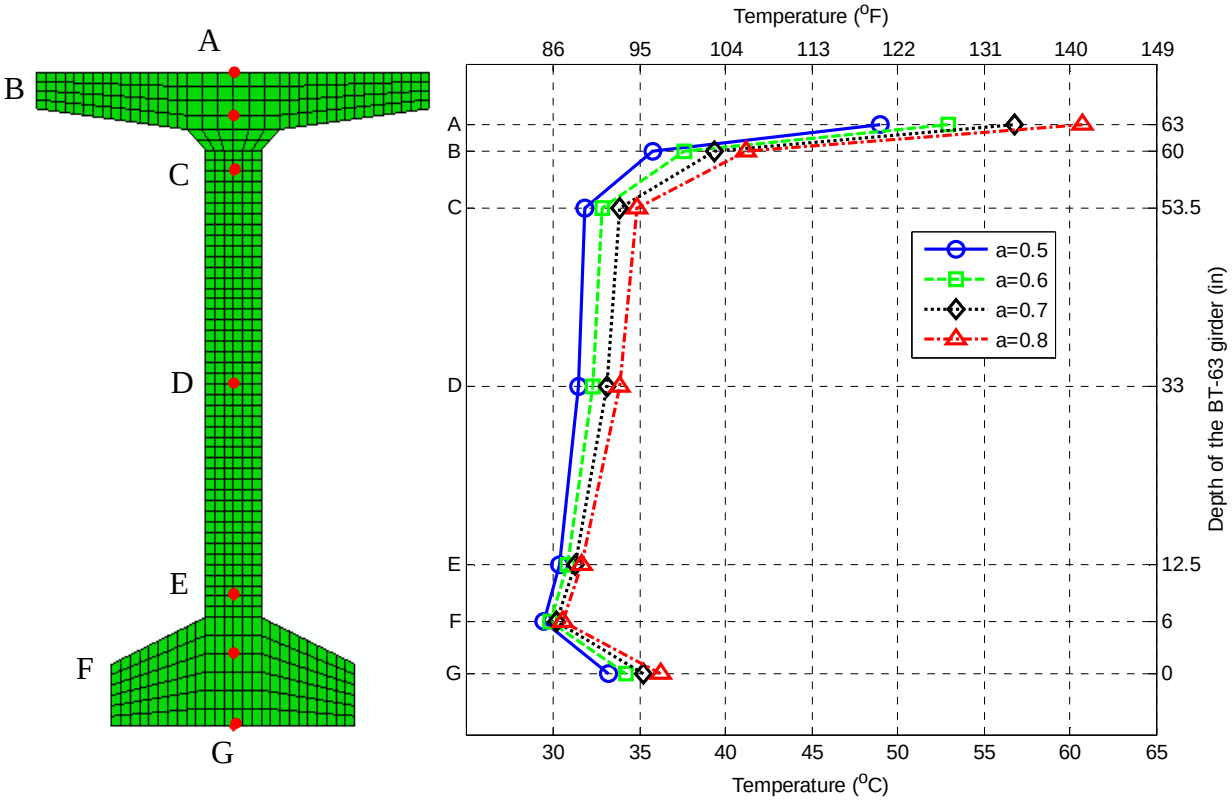

(Units: °C)

Solar Absorptivity	Locations						
	A	B	C	D	E	F	G
0.5	49.00 (0 %)	35.82 (0 %)	31.84 (0 %)	31.48 (0 %)	30.41 (0 %)	29.44 (0 %)	33.25 (0 %)
0.6	52.93 (8.0%)	37.61 (5.0%)	32.85 (3.2%)	32.28 (2.5%)	30.83 (1.4%)	29.80 (1.2%)	34.24 (3.0%)
0.7	56.83 (16.0%)	39.39 (10.0%)	33.86 (6.3%)	33.08 (5.1%)	31.25 (2.8%)	30.16 (2.4%)	35.23 (6.0%)
0.8	60.71 (23.9%)	41.16 (14.9%)	34.87 (9.5%)	33.88 (7.6%)	31.66 (4.1%)	30.52 (3.7%)	36.21 (8.9%)

Figure 7.13: Comparisons of the temperature distributions obtained from the solar absorptivity of concrete, α = 0.5, 0.6, 0.7, and 0.8, through the depth of the BT-63 girder at 2:08 p.m. on June 1, 2009.

7.3.4 The Rate of Temperature Changes with the Thermal Properties of Concrete

Based on the temperature distributions at 2:08 p.m., Figure 7.14 shows changes in the temperature distributions along the depth of the girder with changes in the thermal properties of concrete. The reference values of the thermal properties of concrete were 1.5 W/m·K for thermal conductivity, 1,000 J/kg·K for specific heat, and 0.5 for solar absorptivity. For example, for a parametric study on thermal conductivity, the specific heat and the solar absorptivity of concrete were constants of 1,000 J/kg·K and 0.5, respectively, during the analysis. As discussed previously, with increases in thermal conductivity, Figure 7.14 shows temperature decreased on the surfaces of the girder due to rapid heat absorption on the surface but temperature increased inside the girder. For the specific heat of concrete, the girder temperatures decreased with increases in the specific heat. Figure 7.14 also presents increases in the temperatures with increases in the solar absorptivity.

Furthermore, this study evaluated the rate of temperature increases or decreases with changes in the thermal properties of concrete. Figure 7.15 shows the percentage change of the temperatures in the middle of the top flange, the web, and the bottom flange. The percentage change of the temperatures with increases in the thermal properties of concrete is summarized in Table 7.3. In the web of the girder, as the thermal conductivity and the solar absorptivity of concrete increased by units of 1 W/m·K and 0.1, respectively, the temperatures increased about 2% (1°C). On the other hand, with increases in the specific heat of concrete by a unit of 100 J/kg·K, the temperatures decreased about 2% (1°C). Therefore, in the heat transfer analysis of prestressed concrete bridge girders subjected to environmental thermal effects, the influences of the thermal properties of concrete would be minimal when thermal properties are within reasonable ranges.

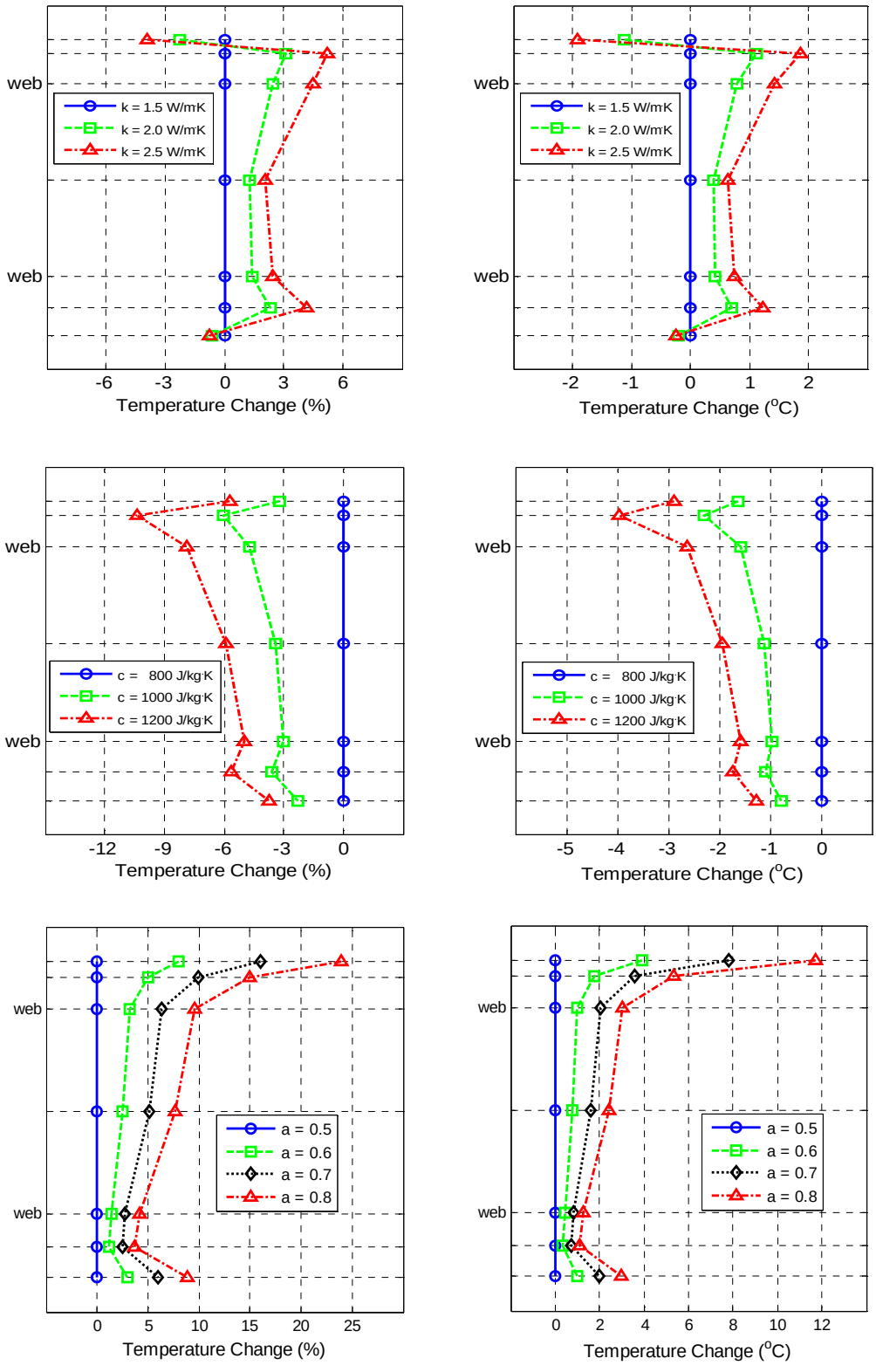

Figure 7.14: Changes in the temperature distributions through the depth of the BT-63 girder with changes in the thermal properties of concrete.

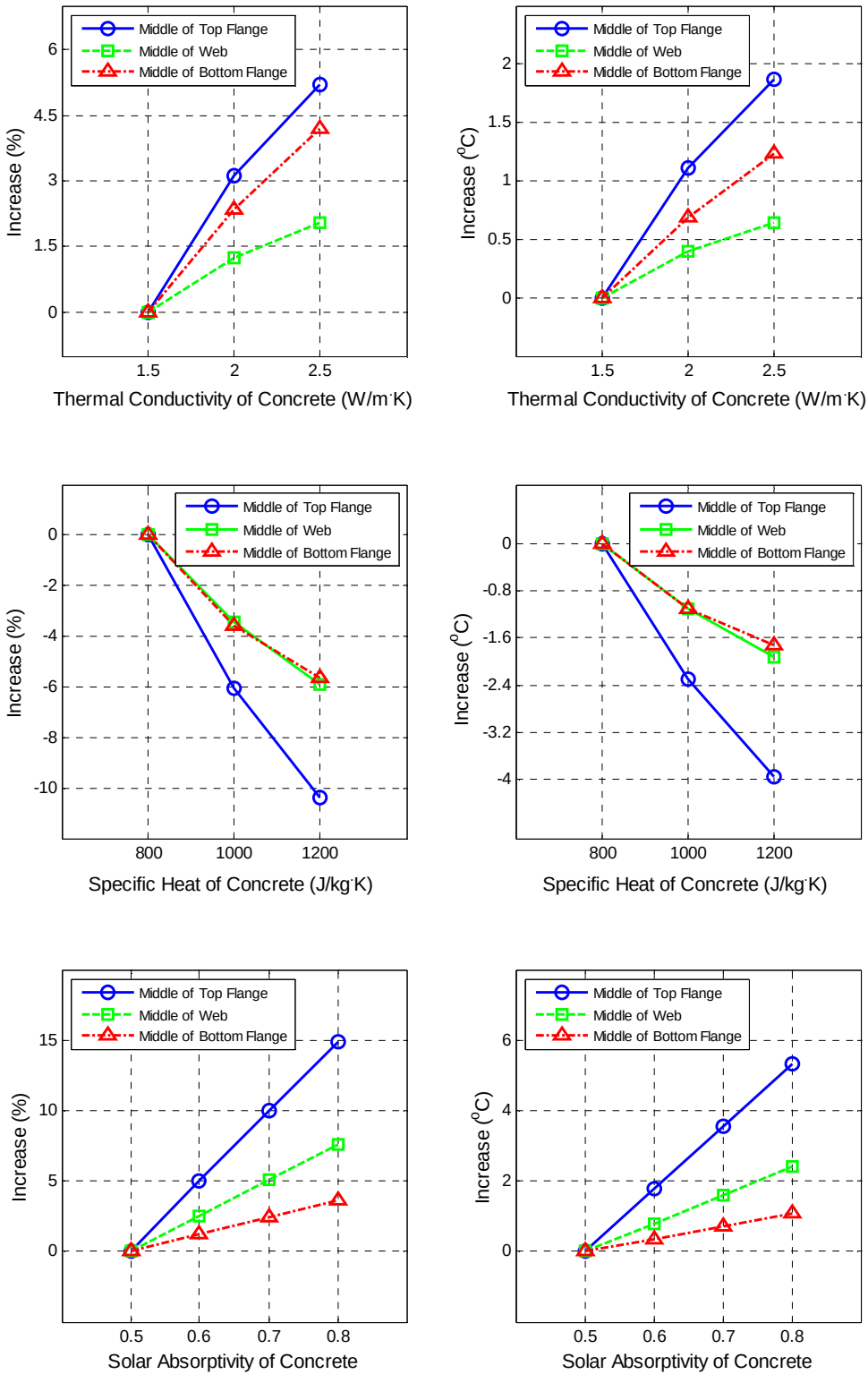

Figure 7.15: The percentage change of the girder temperatures with increases in the thermal properties of concrete.

Table 7.3: The percentage change of the girder temperatures with changes in the thermal properties of concrete.

Thermal Properties	Change Rates of Properties	Percentage Change of Temperatures		
		Top flange	Web	Bottom flange
Thermal Conductivity	1 W/m·K	+ 5% (+2°C)	+ 2% (+1°C)	+ 4% (+1.0°C)
Specific Heat	100 J/kg·K	- 3% (-1°C)	- 2% (-1°C)	- 2% (-0.5°C)
Solar Absorptivity	0.1	+ 5% (+2°C)	+ 3% (+1°C)	+ 3% (+0.5°C)

7.4 Thermal Movements with the Coefficient of Thermal Expansion (CTE)

Furthermore, to evaluate the influence of the CTE in the thermal behavior of prestressed concrete bridge girders, the 3D thermal stress analyses were carried out on the 100-foot BT-63 girder with changes in the CTE from 6 to 12 × 10^{-6} / °C. The other thermal properties of concrete maintained constant: 1.5 W/m·K for thermal conductivity, 1,000 J/kg·K, for specific heat, and 0.5 for solar absorptivity. The CTE of the prestressing strands also remained constant at 12 × 10^{-6} / °C during the analysis. Since the 3D thermal stress analysis consumes more time, this study used hourly temperature fields obtained from extreme summer environmental conditions in Atlanta, Georgia instead of measurements at five-minute intervals on June 1, 2009. The support boundary conditions of elastomeric bearing pads were modeled as rigid vertical restraints as described in Section 4.2.

Figures 7.16 and 7.17 show variations in the vertical and transverse thermal movements at mid-span of the BT-63 girder for the CTE of 6, 9 and 12 × 10^{-6} / °C, respectively. With increases in the CTE, the vertical and transverse thermal movements proportionally increased. The maximum vertical movements were 0.21, 0.31, ad 0.42 inches at 3:00 p.m. in the CTE of 6, 9 and 12 × 10^{-6} / °C, respectively. The maximum

transverse thermal movements also linearly increased from 0.20 to 0.40 inches. Figure 7.18 exhibits the percentage change of the maximum vertical and transverse thermal movements, which double for the CTE that doubles from 6 to 12 × 10^{-6} / °C. Thus, the vertical and transverse thermal movements would change linearly in proportion to the changes in the CTE. For the 100-foot BT-63 girder, the maximum vertical and transverse thermal movements increase by approximately 0.03 inches (16%) with an increase by a unit of 1 × 10^{-6} / °C from 6 × 10^{-6} / °C.

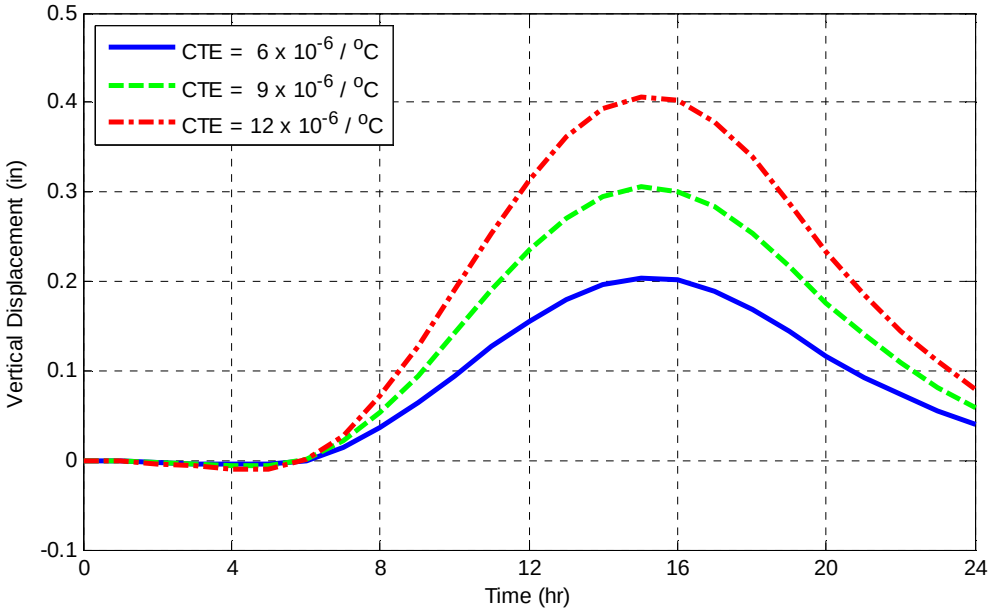

Figure 7.16: Variations in the vertical thermal movements at mid-span of the BT-63 girder with changes in the coefficient of thermal expansion, 6, 9, and 12 × 10^{-6} / °C.

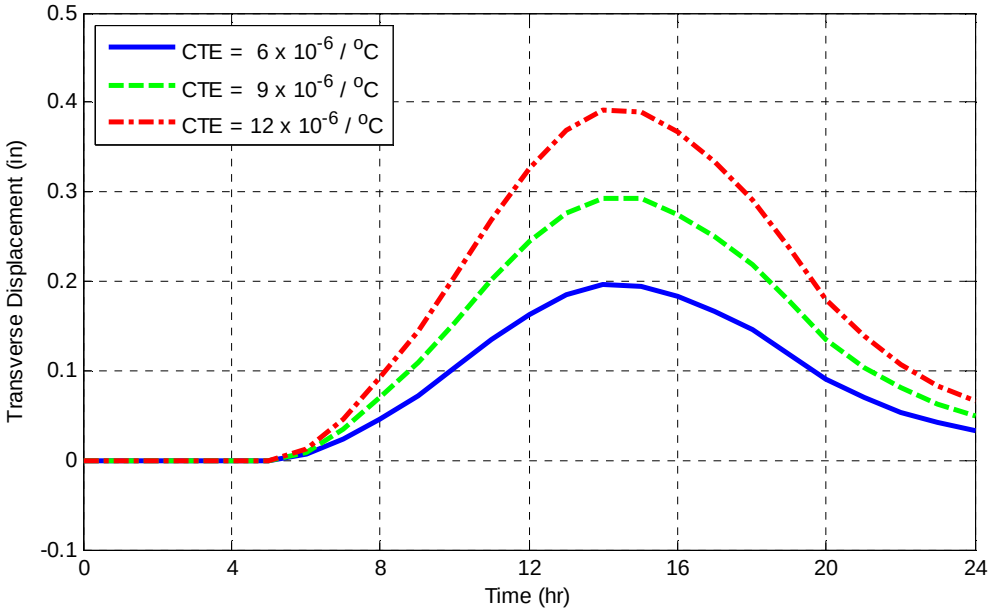

Figure 7.17: Variations in the transverse thermal movements at mid-span of the BT-63 girder with changes in the coefficient of thermal expansion, 6, 9, and 12 × 10^{-6} / °C.

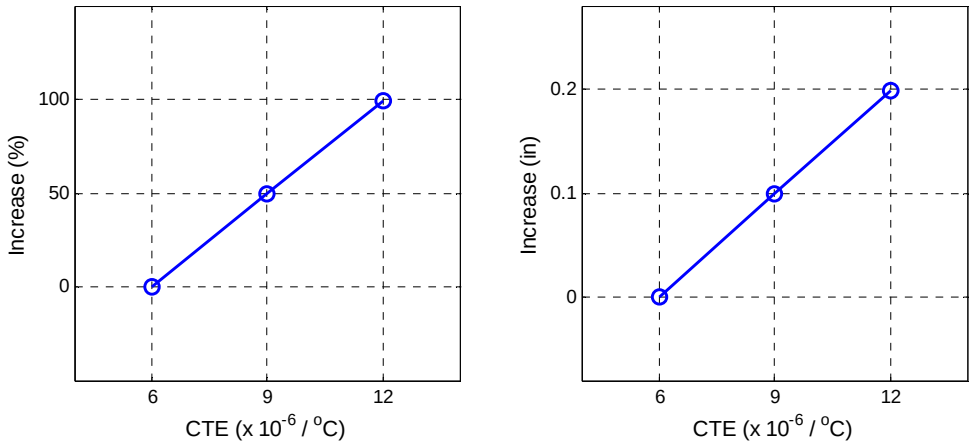

(a) Maximum vertical thermal movements

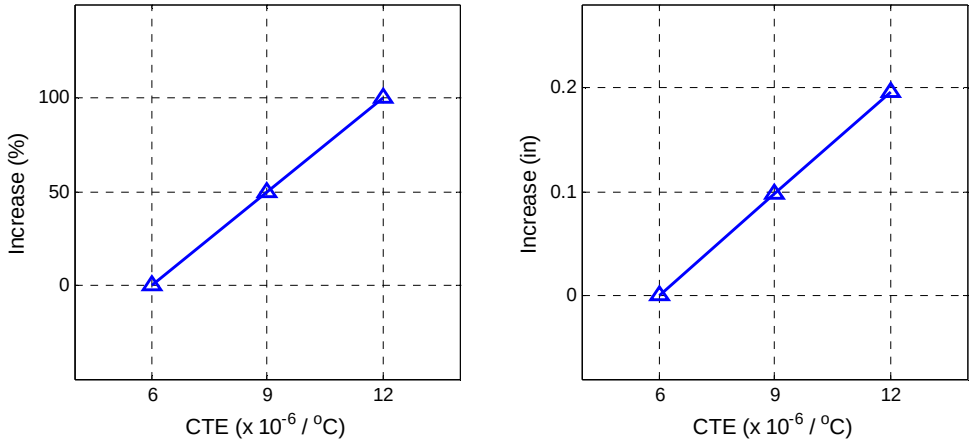

(b) Maximum transverse thermal movements

Figure 7.18: The percentage change of the maximum vertical and transverse thermal movements with increases in the coefficient of the thermal expansion of concrete.

CHAPTER 8

CONCLUSIONS AND RECOMMENDATIONS

8.1 Conclusions

This study first investigated variations in vertical and transverse temperature distributions in prestressed concrete bridge girders due to environmental effects. A two-dimensional (2D) finite element heat transfer model was then developed which accounted for heat conduction in the concrete girder, heat convection between the environment and the girder surface, heat irradiation from the sun, and heat radiation to the surroundings. Since most of weather stations provide only daily solar radiation incident on a horizontal surface, the 2D heat transfer analysis included the calculation of variations in solar radiation with respect to the time of day on each surface of the girder according to the location and geometry of the girder, the position of the sun, and the shadow on the web and the bottom flange of the girder. The magnitudes and the variations of the predicted temperatures were in very good agreement with experimental measurements performed from April 2009 to March 2010.

Based on the relationships between environmental conditions and largest vertical and transverse temperature distributions, seasonal extremes in environmental conditions were determined from the 30-year (from 1961 to 1990) monthly data of the National Solar Radiation Data Base, NSRDB, and the National Climatic Data Center, NCDC. The developed 2D heat transfer model was then employed to determine seasonal extremes in vertical and transverse temperature distributions and gradients for four selected AASHTO-PCI standard girder sections. The influence of girder orientations on the temperature distributions of the girders was also evaluated. The maximum vertical temperature differentials were found in the summer in an east-west orientation, and the

maximum transverse temperature differentials were found in the winter in an east-west orientation. Among the four AASHTO-PCI sections, the deeper and wider sections of Type-V and BT-63 girders exhibited the largest vertical and transverse temperature differentials.

For thermal gradients to be used in the design of prestressed concrete I-girders, a revised vertical thermal gradient was first proposed. Figure 8.1 compares the vertical thermal gradients proposed by the current study with the vertical thermal gradients in the AASHTO specifications (1989, 2007) for Atlanta, Georgia. For a simply supported 100-foot long BT-63 girder, the vertical thermal movement calculated using the proposed vertical thermal gradient was approximately 40% higher than the vertical movement calculated using the gradient in the AASHTO specifications.

The stability of the prestressed concrete girders largely depends on transverse movements in the girder. However, the AASHTO specifications (1989, 2007) do not provide any transverse thermal gradients. Therefore, this study also proposed transverse thermal gradients for the top flange, web, and bottom flange of prestressed concrete I-girders, as shown in Figure 8.2. The proposed vertical and transverse thermal gradients were provided in terms of the locations of the top flange, the web, and the bottom flange of the girders for the easy application to various I-shape girders.

The maximum vertical and transverse temperature differentials were evaluated at eight cities in the United States. The eight cities were selected from the 30-year (from 1961 to 1990) monthly NSRDB and NCDC data based on extreme environmental conditions such as the highest daily solar radiation, the highest record daily maximum temperature, and the largest daily temperature variance: Alamosa, CO; Phoenix, AZ; Medford, OR; Atlanta, GA; Brownsville, TX; Caribou, ME; Hilo, HI; Annette, AK.

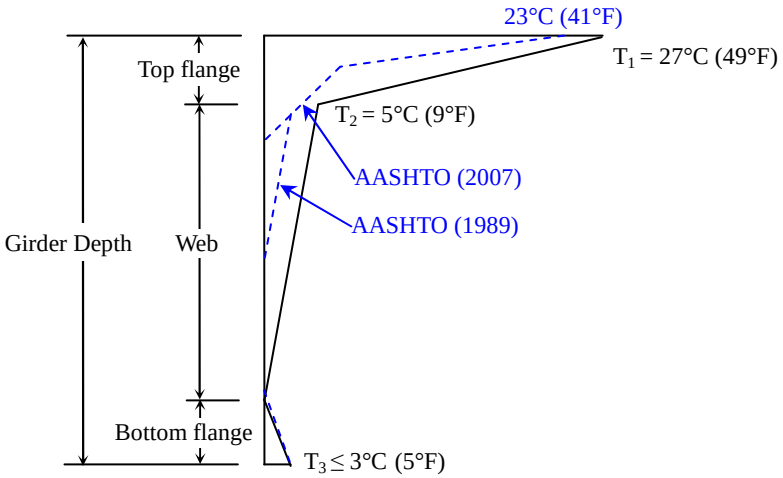

Figure 8.1: The vertical thermal gradients of prestressed concrete bridge I-girders in Atlanta, Georgia proposed by the current study and given in the AASHTO specifications (1989, 2007).

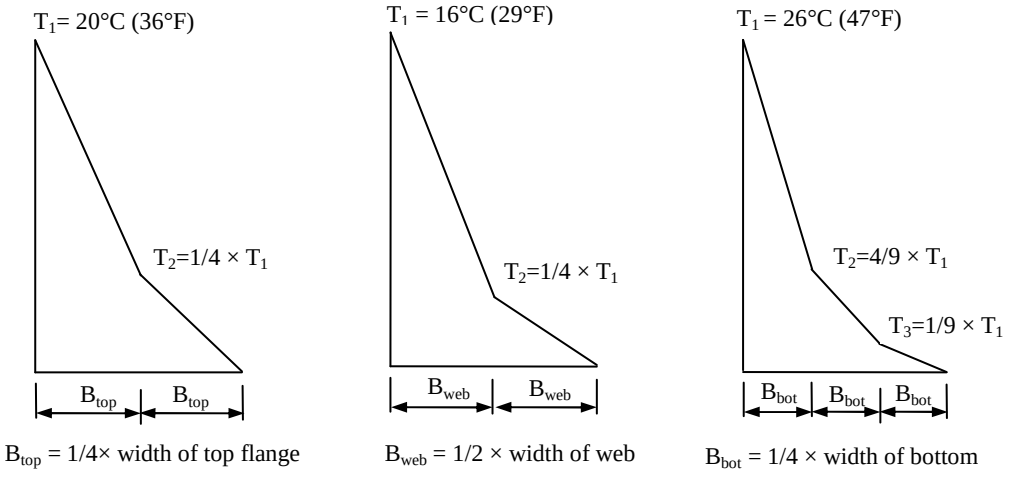

(a) Top flange (b) Web (c) Bottom flange

Figure 8.2: The transverse thermal gradients of prestressed concrete bridge I-girders in Atlanta, Georgia proposed by the current study (Not to Scale).

The maximum girder temperatures were then transferred to the three-dimensional (3D) finite element model of a 100-foot long BT-63 girder located in Atlanta with a constant temperature variation along the length of the girder. The 3D thermal response analysis considered in this study was composed of two sequential analyses; the first 3D static analysis with a simply supported boundary condition and the second 3D thermal stress analysis with elastomeric bearing pads. The bearing pads were modeled as nonlinear springs with the effective vertical stiffness of the bearing pads. The analyses of the girder did not exhibit any instability of the girder due to the combined effects of the self-weight and temperature without any initial sweep or support rotation.

Since thermal effects are combined with fabrication and construction errors prior to the placement of cross bracing and the deck slab, a 3D finite element sequential analysis procedure was developed which accounted for the changes in the geometry and stress state of the girder during construction and erection. This analysis included geometric nonlinear behavior of the girder and the nonlinear behavior of the elastomeric bearing pads. For the 100-foot BT-63 girder, the analyses indicated a possible instability of the girder due to the combination of thermal effects with 4.5 inches of initial sweep and a 5 degree support slope.

This study also developed a beam model with artificial end moments to calculate the vertical and transverse thermal deformations induced by nonlinear temperature distributions for simply supported girders. The end moments which cause vertical deformations are obtained from a vertical temperature gradient along the depth of the cross-section. The end moments which cause transverse deformations are defined as the sum of three transverse temperature gradients of the top flange, the middle of the web, and the bottom flange because the transverse temperature gradients vary from the top to the bottom flanges. Compared with the results from the 3D finite element analysis, the

beam vertical and transverse movements were within 0.03 inches (6%). This study also developed simplified equations for calculating the maximum vertical and transverse thermal movements in terms of the span length of the girders for four selected AASHTO-PCI standard girders; Type-I, Type-IV, Type-V, and BT-63 girders.

8.2 Recommendations for Future Studies

The current experimental and analytical investigations were carried out on a BT-63 prestressed girder to determine variations in environmental conditions and girder temperatures. To provide more generalized conclusions toward design recommendations in the future, both experimental and analytical investigations are recommended for other prestressed concrete girders from the construction stages until service load conditions. The primary measurements and investigations are described below:

(1) A survey of geometry sweep and support imperfections present in newly constructed girders.
(2) Development of criterion for initial slope imperfections
(3) Development of criterion for bracing requirements.
(4) Since the global stability behavior of prestressed concrete bridge girders are largely affected by the behavior of elastomeric bearing pads, experimental and analytical studies are also required to obtain the effective vertical and horizontal stiffness of the bearing pads. Furthermore, the development of the three-dimensional and simplified beam models are recommended for evaluating the influences of the bearing pads on the behavior of the bridge systems under various environmental and loading conditions.

APPENDIX A

A MODEL OF TRANSVERSE TEMPERATURE DISTRIBUTION

For the vertical temperature distribution through the depth of a concrete superstructure, Priestley (1976) proposed a fifth-order temperature decrease from a maximum temperature at the concrete top surface. The Priestley fifth-order model was a basis of the current design specifications in many countries such as New Zealand, North America, and England. However, no model has been suggested for the shape of transverse temperature distributions in the concrete superstructure. The temperatures along the transverse direction of a concrete bridge section are induced by the heating of the vertical surface due to solar radiation and also affected by the vertical heat flow. Thus, in order to describe the gradual decrease from the highest temperature in the transverse direction, this study proposed a second-order model shown in Figure A.1. The temperature $T(x)$, shown in Figure A.1, is calculated using the following second-order equation:

$$T(x) = T_s(x / L)^2 \tag{A.1}$$

in which $T(x)$ = the temperature at a distance of x,

T_s = the surface temperature,

x = the distance from the surface, and

L = the length from the surface to zero temperature.

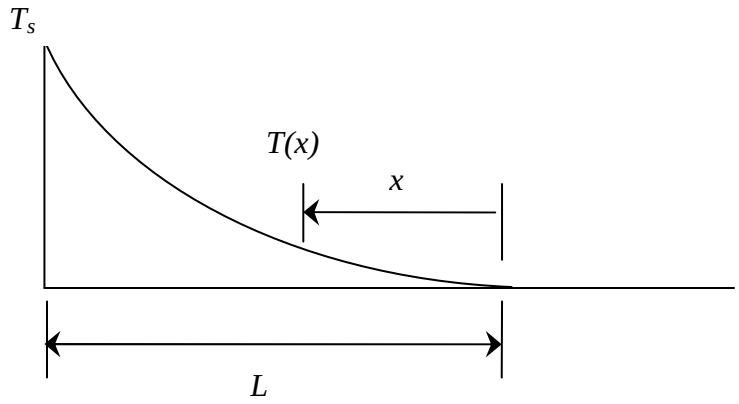

Figure A.1: A model of the transverse temperature distribution.

For November 15, 2009, on which girder temperatures at thermocouple location 9 and 10 were missed due to a poor connection to data-logging system, the proposed second-order model was used to extrapolate the missing temperatures from the surface temperature (thermocouple 14) and the minimum temperature (thermocouple 11). Compared with the temperatures obtained from finite-element heat transfer analysis, those calculated by Equation (A.1) showed average absolute errors of 0.6°C (1.1°F) and 1.3°C (2.4°F) at the locations of the thermocouples 9 and 10, respectively. The maximum difference between the temperatures obtained from the heat transfer analysis and the Equation (A.1) was 3.3°C (5.8°F) at the thermocouple 9 and 2.6°C (4.7°F) at the thermocouple 10.

Furthermore, this study compared maximum transverse temperature distributions measured across the bottom flange (including the extrapolated temperatures at the thermocouples 9 and 10) with those obtained from the finite element heat transfer analysis. Figure A.2 shows the measured and predicted transverse temperature distributions in the bottom flange on November 15, 2009. The magnitudes and shapes of the transverse temperature distribution from the measurements agree well with the results of the heat transfer analysis. The temperatures extrapolated using Equation (A.1) differed

from the results of the heat transfer analysis by only 0.2°C (0.4°F) and 0.7°C (1.3°F) at the thermocouple location 9 and 10, respectively.

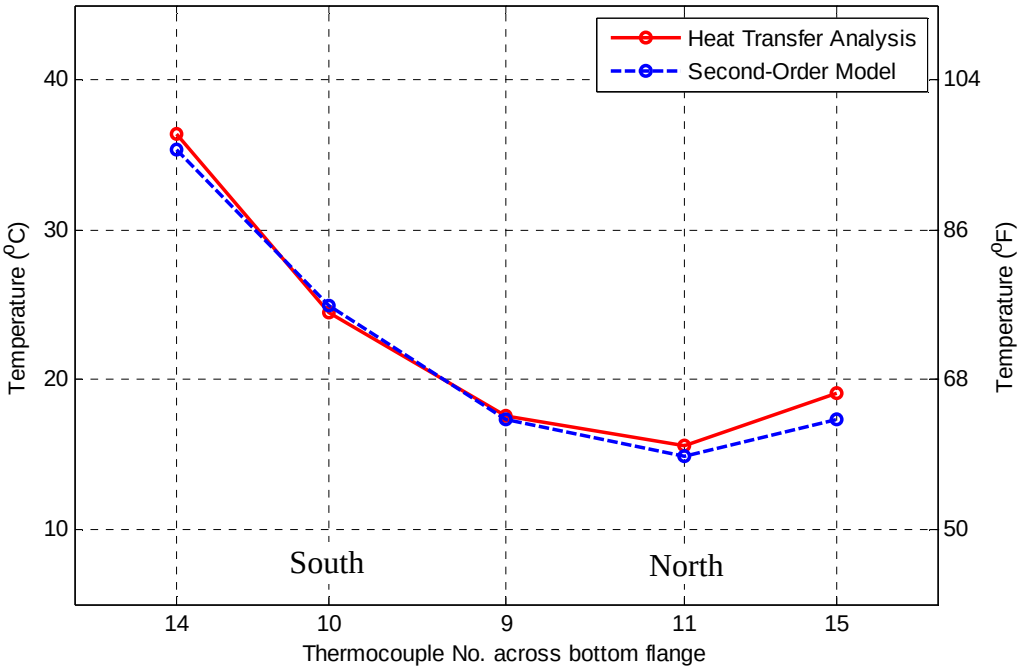

Thermocouple No.	14	10	9	11	15
Heat Transfer Analysis, °C (°F)	36.4 (97.5)	24.5 (76.1)	17.6 (63.7)	15.6 (60.1)	19.1 (66.5)
Second-Order Model, °C (°F)	35.3 [b] (95.6)	24.9 [a] (76.8)	17.4 [a] (63.3)	14.9 [b] (58.8)	17.3 (63.2)
Difference, °C (°F)	1.1 (1.9)	0.4 (0.7)	0.2 (0.4)	0.7 (1.3)	1.8 (3.3)

[a] The temperatures at the thermocouple location 10 and 9 were extrapolated using the second-order equation.

[b] The temperatures at the thermocouple location 14 and 11 were the measured maximum and minimum temperatures, respectively, across the bottom flange.

Figure A.2: Predicted and measured maximum transverse temperature distributions at the thermocouple location across the bottom flange on November 15, 2009.

APPENDIX B

CALCULATION OF SOLAR POSITION

The calculation of solar radiation incident on girder surfaces requires that the relationship between a position on the earth's surface and the position of the sunlight be determined. Figure B.1 shows the position of *P* on the earth's surface and the sun at one time in the summer. Point *P*, which represents a location in the Northern Hemisphere, is expressed as the latitude of ϕ. The declination angle, δ, is the angular position of the sun at solar noon with respect to the plane of the equator. The value of the declination at any time can be calculated from the following equation (Cooper, 1969):

$$\delta = 23.45 \sin\left(360 \frac{284 + n}{365}\right) \tag{B.1}$$

in which *n* is the day of the year. The hour angle, ω, defined as the angular displacement of the sun due to the rotation of the earth on its axis at 15° per hour, is zero at solar noon, negative before solar noon, and positive in the afternoon.

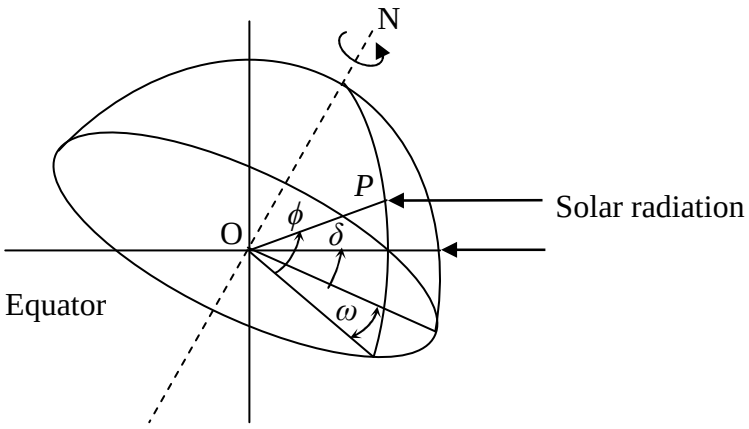

Figure B.1: A position on the earth's surface in relation to the direction of the radiation at one specific time in the summer.

The direct solar radiation incoming on a plane can be described in terms of the geometrical relationships between the plane oriented in a particular direction and the solar radiation. The position of the sun and the location of the plane relative to the sun are defined in Figure B.2, in which the solar and plane angles are as follows.

θ_Z : the zenith angle, defined as the angle between the line overhead and the line to the sun.

θ :the incident angle, defined as the angle between the beam radiation on a horizontal plane and the surface normal.

α_s : the solar altitude angle, defined as the angle between the beam radiation on the horizontal plane and the line to the sun.

γ_s : the solar azimuth, defined as the angle of the projection of the beam radiation on the horizontal plane from the south, with zero due south, negative to the east, and positive to the west.

γ : the surface azimuth, defined as the angle of the projection of the surface normal onto the plane from the south, with zero due south, negative to the east, and positive to the west.

β : the surface angle relative to the horizontal plane.

With the data of the position of the sun related to the plane, solar angles θ_z, θ, and γ_s are calculated by (Liu and Jordan, 1963)

$$\cos\theta_Z = \sin\delta\sin\phi + \cos\delta\cos\phi\cos\omega, \text{ and} \tag{B.2}$$

$$\begin{aligned}\cos\theta = {} & \sin\delta\sin\phi\cos\beta - \sin\delta\cos\phi\sin\beta\cos\gamma \\ & + \cos\delta\cos\phi\cos\beta\cos\omega + \cos\delta\sin\phi\sin\beta\cos\gamma\cos\omega \\ & + \cos\delta\sin\beta\sin\gamma\sin\omega\end{aligned} \tag{B.3}$$

$$\gamma_s = \sin^{-1}\left(\frac{\cos\delta \sin\omega}{\sin\theta_z}\right) \tag{B.4}$$

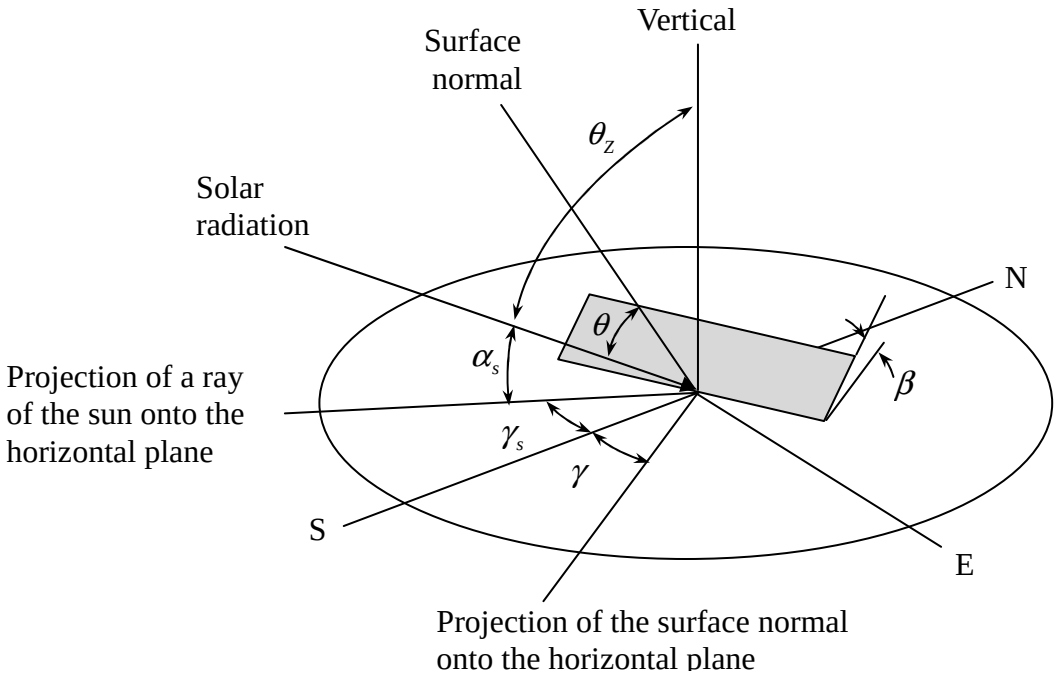

Figure B.2: The angles of the solar position and the slope of a plane oriented in any particular position.

APPENDIX C

CALCULATION OF THERMAL MOVEMENTS USING A BEAM MODEL

For the 100-foot long BT-63 girder, the proposed beam model was used to calculate vertical and transverse thermal movements from hourly vertical and transverse temperature gradients obtained from the 2D heat transfer analysis. The environmental conditions involved in this study were extreme summer and winter environmental conditions in Atlanta, Georgia, when the largest vertical and transverse temperature gradients were respectively found. Figure C.1 show the largest vertical temperature gradient along the depth of the girder in the summer, and Figure C.2 show the transverse temperature gradients across the middle of top flange, web, and bottom flange of the girder in the winter.

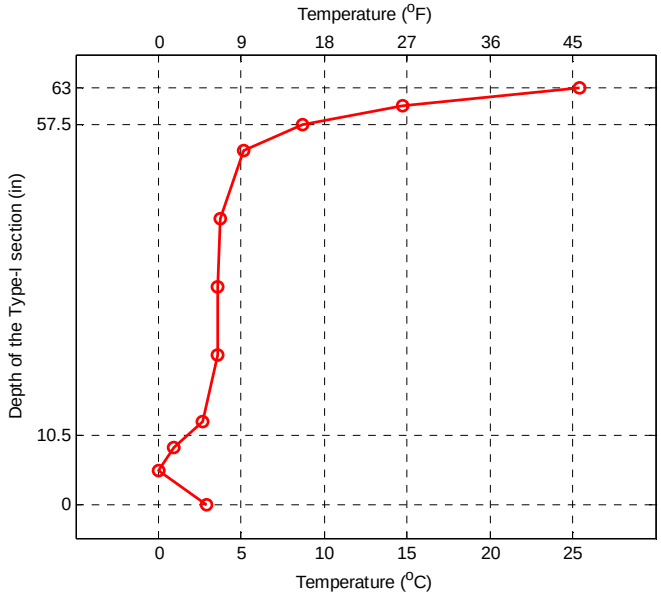

Figure C.1: The largest vertical temperature gradient of the BT-63 girder in the summer in Atlanta, Georgia.

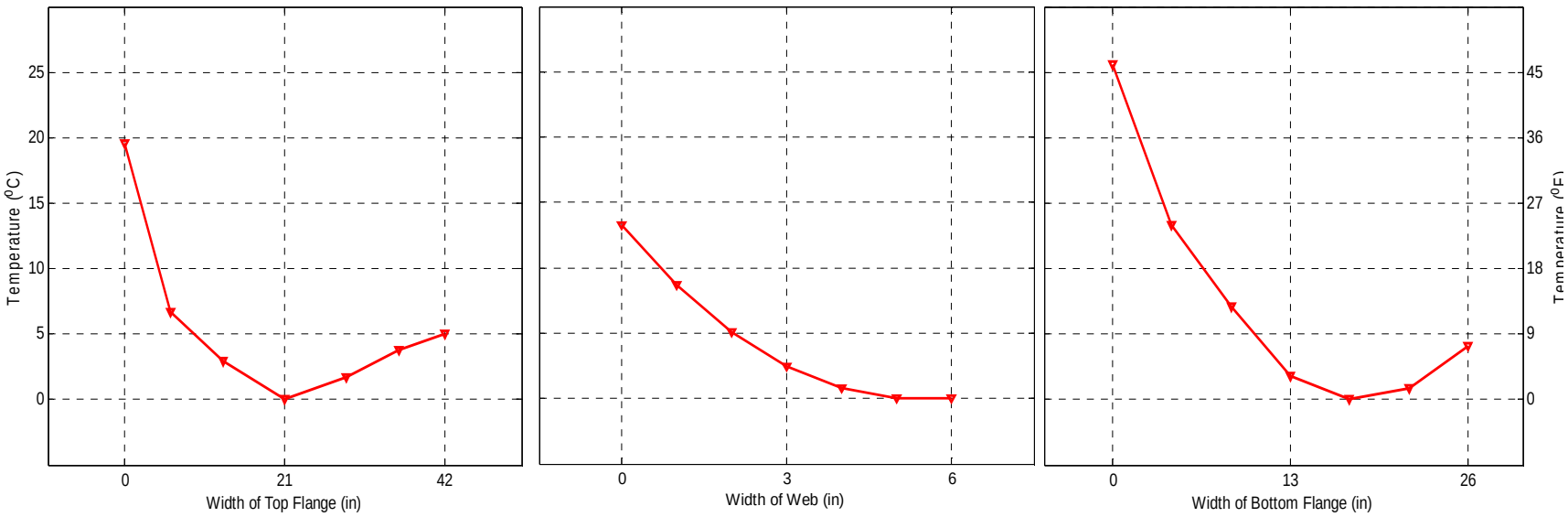

(a) Top flange (b) Web (c) Bottom flange

Figure C.2: The largest transverse temperature gradients of the BT-63 girder in the winter in Atlanta, Georgia.

Figure C.3 illustrates the vertical temperature differential at a depth of y from the center of the gravity of the cross-section. Therefore, the artificial end moment M_x induced by the vertical temperature gradient can be obtained from the following equation:

$$M_x = \int [E \cdot \alpha \cdot \Delta T(y) \cdot b(y) \cdot y] dy = \sum [E_i \cdot \alpha_i \cdot \Delta T(y_i) \cdot b(y_i) \cdot y_i \cdot \Delta y_i] \quad \text{(C.1)}$$

in which E_i = the concrete modulus of elasticity at a depth y_i,

α_i = the coefficient of thermal expansion of concrete at a depth y_i,

$\Delta T(y_i)$ = the vertical temperature differential at a depth y_i, and

$b(y_i)$ = the width of the girder section at a depth y_i,

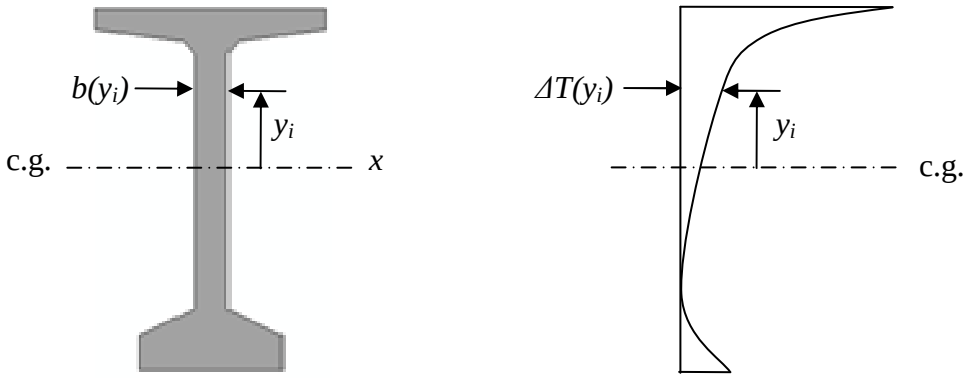

(a) Cross-section (b) Vertical temperature gradient

Figure C.3: The cross-section and vertical temperature gradient of the BT-63 girder.

For a simple span, the vertical deformation δ_y at mid-span is then calculated by

$$\delta_y = \frac{M_x L^2}{8 E I_x} \quad \text{(C.2)}$$

in which I_x is the moment of inertia of the cross-section with respect to the *x*-axis, and *L* is the length of the girder.

Figure C.4 shows variations in the vertical thermal movements of the BT-63 girder calculated using the beam model from the hourly vertical temperature gradients in the summer and the winter in Atlanta, Georgia. The maximum vertical thermal movements were 0.54 inches at in the summer and 0.20 inches in the winter.

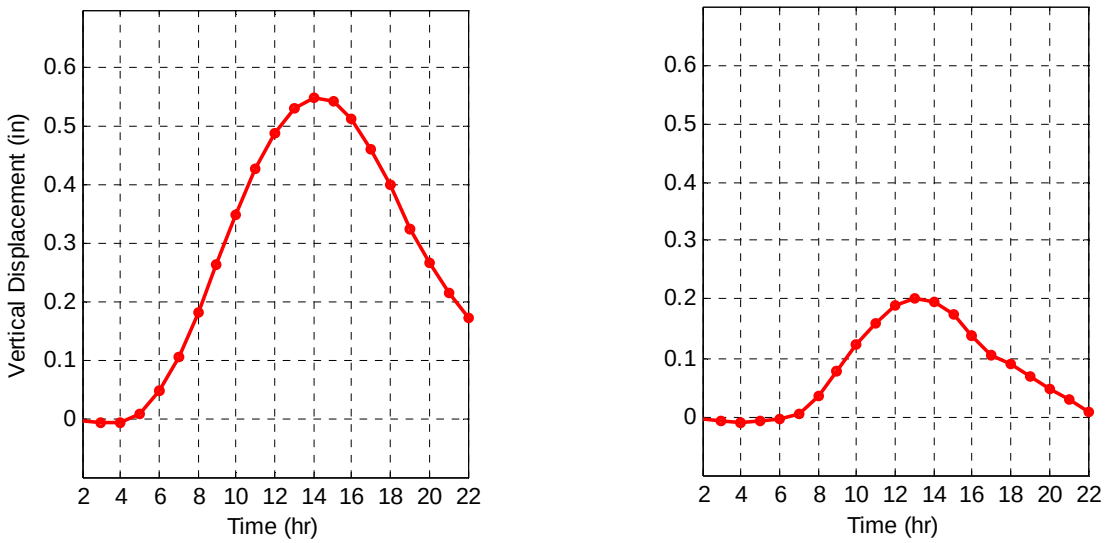

(a) Summer (b) Winter

Figure C.4: Variation in the vertical thermal movements of the 100-foot BT-63 girder under extreme summer and winter environmental conditions in Atlanta, Georgia.

Similarly, for the calculations of the transverse thermal movements, the artificial end moment M_y is determined from the transverse temperature gradients in the middle of the top flange, the web, and the bottom flange as shown in Figure C.5. The end moment M_y calculated from these three transverse temperature gradients is as shown below:

$$M_y = \sum_{top\ flange} [E_i \cdot \alpha_i \cdot T(x_i) \cdot h(x_i) \cdot x_i \cdot dx_i] + \sum_{web} [E_i \cdot \alpha_i \cdot T(x_i) \cdot h(x_i) \cdot x_i \cdot dx_i] + \sum_{bottom\ flange} [E_i \cdot \alpha_i \cdot T(x_i) \cdot h(x_i) \cdot x_i \cdot dx_i] \quad \text{(C.3)}$$

in which E_i = the concrete modulus of elasticity at a width x_i,

α_i = the coefficient of thermal expansion of concrete at a width x_i,

$\Delta T(x_i)$ = the transverse temperature differential at a width x_i, and

$h(x_i)$ = the height of the girder section at a width x_i,

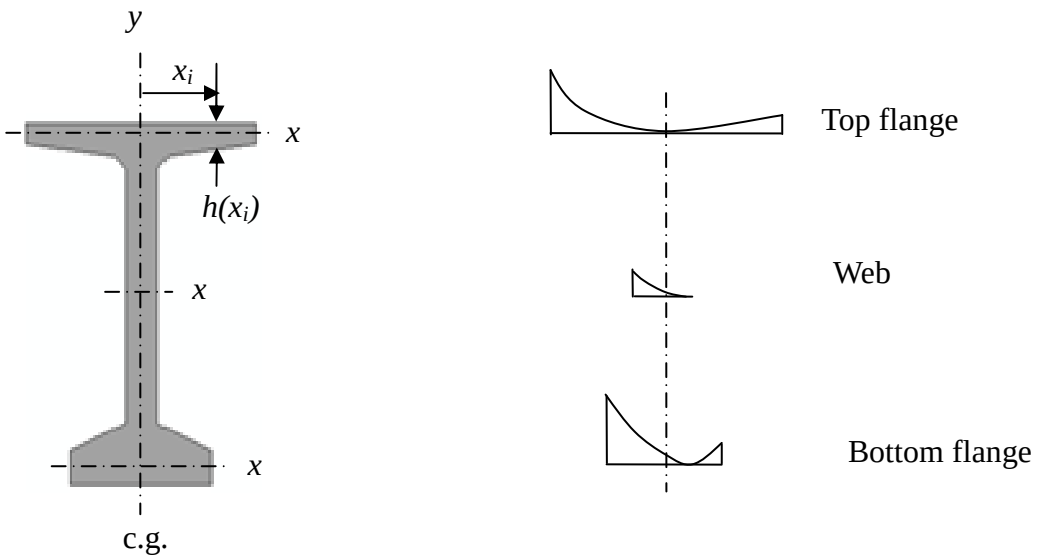

(a) Cross-section (b) Transverse temperature gradients

Figure C.5: The cross-section and transverse temperature gradients of the BT-63 girder.

Like to the vertical thermal movement, the transverse deformation δ_x is then calculated using the end moment M_y:

$$\delta_x = \frac{M_y L^2}{8EI_y} \tag{C.4}$$

in which I_y is the moment of inertia of the cross-section with respect to the *y*-axis, and *L* is the length of the girder. The variations in the transverse thermal movements calculated from the hourly transverse temperature gradients under extreme environmental conditions in the summer and the winter in Atlanta, Georgia are shown in Figure C.6. The calculated maximum transverse thermal movements were 0.39 inches in the summer and 0.81 inches in the winter.

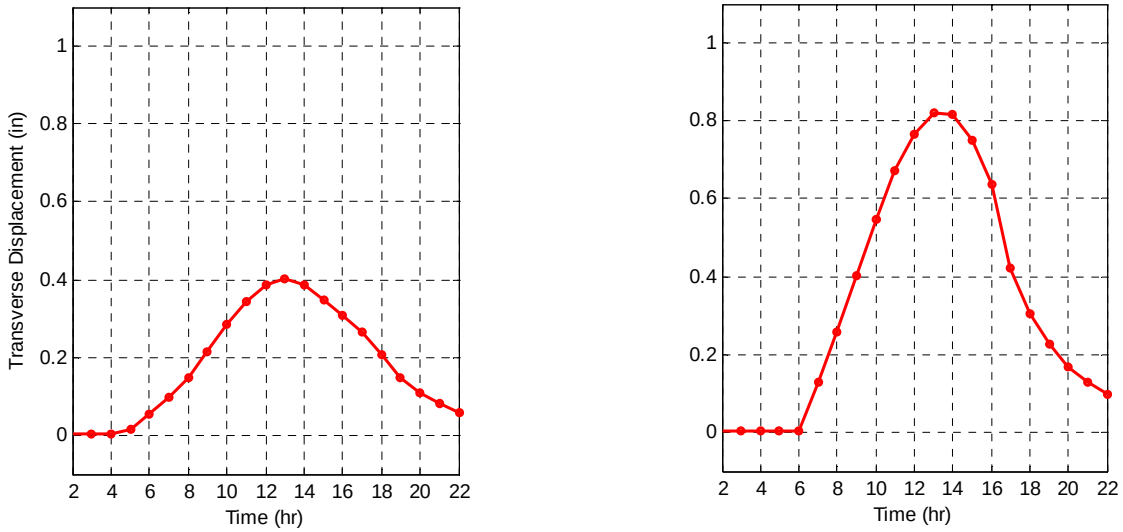

(a) Summer (b) Winter

Figure C.6: Variation in the transverse thermal movements of the 100-foot BT-63 girder under extreme summer and winter environmental conditions in Atlanta, Georgia.

REFERENCES

AASHTO. (1989). AASHTO Guide specifications: Thermal effects in concrete bridge superstructures. Washington, DC: American Association of State Highway and Transportation Officials.

AASHTO. (2007). AASHTO LRFD bridge design specifications: 2008 interim revisions (4th ed.). Washington, DC: American Association of State Highway and Transportation Officials.

AASHTO. (2004). AASHTO LRFD bridge construction specifications: 2006 and 2007 interim revisions (2nd ed.). Washington, DC: American Association of State Highway and Transportation Officials.

AASHTO. (1999). Guide specifications for design and construction of segmental concrete bridges (2nd ed.). Washington, DC: American Association of State Highway and Transportation Officials.

ABAQUS. (2008). Abaqus version 6.8. Providence, RI: Dassault Systems Simulia Corp.

ACI Committee 435. (1995). Control of Deflection in Concrete Structures. ACI Committee Report. Farmington Hills, MI: American Concrete Institute.

Anderson, B. (1977). Solar Energy: fundamentals in building design. New York: McGraw-Hill, Inc.

ASHRAE. (2005). ASHRAE Handbook of Fundamentals. Atlanta, GA: American Society of Heating, Refrigerating, and Air-Conditioning Engineers.

Barber, E. S. (1957). Calculation of Maximum Pavement Temperatures from Weather Reports. Highway Research Board Bulletin, 168, 1-8.

Barr, P. J., Stanton, J. J., & Eberhard, M. O. (2005, March-April). Effects of thermal variations on precast prestressed concrete bridge girders. Journal of Bridge Engineering, 10 (2), 186-194.

Branco, F.A. & Mendes, P.A. (1993, August). Thermal actions for concrete bridge design. Journal of Structural Engineering, 199 (9), 2313-2331.

Chapman, A. J. (1960). Heat transfer (2nd ed.). New York: Macmillan Company.

Churchward, A. & Sokai, Y. J. (1981). Prediction of temperatures in concrete bridges. Journal of Structural Engineering, 107 (11), 2163-2176.

CIBSE. (1985). CIBSE Guide H: Building control systems (1st ed.). Oxford, UK: Butterworth-Heinemann.

Clark, J. H. (1989). Evaluation of thermal stresses in a concrete box girder bridge. Doctoral dissertation, University of Washington.

Cooper, P. I. (1969). The absorption of solar radiation in solar stills. Solar Energy, 12 (3), 336.

Dilger, W. H., Ghali, A., & Cheung, M. S. (1981, November). Field Measurements of Muskwa River Bridge. Journal of Structural Division, 107 (11), 2147-2161.

Dilger, W. H., Ghali, A., Cheung, M. S., & Maes, M. A. (1983). Temperature stresses in composite box girder bridges. Journal of Structural Engineering, 109 (6), 1460-1478.

Duffie, J. A. & Beckman, W. A. (1980). Solar engineering of thermal processes. New York: John Wiley & Sons, Inc.

Elbadry, M. M. & Ghali, A. (1983, October). Temperature variation in concrete bridges. Journal of Structural Engineering, 109 (10), 2355-2374.

Elbadry, M. M. & Ghali, A. (1986, November-December). Thermal stresses and cracking of concrete bridges. Journal of the American Concrete Institute, 83 (6), 1001-1009.

Emanuel, J. H. & Hulsey, J. L. (1978). Temperature distributions in composite bridges. Journal of the Structural Division, 104 (1), 65-78.

Emerson, M. (1973). The calculation of the distribution of temperature in bridge (TRRL Report LR 561). Berkshire, UK: Transport and Road Research Laboratory.

Erbs, D. G., Klein, S. A., & Duffie, J. A. (1982). Estimation of the diffuse radiation fraction for hourly, daily and monthly-average global radiation. Solar Energy, 28 (4), 293-302.

FHWA. (2002). 2002 pavement design guide (FHWA-RD-00-129). McLean, VA: Federal Highway Administration.

FDOT. (1997). FDOT structures design guidelines. Tallahassee, FL: Florida Department of Transportation.

GDOT. (2005). GDOT bridge and structures design policy manual: revised July 2009. Atlanta, GA: Georgia Department of Transportation.

Ghali, A. & Elbadry, M. M. (1989, January-February). Serviceability design of continuous prestressed concrete structures. Journal of the Prestressed Concrete Institute, 34(1), 54-91.

Ghali, A., Favre, R., & Elbadry, M. (2002). Concrete structures: stresses and deformations (3rd ed.). London: Spon Press.

Gilland, J. A., & Dilger, W. H. (1997). Monitoring concrete temperature during construction of the confederation bridge. Canadian Journal of Civil Engineering, 24, 941-950.

Hirst, M. J. S. (1984). Thermal loading of concrete bridges. Canadian Journal of Civil Engineering, 11, 423-429.

Laszlo, G. & Imper, R. R. (1987, November-December). Handling and shipping of long span bridge beams. PCI Journal, 32 (6), 86-101.

Incropera, F. P. & Dewitt, D. P. (2002). Fundamentals of heat and mass transfer (5th ed.). Hoboken, NJ: John Wiley & Sons, Inc.

Jansen, T. J. (1985). Solar engineering technology. Englewood Cliffs, NJ: Prentice-Hall Inc.

Kennedy, J. B. & Soliman, M. H. (1987). Temperature distribution in composite bridges. Journal of Structural Engineering, 113 (3), 475-482.

Kreith, F. (1973). Principles of heat transfer. New York: Harper & Row.

Kreith, F. & Kreider J. F. (1978). Principles of solar engineering. Washington: Hemisphere Publishing Corp.

Kouremenos, D. A., Antonopoulos, K. A., & Doulgerakis, S. (1987). Direct and diffuse solar radiation correlations for tilted surfaces in Athens, Greece. Solar Energy, 38 (3), 203-217.

Kuehn, T. H., Ramsey, J. W., & Threlkeld, J. L. (1998). Thermal environmental engineering (3rd ed.). Upper Saddle River, NJ: Prentice-Hall Inc.

Leonhardt, F., Kolbe, G., & Peter, J. (1965, July). Temperaturunterschiede gefahrden spannbetonbrucke (Temperature differences endanger prestressed concrete bridge, translated into to English). Beton-undStahlbetonbau, 60 (7), 157-163. In German.

Li, D., Maes, M. A., & Dilger, W. H. (2004). Thermal design criteria for deep prestressed concrete girders based on the data from confederation bridge. Canadian Journal of Civil Engineering, 31, 813-825.

Liu, B. Y. H. & Jordan, R. C. (1960). The interrelationship and characteristic distribution of direct, diffuse, and total solar radiation. Solar Energy, 4 (1), 1-19.

Liu, B. Y. H. & Jordan, R. C. (1963). The long-term average performance of flat-plate solar energy collectors. Solar Energy, 7 (2), 53-74.

Marion, W. & Wilcox, S. (1991) Solar radiation data manual for flat-plate and concentrating collectors. Golden, Colorado: National Renewable Energy Laboratory

Mast, R. F. (1989, January-February). Lateral stability of long prestressed concrete beams – part 1. PCI Journal, 34 (1), 34-53.

Mast, R. F. (1993, January-February). Lateral stability of long prestressed concrete beams – part 2. PCI Journal, 38 (1), 70-83.

Mirambell, E., & Aguado, A. (1990, September). Temperature and stress distributions in concrete box girder bridges. Journal of Structural Engineering, 116 (9), 2388-2409.

Moorty, S., & Roeder, C. W. (1992, April). Temperature-dependent bridge movements. Journal of Structural Engineering, 118 (4), 1090-1105.

Neville, A. M. (1996). Properties of Concrete (4th ed.). New Jersey: John Wiley & Sons, Inc.

Oesterle, R. G., Sheehan, M. J., Lotfi, H. R., Corley, W. G., & Roller, J. J. (2007, November). Investigation of red mountain freeway bridge girder collapse (CTLGroup Project No. 262291). Final report to Arizona state department of transportation, CTLGroup.

PCI. (2003). PCI bridge design manual (2nd ed.). Chicago, IL: Precast/Prestressed Concrete Institute.

PCI. (2000). PCI tolerance manual for precast and prestressed concrete construction (1st ed.). Chicago, IL: Precast/Prestressed Concrete Institute.

Pisani, M. A. (2004, August). Non-linear strain distributions due to temperature effects in compact cross-sections. Engineering Structures, 26 (10), 1349-1363.

Priestley, J.N. (1976, September). Design Thermal Gradients for Concrete Bridges. New Zealand Engineering, 31 (9), 213-219.

Priestley, J.N. (1978, May). Design of concrete bridges for temperature gradients. ACI Journal, 75 (23), 209-217.

Roberts-Wollman, C.L., Breen, J.E., & Cawrse, J. (2002, May). Measurements of thermal gradients and their effects on segmental concrete bridge. Journal of Bridge Engineering, 7(3), 166-174.

Saetta, A., Scotta, R., & Vitaliani, R. (1995). Stress analysis of concrete structures subjected to variable thermal loads. Journal of Structural Engineering, 121 (3), 446-457.

Soliman, M. H. & Kennedy, J. B. (1986). Simplified method for estimating thermal stresses in composite bridges (Transportation Research Record 1072, p. 23-31). Washington, DC: National research council.

Suchinda, C. & Will, K. M. (1999, June). A temperature response measurement in fiber reinforced polymeric bridge decks. Proceedings of Sixth Annual International Conference on Composite Engineering. Orlando, FL.

Suchinda, C. (2000). Experimental and analytical investigation of the thermal behavior of a fiber reinforced polymeric bridge deck. Doctoral dissertation, Georgia Institute of Technology.

Threlkeld, J. L. (1970). Thermal environmental engineering, Englewood Cliff, NJ: Prentice-Hall Inc.

VanGreem, M.G., Gajda, J., & Dombrowski, K. (1997). Thermal properties of commercially available high-strength concretes. Cement, Concrete, and Aggregates, 19(1), 38-53.

Will, K. M. (1975). Analytical and experimental investigation of the thermal response of highway bridges. Doctoral dissertation, University of Texas at Austin.

Will, K. M., Johnson, C. P., & Matlock, H. (1977). Analytical and experimental investigation of the thermal response of highway bridges (Research Project 23-2). Interim report to Texas state department of highways and public transportation, University of Texas at Austin.

Williamson, P. J. (1967). Estimation of heat outputs for road heating installations (Road Research Laboratory Report 77). London, UK: Ministry of Transport.

Yazdani, N., Eddy, S. M., & Cai, C. S. (2000, May-June). Validation of AASHTO bearing stiffness for standard precast concrete bridge girders. ACI Structural Journal, 97 (3), 436-443.

Yazdani, N., Eddy, S. M., & Cai, C. S. (2000, August). Effect of bearing pads on precast prestressed concrete bridges. Journal of Bridge Engineering, 5 (3), 224-232.

Zuk, W. (1961, September). Thermal and Shrinkage Stresses in Composite Beams. ACI Journal, 58 (3), 327-340.

Zuk, W. (1965). Thermal Behavior of Composite Bridges—Insulated and Uninsulated. Highway Research Record 76, 231-253.

VITA

JONG-HAN LEE

Jong-Han Lee earned his B.S. and M.S. degrees in Civil Engineering in Korea. He conducted research involving structural dynamics and earthquake analysis associated with structure-soil-fluid interactions, as well as nondestructive evaluation in civil engineering structures. He earned his Ph.D. degree in 2010 in Civil Engineering at the Georgia Institute of Technology in Atlanta, Georgia. During his Ph.D. studies, he focused on the structural stability of reinforced and prestressed concrete bridge systems. This research involved the nonlinear behavior of the structure, the investigation of experimental and analytical methods, and the application of these methods to design.